

CHROMOPHORE-QUENCHER-BASED LUMINESCENCE PROBES FOR DNA

By

NANCY BYRNES THORNTON

A DISSERTATION PRESENTED TO THE GRADUATE SCHOOL
OF THE UNIVERSITY OF FLORIDA IN PARTIAL FULFILLMENT
OF THE REQUIREMENTS FOR THE DEGREE OF
DOCTOR OF PHILOSOPHY

UNIVERSITY OF FLORIDA

1995

Copyright 1995

by

Nancy Byrnes Thornton

To my parents Mary E. Leinfelder Byrnes and Edward E. Byrnes.

ACKNOWLEDGMENTS

I owe a great deal of thanks to those people who have supported and encouraged me to attain this degree including my family, particularly my parents Edward and Mary Byrnes, my very close friend Randy, my supervisor Dr. Kirk Schanze, Dr. James Deyrup, fellow group members (and friends) Brian Hauser, Lucian Lucia, Troy Bergstedt, Rich Burton, Yingsheng Wang, Karen Williamson and others who have worked in our laboratory. I also owe thanks to my friends Paul Wyness, Andrew and Victoria, Pam, Susan, Susannah, Janet, Max and my church which has helped me to develop a strong faith in God.

TABLE OF CONTENTS

ACKNOWLEDGMENTS.....	iii
LIST OF TABLES	vii
LIST OF FIGURES	ix
ABSTRACT	xiii
INTRODUCTION	1
Background.....	1
Fluorescent Probes.....	4
Binding Modes to DNA	9
DNA structure.....	9
Electrostatic binding	14
Groove binding	15
Intercalation.....	18
Alternative Probes: Electron Transfer and Energy Transfer Systems	25
Brief Description of Electron-Transfer Theory	26
Theory of Electronic Energy Transfer	31
Introduction.....	31
Radiative energy transfer.....	31
Nonradiative Energy Transfer	34
Coulombic Energy Transfer: Förster Mechanism.....	37
Electron-Exchange Energy Transfer	39
Description of the Present Study.....	41
REPTZ AND (PHEN)RECH ₂ Q COMPLEXES: PHOTOPHYSICAL AND DNA BINDING STUDIES	44
Introduction.....	44
Studies of RePTZ.....	46
Synthesis of RePTZ.....	50
Photophysical Characterization of RePTZ.....	52
UV-visible absorption.....	52
Steady-state emission spectra.....	55
DNA Titration Studies	60
Discussion of RePTZ Results.....	63
Studies of (phen)ReCH ₂ Q	67
Synthesis.....	68
Photophysical Characterization of (phen)ReCH ₂ Q.....	70
UV-visible absorption.....	70
Steady-state and time resolved emission	70
Transient absorption spectroscopy.....	78

Emission DNA Titrations.....	83
Discussion.....	90
RE-AN COMPLEXES: PHOTOPHYSICAL AND DNA BINDING STUDIES	94
Introduction.....	94
Experimental.....	102
Materials	102
Methods.....	102
Instrumentation.....	103
Syntheses.....	103
Results	106
Structures of the Re-An Complexes: ¹ H NMR.....	106
UV-Visible Absorption Spectra of the Complexes.....	107
DNA absorbance titrations.....	110
Emission Spectra of the Complexes.....	116
Steady-state emission DNA titrations for Re	122
Analysis of emission titration data for DNA binding parameters.....	122
Emission Decays.....	132
Emission Decays with DNA.....	135
Photophysics of AN moiety.....	139
Steady-state emission studies of AN	139
Emission decays for AN moiety	146
Transient absorbance studies	148
Discussion.....	157
Photophysics of Re-An Complexes.....	157
General UV-visible and emission characteristics.....	157
TT ENT quenching of MLCT state	158
Energy transfer quenching of AN : Coulombic mechanism	163
DNA binding studies	166
Absorption titrations.....	167
Emission DNA titrations	170
DNA binding constants from emission titrations.....	171
Conclusions.....	182
EXPERIMENTAL	185
Materials and Syntheses.....	185
(1) Synthesis of BpyRePTZ Complex	186
β-(10-phenothiazyl)propionitrile (PTZpnCN) (1)	186
3-(10H-phenothiazine-10)propionic acid (PTZpnCOOH) (2).....	186
1-[3-(10H-phenothiazine-10)propanoyloxy]-2,5-pyrrolidinedione (PTZpnOSU) (3)	187
N-4-(3-(10H-phenothiazine-10)propanoyl)aminomethylpyridine (PTZpnpyr) (4)	187
fac-(bpy)ReI(CO) ₃ -PTZ (5)	188
Synthesis of (phen)ReCH ₂ X Complexes.....	189
(phen)Re(CO) ₃ CH ₂ B	189
(phen)Re(CO) ₃ CH ₂ Q	190
Synthesis of Re-An Complexes.....	191
Synthesis of Anthryl Ligands.....	191
Pyr3An.....	191
N-(4-pyridyl)methyl-(N-(9-anthryl)methyl)amine (pyr3An)	191

Pyr6An.....	192
(a) N'-(4-Pyridyl)methyl N-CBZ- β -aminoethylamide (pyrGlyCBZ)	192
(b) N-(4-Pyridyl)methyl β -aminoethylamide (pyrGlyNH)	192
(c) N-(4-Pyridyl)methyl β -[N'-(9-anthryl)methyl]aminoethylamide (pyr6An).....	193
Pyr8An.....	194
(a) N'-(4-Pyridyl)methyl N-CBZ- γ -aminobutyramide (pyrGabCBZ).....	194
(b) N-(4-Pyridyl)methyl γ -aminobutyramide (pyrGabNH).....	194
(c) N-(4-Pyridyl)methyl γ -[N'-9-anthryl)methyl]aminobutyramide (pyr8An).....	195
Pyr10An	195
(a) N'-(4-Pyridyl)methyl N-CBZ- ϵ -aminohexanamide (pyrCapCBZ)	195
(b) N-(4-Pyridyl)methyl- ϵ -aminohexanamide (pyrCapNH).....	196
(c) N-(4-Pyridyl)methyl- ϵ -[N'-(9-anthryl)methyl]aminohexanamide (pyr10An).....	196
Metal Complexes	197
Re3An.....	198
Re6An.....	198
Re8An.....	199
Re10An	200
Methods	201
RePTZ and (phen)ReCH ₂ Q solutions: Chapter 2.....	201
Re-An solutions: Chapter 3.....	201
DNA preparation.....	201
General conditions for experimental studies.....	206
RePTZ and (phen)ReCH ₂ Q DNA titrations	206
Re-An DNA titrations	206
Instrumentation	206
UV-visible absorbance and steady-state emission	206
Emission decays	208
Transient absorption.....	208
APPENDIX A.....	210
DNA Binding Analyses	210
Binding Equilibria from Spectroscopic Methods	210
Method I.....	213
Steady-State Emission DNA Titrations	216
Method II.....	216
Method III.....	219
APPENDIX B	226
Emission QY and Lifetime Data for ³ MLCT* State of Re-An Complexes from DNA Titrations	226
LIST OF REFERENCES	228
BIOGRAPHICAL SKETCH.....	238

LIST OF TABLES

<u>Table</u>	<u>page</u>
2.1. UV-Visible Absorption Characteristics of RePTZ and ReCH ₂ B Model.....	54
2.2 Steady-State Emission Characteristics of RePTZ with and without DNA.....	57
2.3 Steady-State Emission Lifetimes of RePTZ and Model.	59
2.4 UV-Visible Absorption Characteristics of (phen)ReCH ₂ Q and (phen)ReCH ₂ B.	72
2.5 Steady-State Emission Characteristics of (phen)ReCH ₂ Q and (phen)ReCH ₂ B with and without DNA.	74
2.6 Emission Lifetimes of (phen)ReCH ₂ Q and (phen)ReCH ₂ B.....	76
2.7 Transient Absorption Decay Rates and Electron-Transfer Data.....	81
3.1 Absorbance Transitions and Molar Absorptivities of Re-An compounds.	109
3.2 Absorbance Changes of Re-An Compounds with DNA.	115
3.3 Absorbance Titration Binding Parameters According to Method I.	117
3.4 Steady-State Emission Characteristics of Re-An Compounds in Solution.	121
3.5 Steady-State Emission Characteristics of ³ MLCT* state in Re-An Compounds with DNA.....	127
3.6 DNA Binding Parameters for Re-An Complexes and ANMOD from Emission QY Data.....	130
3.7 Emission Lifetimes of ³ MLCT* state in Re-An Compounds and ReCH ₂ B.....	134
3.8 Steady-State Emission Characteristics of ¹ AN* in Re-An Compounds with and without DNA.	143
3.9 Emission Lifetimes of ¹ An* state in Re-An Compounds.....	147
3.10 Transient Absorbance Lifetimes and Decay Rates of ³ AN* and ³ MLCT*	152
3.11 Relative Transient Absorbance Intensities at 426 nm.....	154
3.12 Rate Constants for E _N T in Re-An Complexes.	161

3.13 DNA Binding Parameters for Re-An Complexes and Model.....	168
3.14 Literature Binding Parameters for DNA Intercalators with Calf Thymus DNA....	173
B.1 Steady-State Emission QY's for Re-An Complexes from DNA Titrations.	227
B.2 Emission Lifetimes of $^3\text{MLCT}^*$ state for Re-An Complexes from DNA Titrations.	228

LIST OF FIGURES

<u>Figure</u>	<u>page</u>
1.1. Jablonski Diagram.....	3
1.2 Dye Molecules whose fluorescence increases upon binding to DNA.	6
1.3 DNA binding molecules whose fluorescence decreases upon binding.....	7
1.4 Structure of Ruthenium and Rhodium transition-metal complexes which serve as DNA probes.	8
1.5 Non-covalent binding of small molecules to double-stranded DNA.	10
1.6 Crystal structure diagram of double-stranded B DNA.	11
1.7 Diagram of structures of DNA bases, sugar and phosphodiester linkages along with base pairing patterns.....	12
1.8 Illustrations of molecules binding in the minor groove of DNA.....	16
1.9 Structures of groove-binding molecules.....	17
1.10 Crystal structure diagram of duanomycin-d(CpGpTpApCpG) complex.....	20
1.11 Computer-generated models of neighbor exclusion binding rule obeyed and violated.....	22
1.12 Enhanced ET reactivity of excited states.	28
1.13 Diagram of spectral overlap integral.	33
1.14 Illustrations of Coulombic and Electron Exchange energy transfer interaction.....	36
2.1 Diagram of intramolecular ET quenching mechanisms in Re-Q complexes.	45
2.2 Structures of RePTZ, (phen)ReCH ₂ Q and models.....	47
2.3 Derivatives of PTZ and proposed mechanisms of reactivity of chlorinated PTZ derivatives.	49
2.4 Synthetic scheme for RePTZ.....	51
2.5 UV-Visible absorption spectra for ReCH ₂ B, RePTZ and pyrrpPTZ ligand.....	53
2.6 Steady-state emission spectra for ReCH ₂ B, RePTZ and PTZ ligand.	56

2.7 Transient absorption spectrum of RePTZ.	61
2.8 Steady-state emission DNA titration of RePTZ with CT DNA.	62
2.9 Computer-generated models of conformations of CPZ and CPZ sulfoxide.....	66
2.10 Synthetic scheme for (phen)ReCH ₂ Q.....	69
2.11 UV-Visible absorption spectra of (phen)ReCH ₂ B and (phen)ReCH ₂ Q.....	71
2.12 Steady-state emission spectra of (phen)ReCH ₂ Q and (phen)ReCH ₂ B.....	73
2.13 Computer-generated projection of three-dimensional structure of (bpy)ReCH ₂ Q. .	77
2.14 Transient absorption spectra of (phen)ReCH ₂ B in CH ₃ CN and 30% MeOH/buffer solutions.	79
2.15 Transient absorption spectra of (phen)ReCH ₂ Q in CH ₃ CN and 30% MeOH/buffer solutions.	80
2.16 Steady-state emission DNA titration of (phen)ReCH ₂ Q with CT DNA.....	84
2.17 Changes in emission QY's for (phen)ReCH ₂ Q with increasing DNA concentration.	86
2.18 Transient absorption spectra for (phen)ReCH ₂ Q in the presence of DNA.....	89
2.19 Stern-volmer plot for quenching of (phen)ReCH ₂ B by Fe(CN) ₆ ³⁻ in the absence and presence of DNA.....	91
2.20 Molecular modeling study of (phen)ReCH ₂ Q binding to DNA	112
3.1 Structures of Re-An complexes and models.	96
3.2 Excited state energy schemes for Re-An complexes and models.	98
3.3 Electron exchange energy transfer interaction.....	100
3.4 Effect of DNA intercalation on intramolecular quenching by exchange energy transfer.	101
3.5 Synthetic scheme for Re10An, Re8An and Re6An.	104
3.6 Synthetic scheme for Re3An.....	105
3.7 UV-visible absorption spectra of Re6An and models.....	108
3.8 UV-visible absorption titrations of Re8An and ANMOD with CT DNA.	111
3.9 Changes in long-λ region of UV-visible absorption spectra of Re-An complexes with increasing DNA additions.....	113
3.10 Reciprocal plots of changes in UV-visible absorbance intensities at 388 nm for the Re-An complexes with increasing DNA additions.....	114

3.11	Overlays of steady-state emission spectra of Re10An and models- normalized and relative intensities.	118
3.12	Steady-state emission spectra of Re-An complexes in solution.	120
3.13	Steady-state emission DNA titration of Re10An with CT DNA.....	123
3.14	Steady-state emission DNA titration of Re8An with CT DNA.	124
3.15	Steady-state emission DNA titration of Re6An with CT DNA.	125
3.16	Steady-state emission DNA titration of Re3An with CT DNA.	126
3.17	Plot of changes in steady-state ³ MLCT* emission QY's of Re-An complexes with increasing DNA concentrations.	128
3.18	Plot of changes in median ³ MLCT* emission lifetimes of Re-An complexes with increasing DNA concentrations.	137
3.19	Plots of changes in $\tau_1 \times \alpha_1$, $\tau_2 \times \alpha_2$ and $\tau_3 \times \alpha_3$ for Re-An complexes with increasing DNA concentrations.	138
3.20	Plots of relative changes in $\tau_i \times \alpha_i$ with increasing DNA/Re ratios within each Re-An complex.....	140
3.21	Plot of changes in the steady-state ¹ AN* emission QY's of the Re-An complexes with increasing DNA concentrations.	142
3.22	Steady-state emission spectra of ¹ AN* fluorescence bands of Re-An complexes in the absence and presence of DNA.	145
3.23	Transient absorption spectra of ANMOD in the absence and presence of DNA... ..	149
3.24	Transient absorption spectra of Re6An in the absence and presence of DNA.	150
3.25	Transient absorption spectra of Re10An in the absence and presence of DNA....	151
3.26	Spectral overlap for ³ MLCT* emission and ³ AN absorption spectra, and ¹ AN* fluorescence and Re MLCT absorption spectra.	160
3.27	Excitation emission spectra of Re10An, Re6An and ReCH ₂ B normalized to their absorption spectra.....	164
3.28	Structures of AN derivatives listed in Table 3.14.....	175
3.29	Computer modeled structure of mitoxantrone intercalated in a tetradeoxynucleotide duplex.....	177
3.30	Crystal structure based diagrams of proflavin intercalated in dCpG and CpG.	178
4.1	¹ H NMR spectra of Re3An and pyr3An ligand.....	202

4.2 ^1H NMR spectra of Re6An and pyr6An ligand.....	203
4.3 ^1H NMR spectra of Re8An and pyr8An ligand.....	204
4.4 ^1H NMR spectra of Re10An and pyr10An ligand.....	205
A.1 Method I absorption titration binding plots for Re10An and Re8An.	214
A.2 Method I absorption titration binding plots for Re6An and Re3An.....	215
A.3 Igor curve fits to experimental emission DNA titration QY data for Re10An and Re8An.....	217
A.4 Igor curve fits to experimental emission DNA titration QY data for Re6An and Re3An.....	218
A.5 Method II emission DNA titration binding analyses for Re10An and Re8An.	220
A.6 Method II emission DNA titration binding analyses for Re6An and Re3An.....	221
A.7 Method III emission DNA titration binding analyses for Re10An and Re8An.	224
A.8 Method III emission DNA titration binding analyses for Re6An and Re8An.....	225

Abstract of Dissertation Presented to the Graduate School
of the University of Florida in Partial Fulfillment of the
Requirements for the Degree of Doctor of Philosophy

CHROMOPHORE-QUENCHER-BASED LUMINESCENCE PROBES FOR DNA

By

Nancy Byrnes Thornton

May, 1995

Chairman: Kirk S. Schanze
Associate Professor of Chemistry
Major Department: Organic Chemistry

The purpose of the present study is to apply a novel approach to the detection of nucleic acids by utilizing the spectroscopic and photophysical properties of rhenium-based chromophore-quencher (CQ) complexes which also possess the ability to bind to DNA. The complexes are composed of the *fac*-(b)Re^I(CO)₃-L chromophore (where (b) is a bidentate diimine ligand) covalently attached by way of a flexible linker chain to either an energy acceptor (anthracene) or electron donor / acceptor moiety (phenothiazine or dimethylaniline) designated the quenching species (Q). Rhenium-based CQ complexes have been extensively studied in regards to their rates of electron transfer and energy transfer and the factors affecting their photophysical properties. However, systems of this type have not been exploited for their potential bio-medical applications.

The structural design of the CQ complexes consists of two possible approaches: (system I) where the linked quenching (Q) molecule also serves as a DNA intercalator, or (system II) where the diimine ligand directly attached to the Re chromophore is responsible for binding to DNA while the Q moiety attached through the flexible linker is strictly a

quenching species and does not participate in intercalative binding. The premise operating behind their design rests on the assumption that in solution the emission from the Re chromophore in the CQ complexes would be highly quenched due to energy transfer or electron transfer to or from Q. However, upon binding to double stranded DNA contact between Re and Q would be hindered by the bulky helix and therefore would result in a reduction in quenching and an increase in Re emission. Essentially this mimics the turning on of a light switch upon attachment to nucleic acids. Important aspects of these studies include (1) the emphasis placed on characterizing the DNA binding of these complexes through changes in their photophysical, particularly luminescent, properties and (2) relying on an intercalative interaction as the major binding force to ds DNA.

Photophysics of three different types of CQ systems are studied in solution and in the presence of calf-thymus (CT) DNA. In the case of the first two complexes examined, (b)RePTZ (b = bipyridyl, PTZ = phenothiazine) a type I system and phenReCH₂Q (phen = 1, 10-phenanthroline) a type II system, their mechanisms of quenching operate through reductive ET from the attached quencher to photo-excited Re. The third, and most comprehensive, study examines the photophysics and DNA binding of a series of (b)Re-AN (b = bipyridyl, AN = anthracene) energy transfer (E_NT) CQ complexes which are of the type I system. By varying the length of the flexible linker chain between Re and AN with 3, 6, 8 and 10 atoms, the distance dependence of the E_NT mechanism is examined as well as the DNA binding strengths of the different complexes. The studies reveal that MLCT luminescence of all, except the shortest-chained CQ molecule, undergo profound increases in intensity upon interaction with calf thymus DNA. The increases follow the order Re10An > Re6An > Re8An >> Re3An, where Re10An and Re6An show the largest emission quantum yields at high DNA concentrations. However, their binding strengths follow the order Re8An > Re10An > Re6An > Re3An according to analyses of UV-vis absorption and emission DNA titration data. Differences in binding are attributed to the length and nature of the chain linking the Re and An chromophores.

CHAPTER 1 INTRODUCTION

Background

In this age of the genetic revolution the once enigmatic term DNA (deoxyribonucleic acid) has now become a well-known household topic. Most commonly it has been linked with the cause and treatment of the disease cancer. However, more recently DNA has been taking precedence in the headlines concerning genetic engineering, forensic evidence, paternity suits, and criminal profiles.¹ The Human Genome Project,² headed by Dr. Francis Collins at the National Institute of Health, was initiated in 1987 and is federally funded for 15 years with the primary goal of creating a map of the entire human genome. The outcome of this project, while tied into explosive moral issues, has extensive potential in aiding the battle against human disease. Already genes responsible for breast cancer, some forms of colon cancer, Huntington's disease, Lou Gehrig's disease and cystic fibrosis, among others, have been located. Efforts are being channeled, as well, into new methods of treatment for those diseases which once were certain sentences to a slow and painful death. With all this focus on understanding the mysteries of our genetic makeup, and using this new-found information towards improving the quality of life, there is much need to create more advanced technologies which can aid in accomplishing these objectives. Among the many methods currently available to molecular biology, fluorescence detection techniques have become increasingly important in the study of DNA and the interactions of small molecules and proteins with DNA. Fluorescence, or luminescence, is particularly useful for these purposes due to the inherent sensitivity of its signals to the local environment of the fluorophore, the favorable time scale of the process ($\sim 10^{-8}$ sec) and its high detection sensitivity towards small quantities of material down to the pico-gram level.

For those unfamiliar with luminescence, it is the emission of photons (light) from electronically excited states of a chromophore.³ The excited states are generated by absorption of light that is of sufficient energy to promote an electron from a lower energy orbital to a higher-energy empty orbital. The process is illustrated in Figure 1.1. There are two types of luminescence which can occur from an excited chromophore depending on the spin of the promoted electron. Normally in the ground (unexcited) state (S_0) of a chromophore the electrons in its highest occupied orbital (HOMO) are paired with opposite spins (Pauli principle). Upon excitation one of the electrons is promoted to the lowest unoccupied orbital (LUMO) with its spin remaining in an orientation opposite to the second electron in the lower orbital (Figure 1.1b). This configuration is called the first excited singlet state (S_1). If the electron returns directly back to the ground state from S_1 by releasing its excess energy in the form of a photon, $-h\nu$, this process is called fluorescence. Alternatively, the electron in S_1 can intersystem cross (isc) to a lower energy configuration where its spin flips to an orientation that is of the same spin as the second electron in the lower orbital (Figure 1.1c). This is the triplet state (T_1) and its lower energy is a result of reduced spin - spin repulsion between electrons occupying different orbitals when their spins are parallel (Hund's rule of maximum multiplicity). Relaxation of the excited electron from T_1 to the ground state S_0 by emission of light is termed phosphorescence. According to selection rules this is a spin-forbidden process since the electron has to change its spin from parallel to anti-parallel with respect to the second electron in the process of returning to the ground state. Due to this spin-forbiddenness the time scale of phosphorescence is typically in the range of $\sim 10^{-6}$ to 1 second while fluorescence occurs much more rapidly with a considerably shorter time scale in the range of $\sim 10^{-7}$ to 10^{-12} seconds.⁴ In either case, while the electron remains in the excited state there is sufficient time for events to occur such as solvent-cage relaxation, protonation or deprotonation reactions, local conformational changes, processes coupled to translational and rotational motion, and electron-transfer or energy-transfer reactions.

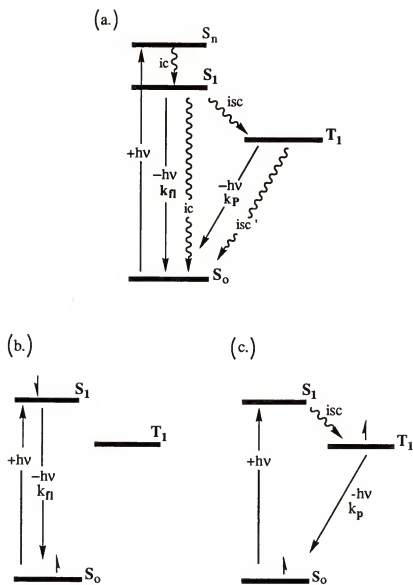


Figure 1.1. (a.) Jablonski diagram for excited-state processes which can occur in a chromophore. (b.) Electronic spin configuration for first excited singlet state prior to fluorescence. (c.) Electronic spin configuration for excited triplet state prior to phosphorescence.

A number of luminescent signal changes can be monitored including fluorescence intensity, quantum yield, emission maximum, luminescence lifetime, fluorescence anisotropy, and rotational correlation time.⁵ It has been demonstrated that applications such as gel-based electrophoresis, which is used in gene mapping, genome fingerprinting, restriction fragment sizing, forensics, and studies of DNA-binding proteins, can use highly fluorescent DNA-binding dyes for sensitive detection in the band-shift analyses.^{6,7} A newly developed separation technique, capillary array electrophoresis,^{8,9} relies on a laser-excited confocal fluorescence detection system that scans across capillary arrays. Light scattering techniques,¹⁰ and more recently fluorescence microscopy,¹¹ are optical methods which measure scattered light or fluorescence from bound dyes to observe the shapes of DNA molecules in solution. Fluorescence imaging is a rapidly expanding field that utilizes fluorescent dyes to image the genetic material¹² as well as other constituents^{13,14} in cells, follow cellular processes,^{13,14} locate and visualize the interior of tumors,¹⁵ and even study muscular contractions.¹⁶ Steady-state fluorescence spectroscopy has been widely applied to drug-DNA binding studies. The information gained from methods based on this technique has been instrumental to the fields of biochemical pharmacology and medicinal chemistry towards advancing knowledge concerning the biological targets and mechanisms of activity of anticancer cancer drugs.

Fluorescent Probes

A large variety of luminescent chromophores exist and many have been applied in studies of biological systems. Additionally several methods are available by which the probes can be attached to their targets. Proteins are frequently labeled with dansyl chloride, fluorescein or rhodamine dyes through covalent attachment to lysine and cysteine amino acids on the protein. By monitoring changes in the fluorescence polarization, circular dichroism and emission of the dye, associations of small molecules with proteins can be

examined.^{17,18,19} Covalently attached probes have also been useful in studying the movements of muscle proteins.²⁰

The most widely used probe for studying nucleic acids has been ethidium bromide (EB).^{21,22,23,24} In aqueous solution EB has the convenient property of having very weak fluorescence but upon binding to DNA its emission intensity increases dramatically (see Figure 1.2 for structure). This "light switch" property allows the quantitation of nucleic acids without having to remove from solution those dye molecules which are not bound. Acridine orange²⁵ and more recently dimeric complexes of EB, thiazole orange (TOTO) and oxazole yellow (YOYO)^{6,7,26} have been used extensively in electrophoretic assays and for quantitation of DNA in solution due to their substantial increases in fluorescence upon binding to nucleic acids.

In contrast, organic molecules such as (9-anthrylmethyl)ammonium chloride,²⁷ derivatives of pyrene,^{28,29} and the anthracycline antibiotics daunomycin³⁰ and adriamycin^{31,32} show dramatic decreases in fluorescence quantum yields and lifetimes when bound to DNA (Figure 1.3). These changes in emissive properties provide information pertaining to the degree and type of DNA interaction of these molecules and, as a result, can lead to rational design of more effective therapeutic agents. Cationic transition-metal complexes containing planar aromatic ligands such as the complexes $[\text{Ru}(\text{bpy})_2(\text{phi})]^{2+}$ ($\text{bpy} = 2,2'$ -bipyridyl, $\text{phi} = 9,10$ -phenanthrene-quinonediimine),³³ $[\text{Rh}(\text{phen})_2(\text{phi})]^{3+}$ ($\text{phen} = 1,10$ -phenanthroline),^{34,35,36} $[\text{Ru}(\text{bpy})(\text{hat})_2]^{2+}$ ($\text{hat} = 1,4,5,8,9,12$ -hexaazatriphenylene)³⁷ bind to DNA with differential changes in their emissive properties (Figure 1.4). Additionally these metal complexes exhibit shape selectivity for certain types of nucleic acids, and in the case of $\text{Rh}(\text{phen})_2(\text{phi})^{3+}$, cause cleavage of the DNA stands. Therefore they can serve as probes for recognition between right- and left-handed helices and as photonucleases.

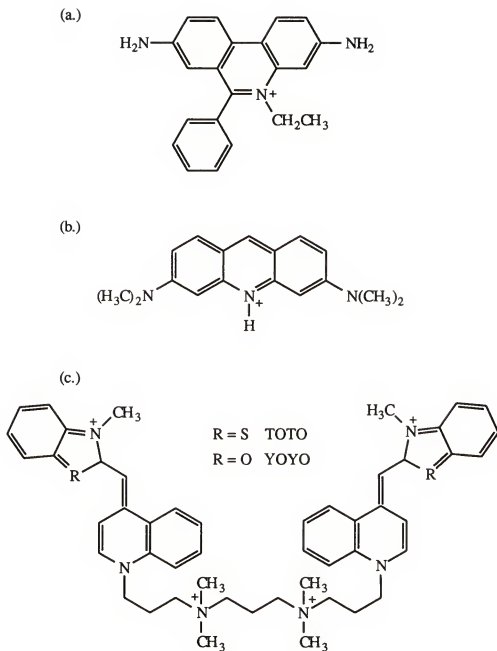
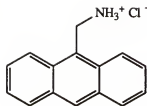
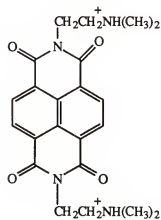


Figure 1.2. Dye molecules whose fluorescence increases upon binding to DNA. (a) Ethidium Bromide; (b) Acridine Orange; (c) homodimeric complexes of Thiazole Orange (TOTO) and Oxazole Yellow (YOYO).

(a.)



(b.)



(c.)

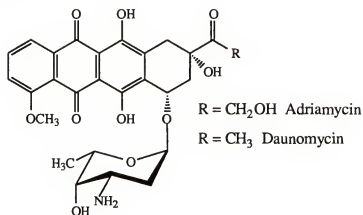


Figure 1.3. DNA binding molecules whose fluorescence decreases upon binding. (a) 9-AMAC; (b) a pyrene derivative; (c) anthracycline antibiotics Adriamycin and Daunomycin.

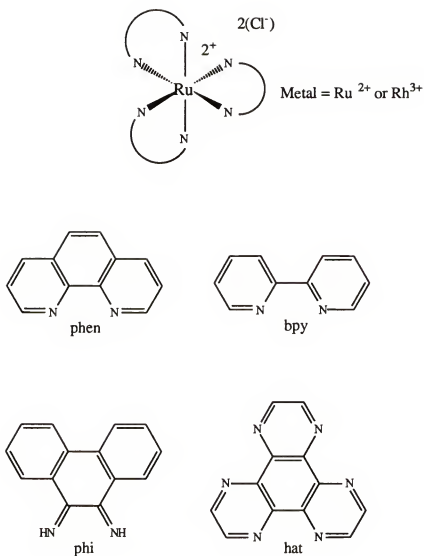


Figure 1.4. Structure of Ruthenium and Rhodium transition-metal complexes which serve as DNA probes. Diimine ligands are shown below the metal structure. Different complexes mentioned in text are $[\text{Ru}(\text{bpy})_2(\text{phi})]^{2+}$, $[\text{Rh}(\text{phen})_2(\text{phi})]^{3+}$, and $[\text{Ru}(\text{bpy})(\text{hat})_2]^{2+}$.

Binding Modes to DNA

All the above mentioned DNA binding chromophores have, in addition to fluorescent properties, another convenient characteristic in common with each other. They all noncovalently bind to DNA by way of intercalation. First described by Lerman in 1961,³⁸ intercalation is a noncovalent interaction with double-stranded (ds) DNA where a flat or relatively planar polycyclic aromatic molecule slides in-between adjacent base pairs of the DNA helix in a sandwich-type fashion. The process is illustrated in Figure 1.5a. Intercalation is one of three noncovalent modes by which molecules tend to interact with (ds) nucleic acids. For comparison examples of groove binding (Figure 1.5b) and electrostatic association (Figure 1.5c) are also displayed.³⁹ Intercalation is inherently useful because it is noninvasive, no physical attachment step is required, and has been shown to be strong enough an interaction to withstand electrophoretic mobility assays.^{6,7} Additionally intercalation is one of the most important binding modes through which coplanar polycyclic compounds exert their biological activity.

DNA structure

In solution nucleic acids tend to form a double-helical structure where each strand is composed of polynucleotide units, purine and pyrimidine bases each attached to a pentose sugar, that are joined through phosphodiester linkages (Figures 1.6 and 1.7). The two strands run in opposite direction to each other, 3' → 5' and 5' → 3'. The bases consist of the pyrimidines thymine (T) and cytosine (C), and the purines adenine (A) and guanine (G). Important characteristics of native DNA are that the concentration of purine bases equals the concentration of pyrimidine bases, and the concentrations of adenine and thymine are equal, as are the concentrations of guanine and cytosine. The base composition (percent G + C) varies among species but is the same or closely the same in all cells of an organism and within a species, which for animals is ~ 40 %.⁴⁰ According to the Watson and Crick⁴¹ model of the three-dimensional structure of DNA, at physiological conditions the polynucleotide chains form a right-handed double helix with the bases located on the

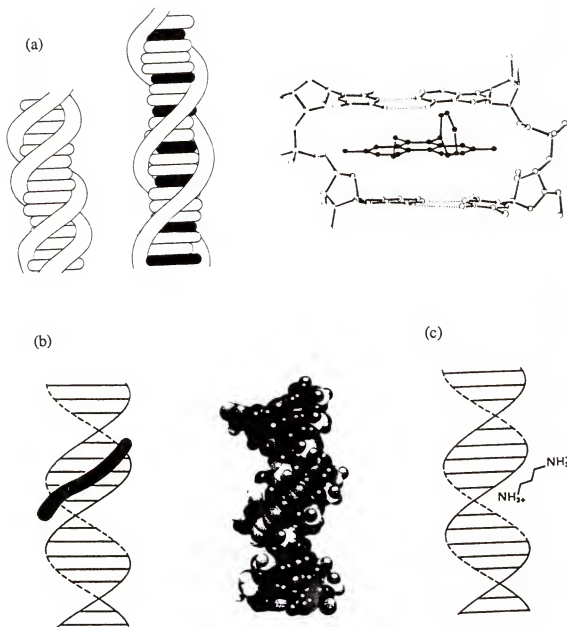


Figure 1.5. Non-covalent binding of small molecules to double-stranded DNA. (a) (top left) Intercalation where a molecule binds by sliding in-between base pairs in a sandwich-type fashion causing lengthening of the helix. (top right) X-ray structure of a complex of ethidium intercalated between base pairs of a dinucleotide (Tsai, C. C., et al. *Proc. Natl. Acad. Sci. USA*, 1975, 72, 628.); (b) Groove binding (far left bottom) showing a schematic of a molecule lying inside the groove and (middle) model structure of Hoechst 33258 bound in the minor groove of CGCGAATTCGCG (Goodsell, D. S., *RMS. J. Mol. Graphics*, 1988, 6, 39-44.); (c) electrostatic association (right bottom) in which a cation is loosely associated with the outside of the helix attracted to the negatively charged phosphate groups.

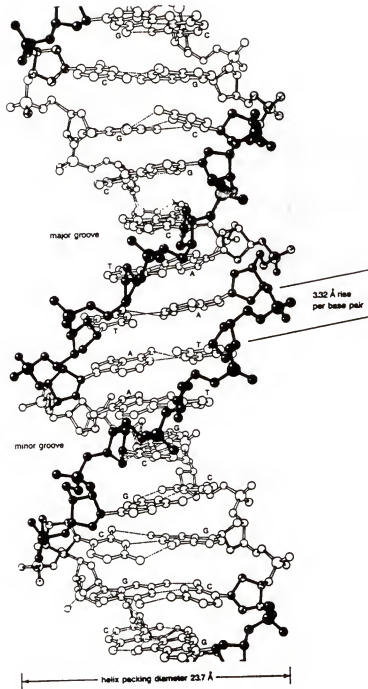


Figure 1.6. Tertiary structure of double-stranded B DNA (right-handed helix) drawn from crystal structure data showing the major and minor grooves, the spacing and orientation of the bases in relation to the helical axis, and their base pairing patterns. From *Practical Handbook of Biochem. & Molec. Biol.*; Fasman, G. D. (eds); CRC Press; Boca Raton, Fla., 1989. Original reference Dickerson et al., *Nucleic Acids Res., Future Dev., [Proc. Symp.]*; 1981, 35 - 39.

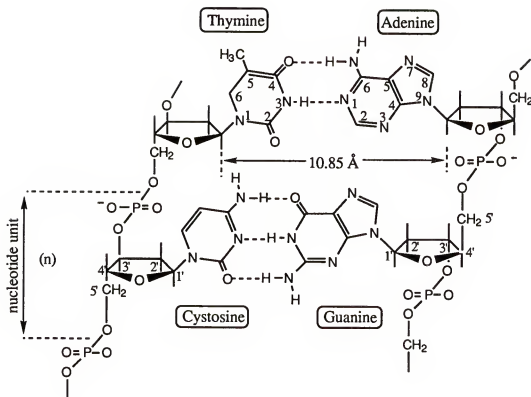


Figure 1.7. Structures of DNA bases, sugar and phosphodiester linkages which make up the nucleotide units. The base pairing patterns are also displayed.

inside and the negatively charged phosphodiester backbone facing outward. This right-handed helical structure of ds nucleic acids, termed B-DNA, is the most common form of native DNA found under physiological conditions. The bases are spaced 3.4 Å apart along each chain and there are ~10 base pairs per helical turn resulting in a pitch height of 34 Å.⁴² Nucleic acids are found in other structures such as in a left-handed helix (Z-DNA) or with different degrees of spacing between bases; however, less is known about these forms and about their physiological significance.

Studies indicate that the driving force for formation of the helix is mainly hydrophobic⁴³ in nature. In addition to the intermolecular stacking forces experienced between the hydrophobic bases in the monomers, there is overall release of free energy from the reduction of surface area exposed to the aqueous solvent and from release of bound water molecules through aggregation of the polymeric strands. Additionally, aggregation results in a reduction of surface tension which also contributes to the helix formation. Other forces which most strongly stabilize the helix are hydrogen bonding between adjacent base pairs (horizontal to the plane of the bases) and base stacking interactions (perpendicular to the plane of the bases). The hydrogen bonds between bases on opposite strands are of the type N-H...N and N-H...O. Guanine and cytosine form three complementary H-bonds while adenine and thymine can only form two H-bonds (Figure 1.7). Importantly this complementarity is the basis of the genetic code. Stacking forces are a combination of van der Waals (dipole-dipole, dipole-induced dipole and π -electronic interactions) and London dispersion energies which occur between the ordered array of vertically stacked heterocyclic bases. The stabilization from stacking forces depends on the base composition and sequence. Studies show that the strength of this interaction between the bases follows the trend purine - purine > pyrimidine - purine > pyrimidine - pyrimidine.^{44,45} These attractive forces arise from electrokinetic interactions between the closely-spaced bases. Dipoles that are created due to fluctuations in electronic charge distributions in one molecule polarize the electronic system of neighboring

molecules. This causes the formation of induced parallel dipoles which attract each other, and decrease with the sixth power of the distance between them. The forces are attractive and increase with the product of the polarizabilities of the paired molecules. Additionally if one or both of the molecules also possesses a permanent dipole moment, the combination of the two forces leads to significant effects which are more pronounced in the purine bases than in the pyrimidine bases.

Electrostatic binding

The DNA polymer, as mentioned above, is charged due to the negatively-charged phosphate groups which link the deoxyribose units of the nucleotides. In order for the ds helix to be stable in solution it exists paired with cations to counterbalance the repulsion of the negative charges. This process is called counter-ion condensation and theory predicts an average of 0.76 monovalent counterions condensed per phosphate group.^{46,47,48} In solution associated ions, such as Na^+ , are responsible for reducing the effective charge of the ds polymer and therefore have a large influence on its solution properties and binding interactions. If the salt concentration is too low ($\text{Na}^+ < 0.1 \text{ mM}$)⁴⁹ the double-helical structure will be destabilized by the charge repulsion between phosphates thus causing denaturation to occur. High salt conditions can result in aggregation of the polymer and possible triple helix formation.^{50,51} The number of counterions condensed per DNA phosphate group is known to remain constant over a wide range of ionic strengths. This will affect the equilibrium constant for binding of molecules to DNA since at high salt concentrations the association kinetics will be reduced. Simple cations such as Mg^{2+} or small polyamines $[\text{H}_3\text{N}(\text{CH}_2)_3\text{NH}_3]^{2+}$ interact with DNA by way of outside electrostatic association. The mechanism of this "binding" is a nonspecific condensation reaction involving exchange with the counterions (i.e. Na^+) associated with the DNA helix in solution. The energy resulting from ion pair formation with the nucleic acids, and increased entropy due to the release of counterions contributes in a large part to the binding free energy of all cationic species with DNA.⁵² Thus any cationic molecule can initially

associate with DNA by way of a condensation reaction. However, for simple cationic species that interact only by this electrostatic mode they will be associated in a nonspecific, loosely held complex moving along the outside of the helix and involved in a rapidly exchanging equilibrium.

Groove binding

Binding inside the groove of the double helix, a second type of noncovalent interaction molecules tend to have with ds nucleic acids (Figures 1.5b and 1.8), has been extensively studied due to the sequence specificity inherent in this binding mode. The drug-DNA complex is stabilized through a mixture of hydrogen-bonding, electrostatic and hydrophobic contacts. Generally groove binding molecules are multiply cationic and contain small aromatic groups such as pyrrole, furan and benzene which are linked through polypeptide and methylene chains. The linkages, in addition to providing hydrogen-bonding moieties, supply torsional freedom for fitting the twist of the helical groove. Examples of well characterized groove binders include the natural products distamycin^{53,54,55} (binds selectively to AT-rich sequences in minor groove) and netropsin,^{56,57} and synthetic compounds such as Hoechst 33258,^{58,59} pentamidine,^{57,60} and DAPI⁶¹ (see Figure 1.8). Netropsin and distamycin are known antiviral antibiotics, Hoechst 33258 is an antibiotic and chromosome stain, pentamidine has been used extensively for treatment of *P. carinii* pneumonia,⁶² and DAPI is a trypanocide but is used mainly as a DNA probe due to its large increase in fluorescence upon binding to ds DNA.⁶³ All of these compounds bind to AT-rich (adenine-thymine) regions of the DNA minor groove, a characteristic which is largely common for most groove binding small molecules. This is explained on the basis that the smaller more narrow minor groove (~ 5.7 Å wide and 7.5 Å deep for B DNA),⁴² compared to the major groove (~11.7 Å wide and 8.5 Å deep for B DNA), more closely fits the aromatic chains to form van der Waals contacts along the floor of the groove. The preference for AT-rich regions has been attributed to the fact that (1) AT-rich regions relative to GC-rich (guanine-cytosine) regions

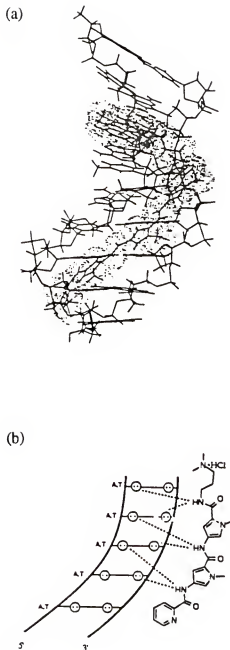


Figure 1.8. (a) Energy-minimized molecular modeling structure of the complex between a distamycin-ellipticine hybrid (Distel (2+)) and $d(\text{GCATATGC})_2$ where the distamycin moiety lies in the minor groove and the ellipticine chromophore is intercalated in the (TpG)-(CpA) site. Calculated by the JUMNA program from Lavery, R., Zakrzewska, K., Pullman, A. *J. Biomol. Struct. Dyn.*, **1984**, 5, 363. (b) Minor groove binding model for the complex between the synthetic peptide 2-PyN, a derivative of distamycin, and a 5'-(A-T)5-3' sequence. (Wade, W. S., Mrksich, M., Dervan, P. *Biochemistry*, **1993**, 32, 11385.)

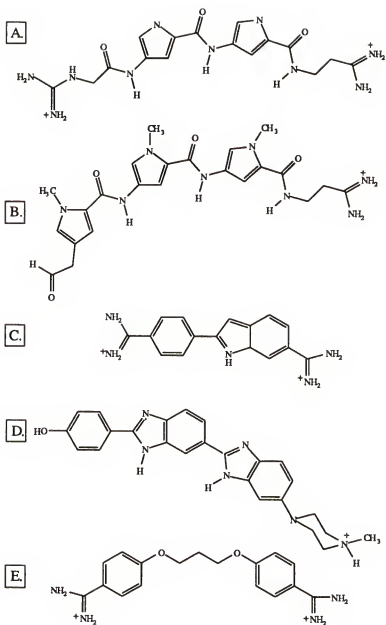


Figure 1.9. DNA groove-binding molecules. (a) Netropsin; (b) Distamycin; (c) DAPI; (d) Hoechst 33258; (e) Pentamidine.

in the minor groove are generally narrower, (2) the adenine N-2 nitrogen and thymine C-2 carbonyl in A:T base pairs are available for hydrogen bonding interactions and (3) steric hindrance is caused by the guanine amino group which is H-bonded with the cytosine carbonyl oxygen.³⁹ Through variation of the aromatic groups,^{63,64,65} the amide linkages, and lengths of methylene chains,⁶⁶ among other structural changes,⁶⁷ analogs of several biologically active groove binding molecules have been prepared. The new designs provide higher sequence specificity, differences in activity and in some cases less toxic side effects.

Intercalation

As described earlier, intercalation is a noncovalent interaction with double-stranded (ds) DNA where a flat or relatively planar polycyclic aromatic molecule slides in-between adjacent base pairs of the DNA helix (Figure 1.5a). The first evidence for intercalation came from hydrodynamic and x-ray fiber diffraction studies of DNA in the presence of acridine dyes.³⁸ Observations from these studies were the continued presence of the 3.4 Å meridional repeat in diffraction patterns caused by base-pair stacking, and decrease in mass per unit length of the DNA caused by lengthening of the helix. Insertion of the molecule into DNA causes a separation of the stacked base-pairs by approximately 3.4 Å which is the thickness of the aromatic ring system.⁶⁸ This results in unwinding of the helix by ~ 10 to 26 Å (from the normal pitch of 34 Å for B DNA), the amount of which depends on the size of the intercalating species. These changes in structure cause an overall stiffening to make the helix like a hard rigid rod.¹¹ This contrasts to the effect of groove binding which results in a contraction of the polymer due to a decrease in repulsive charges between anionic phosphate groups on account of shielding. Driving forces behind intercalative binding include van der Waals (dispersive) forces, hydrophobic interactions, electrostatic interactions, and hydrogen bonding. Stacking interactions (dipole-dipole, etc.) between the intercalator and the base-pairs result in stabilization of the double helix as evidenced from increased temperatures for melting curves of the helix. Side chains on the chromophore can participate in hydrogen bonding with the bases in the groove as well as with the

phosphodiester backbone. An example of an intercalated complex capable of making H-bonding contacts with its side chain that extends into the groove is shown in Figure 1.10. This shows a crystal structure of the daunomycin - d(CpGpTpApCpG) complex⁶⁹ viewing from the top looking perpendicular to the plane of the base pairs and from the side (where only half of the complex is drawn). Hydrogen bonding interactions can be seen between the C₉ hydroxyl of daunomycin and G₂ (guanosine #2) and between the daunomycin C₁₃ acetyl keto group and O₂ of cytosine C₁, mediated by a water molecule W.

Binding of cationic intercalators causes release of counterions from DNA as a result of initial neutralization of phosphate charges and from conformational changes of the double helix upon intercalation.⁵² This causes the interaction of cationic intercalators with DNA to have a salt dependence according to condensation theory. The phenomenon has been extensively studied using the structurally similar mono- and dicationic phenanthridinium ions, ethidium and propidium.^{21,48,70,71} Two models have been proposed for the mechanism of intercalation⁴⁸, the first being a direct binding mechanism where there is a helix-opening step (1.1a) followed by the intercalation reaction (1.1b):



where D is native DNA, D* is the open DNA complex available for intercalation, L is the ligand (intercalator) and C is the bound ligand-DNA complex. This model has been suggested to represent the mechanism by which neutral intercalators bind to DNA. The second model involves formation of an initial loosely associated outside complex of the ligand with the double helix in a condensation type of reaction (1.2a). Intercalation of the associated ligand can then occur upon breathing or base-pair opening of the double helix (1.2b):



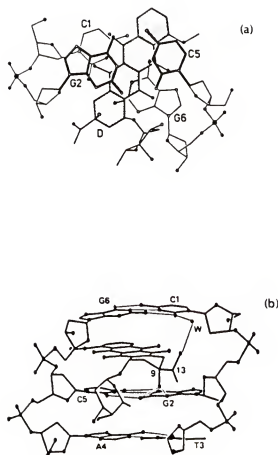


Figure 1.10. Crystal structure of daunomycin - d(CpGpTpApCpG) complex. (a) Top view looking down the helix axis perpendicular to the plane of the base pairs. Daunomycin is shaded. (b) Side view looking parallel to the base-pair plane and showing only half of the DNA complex. The daunomycin is intercalated between the terminal CpG sequences, and is making H-bonding contacts between its C₉ hydroxyl and G₂ and between its C₁₃ acetyl keto group and O₂ of cytosine (C₁). From Quigley, G. J., Wang, A. H.-J., Ughetto, G., van der Marel, G., van Boom, J. H., Rich, A. *Proc. Nat. Acad. Sci. USA*, **1980**, 77, 7204-7208.

where L and D are defined above and $L \cdot D$ is the associated outside complex. According to this mechanism the initial step will depend primarily on the charge of the ligand and only minimally on its structure. However, the second intercalation step will strongly depend on interaction factors such as orientation and sterics between the ligand and the DNA helix. This model is proposed to fit the binding kinetics of cationic intercalators, and predicts a larger effect of salt on the association reaction with DNA than on the dissociation reaction. As a result of the salt dependence of the association step, molecules with greater cationic charge should experience a larger sensitivity to changes in the ionic strength of the solution. This was indeed shown by Wilson et al.⁴⁸ in the studies of ethidium and propidium. The rate of initial association of the dicationic propidium with ds DNA was reduced significantly on going from 0.2 M Na^+ solutions to 0.5 M Na^+ solutions, to a rate considerably slower than that of ethidium at 0.5 M Na^+ . Yet the measured dissociation rates of the two molecules from DNA at this high ionic strength were within close proximity to each other. At the lower ionic strength (0.2 M Na^+) propidium showed a higher association rate and a much slower dissociation rate than ethidium at 0.5 M Na^+ which indicated overall much stronger binding (data for ethidium at 0.2 M Na^+ was not listed). Similar findings were shown by Breslauer et al.⁷¹ who identified the enhanced binding at low salt to be electrostatic in origin and is a reflection of a more favorable entropic driving force for propidium binding. It is important to note that in both of the above binding models salt dependent terms were intentionally omitted for simplification of the discussion. However, for correct consideration of these kinetics it is essential that the salt effects be included.

An important principle of intercalative binding is the observation that every second intercalation site along the DNA double helix remains empty (see Figure 1.11). This is the nearest neighbor exclusion principle⁷² which has most often been explained to be due to local distortions of the DNA bases caused by the intercalated ligand. Another argument suggests that local release of counterions due to intercalation could lead to reduction of

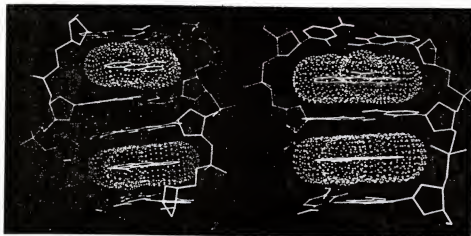


Figure 1.11. Computer-generated molecular modeling structures of 9-aminoacridine double intercalated in d(CGCGCGC) - d(GCGCGCG) where the neighbor exclusion rule is violated (right) and where it is obeyed (left). (Only the base pairs closest to the acridines are shown). From Rao, S. N. *Nucleic Acid Targeted Drug Design*; Propst, C. L., Perun, T. J. (eds); Marcel Dekker; New York; 1992; 65-91.

binding by molecules at nearby sites.^{39,73} The actual mechanics might be a combination of both effects. It has been observed that the size of chains or appended groups attached to the main intercalating structure can affect the size of the binding site.

Intercalative binding affects not only the conformation of ds DNA but also causes the intercalated ligand to be rigidly held while in this complex. As a result experimental evidence for this type of binding can be obtained from changes in the physical properties of both the nucleic acids and the intercalator. There are a number of experimental techniques available for determining intercalative binding. Viscometric measurements detect increases in the solution viscosity of bulk DNA due to intercalation, while the electrophoretic mobility of closed circular DNA is decreased upon intercalation due to the unwinding of the helix.⁷⁴ These changes in higher order structure can also be evaluated through fluorescence microscopy which quantitatively measures the changes in persistent length and contour length.¹¹

Dichroic methods, such as circular and linear dichroism, can be used to measure the orientation of molecules bound to DNA. In the technique of circular dichroism the changes in left and right circularly polarized light are monitored after passing through an optically active medium. Thus CD is useful in tracking the changes induced in the optical activity of molecules upon incorporation into a structured matrix like ds DNA, as well as detecting changes in the intrinsic CD bands of DNA itself when molecules bind to the double-helix. Linear dichroism measures the absorption anisotropy of a sample. Here absorption measurements are performed using plane polarized light which is polarized parallel and perpendicular to the z axis. Those portions of the sample which are in ordered arrays, depending on whether they are oriented perpendicular or parallel to the incident light, will show strong absorption in the direction of light which is parallel to their orientation. LC is particularly useful in defining the orientation of molecules bound to DNA. By measuring the LD signal of a molecule bound to DNA and comparing it to the LD signal of the DNA bases, one can determine the orientation angle of the bound chromophore relative to the

base pairs. Fluorescence polarization similarly measures the orientation of the intercalated complex through detecting increases in polarized fluorescence due to the reduced mobility of the rigidly held chromophore.

Electronic interactions between the bound ligand and the nucleic acid bases provide the basis for another set of experiments for detection of intercalation. Hypochromism (decreased absorption) and red shifts in the UV-visible long-wavelength absorption bands of the intercalating moiety are strong evidence of a stacked array of molecules. The effect is due to electronic interactions between the dipole moment of the absorbing chromophore and the induced dipoles of the nearby DNA bases. When the dipoles are oriented parallel to each other, as in an ordered stack, they are in a repulsive array and result in reduction of the transition intensity. Dispersion forces involving the coupling of lower energy transitions in the chromophore with higher energy ones in the DNA bases also contribute to hypochromic effects.^{75,76}

For molecules which luminesce, increases or decreases in emission upon binding can be followed by emission spectroscopic techniques. As mentioned earlier, parameters which can be measured include steady-state emission quantum yield, luminescence intensity, emission maximum, luminescence lifetime, fluorescence polarization, and rotational correlation time. Increases in emission upon intercalation can be derived from several sources. For some chromophores, such as ethidium bromide, removal from the quenching solvent into the hydrophobic environment of the DNA bases produces dramatic increases in its fluorescence quantum yield.⁷⁷ This has also been demonstrated for ruthenium⁷⁸ and rhenium⁷⁹ metal complexes which contain the DPPZ ligand (dipyrido[3,2-a:2',3'-c]phenazine) whose emission is strongly quenched by excited state protonation in aqueous solution but increases considerably when bound to DNA. The protective environment of the DNA bases additionally shields the bound chromophore from *collisional* quenching by the solvent, again resulting in increased emission quantum yield and excited state lifetime. Luminescence decreases have been attributed to quenching of

emission from the bound chromophore by the DNA bases. Several groups are currently investigating this phenomenon in order to determine the mechanism by which it occurs.^{80,81} For some intercalators, such as adriamycin, the fluorescence quenching has been suggested to be due to reductive electron transfer from the bases to the bound chromophore.³¹

Alternative Probes: Electron Transfer and Energy Transfer Systems

Since there are a limited number of DNA intercalating compounds which exhibit luminescent properties, innovative techniques are being sought in order to expand this area of research. One such route is to exploit the distance dependence of energy and electron transfer processes. These reactions are particularly useful because of their strong dependence upon distance and orientation between the participating molecules (particularly in the case of energy transfer).

These techniques have been extensively applied to protein studies in measurement of distances between binding sites of a protein,⁸² determining association of macromolecules in solution,⁸³ following conformation changes of proteins and membranes⁸⁴ and monitoring the activities of proteins.⁸⁵

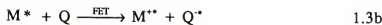
In contrast, in only a few instances have electron transfer and energy transfer been used to study DNA conformations and distances between binding sites or base-pair sites. Studies concerning electron transfer (ET) between molecules bound to ds DNA have focused on: (1) the dynamics of ET between two different intercalated molecules and the effect of the interspersed bases;⁸⁶ (2) ET between an intercalated molecule and a condensed mobile cationic species;⁸⁷ (3) ET or EnT between covalently attached labels.⁸⁸ In some cases the quenching activity of the reducing agent was related to its biological activity.⁷⁷ In general electron transfer processes have not been utilized in molecular probe technology, but rather in the fast growing area of photodynamic therapy.⁸⁹

Fluorescence energy transfer (E_NT) has been more directly applied to studies of the solution structure and distances between bound molecules and sequences in ds DNA. Several techniques have been used such as: (1) monitoring the E_NT efficiency between DNA intercalated homodimeric⁹⁰ and heterodimeric⁹¹ complexes and applying the results to Förster energy transfer theory; (2) measuring E_NT between two separate intercalated molecules⁹² and relating the results to conformation changes upon binding; (3) E_NT between covalently attached labels on separate strands to determine unusual conformations of the helix^{93,94} and orientation of oligodeoxynucleotides and;⁹⁵ (4) E_NT between heterodimeric intercalated dyes for multiplex detection of various targets.⁹⁶ In the latter study, the complexes were composed of donor molecules that all had a common strong absorption maximum at 488 nm but with different covalently attached acceptor chromophores having distinctive fluorescence emission maxima. Efficient energy transfer was observed in the DNA-bound heterodimers (> 90% quenching of donor emission), with large enhancements in the acceptor fluorescence. They observed differential binding strengths of the heterodimers depending on the chromophores used. The properties of these intercalating complexes clearly demonstrate the potential feasibility of dimeric chromophore-quencher complexes as probes for nucleic acids.

Brief Description of Electron-Transfer Theory

The study of ET in excited-state species has been extensively studied on account of the fact that the electronically excited state of a molecule will act as a more powerful electron donor (reductant) or acceptor (oxidant) compared to the ground state.⁹⁷ This reactivity makes photoinduced ET (PET) an integral step in many bimolecular photoactive systems. An important result of the ET process is that the electron transfer step quenches the emission of the excited chromophore. General expressions for photoinduced electron transfer between an excited molecule (M^*) and a quenching species (Q) is given by:





where eqn. 1.3a is the excitation step, eqn. 1.3b depicts oxidative ET quenching of the excited state species and eqn. 1.3c represents reductive ET quenching. In the ET equations FET indicates forward electron transfer and the symbols $+ \bullet$ and $- \bullet$ represent the oxidized and the reduced molecules, respectively. The mechanisms by which the quenching occurs (i.e., oxidative or reductive quenching) will depend on the redox properties of the donor-acceptor pair. This ability of an excited state to act as either an electron donor (D) or an electron acceptor (A) is illustrated in Figure 1.12. The overall free energy change (ΔG^0 also called the thermodynamic driving force) for the photoinduced ET reaction is determined from the redox potentials of the reactants combined with the 0-0 excitation energy of the excited species to obtain:

$$\Delta G^0 = E_{1/2}(D/D^+) - E_{1/2}(A/A^-) - \Delta E_{0-0}^{D^*} \quad 1.4$$

$$\Delta G^0 = E_{1/2}(D/D^+) - E_{1/2}(A/A^-) - \Delta E_{0-0}^{A^*} \quad 1.5$$

where $E_{1/2}(D/D^+)$ and $E_{1/2}(A/A^-)$ are the half-wave oxidation and reduction potentials for the donor and acceptor, respectively, and ΔE_{0-0} is the excited-state energy.

The rate of photoinduced ET between a donor/acceptor pair can be determined from experimental quantities such as the emission lifetime (τ) or quantum yield (ϕ) of the donor in the absence and presence of the acceptor. Equations which have been used for calculating ET rate (k_{ET}) constants are provided by the following:

$$k_{ET}(\tau) = \frac{1}{\tau} - \frac{1}{\tau_o} \quad 1.6$$

$$k_{ET}(\phi) = \left(\frac{\phi_o}{\phi} - 1 \right) \frac{1}{\tau_o} \quad 1.7$$

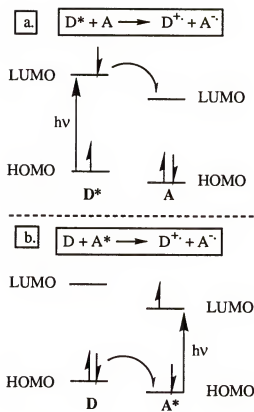


Figure 1.12. Enhanced ET Reactivity of Excited States. (a) Excited-State electron donor (oxidative quenching). (b) Excited-State electron acceptor (reductive quenching).

where τ and ϕ are the emission lifetime and quantum yield, respectively, of the donor in the presence of the acceptor, while τ_0 and ϕ_0 are the same parameters in the absence of the acceptor. These equations are valid if D and A are linked by a spacer chain or through a matrix and if the attachment does not significantly alter the electronic properties of the two molecules (i.e., the intrinsic decay rate of D is not changed by the attachment).

According to semiclassical theory the ET rate constant can be expressed as the product of an effective nuclear-vibration frequency (ν_n), an electronic transmission coefficient (κ_{el}) and a nuclear transmission coefficient (κ_n):^{77,98}

$$k_{ET} = \nu_n \kappa_{el} \kappa_n \quad 1.8$$

$$\text{where} \quad \kappa_n = \exp \left\{ -\frac{(\Delta G_{ET} + \lambda)^2}{4\lambda RT} \right\} \quad 1.9$$

$$\nu_n \kappa_{el} = \left\{ \frac{2(H_{AB})^2}{h} \right\} \left\{ \frac{\pi^3}{\lambda RT} \right\}^{1/2} \quad 1.10a$$

$$\lambda = \lambda_{in} + \lambda_{out} \quad 1.10b$$

In eqn. 1.9, ΔG^0 is the free energy change for ET, R is the gas constant, T is temperature, and λ is the total reorganization energy. In eqn. 1.10, H_{AB} is the donor-acceptor electronic coupling matrix element and h is Planck's constant. This equation is for the case of non-adiabatic ET ($\kappa_{el} < 1$ for nonadiabatic, while $\kappa_{el} = 1$ for adiabatic). The reorganization energy, λ , is the energy necessary for moving from the equilibrium configuration of the reactants to the equilibrium configuration of the products while remaining on the reactant free-energy surface. The reorganization energy (eqn. 1.10b) is comprised of an inner sphere component, λ_{in} , which is associated with bond length and angle changes within D and A, and an outer sphere component, λ_{out} , which is related to solvent reorganization

around D and A. Marcus and Hush derived a two-sphere dielectric continuum model to estimate the contribution of λ_{out} to the total reorganization energy such that,

$$\lambda_{out} = e^2 \left[\frac{1}{2r_D} + \frac{1}{2r_A} - \frac{1}{r_{DA}} \right] \left[\frac{1}{\epsilon_{op}} - \frac{1}{\epsilon_s} \right] \quad 1.11$$

where e is the electron charge, r_D and r_A are the radii of the donor and acceptor, r_{DA} is the donor-acceptor separation distance, and ϵ_{op} and ϵ_s are the optical and static dielectric constants, respectively. In nonpolar solvents λ_{out} is small since the polarization of the solvent does not change to any great degree as the electron is transferred, however as the solvent polarity increases, the contribution from λ_{out} also increases. Moreover, notice that λ_{out} increases as the radii of the reactants decrease or as the donor-acceptor separation increases. The decay of κ_n with increasing donor-acceptor separation has been mainly attributed to the effect of distance on λ_{out} , although the other the terms in eqn. 1.9 also contribute to the effect. The distance dependence of ET arises not only from the reorganization energy but also from the electronic coupling matrix element, H_{AB} , according to equation 1.12:

$$H_{AB} = H_{AB}^0 \exp \left[\frac{-\beta(r-r_0)}{2} \right] \quad 1.12$$

where r is the center-to-center separation distance between D and A, r_0 is the sum of the van der Waals radii of D and A, H_{AB}^0 is the electronic coupling when $r = r_0$ and $\beta/2$ is a term which expresses the dependence of electronic coupling on distance. From eqn. 1.12 it is evident that as the separation between D and A increases, H_{AB} exponentially decreases, and consequently κ_{el} decreases according to eqn. 1.10a.

Considering all the factors which contribute to the distance dependence of k_{ET} , a general expression can be given as follows:

$$\ln k_{ET}(r) = -\beta(r-r_0) + \ln \kappa_n(r) + \ln v_n \quad 1.13$$

Theory of Electronic Energy Transfer

Introduction

A second mechanism by which molecular luminescence can be quenched is energy transfer (E_{NT}). This is a bimolecular process involving the transfer of excited state energy from a donor (M) to an acceptor (Q), and can be written as:



Energy which is initially provided to the donor (M) via absorption of a photon ends up in Q, concomitant with a reduction in the concentration of excited M molecules and therefore a reduction in the total emission from M*. A requirement of this reaction is that the energy level of Q* must be lower or equal to the energy level of M*.

There are three different mechanisms by which energy transfer can occur. These mechanisms are radiative, nonradiative coulombic and nonradiative electron exchange.^{99,100} Each will be considered separately.

Radiative energy transfer

Radiative energy transfer, often referred to as "trivial", is the process where the emission of a quantum of light emitted by M* is reabsorbed by Q. It is a two-step process wherein no physical interaction is involved between M* and Q. The reaction is depicted by eqn. 1.15:

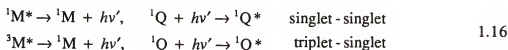


Since the trivial mechanism requires that the photon emitted by M* is absorbed by Q, radiative energy transfer follows the same principles that determine the intensity of absorption transitions. Therefore, the probability of energy transfer from M* to produce Q* depends on (1) the emission quantum yield of M* (Φ_e^M), (2) the concentration of acceptor molecules (Q) in the path of the emitted photons from M*, (3) the strength of the light

absorption transition in Q, and (4) the extent of the overlap between the emission spectrum of M* and the absorption spectrum of Q.

Radiative transfer is most favorable when each of the four factors is maximized. That is, when $\Phi_e^M \sim 1$, the concentration of Q is high, the molar absorptivity of Q is large, and there is good overlap between the experimental absorption curve of Q and the emission curve of M*.

The requirement that Q have a large molar absorptivity in the spectral region where M* emission occurs rules out the possibility of singlet-triplet and triplet-triplet radiative transfer. This is due to the low intensity of the spin-forbidden $S_0 \rightarrow T_1$ absorption transition. The predominant transfer processes for the radiative mechanism are:



The fourth of the above listed factors which affect radiative transfer, called the spectral overlap integral, J , is depicted in Figure 1.13. It corresponds to the area of the overlap of the emission spectrum of M* and the absorption spectrum of Q. The spectral overlap integral is described mathematically as (1.17):

$$J = \int_0^\infty F_M(\tilde{\nu}) \varepsilon_Q(\tilde{\nu}) d\tilde{\nu} \quad 1.17$$

where $F_M(\tilde{\nu})$ corresponds to the graph of the emission spectrum of M*, $\tilde{\nu}$ represents the wavenumber, and $\varepsilon_Q(\tilde{\nu})$ represents the absorption spectrum of Q.

The probability of radiative energy transfer, P_{RT} , can then be given by (1.18):

$$P_{RT} \approx 2.3026 [Q] l \int_0^\infty F_M(\tilde{\nu}) \varepsilon_Q(\tilde{\nu}) d\tilde{\nu} \quad 1.18$$

where l is the path length. From eqn. 1.18 it can be seen that by using concentrations less than $\sim 10^{-3}$ M and small path lengths during experimental measurements of energy transfer emission, one can substantially reduce the contribution of trivial emission reabsorption.

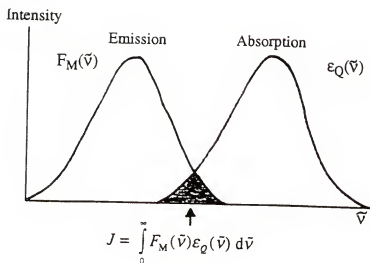


Figure 1.13. Overlap between the absorption spectrum ($\epsilon_Q(\tilde{\nu})$) of an energy acceptor (Q) and the emission spectrum ($F_M(\tilde{\nu})$) of the donor (M^*) where the shaded area is the overlap, termed the spectral overlap integral, J .

Nonradiative Energy Transfer

In contrast to radiative energy transfer which does not require any specific interaction between donor and acceptor, the nonradiative mechanisms involve mutual perturbation of the electronic structures of M^* and Q . According to Fermi's Golden Rule the rate of occurrence of transitions between two states is related to the magnitude of the perturbation or force which alters the positions or motions of the particles of the initial state (ψ_m^M) in such a way that ψ_m^M evolves to the final state (ψ_n^Q). The expression used to describe the rate of change of the probability of finding the molecule in the final state ψ_n^Q as a function of time is given by eqn. 1.19:

$$\frac{d}{dt}P_n = \frac{2\pi}{\hbar} \bar{\rho}_n \langle \psi_n^Q | \hat{H}' | \psi_m^M \rangle^2 \quad 1.19$$

where P_n refers to the probability of the final "n" state, the matrix element \hat{H}' refers to the perturbation which couples the initial wavefunction ψ_m^M and the final wavefunction ψ_n^Q , and $\bar{\rho}_n$ corresponds to the number or density of final vibronic (acceptor) states which are isoenergetic with the vibronic level in the initial state. In solution phase the initial vibronic state will be the lowest vibrational level of the initial electronic state since for most organic molecules $k_{ic}(S_n \rightarrow S_1)$ occurs with a rate constant of the order of that for vibrational motion ($10^{11} - 10^{13} \text{ sec}^{-1}$).

When considering nonradiative transitions, the term ψ_m^M in eqn. 1.19 represents the initial state $\psi(M^*)\psi(Q)$, while ψ_n^Q corresponds to the final state $\psi(M)\psi(Q^*)$, and the perturbation part of the Hamiltonian \hat{H}' represents the matrix elements responsible for causing energy splittings of states. In the case of radiative transitions, the perturbation part of the Hamiltonian responsible for the transition is the scalar product of the electric field and dipole moment vectors.

According to the Born-Oppenheimer approximation, $\langle \psi_n^Q | \hat{H}' | \psi_m^M \rangle$ can be factored into an electronic matrix element and a vibrational overlap integral:

$$\langle \psi_n^Q | \hat{H}' | \psi_m^M \rangle = \langle E_n^Q | \hat{H}' | E_m^M \rangle \langle N_n^Q | N_m^M \rangle \quad 1.20$$

where \hat{H}' is the interaction Hamiltonian which is responsible for the energy transfer process, E is the electronic wavefunction and N is the nuclear wavefunction. The electronic matrix element in eqn. 1.20 can be defined as $\beta_e = \langle E_n^Q | \hat{H}' | E_m^M \rangle$ if the assumption is made that it does not vary significantly for different pairs of m, n vibronic levels. Therefore the overall radiative rate can be written as:

$$\frac{d}{dt} P_n = \frac{2\pi}{h} \beta_e^2 \sum_{n,m} \left| \langle N_n^Q | N_m^M \rangle \right|^2 \bar{P}_n \quad 1.21$$

Equation 1.21 can be simplified by noting that the last term, the probability density of the area of the vibrational overlap integral (Franck-Condon factor) times the density of vibrational levels in the acceptor, is closely related to the spectral overlap integral (J) such that:

$$\frac{d}{dt} P_n = \frac{2\pi}{h} \beta_e^2 J = \frac{2\pi}{h} \beta_e^2 \int_0^\infty F_M(\tilde{\nu}) \epsilon_Q(\tilde{\nu}) d\tilde{\nu} \quad 1.22$$

Equation 1.22 is a general description of energy transfer and can be applied to either one of the nonradiative mechanisms. The difference lies in the electronic matrix element β_e that contains the interaction Hamiltonian \hat{H}' . The electronic matrix term can be split up into two types of interaction, an electrostatic (Coulombic) interaction and an electronic (exchange) interaction. These nonradiative mechanisms can be visualized from Figure 1.14. The coulombic mechanism is a long-range dipole-dipole interaction in which the oscillating electron in the LUMO of M^* induces a corresponding oscillation of an electron in the HOMO of a neighboring acceptor molecule (Q). This interaction can occur over large intermolecular distances (up to 100 Å) and electrons that are resident on M^* remain on the de-excited M.

Electron exchange energy transfer presents a different mechanism of interaction between the donor (M^*) and acceptor (Q). In this case there is a double exchange of

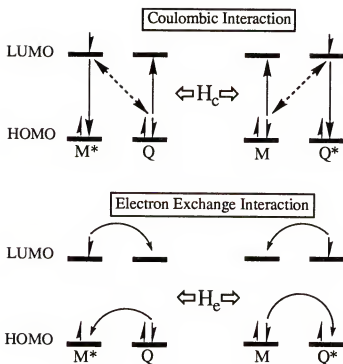


Figure 1.14. Coulombic (top) and Electron Exchange (bottom) Energy Transfer Interactions. H_c and H_e are the interaction Hamiltonians for the coulombic and electron exchange energy transfer mechanisms, respectively.

electrons whereby the excited electron in the LUMO of M^* transfers to the corresponding LUMO of Q , while at the same time an electron in the HOMO of the ground state of Q "hops" over into the HOMO of M^* . The net result is excitation of Q to give Q^* and de-excitation of M^* to give M . Close physical contact between donor and acceptor (6-20 Å) is required in this process in order to allow overlap of the electron orbitals involved. To understand the exact nature of these two mechanisms theoretical treatment is necessary.

Coulombic Energy Transfer: Förster Mechanism

Long-range or Coulombic energy transfer involves an electrostatic interaction of the electronic charge clouds of donor (M^*) and acceptor (Q) molecules. Classical theory is used to describe the factors which determine the magnitude of the Coulombic interaction and relate it to the rate of M^* to Q energy transfer. An electronically excited molecule is surrounded by an electric field that is considered to behave like a field generated by an oscillating dipole possessing a frequency of oscillation, ν , and an instantaneous dipole moment, μ . The energy of interaction between two electric dipoles is defined by:

$$E \propto \beta_e \propto \frac{\mu_M \mu_Q}{r^3} \quad 1.23$$

where μ_M and μ_Q are the dipole moments of M^* and Q , respectively, and r is the distance between them. Substituting this quantity into equation 1.22 gives the following expression:

$$\frac{d}{dt} P_n = \frac{2\pi}{h} \frac{\mu_M^2 \mu_Q^2}{r^6} J \quad 1.24$$

In his theory of energy transfer Förster^{101,102} related the transition dipole moments of the donor/acceptor pair to the oscillator strengths for the $M^* \rightarrow M$ and $Q \rightarrow Q^*$ radiative electronic transitions. The following equation (1.25) illustrates the relationship between the transition dipole moment and the oscillator strength:

$$f_{nm} = \left[\frac{8\pi^2 m_e c}{3e^2 h} \right] \bar{\nu}_{nm} |\mu_{nm}|^2 \quad 1.25$$

where m_e is the mass of an electron, c is the speed of light, e is electronic charge and $\bar{\nu}_{nm}$ is the wavenumber of the transition ($\bar{\nu}_{max}$). Förster was consequently able to show how the theoretical quantities were related to the experimental absorption coefficient of Q and the inherent radiative lifetime of M^* using the following equations (1.26 and 1.27):

$$f_{nm} = \left[\frac{4\epsilon_0 m_e c^2 \ln(10)}{N_A e^2} \right] \int \epsilon(\bar{\nu}) d\bar{\nu} \quad 1.26$$

$$k_r^o = \frac{1}{\tau_r^o} = \frac{\bar{\nu}_{nm} n^2}{3.417 \times 10^8} \int \epsilon(\bar{\nu}) d\bar{\nu} \quad 1.27$$

where ϵ_0 is the permittivity of a vacuum, N_A is Avogadro's constant, n is the mean refractive index of the solvent k_r^o is the radiative rate coefficient, τ_r^o is the natural lifetime of a radiative transition and $\int \epsilon(\bar{\nu}) d\bar{\nu}$ is the integrated absorption coefficient which is carried out over the whole absorption band. The final expression is therefore (1.28):

$$\frac{d}{dt} P_n = \frac{0.5291 \kappa^2}{n^4 N_A r_o^6 \tau_M} \int_o^{\infty} F_M(\bar{\nu}) \epsilon_Q(\bar{\nu}) \frac{d\bar{\nu}}{\bar{\nu}^4} \quad 1.28$$

where κ is an orientation factor which accounts for the fact that the interaction between the two dipoles depends on the orientation of the dipoles in space. In solution the molecules would have a random distribution of their dipoles and κ^2 would have the value $2/3$. To simplify equation (1.28) it is convenient to define a critical transfer distance such that:

$$r_o^6 = \frac{0.5291 \kappa^2}{n^4 N_A} \int_o^{\infty} F_M(\bar{\nu}) \epsilon_Q(\bar{\nu}) \frac{d\bar{\nu}}{\bar{\nu}^4} \quad 1.29$$

and therefore

$$\frac{d}{dt}P_n = \tau_M^{-1} \left(\frac{r_0}{r} \right)^6 \quad 1.30$$

The critical transfer distance r_0 is the distance between M and Q for which there is equal probability of energy transfer from M* to Q and emission from M* (i.e., 50% quenching of M* luminescence). Thus when $r < r_0$ energy transfer will be the dominant process, while if $r > r_0$ then deactivation of M* will be the major process. Experimentally r_0 can be measured by examination of the steady-state or time-resolved kinetics of the M* emission as a function of [Q].

Energy transfer by the Coulombic mechanism is most favorable when there is good overlap between the emission spectrum of M* and the absorption spectrum of Q, the magnitude of ϵ_A^{\max} for Q is large, M* has a large radiative rate, and the two molecules are close to each other ($< 100 \text{ \AA}$). The requirement for a large ϵ_A^{\max} for the acceptor rules out processes which involve a change in spin multiplicity since these would have small ϵ_A^{\max} values, and consequently inefficient energy transfer. Therefore the processes which are allowed for the Förster mechanism are:



Electron-Exchange Energy Transfer

The second non-radiative energy transfer mechanism depicted in the lower portion of Figure 1.14 involves a double electron transfer between M* and Q. The distinguishing feature of this mechanism is the requirement that M* and Q be sufficiently close together to allow overlap of the electron orbitals involved (ca. $6\text{--}20 \text{ \AA}$). Recall that the electronic matrix element β_e (eqn. 1.20) can be split into two terms:

$$\beta_e = \langle E_n^Q | \hat{H}^I | E_m^M \rangle = \left[\langle \psi(M^*) \psi(Q) | H_C | \psi(M) \psi(Q^*) \rangle^2 + \langle \psi(M^*) \psi(Q) | H_e | \psi(M) \psi(Q^*) \rangle^2 \right] \quad 1.32$$

where H_C is the coulombic interaction Hamiltonian and H_e is the exchange interaction Hamiltonian. The the second term in eqn. 1.32 represents the part of the electronic matrix element that describes the electron exchange mechanism. Since electron densities usually decrease exponentially as the distance between the electron and the nucleus increases, it follows that the rate for energy transfer by electron exchange would decrease exponentially as the separation distance between M^* and Q increases. This distance dependence of the electron exchange $E_N T$ mechanism is similar to the electronic coupling matrix element, H_{AB} , for electron transfer described by eqn. 1.12. Therefore exchange energy transfer occurs only when M^* and Q have small separation such as in an encounter complex. As shown in eqn. 1.22, the general expression for non-radiative $E_N T$, the energy transfer rate also depends on the overlap of the emission spectrum of M^* and the absorption spectrum of Q (spectral overlap integral J) normalized to the extinction coefficient of Q .

The phenomenon of electron exchange energy transfer was first explained by Dexter¹⁰³ who showed that the transfer probability by the exchange mechanism could be written as (1.33):

$$\frac{d}{dt} P_n = \frac{2\pi}{h} Z^2 \int_0^\infty F_M(\bar{\nu}) \epsilon_Q(\bar{\nu}) d\bar{\nu} \quad 1.33$$

The parameter Z^2 was found by Dexter to be:

$$Z^2 \propto e^{-2r/l}$$

where r is the distance between donor and acceptor molecules and l is the van der Waals radius of the donor-acceptor pair. The value of Z^2 increases the closer the molecules

approach and rapidly diminishes as they separate beyond the sum of their van der Waals radii.

There is an important difference between J for the exchange (Dexter) mechanism as compared to J in the coulombic (Förster) mechanism. Since in the Dexter mechanism J is normalized for ε_A , it does not depend on the magnitude of ε_A and therefore the rate is independent of the absorption characteristics of the acceptor. Consequently, the exchange mechanism allows transfer to and excitation of Q by all types of allowed and forbidden transitions. The formation of an encounter complex between M^* and Q means the restrictions on electron spin changes are determined by the total spin of the formed complex. This is based on the Wigner¹⁰⁴ rule of spin conservation which requires the total spin (S_T) of the reactant molecules have at least one value in common with the total spin of the products.

Description of the Present Study

The purpose of the present study is to apply a novel approach to the detection of nucleic acids by utilizing the spectroscopic and photophysical properties of rhenium-based chromophore-quencher (CQ) complexes which also possess the ability to bind to DNA. The complexes are composed of the *fac*-(b)Re^I(CO)₃-L chromophore (where (b) is a bidentate diimine ligand) covalently attached by way of a flexible linker chain to either an energy acceptor or electron donor / acceptor moiety (designated the quenching species). Rhenium-based CQ complexes have been extensively studied in regards to their rates of ET and E_NT and the factors affecting their photophysical properties.^{105,106,107,108,109,110} However, systems of this type have not been exploited for their potential bio-medical applications.

For the purposes of this study the design of the CQ complexes consists of two possible approaches: (system I) where the linked quenching (Q) molecule also serves as a DNA intercalator, or (system II) where the diimine ligand directly attached to the Re

chromophore is responsible for binding to DNA while the Q moiety attached through the flexible linker is strictly a quenching species and does not participate in intercalative binding. The premise operating behind their design rests on the assumption that in solution the emission from the Re chromophore in the CQ complexes would be highly quenched due to energy transfer or electron transfer to or from Q. However, upon binding to ds DNA contact between Re and Q would be hindered by the bulky helix and therefore would result in a reduction in quenching and an increase in Re emission. Essentially this mimics the turning on of a light switch upon attachment to nucleic acids. Important aspects of these studies include (1) the emphasis placed on characterizing the DNA binding of these complexes through changes in their photophysical properties and (2) relying on an intercalative interaction as the major binding force to ds DNA.

The favorable synthetic and photophysical properties of the *fac* -(b)Re^I(CO)₃-L chromophore lend this study a variety of alternative approaches. In addition to its synthetic versatility pointed out above, the chromophore possesses moderately long-lived luminescence in solution which is assigned to a $d\pi(\text{Re}) \rightarrow \pi^*$ (diimine) metal-to-ligand charge-transfer (MLCT) state.^{111,112,113} The energy of the MLCT state can be selectively tuned by varying the type of diimine ligand attached to Re as well as by varying substituents on the diimine ligand. Therefore the photophysical and redox properties of the Re chromophore can be changed to suit the needs of a particular study.¹¹⁴

In Chapter 2 the interactions of two different CQ complexes with DNA are examined. Their mechanisms of quenching operate through reductive ET from the attached quencher to photo-excited Re, however their binding modes to DNA differ. The first CQ complex, (b)RePTZ (b = bipyridyl, PTZ = phenothiazine), interacts with the nucleic acids by way of its linked PTZ quencher and thus is a type I system. The second complex, phenReCH₂Q (phen = 1, 10-phenanthroline), is a type II system where the phenanthroline diimine ligand which is directly attached to Re is responsible for DNA binding.

Chapter 3 encompasses a comprehensive study of the DNA binding properties of a series of (b)Re-AN (b = bipyridyl, AN = anthracene) energy transfer CQ complexes which are of the type I system. The investigation examines the distance dependence of the E_{NT} mechanism by varying the length of the linker chain between Re and AN and determines how this affects the binding properties of these complexes.

The synthetic procedures and general materials and methods for all the studies are contained in Chapter 4.

CHAPTER 2 REPTZ AND (PHEN)RECH₂Q COMPLEXES: PHOTOPHYSICAL AND DNA BINDING STUDIES

Introduction

This chapter presents the results of spectroscopic DNA binding studies conducted on two different chromophore-quencher (CQ) complexes whose quenching mechanisms operate through reductive ET (see Figure 1.12 in Chapter 1). The term quenching, in general, refers to a mechanism by which the luminescence from the metal-to-ligand charge-transfer state (³MLCT*) of photoexcited Re is significantly reduced. For both complexes in this study the quencher (Q) serves as the electron donor and the excited (b)Re^I(CO)₃ chromophore is the electron acceptor as illustrated in Figure 2.1. This is a common feature of Re(I)-based CQ complexes since (b)Re^I(CO)₃ is a stronger oxidant and thus favorable to reduction by even moderately strong electron donors.¹¹³ The sensitivity of the ET mechanism to the distance between the donor and acceptor molecules fueled the concept of utilizing CQ complexes as luminescent probes for nucleic acids. Previous studies examining long-range photoinduced ET from a dimethylaniline electron donor to photoexcited (bpy)Re^I(CO)₃ across conformationally restricted peptide spacers showed the rate of forward ET (k_{FET}) decreased by a factor of 20 with each added amino acid residue.¹¹⁴ The attenuation in rate was attributed to reductions in both the nuclear and electronic terms (κ_n and κ_{el} , eqn. 1.8) with increasing separation distance. As discussed in Chapter I, these dependencies arise specifically from attenuation in the electronic coupling which decays exponentially as the distance between D and A becomes larger, and from increases in outer-sphere reorganizational energy, λ_0 , with increasing D-A separation (eqn. 1.8 - 1.13). Based on these properties, by linking the Re chromophore to a quenching

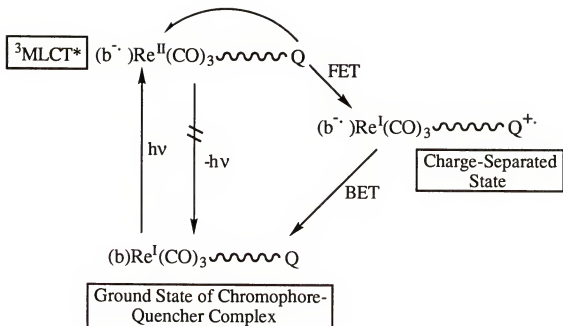


Figure 2.1 Intramolecular quenching of the $Re\ ^3MLCT^*$ state in a CQ complex by forward electron transfer (FET) to give the charge-separated state which can then relax to the ground state by back ET (BET). The FET step quenches the emission of light from the $^3MLCT^*$ state.

species via a relatively long flexible linker chain, the rate of ET could be varied depending upon the conformation of the chain. In solution these complexes would prefer to be folded over such that Re and Q are in close proximity, experiencing strong electronic coupling and, as a result, efficient ET quenching of the Re excited state. However, if the CQ complex is placed in an environment, such as a matrix, where Re and Q are constrained from close contact, then a significant reduction in ET quenching should occur, resulting in a large increase in Re luminescence. A large polymer like ds DNA could function as such a matrix and, through incorporation of a DNA-binding moiety into the CQ complexes, they could be made to bind to the double helix and experience decreased ET quenching activity. This interaction is illustrated in Figure 2.1. The attractive feature of these nucleic acid probes is their relative absence of emission in solution, but immediate luminescent response upon binding to the ds polymer. In addition, the nature of Re-Q compounds enables the flexible design of complexes where either the Re moiety or the Q moiety could incorporate a ligand which possesses DNA-binding properties.

Structures of the two complexes examined in this study, RePTZ and phenReCH₂Q are illustrated in Figure 2.2, along with their model complexes. As discussed in Chapter I, the RePTZ CQ complex is a Type I system since the quencher, PTZ, serves as the DNA binder, while the phenReCH₂Q complex is a Type II system since the diimine ligand, 1,10-phenanthroline, which is directly attached to the Re chromophore, is primarily responsible for DNA-binding. The results of the photophysical and DNA binding studies of these two CQ complexes will be discussed separately beginning with RePTZ.

Studies of RePTZ

Previous work by Meyer et al.^{115,116} has shown that PTZ strongly quenches the $d\pi(\text{Re}) \rightarrow \pi^*(\text{bpy})$ metal-to-ligand charge transfer state ($^3\text{MLCT}^*$) by reductive ET as shown in eqn. 2.1 - 2.3. The first step in this scheme is the generation of the $^3\text{MLCT}^*$ state (2.1) which is subsequently followed by forward ET (FET) from PTZ to form the charge-

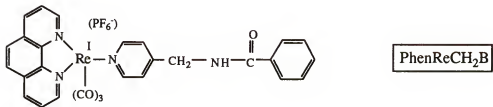
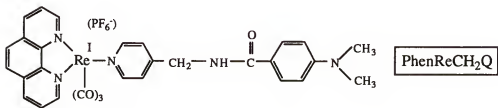
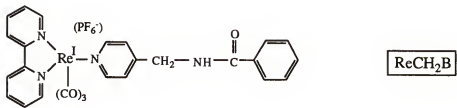
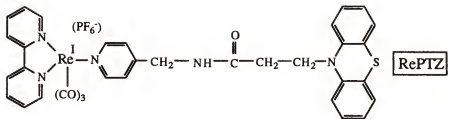
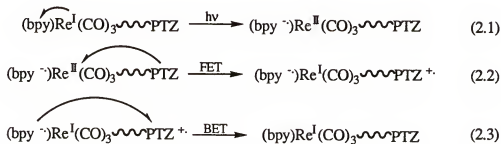


Figure 2.2. Structures of the CQ complexes, RePTZ and (phen)ReCH₂Q with their model compounds.

separated state (2.2). The charge-separated state consequently returns to the ground state (2.3) by back ET (BET) through ligand-to-ligand charge transfer (LLCT). The driving force for FET is exothermic with a value of $\Delta G^0 \sim -0.4$ eV in CH_3CN . This is calculated according to eqn. 1.5 where $E_{1/2}(\text{PTZ}^{0/+}) = 0.85$ eV, $E_{1/2}(\text{Re}^{+/0}) = -1.164$ eV¹¹³ and $E_{0,0} = 2.4$ eV.



Scheme 2.1.

In addition to its favorable electronic properties, PTZ is among a large class of biologically active compounds.¹¹⁷ Phenothiazine and its many derivatives are clinically prescribed drugs used for treatment of medical conditions such as psychoses, nausea and allergies.^{118,119} Biological stains, such as Methylene Blue and Toluidine Blue (see Figure 2.3a), are derivatives of PTZ which exhibit anti-cancer activity and are known to bind to ds DNA via intercalation.^{120,121} Studies on the antitumor activity of phenothiazines in combination with cyclophosphamide against sarcoma 180 ascites tumor in mice, produced the following observations: (1) the PTZ ring may be essential for antitumor activity, (2) the aliphatic side chain at 10-position must be a propylene rather than ethylene linkage, (3) a heterocyclic ring, in particular a piperazine, in the side chain increases both the antitumor and enhancing activities and (4) substitution of the 2-position with CF_3 , SC_2H_5 , OCH_3 or Cl increases the antitumor effects.^{122,123} Chlorpromazine (CPZ), a tranquilizer used in treatment of psychiatric disorders, causes several undesirable side effects including photoallergy, enhanced sensitivity of exposed areas of the skin to sunlight, hyperpigmentation of the skin and ocular opacity.¹¹⁸ CPZ is known to be photomutagenic

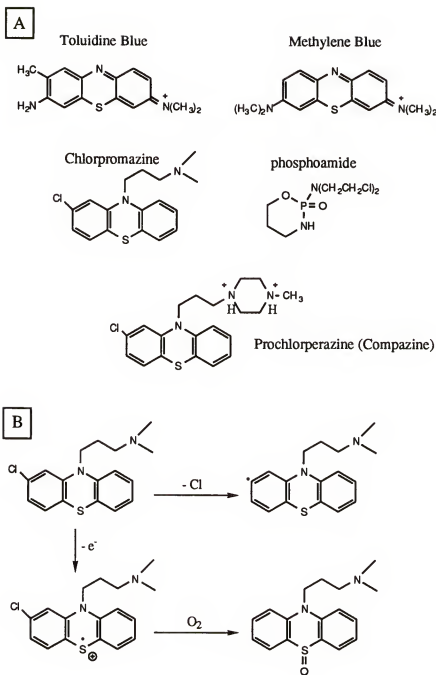


Figure 2.3. (a) Derivatives of PTZ; the dyes Methylene Blue & Toluidine Blue, and clinically used drugs Biologically active Chlorpromazine and Compazine. Cyclophosphamide is shown since it has been used in conjunction with phenothiazines for enhanced reactivity of the latter compounds. (b) Mechanisms suggested to be responsible for phototoxicity of chlorinated PTZ derivatives.

to DNA, and results from one study suggest its highest reactivity to be with the DNA base guanine.¹²⁴ The exact mechanism responsible for its *in vivo* phototoxicity, although not entirely known, has been suggested to be due primarily to reaction of the unstable promaziny radical with cellular biological molecules, where the radical is formed by dechlorination (Figure 2.3b).¹²⁵ Other studies support these findings which indicate that among the PTZ derivatives, those containing a chlorine substituent are the most potent photomutagens. One exception to this finding is the compound methylene blue, which does not contain a chlorine substituent but is known to photooxidize guanine residues.¹¹⁹ It is believed the mutagenic action of the latter compound differs significantly from that of the chlorinated analogs due to its difference in structure, specifically the presence of two amino groups attached to the ring at carbons 3 and 7. Greater activity was also found among those compounds containing an amine in the side chain attached to the N-10 ring position, possibly indicating greater DNA intercalating activity. A second major photoproduct produced from irradiation of PTZ derivatives, aside from dechlorination, is ionization to the radical cation which can subsequently react with molecular oxygen to produce the sulfoxide (Figure 2.3b). The major metabolic route *in vivo* for CPZ has been found to be sulfoxidation of the central thiazine ring, however the sulfoxidized compound is not considered to play a major role in the phototoxic and photoallergic reactions observed *in vivo*.¹²⁵

Synthesis of RePTZ

A complete experimental procedure for the synthesis of the RePTZ complex is provided in Chapter 4. The synthetic route is outlined in entirety in Figure 2.4. The pyrrpnPTZ ligand was built in four steps starting with the readily available parent compound, phenothiazine. In the first step N-alkylation was achieved through Michael addition to acrylonitrile in the presence of N-benzyltrimethyl ammonium hydroxide in 40% MeOH (Triton B) to give the PTZ-propionitrile in 69% yield. The nitrile was converted to the carboxylic acid (step 2) through alkaline hydrolysis for 16 hr. under reflux (30% yield

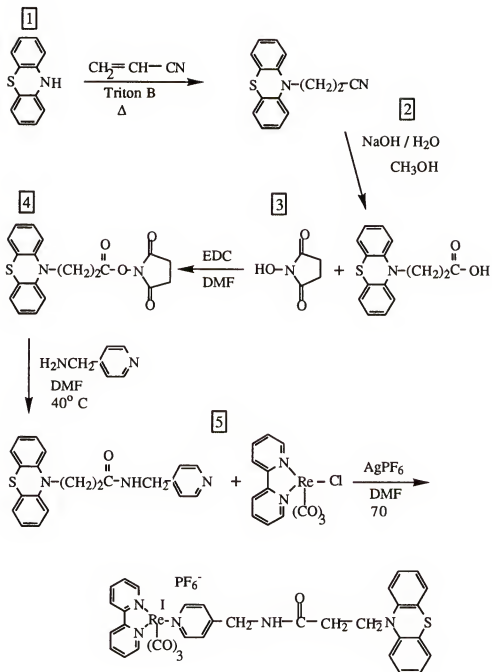


Figure 2.4. Synthesis of RePTZ CQ complex.

after recrystallization). The 4-(aminomethyl)pyridine could not be directly coupled with the carboxylic acid. Therefore the most successful approach involved a method used in peptide synthesis (step 3) where the acid was converted to the N-hydroxy-succinimide ester in the presence of EDC (1-(3-dimethyl-aminopropyl)-3-ethylcarbodiimide) in room temperature dimethyl formamide (DMF) to yield 52% of the activated ester. Subsequent nucleophilic substitution with 4-(aminomethyl)pyridine in DMF with mild heating (step 4) followed by silica column purification achieved 78% of pyrpnPTZ ligand (8.5% overall). The target metal complex was prepared via routine chemistry developed by our group for formation of rhenium complexes. In approximately 2 to 1 ligand to metal ratios pyrpnPTZ was coupled with the $\text{bpyRe}(\text{CO})_3\text{Cl}$ complex (step 5) in DMF at 70^o C in the presence of AgPF_6 salt to produce 39% of the final product, RePTZ, after column purification.

Photophysical Characterization of RePTZ

UV-visible absorption

In Figure 2.5 overlays of the relative UV-visible absorption spectra for RePTZ, the model ReCH_2B , and the pyrpnPTZ ligand, all in 5 mM Tris/50 mM NaCl buffer, are displayed. This figure clearly shows the spectrum of the RePTZ complex to be a sum of the spectra of the component chromophores, indicating the electronic interaction between Re and PTZ upon linkage is very weak. The lowest energy band centered around 350 nm corresponds to the $d\pi(\text{Re}) \rightarrow \pi^*(\text{bpy})$ MLCT transitions, while the peak at 320 nm is both $\pi - \pi^*(\text{bpy})$ and $\pi - \pi^*(\text{PTZ})$ in character as is the higher energy peak centered at 254 nm. The assignments and molar absorptivities for peaks in the RePTZ absorbance spectrum in ethanol solution are listed in Table 2.1 along with corresponding values for the ReCH_2B model. The spectrum of RePTZ is essentially the same in the polar alcoholic solvent as in buffer, thus allowing extrapolation of the ϵ values to buffer solutions and circumventing problems associated with the low solubility of the PF_6 salt of RePTZ in aqueous solvent.

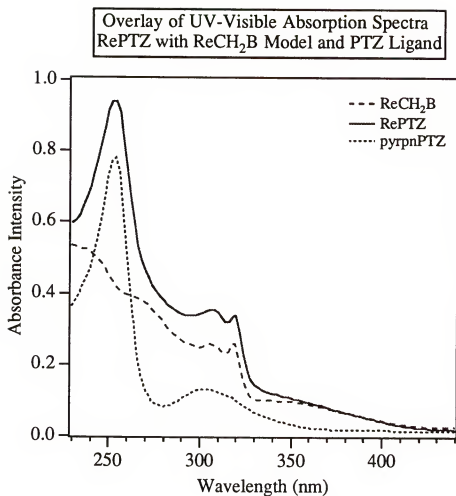


Figure 2.5. UV/visible absorption spectra for ReCH₂B, RePTZ and pyrpnPTZ ligand in 5 mM Tris/50 mM NaCl buffer pH 7.1 where the concentration of all samples is 3.0×10^{-5} M.

Table 2.1. UV-Visible Absorption Characteristics of RePTZ and ReCH₂B Model

Compound ^a	Abs. λ (nm)	Assignment	ϵ (M ⁻¹ cm ⁻¹)
RePTZ ^b	254	$\pi - \pi^*$ (PTZ & bpy)	43,540 \pm 1%
	320	$\pi - \pi^*$ (bpy & PTZ)	13,311 \pm 1%
	350	MLCT	3740 \pm 2%
ReCH ₂ B ^c	254	$\pi - \pi^*$ (bpy)	26,600 ^d \pm 1%
	320	$\pi - \pi^*$ (bpy)	11,800 \pm 1%
	350	MLCT	3400 \pm 1%

^a Complexes are PF₆ salts (e.g. [Re^IPTZ][PF₆⁻]).

^b Measured in ethanol solutions.

^c Measured in 20% MeOH/Buffer solutions unless otherwise noted.

^d In ethanol solution.

Steady-state emission spectra

An overlay of the "normalized" steady-state emission spectra for RePTZ, ReCH₂B and the pyrrpnPTZ ligand in buffer solutions is displayed in Figure 2.6. Samples were excited at 350 nm (the ligand was excited at 304 nm), however the spectra were recorded at different concentrations and conditions (different slit widths in the monochromators) and are presented purely for the purpose of comparing the position of transitions in the component chromophores. If the spectra were recorded under the same instrumental conditions at equal concentrations, the RePTZ spectrum would be substantially weaker by comparison to the model because of the ET quenching mechanism. Both RePTZ and ReCH₂B exhibit a broad unstructured band centered at 590 nm which corresponds to ³MLCT* luminescence. It is important to note that the ³MLCT* luminescence band for RePTZ is superimposable over the corresponding radiative transition in the model compound thus confirming the luminescence originates from the same excited state (and is of the same energy). The PTZ chromophore shows weak fluorescence centered at 450 nm as indicated by the ligand spectrum. In the CQ complex this emission is observed due to fact that the PTZ chromophore has a weak absorption at the excitation wavelength used for the studies (350 nm). Emission quantum yields for the ³MLCT* state (ϕ_{emRe}) for RePTZ and ReCH₂B determined in several different solvents are listed in Table 2.2 as well as the positions of the band maxima. An interesting feature in the spectra are the shifts observed in the maxima of the MLCT bands for both complexes upon going from ethanol to buffer solutions. This is characteristic of the unsymmetrically-shaped *fac*-(b)Re(CO)₃L chromophore where the energy of its ³MLCT* state is influenced by the polarity of the surrounding solvent.¹²⁶ The lower energy of the (bpy⁻)Re^{II}(CO)₃ MLCT* state in aqueous solvent, as compared to the less polar ethanol, indicates a greater degree of stabilization of the excited state in the former solvent. Most important among the data listed in Table 2.2 are the difference in emission quantum yields between the model ReCH₂B and the CQ complex RePTZ. The ϕ_{emRe} for RePTZ are significantly reduced in value compared

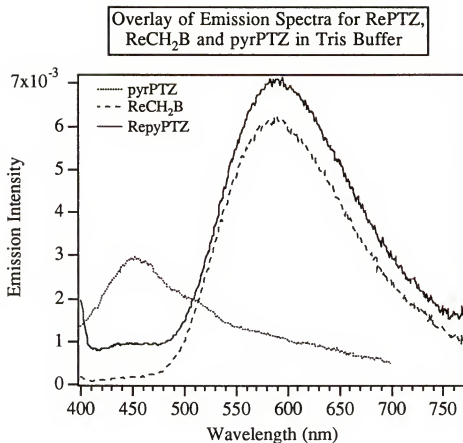


Figure 2.6. Steady-state emission spectra for ReCH₂B, RePTZ and PTZ ligand in air saturated 5 mM Tris/50 mM NaCl pH 7.1 buffer solutions illustrating the similarity in position of the ³MLCT* emission band of RePTZ and the model compound. RePTZ and ReCH₂B were excited at 350 nm, while pyrPTZ was excited at 340 nm. The spectra were recorded under different instrumental conditions therefore their intensities cannot be directly compared.

Table 2.2. Steady-State Emission Characteristics of RePTZ with and without DNA.

Compound	Solvent	λ Em. Peak (nm)	$\phi_{\text{emRe}}^{\text{a}}$ 0 [DNA] _{bp}	$\frac{\phi_{\text{emRe}}}{\text{DNA}} = 20^{\text{b}}$ Re	Incr. $\phi_{\text{emRe}}^{\text{c}}$ $\frac{20 \times \text{DNA}}{0 \text{DNA}}$
RePTZ	EtOH	585	---	---	---
	5 mM Tris/ 50 mM NaCl	591	0.0007 ^e $\pm 15\%$	0.0008 $\pm 15\%$	1.14 ± 0.1
	30% MeOH/ Tris pH 7.1	580	0.002 $\pm 15\%$	0.0019 $\pm 15\%$	0.95 ± 0.1
	30% MeOH/ Acet ^d pH 6.1	580	0.0009 $\pm 15\%$	0.0010 $\pm 15\%$	1.11 ± 0.1
ReCH ₂ B	EtOH	584	---	---	---
	5 mM Tris	590	0.023 $\pm 2\%$	0.022 $\pm 2\%$	0.96 ± 0.05
	10 % MeOH/ Tris pH 7.1	590	0.027 $\pm 2\%$	0.026 $\pm 2\%$	0.96 ± 0.05

^a Quantum yields calculated according to eqn. 4.1 in Chapter 4 using the integrated area of the MLCT emission in the 500 to 770 nm region. The yields were determined relative to Ru(bpy)₃²⁺ in air-saturated H₂O ($\phi = 0.0379$) and are in argon degassed solvent unless otherwise noted.

^b Refers to the QY where the DNA concentration (in base pairs) is 20 times larger than the metal complex concentration. [Re] concentrations typically ranged from 2×10^{-5} M to 6×10^{-5} M.

^c Indicates the increase in quantum yield on going from 0 [DNA]_{bp} to 20 times [DNA]/[Re] ratios and is calculated by dividing the value of ϕ_{emRe} at DNA/Re = 20 by ϕ_{emRe} at [DNA] = 0.

^d Refers to 0.1 M sodium acetate/50 mM NaCl buffer.

^e Measured in air-saturated solutions.

to ϕ_{emRe} for the model. In Tris buffer the ϕ_{emRe} for RePTZ is only 3% of ReCH₂B's quantum yield. This reduction of the MLCT emission by nearly 100% strongly supports the occurrence of an excited-state reaction which effectively quenches the ³MLCT* radiative transition in the RePTZ complex, and is attributed to reductive ET from PTZ to Re* as shown in Scheme 2.2.

Further evidence for the quenching mechanism is provided from the steady-state emission decay data listed in Table 2.3. The samples, in degassed Tris buffer, were excited at 355 nm and the emission decays collected through a 70 nm wide band pass interference filter with maximum transmittance at 600 nm. The data are listed as lifetimes (τ_i) where i corresponds to the number of the component ($i = 1, 2$ or 3 depending on whether there are one, two or three components to the overall decay), and the symbol α_i corresponds to the fractional contribution of the corresponding component lifetime to the overall decay profile. The median lifetime, $\langle \tau \rangle$, is equal to the sum of the component lifetimes multiplied by their fractional contributions:

$$\langle \tau \rangle = \sum_n \tau_n \times \alpha_n \quad 2.4$$

Examination of Table 2.3 shows that the model compound exhibits a mono-exponential decay with a lifetime of 102 ns, while the decay for RePTZ was fit to triple-exponential kinetics. The three component lifetimes for RePTZ, τ_1 , τ_2 and τ_3 , are composed of a very short-lived species $\tau_1 = 1.05$ ns, a slightly longer-lived one $\tau_2 = 9.5$ ns and a long-lived species $\tau_3 = 103$ ns with a lifetime comparable to the model compound. The two short-lived lifetimes correspond to quenched ³MLCT* emission and the 103 ns lifetime is from those molecules in which the MLCT luminescence is not quenched. Notice that the fractional contribution (α_3) of τ_3 is only 8% indicating only a small percentage of the RePTZ molecules escape ET quenching which would be those complexes which are in a more extended conformation. The largest contributor to the overall lifetime is τ_1 with $\alpha_1 = 79\%$, corresponding to those molecules which are most likely in a tightly folded

Table 2.3. Steady-State Emission Lifetimes of RePTZ and Model.^a

Compound	No DNA				High [DNA] _{bp}		
	τ_1 (ns) (α_1 %)	τ_2 (ns) (α_2 %)	τ_3 (ns) (α_3 %)	$< \tau >$ (ns)	τ_1 (ns) (α_1 %)	τ_2 (ns) (α_2 %)	τ_3 (ns) (α_3 %)
RePTZ ^b	1.05 (79%)	9.5 (13%)	103 (8%)	10.2	0.92 (73%)	9.1 (18%)	105 (8.8%)
ReCH ₂ B ^c	107 (100%) $\pm 5\%$			107 $\pm 5\%$	107 (100%) $\pm 5\%$		
							11.6 $\pm 5\%$

^a Decays measured in argon degassed 5 mM Tris/50 mM NaCl pH 7.0 buffer solutions. Samples were excited at 355 nm and emission collected at ~ 600 nm. Data for RePTZ is representative of a single measurement and therefore does not include % error.

^b Concentration for RePTZ was 2.3×10^{-5} M for both measurements. DNA concentration was 5.75×10^{-4} M_{bp} for measurement at high DNA.

^c Concentration of ReCH₂B was 1.9×10^{-5} M for both measurements and DNA concentration was 1.9×10^{-4} M_{bp} for measurement at high [DNA].

conformation such that Re* and PTZ are sufficiently close together for efficient quenching by ET. The species with $\tau_2 = 9.5$ ns, contributing 13% to the overall decay, could be assigned to molecules in which ET is slightly less efficient due to a loosely-held arrangement, perhaps intermediate between fully-extended unquenched and tightly-folded fully quenched. Adding together the component lifetimes multiplied by their fractional contributions gives a median lifetime of $\langle \tau \rangle = 10$ ns which is considerably shorter than 102 ns for the model.

Transient absorption (TA) experiments provide direct evidence for formation of the $[(bpy^-)Re^I(CO)_3(PTZ^+)]$ charge-separated state. The TA spectra for RePTZ in degassed acetonitrile solution is displayed in Figure 2.7. Following laser flash excitation at 355 nm a strong absorption feature appeared at ~ 515 nm which decayed with a lifetime of 27 ns. This species is not present in the TA spectrum for the model, and previous studies on a similar complex have identified the ~ 500 nm transient with the PTZ radical cation that had a lifetime of 25 ns in their complex.¹¹⁵ These results are therefore consistent with initial excitation into the $^3MLCT^*$ state, followed by intramolecular ET to give the charge-separated state as shown by step 2 of Scheme 2.1.

DNA Titration Studies

Steady-state emission DNA titrations of RePTZ were conducted where the metal complex concentration was held constant (typically $\sim 2 \times 10^{-5}$ M) and the amount of DNA varied. Solutions were mixed and degassed, while protected from light, and subsequently their emission spectra recorded. A representative emission titration is illustrated in Figure 2.8 where the $[DNA]_{bp}/[Re]$ ratios are increased from 0 to 15. Addition of DNA did not cause any significant changes in the $^3MLCT^*$ emission as evidenced by the small irregular fluctuations in ϕ_{emRe} values for RePTZ at high DNA/Re ratios listed in Table 2.2. Experimental conditions were varied in order to improve the likelihood of binding, such as lowering the pH in small increments to protonate the N-10 ring nitrogen of PTZ, degassing

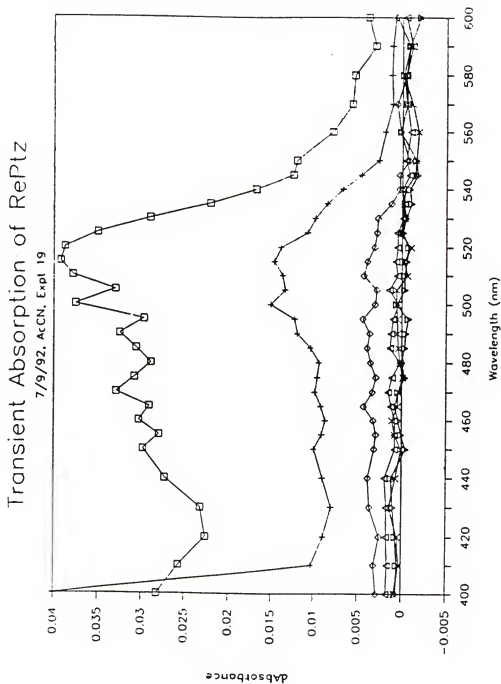


Figure 2.7. Transient absorption spectrum of RePTZ in argon degassed acetonitrile with excitation at 355 nm.

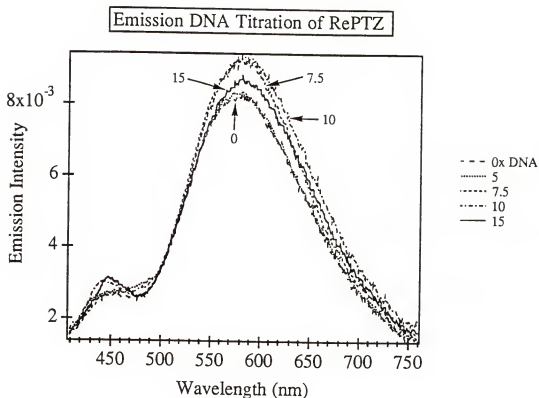


Figure 2.8. Steady-state emission titration of RePTZ with CT DNA in argon degassed 30% MeOH/0.1 M Acetate:50 mM NaCl buffer pH 6.1. The DNA concentrations are expressed as $[\text{DNA}]_{\text{bp}}/[\text{Re}]$ ratios where the $[\text{Re}]$ concentration is equal to 3.5×10^{-5} M. Separate solutions were used for each measurement (fresh aliquots from RePTZ stock soln.) and the $[\text{DNA}]_{\text{bp}}$ concentration varied. Excitation was at 350 nm and the slit widths were 2.50 for excitation and emission monochromators.

solutions and minimizing light exposure prior to measurements to reduce chances of premature ET and formation of the radical cation before binding. Occasionally systematic increases in emission with addition of nucleic acids resulted, however the results were not reproducible. Titrations of the model ReCH_2B suggest that the $(\text{bpy})\text{Re}(\text{CO})_3$ chromophore does not bind to ds DNA, since its Φ_{emRe} and λ_{em} max remained constant in the presence of nucleic acids (Table 2.2). No changes in the MLCT absorption band are observed in parallel DNA absorption titration experiments for both the model and Re-PTZ providing further evidence that the $(\text{bpy})\text{Re}(\text{CO})_3$ chromophore does not bind to DNA.

The emission decay of the RePTZ complex in the presence of high DNA concentration ($[\text{DNA}]_{\text{bp}}/[\text{Re}] = 25$) remained remarkably similar to the decay in the absence of DNA (see Table 2.3). The triple-exponential decay contained three component lifetimes with values nearly equal in length and fractional contribution to the complex when it is free in solution. A slight decrease in the shortest-lived species (τ_1) with corresponding increases in τ_2 and τ_3 were apparent, but the changes are within experimental error. The decay of the model in the presence of DNA remained single-exponential with the same lifetime of 107 ns as in the absence of DNA.

Discussion of RePTZ Results

In solution the RePTZ complex displays efficient intramolecular ET evidenced by attenuation of its emission quantum yields in comparison to the model, ReCH_2B , which does not contain a quenching ligand (Table 2.2). Results from the emission decays support the steady-state emission data indicating the lifetime of the $^3\text{MLCT}^*$ state is decreased by $\geq 90\%$ relative to the lifetime of the model. Furthermore, the PTZ radical cation, which is formed upon ET from PTZ to the photoexcited Re chromophore, is directly seen by transient absorption spectroscopy as evidenced by a strongly absorbing species at 515 nm readily formed after 355 nm laser excitation. The rate of decay of the $^3\text{MLCT}^*$ state and

formation of the PTZ^{•+} radical could not be resolved within the bounds of this instrumentation due to the fast kinetics of FET in the CQ complex.

The ultimate goal of this study was to determine whether interaction of the RePTZ CQ complex with ds DNA would cause a reduction in the intramolecular ET mechanism and hence an increase in luminescence from the ³MLCT* state, according to Figure 2.1. Based on the known biological activity of PTZ and its derivatives, and their DNA binding properties where the relatively planar aromatic heterocyclic structure intercalates in-between base pairs of the DNA helix, it seemed reasonable to assume the RePTZ complex would behave in a similar fashion. Intercalation of the PTZ moiety into ds DNA would most likely occur in such a way that the Re chromophore would be lying in the major groove or extended outside the polymer. In either mode, the distance between PTZ and the Re chromophore would be increased enough to show a significant decrease in the ET rates. However, the results from steady-state emission DNA titrations and the emission decays in the presence of high [DNA] indicate that addition of DNA to solutions of the RePTZ complex have little or no effect on the ET quenching. Several possible explanations could account for this phenomenon. First, the PTZ complex may not bind to DNA due to formation of the sulfoxide at the central thiazine ring. The PTZ radical cation is known to form the sulfoxide (PTZSO) in aqueous solvent.^{124,127} Evidence for the presence of PTZSO can be seen by the formation of absorption peaks at ~ 338 nm, 298 nm, and 270 nm¹²⁷ and the presence of an emission feature at 380 nm.¹²⁴ Closer inspection of the emission spectra for the RePTZ complex reveals the tail end of a strongly emissive component at 400 nm. This feature does not appear to be present in the spectrum of the ligand, nor that of the model. Slight deformities in the UV-visible absorption of the RePTZ complex corresponding to grow-in of broad peaks at 270 nm, 500 nm, 340 nm and in some cases, 516 nm (radical cation peak) appeared in some of the spectra prior to the titrations. Studies have shown the sulfoxides of several PTZ derivatives to be nearly completely inactive in a variety of different biological systems, for instance, displaying

virtually no binding affinity to dopamine D₂ receptors in the brain.¹²³ Molecular mechanics and computer molecular dynamics simulations on CPZ, levomepromazine (LM), methoxypromazine (MP) and their sulfoxides indicated that the sulfoxides possessed greater conformational mobility in the positions of their side chains.¹²³ The energy differences between 'up' and 'down' conformations of the side chains were smaller for the sulfoxides as were the energy barriers for changing between conformations (see Figure 2.9). The 'down' conformations of the side chain resulted in exposure of strong negative electrostatic potentials around the sulfoxyl group in the sulfoxides. This conformation is suggested to weaken the electrostatic interaction of the compounds with dopamine receptors, and to be the cause for inactivity of the sulfoxides in dopamine receptor binding and related tests. The DNA polymer has a highly charged negative potential due to the phosphodiester groups which form the backbone of the helix. The initial step in binding of many intercalating molecules to DNA is considered to be electrostatic in nature, where positively charged groups on the intercalator associate with the negatively charged phosphates. A molecule with strong negative potential would be repelled by the phosphate groups, and as a consequence would not bind to the polymer. Additionally, the conformation of the sulfoxide, which extends upwards above the plane of the central ring, could create steric hindrance to intercalative binding. The PTZ radical cation can also proceed on to degradation, polymerization or react with other nucleophiles to form undesirable side products.¹²⁸ The chain linking Re and PTZ may also inhibit DNA binding of the complex since it contains no positively-charged amine functionality available for electrostatic interactions.

In light of preliminary results regarding the binding of RePTZ with ds DNA, the complex does not appear to possess favorable characteristics for use as a CQ probe for nucleic acids. Excessive reactivity of the PTZ quencher produces an unstable complex which seemingly is inactivated towards binding to DNA. Clearly CQ systems with more suitable properties need to be considered in the design of complexes for this study.

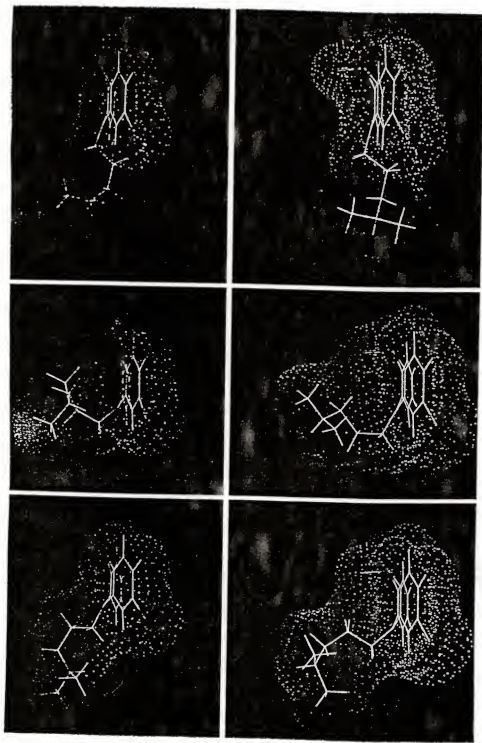


Figure 2.9. Results of Molecular mechanical geometry optimization and molecular dynamics simulations showing the minimum energy conformations of chlorpromazine (CPZ) (top row) and CPZ sulfoxide (bottom row) in vacuo. The conformations of the side chain are as follows: left, extended 'up'; middle, folded 'up'; right, extended 'down'. Dots show water accessible surfaces. From Dahl et al. *J Computer-Aided Mol. Design*, 1992, 6, 207.

Studies of (phen)ReCH₂Q

The preceding study emphasized the requirement that CQ complexes must be stable to their redox (or energy transfer) properties in order to be useful as luminescent DNA probes. Based on this requirement, a second CQ complex was designed which incorporated a dimethylaniline quencher (CH₂Q) having an oxidation potential of +1.00 V (vs. SCE in CH₃CN),¹²⁹ which is +0.15 V higher than the oxidation potential of PTZ, and therefore is a less reactive quencher. However, since the CH₂Q ligand does not possess the polycyclic aromatic ring structure characteristic of DNA intercalating compounds it was inferred that this quencher ligand would not serve well as the binding species within the CQ complex. Consequently the diimine ligand on the Re chromophore was switched from 2,2'-bipyridyl, which had been used in the previous study and does not interact with DNA, to 1,10-phenanthroline which is known to bind to DNA by intercalation. The result, (phen)ReCH₂Q, is a type II system where the Re chromophore is largely responsible for the binding interactions, and the attached CH₂Q ligand serves solely as a quencher although it may participate in some limited binding interactions. The structures of (phen)ReCH₂Q and its model, (phen)ReCH₂B, are shown above in Figure 2.2.

As discussed in the introduction to this chapter, the CH₂Q ligand quenches the emission of the ³MLCT* state by reductive ET where the dimethylaniline moiety serves as the electron donor and photoexcited Re is the acceptor according to Figure 2.1. This mechanism was determined from previous studies on the CQ complex, (bpy)ReCH₂Q,¹²⁹ where the driving force for FET in CH₃CN was given as $\Delta G_{FET}^0 = -0.22$ eV. The thermodynamic driving force for FET in the (phen)ReCH₂Q complex can be calculated according to eqn. 1.5 using $E_{1/2}(\text{CH}_2\text{Q}^{0/+}) = 1.0$ V, $E_{1/2}(\text{Re}^{+/0}) = 1.15$ V (vs. SCE in CH₃CN) and $E_{0-0} = 2.44$ eV, giving a value of $\Delta G_{FET}^0 \sim -0.29$ eV. This value is considerably lower than the FET driving force calculated for the RePTZ complex ($\Delta G_{FET}^0 \sim -0.4$ eV), although slightly more exothermic (~ -0.07 eV) than for the bpy analog. E_{0-0} was calculated from analysis of the emission spectra of the complex in 30% MeOH/Buffer

solution. The position of E_{0-0} is typically near the high-energy side of the emission maximum, where the intensity is one third the maximum intensity.¹⁰⁷

Studies by Barton et al.^{130,33} on the complex $[\text{Ru}(\text{phen})_3]^{2+}$ have indicated that the metal chromophore binds to DNA with one of the phen ligands intercalated between base pairs in the double helix and the other two ligands providing van der Waals contacts within the closely-fitting groove. Emission enhancements of 1.87 (I/I_0 where I_0 is the intensity in the absence of DNA and I is the intensity at high DNA concentrations) and red-shifts of the emission maximum of 2 nm were observed for this complex in the presence of calf thymus (CT) DNA. Other studies have clearly demonstrated the DNA intercalating ability of the 1,10-phenanthroline molecule.¹³¹ By inference it seems reasonable that the $(\text{phen})\text{ReCH}_2\text{Q}$ complex would also bind to DNA with the phenanthroline ligand at the Re center intercalated in-between DNA base pairs and the CH_2Q ligand lying in the groove providing H-bonding contacts with the amide group in the linker chain and the dimethylamine group on aniline.

Synthesis

A detailed discussion of the synthesis of $(\text{phen})\text{ReCH}_2\text{Q}$ and the model $(\text{phen})\text{ReCH}_2\text{B}$ are provided in Chapter 4. A general outline for the $(\text{phen})\text{ReCH}_2\text{Q}$ synthesis is illustrated in Figure 2.10 starting with (step 1) formation of the $(\text{phen})\text{Re}(\text{CO})_3\text{Cl}$ by refluxing 1,10-phenanthroline with $\text{Re}(\text{CO})_5\text{Cl}$ in toluene, the routine procedure used for coupling most diimine ligands to the metal center. The N-(4-pyridyl)methyl-N',N'-dimethylaminobenzamide ligand (termed CH_2Q for simplification in this study) was previously prepared by D. B. MacQueen in this laboratory (see reference in materials section Chapter 4). Coupling of the CH_2Q ligand with $(\text{phen})\text{Re}(\text{CO})_3\text{Cl}$ (3:1 molar ratio) followed the routine synthesis (step 2) of heating at 70 °C in DMF solvent in the presence of AgPF_6 salt, yielding 35% pure product after purification by column chromatography.

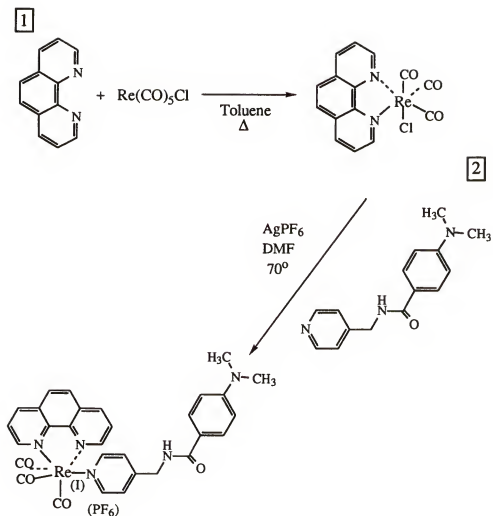


Figure 2.10. Synthesis of (phen)ReCH₂Q complex.

Photophysical Characterization of (phen)ReCH₂Q

UV-visible absorption

The weak bands centered at 360 nm in the UV-visible absorption spectra for (phen)ReCH₂Q and the model (phen)ReCH₂B, corresponding to the $d\pi(\text{Re}) \rightarrow \pi^*(\text{phen})$ MLCT transition, are essentially equal in position and intensity, as shown by Figure 2.11. The MLCT band in the phen complexes is also approximately equal in position to the MLCT absorption transition in the bpy complexes (see Figure 2.5), demonstrating the similar electronic properties of the two diimine ligands. The higher energy peaks in the absorption spectra of (phen)ReCH₂Q and (phen)ReCH₂B are assigned to intraligand $\pi - \pi^*$ transitions. Table 2.4 lists the molar absorptivities (ϵ) at 350 and 360 nm of the MLCT for (phen)ReCH₂Q and (phen)ReCH₂B in 30% MeOH/Tris buffer solutions. In comparison to the bpy complexes, the ϵ values for the phen complexes are slightly greater in intensity.

Steady-state and time resolved emission

The steady-state emission spectrum of (phen)ReCH₂Q in 30% MeOH/Buffer solution displays a broad unstructured envelope in the 470 to 800 nm region which is superimposable on the ³MLCT* spectrum of the model compound obtained under the same conditions. This indicates the luminescence of the CQ complex emanates from the same excited state as that of the model. In contrast to the model spectrum, the intensity of emission from (phen)ReCH₂Q in solution is dramatically reduced compared to the model as shown in the overlay of their steady-state emission spectra in Figure 2.12. Quantum yields for ³MLCT* emission in the complexes, which were measured in Tris buffer and in 30% MeOH/Buffer solutions under air saturated conditions, are listed in Table 2.5. The steady-state emission spectra and the emission quantum yields clearly show that the luminescence from (phen)ReCH₂Q is quenched by 95% in comparison to the luminescence of the model.

Experimental data from fits of the luminescence decays of (phen)ReCH₂Q and (phen)ReCH₂B, in degassed and air-saturated 30% MeOH/Tris buffer, are listed in

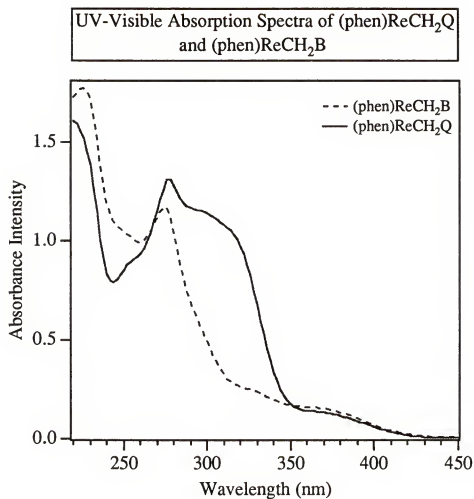


Figure 2.11. Overlay of UV-visible absorption spectra of (phen)ReCH₂B [3.27×10^{-5} M] and (phen)ReCH₂Q [3.24×10^{-5} M] in 30% MeOH/25 mM Tris pH 7.1 showing the long-wavelength shoulders of the MLCT bands of the chromophores (350 - 420 nm region).

Table 2.4. UV-Visible Absorption Characteristics of (phen)ReCH₂Q and (phen)ReCH₂B.^a

Compound ^b	Abs. λ (nm)	Assignment	ϵ (M ⁻¹ cm ⁻¹)
(phen)ReCH ₂ Q	350	MLCT	4980 \pm 15%
	360	MLCT	4270 \pm 5%
(phen)ReCH ₂ B	350	MLCT	5500 \pm 10%
	360	MLCT	4960 \pm 5%

^a Measured in 30% MeOH/25 mM Tris pH 7.1 buffer solutions.^b Complexes are PF₆ salts (e.g. [(phen)Re^ICH₂Q][PF₆⁻]).

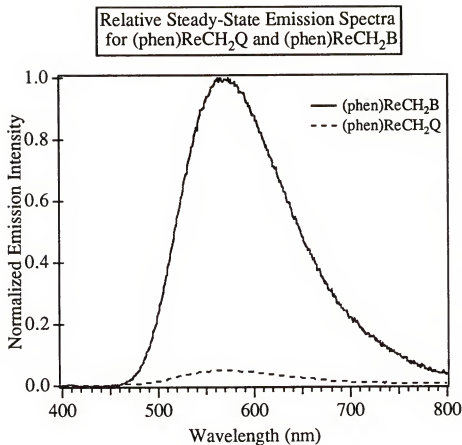


Figure 2.12. Steady-state emission spectra of (phen)ReCH₂Q and (phen)ReCH₂B in air-saturated 30% MeOH/25 mM Tris pH 7.2 solutions. The spectra have been normalized to the QY of (phen)ReCH₂B in order to illustrate the effect of the intramolecular ET quenching of the ³MLCT* state by the dimethylaniline ligand in (phen)ReCH₂Q. Samples were excited at 350 nm.

Table 2.5. Steady-State Emission Characteristics of (phen)ReCH₂Q and (phen)ReCH₂B with and without DNA.^a

Compound	Solvent	λ Excitation (nm)	Em. Maximum (nm)	ϕ_{emRe}^b 0 [DNA] _{bp}	ϕ_{emRe}^c High [DNA] _{bp}	DNA/Re Ratio ^d	Incr. ϕ_{emRe}^e HighDNA/DNA
(phen)ReCH ₂ Q	25 mM Tris	360	577	0.0029 \pm 5%	0.0040 \pm 5%	45	1.38
	30% MeOH/Tris pH 7.2	350 or 360	570	0.0029 \pm 5%	0.0043 \pm 5%	30	1.50
(phen)ReCH ₂ B	25 mM Tris	360	573	0.059 \pm 5%	0.0591 \pm 5%	25	1.0
	30% MeOH/Tris pH 7.2	360	571	0.067 \pm 5%	0.066 \pm 5%	45	0.98

^a Measurements obtained at room temperature in air-saturated solutions.

^b Quantum yields calculated according to eqn. 4.1 in Chapter 4 using the integrated area of the MLCT emission in the 400 to 800 nm region relative to Ru(bpy)₃²⁺ in air-saturated H₂O ($\phi = 0.0379$).

^c Refers to the QY in the presence of high concentrations of [DNA]_{bp}. The ratios of [DNA]_{bp} concentration to metal complex concentration are listed in the next column to the right.

^d Refers to the concentration of the DNA (in base pairs) divided by the concentration of metal complex ($\sim 3.5 \times 10^{-5}$ M) and corresponds with the QY values in the presence of DNA listed in the column immediately to the left.

^e Indicates the increase in quantum yield on going from 0 [DNA]_{bp} to high [DNA]_{bp} ratios and is calculated by dividing the value of ϕ_{emRe} at high DNA/Re by the ϕ_{emRe} at [DNA] = 0.

Table 2.6. Focusing first on the model, its decay follows mono-exponential kinetics with a lifetime (τ) of 1.024 μ s in degassed solution and 550 ns in air-saturated solution. The shortened lifetime under air-saturated conditions is due to diffusional quenching by oxygen which can occur within the long time-frame of the $^3\text{MLCT}^*$ lifetime for this complex. The lifetime of the CQ complex is considerably shortened in length compared to the model. The decay of (phen)ReCH₂Q was fit to triple-exponential kinetics and showed similar values in both air-saturated and degassed solutions. Three separate lifetime components were resolved from the fits composed of a very short-lived species (τ_1) with a lifetime of ~ 0.7 ns, an intermediate-lived species (τ_2) possessing a lifetime of ~ 12 ns and a longer-lived species (τ_3) that has a lifetime of ~ 168 ns. The contributions of the shorter-lived components (τ_1 and τ_2) are similar in magnitude (as evidenced from their fractional contributions, α_1 and α_2), and the overall lifetime ($\langle\tau\rangle$) is comprised mainly of these two species. The three lifetime components for (phen)ReCH₂Q can be assigned to differentially quenched complexes where τ_1 would correspond to molecules in a conformation where the CH₂Q ligand is oriented in a folded position lying within close proximity to the Re chromophore and able to participate in highly efficient ET. τ_3 would most likely represent those molecules which are in a more or less extended conformation and whose ET quenching rates are slowed by the increased distance between Q and Re, while τ_2 would represent molecules where the CH₂Q ligand is oriented in a conformation intermediate between fully-extended and bent over. A three-dimensional structural projection from molecular modeling studies on the (bpy)ReCH₂Q complex¹²⁹ illustrating the range of orientations available to the CH₂Q ligand is displayed in Figure 2.13. Three representative structures are superimposed differing in conformation of the CH₂Q ligand, where the main degrees of conformational freedom for the complex were found to be rotation around the single bonds between the methylene group and the 4-pyridyl carbon and the methylene group and the amide nitrogen. The modeling was performed using the SYBYL program with Tripos force field.¹³² Although a wide range of conformations are available to the

Table 2.6. Emission Lifetimes of (phen)ReCH₂Q and (phen)ReCH₂B.^a

Compound	No DNA					High DNA				
	τ_1 (ns) (α_1 %)	τ_2 (ns) (α_2 %)	τ_3 (ns) (α_3 %)	τ_1 (ns) (α_1 %)	τ_2 (ns) (α_2 %)	τ_3 (ns) (α_3 %)	τ_1 (ns) (α_1 %)	τ_2 (ns) (α_2 %)	τ_3 (ns) (α_3 %)	$\langle \tau \rangle$ (ns)
(phen)Re-CH ₂ Q ^b	0.70 (42%)	11.6 (57%)	169 (0.61%)	0.71 (48%)	11.8 (52%)	164 (0.65%)	0.71 (48%)	11.8 (52%)	164 (0.65%)	7.54
Air Saturated	0.57 (46%)	11.8 (53%)	156 (0.60%)	0.74 (45%)	11.2 (52%)	136 (0.70%)	0.74 (45%)	11.2 (52%)	136 (0.70%)	7.11
(phen)Re-CH ₂ B ^c	1025 (100%)			979 (100%)			979 (100%)			979
Air Saturated	$\pm 5\%$ 550 (100%) $\pm 6\%$			$\pm 5\%$ 550 (100%) $\pm 6\%$			$\pm 6\%$ 500 (100%) $\pm 6\%$			$\pm 6\%$ 500 $\pm 6\%$

^a Decays measured in 30% MeOH/ 25 mM Tris buffer solutions. Samples were excited at 355 nm and emission collected at ~ 600 nm.

^b Measured in degassed solution. The concentration of (phen)ReCH₂Q was [6.1E-5M] and the DNA concentration (for measurements with DNA) was [1.15E-3M] for both the degassed and air-saturated data sets. This data is from measurements obtained on the same day. Similar studies were conducted under slightly different conditions resulting in slightly different lifetime values for τ_3 , in particular, however the changes with added DNA were the same as observed for this data set.

^c Measured in degassed solution. The concentration of (phen)ReCH₂B was [3.35E-5M] and the DNA concentration (for measurements with DNA) was [8.35E-4M] for both the degassed and air-saturated data sets.

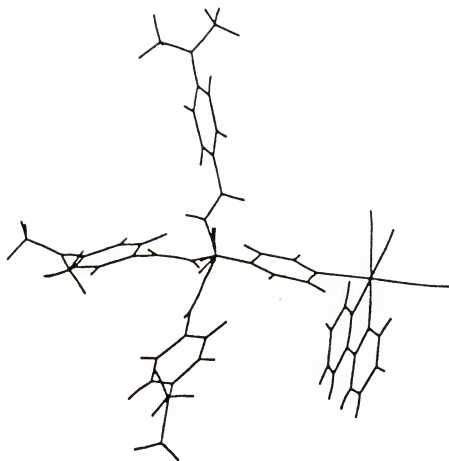


Figure 2.13. Computer-generated (SYBYL program) projection of the three-dimensional structure of (bpy)ReCH₂Q showing the superposition of three typical energetically accessible conformations of the dimethylaniline ligand. From MacQueen, D. B., Schanze, K. S. *J. Am. Chem. Soc.*, **1991**, 113, 7470.

complex due to the relatively unhindered rotation around the two single bonds, the distance between the Re atom and the center of the dimethylaminobenzyl ring is shown to remain within the range of 9.0 - 10.5 Å. Importantly the studies indicate that the orientation of the CH₂Q ligand is unconstrained and likely to be fluctuating rapidly on the time scale of the ET process, however the separation distance between the Re chromophore and the donor ligand is relatively confined.

The rate for the intramolecular forward ET (k_{FET}) reaction in (phen)ReCH₂Q was calculated from the emission lifetimes (degassed conditions) according to equation 1.6, giving a value of $1.25 \times 10^8 \text{ sec}^{-1}$ as listed in Table 2.7. The k_{FET} for The phen CQ complex possesses a greater driving force ($\Delta G_{FET}^0 = -0.29 \text{ V}$) and a faster FET rate than the (bpy)ReCH₂Q complex, which displays a $k_{FET} = 8.6 \times 10^7 \text{ s}^{-1}$ in degassed CH₃CN with a driving force of $\Delta G_{FET}^0 = -0.22 \text{ V}$, as stated earlier. This is consistent with semi-classical theory which has shown that k_{FET} increases with increasing driving force,^{133,134} however caution must be taken since comparison of rates in different solvents will affect the reorganizational energies and therefore the FET rates (see Chapter I, eqn. 1.11).

Transient absorption spectroscopy

Transient absorption spectroscopic experiments were carried out on (phen)ReCH₂Q and its model in argon degassed CH₃CN and 30% MeOH/Tris buffer solutions by using the third harmonic output of a Q-switched Nd:YAG laser for excitation (355 nm, 10 mJ/pulse, 10 ns fwhm). The spectra for both the CQ complex and the model display strong transient absorption in the wavelength range from 350 to 700 nm, however the spectra for (phen)ReCH₂Q are markedly different from those of the model. Figures 2.14a and 2.16a display the TA spectra for the model (phen)ReCH₂B in degassed CH₃CN and 30% MeOH/25 mM Tris buffer solutions, respectively, taken at delay times ranging from 0 to 3.2 μs following the laser pulse. The spectra are essentially the same in the two solvents, showing broad, relatively unstructured absorption which decays by monoexponential kinetics with a lifetime of $\tau = 1.0 \mu\text{s}$ (see Table 2.7). This is in close agreement to the

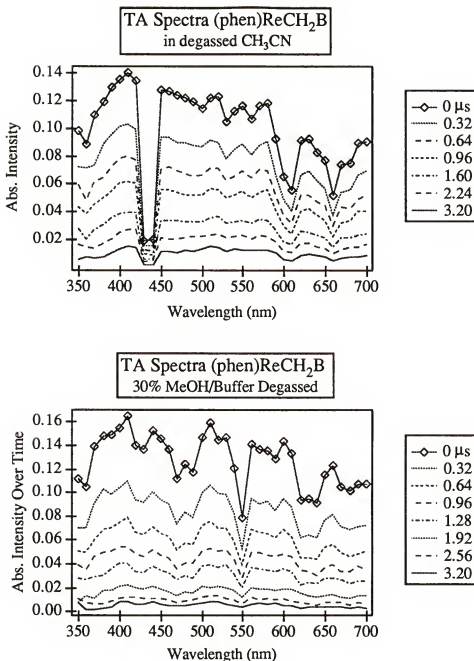


Figure 2.14. Transient absorption spectra of ReCH₂B in (a) degassed CH₃CN [1.4×10^{-4} M] and (b) in degassed 30% MeOH/25 mM Tris buffer [2×10^{-4} M]. Samples were excited at 355 nm and a background emission correction was implemented for the measurements. The delay times corresponding to the different spectra recorded after excitation are shown (in μ s) in the legends.

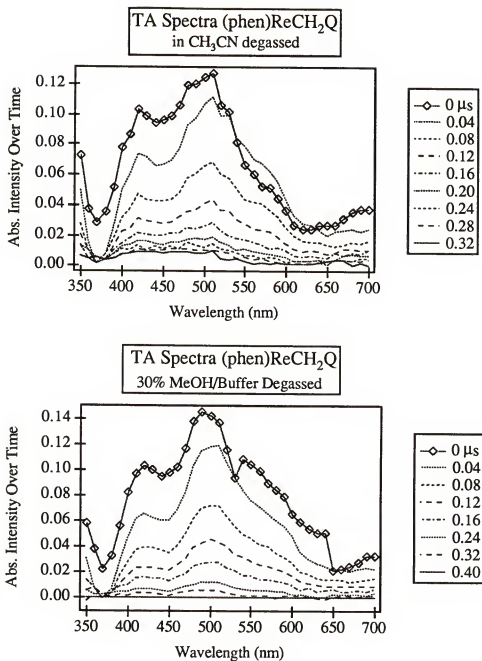


Figure 2.15. Transient absorption spectra of (phen)ReCH₂Q in (a) degassed CH₃CN [1.2×10^{-4} M] (b) degassed 30% MeOH/25 mM Tris buffer [2.4×10^{-4}]. Samples were excited at 355 nm and the delay times after excitation corresponding with the recorded spectra are listed as μs in the legend.

Table 2.7. Transient Absorption Decay Rates and Electron-Transfer Data.

Compound	Solvent ^a	ΔG_{BET}^a (eV)	τ_{TA} (ns)	k_{BET} (s ⁻¹)	ΔG_{FET} (eV)	k_{FET} (s ⁻¹)
(phen)ReCH ₂ Q	CH ₃ CN	-2.15	78	1.30×10^7	-0.29	1.25×10^8
	30% MeOH/ Tris Buffer		80	1.24×10^7		
	w / CT DNA		83	1.20×10^7		
(phen)ReCH ₂ B	CH ₃ CN					1.32×10^8
	30% MeOH/ Tris Buffer		950			

^a All in argon degassed solutions. See the corresponding figures for details concerning sample concentrations.

steady-state emission lifetime measured for this complex in degassed solution listed in Table 2.6. The agreement between the emission and transient absorption lifetimes is strong evidence that the TA spectra for (phen)ReCH₂B can be assigned to the $d\pi(\text{Re}) \rightarrow \pi^*(\text{phen})$ MLCT state. The TA spectra for (phen)ReCH₂Q measured in degassed CH₃CN and 30% MeOH/buffer solutions, respectively, taken at delay times ranging from 0 to 400 ns after laser excitation are displayed in Figures 2.14b and 2.15b. The CQ complex exhibits a strong absorption feature in the 400 to 600 nm region that is centered at 500 nm and decays with a lifetime of $\tau = 80$ ns in either solvent (Table 2.7). The transient absorption lifetime for (phen)ReCH₂Q is considerably shorter than the TA and emission lifetimes of the MLCT state of the model, however it is longer than the median emission lifetime, $\langle \tau \rangle = 7$ ns, for the MLCT state of the CQ complex (see Table 2.6). In addition, TA spectra for the (bpy)ReCH₂Q CQ complex show similar absorption in the 450 - 550 nm region that decays with a lifetime of 77 ns in degassed CH₃CN solution.¹²⁹ From studies of substituted dimethylaniline radical cations in low-temperature glasses it is suggested that the DMAB radical cation should absorb near 500 nm.¹³⁵ On these lines of evidence the TA spectra of (phen)ReCH₂Q can be assigned to the ligand-to-ligand charge-transfer (LLCT) state, $[(\text{phen}^-)\text{Re}^{\text{I}}(\text{CO})_3\text{-CH}_2\text{Q}^+]\text{ }^+$, which is formed from FET according to Figure 2.1.

The TA lifetimes provide a direct route to determination of the back ET rate (k_{BET}) according to equation 2.5:

$$k_{\text{BET}} = \frac{1}{\tau_{\text{TA}}} \quad 2.5$$

The rates of BET for the (phen)ReCH₂Q in CH₃CN and 30% MeOH/Buffer are listed in Table 2.7 along with the estimated thermodynamic driving force for the BET reaction determined according to equation 2.6:

$$\Delta G_{\text{BET}} \approx E_{1/2}(b/b^-) - E_{1/2}(\text{CH}_2\text{Q}/\text{CH}_2\text{Q}^+) \quad 2.6$$

where $E_{1/2}(\text{CH}_2\text{Q}/\text{CH}_2\text{Q}^+)$ is the oxidation potential of the CH_2Q quencher and $E_{1/2}(\text{b}/\text{b}^-)$ is the reduction potential of the diimine ligand on the Re chromophore. Using $E_{1/2}(\text{CH}_2\text{Q}/\text{CH}_2\text{Q}^+) = 1.0 \text{ V}$ and $E_{1/2}(\text{b}/\text{b}^-) = 1.15 \text{ V}$ (both vs. SCE in CH_3CN) gives $\Delta G_{\text{BET}} = -2.15 \text{ V}$, which is slightly less exothermic than ΔG_{BET} for $(\text{bpy})\text{ReCH}_2\text{Q}$ which has been determined to be -2.25 V in CH_3CN with a corresponding BET rate equal to $1.3 \times 10^7 \text{ sec}^{-1}$.

Emission DNA Titrations

Having established the general photophysical properties of $(\text{phen})\text{ReCH}_2\text{Q}$ and its model, steady-state emission DNA titrations were conducted in order to determine whether the complexes bound to CT DNA and if binding caused changes in their luminescent properties. The titrations were performed in air saturated 25 mM Tris buffer and 30% MeOH/25 mM Tris where the metal complex concentration was held constant and the $[\text{DNA}]_{\text{bp}}$ concentration varied. Separate solutions, prepared from the same metal complex stock solution with the appropriate amount of added DNA, were used for each measurement. Samples were excited at either 350 or 360 nm and their emission monitored from 400 to 800 nm. A more detailed description of the experimental conditions can be found in the experimental section of Chapter 4. Figure 2.16 displays the emission spectra from the titration of $(\text{phen})\text{ReCH}_2\text{Q}$ with increasing amounts of CT DNA (up to $[\text{DNA}]_{\text{bp}}/[\text{Re}] = 35$ where $[\text{DNA}]_{\text{bp}}/[\text{Re}]$ (or DNA/Re) refers to the concentration of DNA in base pairs divided by the concentration of the metal complex). The spectra, in general, show gradual luminescence enhancements with added increments of DNA although the increases are not completely linear. Slight red-shifts, $\sim 3-4 \text{ nm}$, of the MLCT emission bands are evidenced in the spectra with increasing DNA. Table 2.5 lists the quantum yields for $(\text{phen})\text{ReCH}_2\text{Q}$ and the model at high DNA/Re ratios, and the relative increases in QY which were determined from the MLCT emission QY in the presence of high $[\text{DNA}]_{\text{bp}}$ (ϕ_{emDNA}) divided by the MLCT emission QY in the absence of DNA (ϕ_{emRe}).

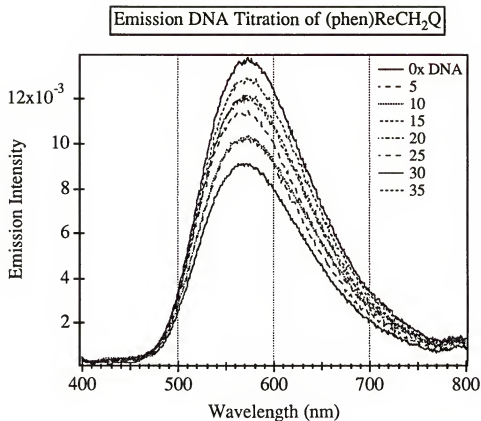


Figure 2.16. Steady-state emission titration of (phen)ReCH₂Q [3.2×10^{-5} M] with CT DNA in air-saturated 30% MeOH/25 mM Tris buffer pH 7.2. Excitation was at 350 nm and the slit widths were 2.5 on the excitation monochromator and 1.25 on the emission monochromator. DNA concentrations are expressed as [DNA]_{bp}/[Re] ratios and are listed in the legend.

Enhancements in the QY for (phen)ReCH₂Q range from 40% to 55% while the emission QY and the λ_{em} max for the model (phen)ReCH₂B do not change, within experimental error, upon addition of nucleic acids. These results indicate that the luminescence enhancements observed in the titrations of the CQ complex with DNA are due mainly to a reduction in the quenching ability of the CH₂Q ligand and not from changes in the environment of the metal center. Studies on other transition metal complexes have shown that intercalation of one of the diimine ligands directly attached to the metal center can result in luminescence enhancements due to electronic interactions with the DNA bases and reduction of non-radiative emission processes.⁷⁴

To better visualize the luminescence increases for (phen)ReCH₂Q in the presence of ds DNA, the emission QY's from several experiments versus [DNA]_{bp}/[Re] ratios are plotted in Figure 2.17 (points in the graph are the experimental data). It is clear from the graph that the emission enhancements rise over a wide span of DNA concentrations and do not appear to reach saturation by DNA/Re ratios as large as 45. The emission QY data was analyzed in order to estimate the binding constant, K_b , of the CQ complex to DNA and the size of the binding site, n , which is the number of DNA base pairs covered by the bound molecule. The binding parameters were determined according to a fitting program described in Appendix A as Method III which is based on the Scatchard equation. From the best fit curve to the QY data, displayed as the solid line in Figure 2.17, a binding constant of $K_b = 5.5 \times 10^3 \text{ M}^{-1}$ and a site size of $n \cong 5$ base pairs were determined for binding of (phen)ReCH₂Q to CT DNA. The site size for this complex is comparable to values determined for other DNA intercalators, which generally range from 2 to 6 base pairs, and can vary depending upon the experimental conditions and the type of analysis used. For instance, the site size for N-methylphenanthrolium cation in 10 mM MES (2-(N-morpholino)ethanesulfonic acid) buffer (5 mM in Na⁺) was determined by Gabbay et al.¹²³ to be $n = 4.05$ with a binding constant of $4.03 \times 10^4 \text{ M}^{-1}$. According to studies by Barton et al.³³ the cationic transition metal complex [Ru(phen)₃]²⁺ possesses a binding

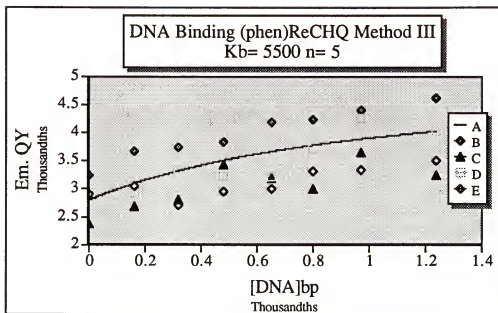


Figure 2.17. Changes in the steady-state emission QY for (phen)ReCH₂Q with increasing [DNA]_{bp} concentration. The markers correspond to data from four different experiments and the solid line (A) is a best-fit curve generated according to the method III binding analysis in Appendix A. The intrinsic binding constant, K_b , and site size, n , were obtained from the curve-fitting process. Experimental conditions for the data are as follows: B = [3.24E-5M] in 30% MeOH/25 mM Tris with λ_{ex} at 360 nm; C = [3.18E-5] in 30% MeOH/25 mM Tris with λ_{ex} at 350 nm; D = [4.1E-5M] in 25mM Tris with λ_{ex} at 360 nm; E = [3.14E-5M] in 30% MeOH/5 mM Tris:50 mM NaCl with λ_{ex} at 350 nm.

constant for CT DNA of $K_b \equiv 5.5 \times 10^3 \text{ M}^{-1}$ and a site covering size of 4 base pairs in 5 mM Tris/50 mM NaCl solution. Remarkably the (phen)ReCH₂Q complex and [Ru(phen)₃]²⁺ share both the same binding constant and site size to CT DNA, within experimental error. However, these binding constants are relatively weak in comparison to classical intercalators such as ethidium bromide which binds to CT DNA with an intrinsic binding constant of $2.5 \times 10^6 \text{ M}^{-1}$ in 25 mM Tris/15 mM NaCl buffer.²¹

Emission decays for (phen)ReCH₂Q and (phen)ReCH₂B were recorded in 30% MeOH/Buffer solutions containing [DNA]_{bp}/[Re] ratios of 20 and 25, respectively, under degassed and air-saturated conditions. Results of the experimental fits to the decays are listed in Table 2.6 to the right of the decay data in the absence of DNA. Comparing the median lifetimes, $\langle \tau \rangle$, between 0 DNA and high DNA for both complexes, minor *decreases* of approximately 5% in their overall lifetimes are apparent on going from 0 to high DNA concentration. Focusing on the individual lifetime components for (phen)ReCH₂Q, τ_1 , τ_2 and τ_3 , the three lifetimes are essentially the same length as in the absence of DNA, except for τ_3 , which is slightly attenuated in the presence of DNA, and τ_1 in the air-saturated measurements which lengthens from 0.57 to 0.74 ns. The fractional contributions, α_1 , α_2 and α_3 , show small shifts toward more contribution of τ_3 in the presence of DNA. The decrease in overall lifetime for (phen)ReCH₂Q appears to be caused by attenuation of the lifetime of the long-lived species, τ_3 , and since the model experiences this effect to the same degree it likely is due to disturbance of the MLCT decay rate by the nucleic acids. The increased contribution of τ_3 could be a reflection of a greater number of CQ complexes in a fully extended conformation, due to binding to the DNA, however all the changes in lifetimes are within experimental error and therefore can not be significantly weighted in their implicit meaning. The latter is particularly relevant since repeat experiments produced similar results. More importantly the lack of visible change in the lifetime of the CQ in the presence of DNA could indicate that (1) it does not bind very strongly to the double-helix and therefore the Re chromophore is still accessible to

quenching by the CH₂Q ligand, (2) binding is not occurring or (3) binding *enhances* the FET rate.

Measurement of the transient absorption spectra for (phen)ReCH₂Q in degassed 30% MeOH/Buffer solution under the same experimental conditions as described above except for the presence of DNA (where the DNA/Re ratio was ~22) showed no difference in the appearance of the transient absorption peak, as illustrated in Figure 2.18, and only a slight increase in the lifetime of the transient species ($\tau = 83$ ns, see Table 2.8).

In order to provide more information towards understanding the binding mode of (phen)ReCH₂Q to ds DNA, Stern-Volmer quenching experiments were performed using the model (phen)ReCH₂B with the quencher [Fe(CN)₆]³⁻ in the absence and presence of CT DNA. Free in solution the rate of intermolecular quenching of the ³MLCT* state by [Fe(CN)₆]³⁻ should be diffusion controlled with a quenching constant of $k_{\text{DIF}} \sim 10^{10} - 10^9 \text{ M}^{-1} \text{ sec}^{-1}$. In the presence of DNA, depending on the binding interaction, the (phen)ReCH₂B complex should be shielded from the quenching species due to repulsion between the negatively charged quencher and the negative charge on the DNA phosphate groups resulting in a reduction of the quenching rate. The respective quenching rates are obtained from plots of the experimental emission quantum yields ($\phi_{\text{em Re}}^0 / \phi_{\text{em Re}}$) versus quencher concentration [Q] according to eqn. 2.7:

$$\frac{\phi_{\text{em Re}}^0}{\phi_{\text{em Re}}} = 1 + k_q \tau^0 [Q] \quad 2.7$$

where $\phi_{\text{em Re}}^0$ is the emission QY of the chromophore in the absence of quencher, $\phi_{\text{em Re}}$ is the emission QY in the presence of quencher, τ^0 is the emission lifetime of the chromophore in the absence of quencher (which is equal to $1/k_r$, the inverse of the radiative rate in the absence of quencher), [Q] is the quencher concentration and k_q is the quenching rate. The experiments were conducted in air saturated 25 mM Tris buffer and the ratio of [DNA]_{bp} to [Re] in the second experiment was 25. Results of the two experiments are

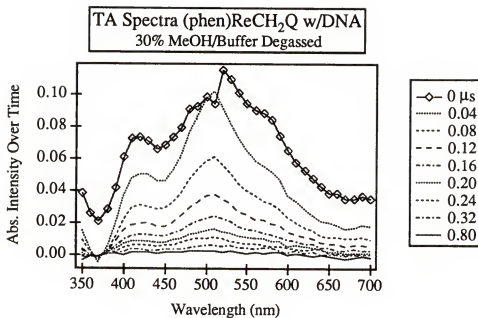


Figure 2.18. Transient absorption spectra of (phen)ReCH₂Q [1×10^{-4} M] with CT DNA where the $[DNA]_{bp} = 2.25 \times 10^{-3}$ M. The sample was excited at 355 nm and the time increments after the laser pulse corresponding to the spectra displayed are given in the legend as μ s.

plotted in Figure 2.19, and the rates of quenching obtained from the slopes of the lines, with $\tau^0 = 500$ ns, were determined to be $k_{q0} = 7.93 \times 10^9 \text{ M}^{-1} \text{ sec}^{-1}$ and $k_{q\text{DNA}} = 6.08 \times 10^9 \text{ M}^{-1} \text{ sec}^{-1}$ for quenching in the absence and presence of DNA, respectively. Clearly the quenching rate is decreased with added DNA, showing a 23% reduction in rate, however the decrease is comparable to a complex experiencing only partial shielding from the quencher.

Discussion

The picture which emerges from piecing together the results of the DNA binding studies of the (phen)ReCH₂Q complex is that of a molecule which is bound to the double-helix in a loosely-held fashion in such a way that does not greatly disrupt the ability of the linked CH₂Q ligand to quench the ³MLCT* state. The increases in the MLCT QY's with addition of DNA and the reduction of Stern-Volmer quenching of the model in the presence of DNA suggests the complex might be lying in the groove with the phen ligand on the Re chromophore partially intercalated in-between base pairs. Considering the size of the metal center and the fact that most transition-metal complexes tend to bind to the major groove of B-DNA,³³ it is likely that (phen)ReCH₂Q also binds by way of the more open major groove. Additionally, the dimethylaniline quencher would likely be neutral at pH 7.0 (pK_a ≈ 5.1) and therefore slightly repulsive to the minor groove which possesses a net negative potential. Molecular modeling studies using Macromodel suggest that the geometry at the metal center causes steric constraint to intercalation. The 90 degree angle between the facial diimine (phen) and the CH₂Q ligand, as well as the 90° angle between phen and the adjacent carbonyls attached at the Re center, allow the metal complex to only partially insert in-between base pairs, and more likely lie within the major groove (Figure 2.20).

The rate of intramolecular electron-transfer from the DMAB electron donor to photoexcited Re, according to the steady-state emission quantum yields, show small reductions in the quenching rate with addition of DNA, however the emission lifetimes

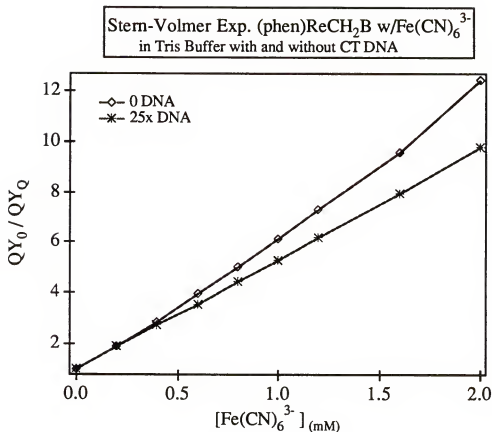


Figure 2.19. Stern-volmer quenching experiment comparing the quenching of the $^3MLCT^*$ state of (phen)ReCH₂B by $Fe(CN)_6^{3-}$ in solution (diamonds) and in the presence of 25 times $[DNA]_{bp}$ to $[Re]$ concentration (stars). The $[Re]$ concentration for the experiment in the absence of DNA was 1.2×10^{-5} M and in the presence of DNA the $[Re]$ concentration was 9.2×10^{-6} M. All measurements were done in air-saturated solutions. See equation 2.7 for explanations of terms.



Figure 2.20. Computer-generated model (Macromodel) of (phen)ReCH₂Q binding from the major groove side of a dodecamer of poly dG poly dC. The phenanthroline ligand at the Re center is partially inserted in-between base pairs. Molecular modeling studies were performed with the help of Maxwell H. Muir. The model of the dodecamer of poly dG poly dC was provided by W. D. Wilson.

indicate slight increases in the quenching rate. These changes, in either case, are not prominent enough to be considered significant with respect to experimental error. Evidence suggests that the distance between the Re chromophore and the DMAB quencher, even in the fully extended orientation, may not be great enough a separation for retardation of the ET quenching to any great degree. Calculations from molecular modeling studies on the bpyReCH₂Q complex shown in Figure 2.13 indicate that within all the accessible conformations of the complex, the separation distance between the Re center and the DMAB ring remains within 9.0 - 10.5 Å.¹²⁹ This suggests that changes in the conformation of the complex might not appreciably affect the distance dependence of the ET rate. Studies of intermolecular ET between donor and acceptor molecules bound to DNA have demonstrated enhanced FET rates through the DNA matrix suggesting the nucleic acids play a role in facilitating the ET process.¹³⁶ It is possible that this could be occurring within the (phen)ReCH₂Q complex when bound to DNA, however further studies would be necessary in order to confirm this hypothesis.

Improvements to this type II CQ complex could include: (1) a larger polycyclic aromatic diimine ligand at the octahedral metal center which is extended out enough to allow deep intercalation in-between base pairs; (2) a longer linker chain between the chromophore and quencher moieties that incorporates a greater number of H-bonding groups (i.e., peptide chains) for groove binding interactions, and positively charged amines for increased electrostatic association with DNA phosphates and improved water solubility; and (3) utilizing an intercalating quencher in conjunction with the DNA intercalating ligand at the Re center therefore increasing the binding constant for the complex. Studies of bifunctional intercalators have shown that the minimum interchromophore separation required to permit bis-intercalation is on the order of 10 Å (equal to ~ 3 base pairs) which takes into account neighbor exclusion.¹³⁷ Considering the bulky geometry of the Re chromophore and the exponential dependence of ET on distance, a tether of 12 to 20 Å in length would more likely fulfill the binding and quenching requirements of the complex.

CHAPTER 3 RE-AN COMPLEXES: PHOTOPHYSICAL AND DNA BINDING STUDIES

Introduction

In the previous chapter the photophysical properties of the chromophore-quencher (CQ) complexes Re-PTZ and (phen)ReCH₂Q were examined in the presence of double-stranded DNA. Their quenching mechanisms operate through electron transfer from the covalently attached ligands (L = PTZ or DMA) to the photoexcited Re chromophore, a process which effectively shuts down the Re emission pathway.



Changes in their quenching rates were monitored with increasing addition of DNA in order to determine (1) if the complexes bind to DNA and (2) whether binding causes changes in the rates of electron transfer quenching within the complexes.

In the Re-PTZ complex studied in chapter two, the quencher, PTZ, served as the DNA binder. This is categorized as a Type I system where the quencher also is the binder. The high rate of electron transfer (ET) between PTZ and photoexcited Re caused instability of the complex and made it difficult to determine binding properties with DNA. This led to study of the Type II complex (phen)ReCH₂Q, in which the diimine ligand, 1,10-phenanthroline that is directly coordinated to the metal center, served as the DNA binder. Weak interactions with nucleic acids were observed for this system, and molecular modeling studies suggested the bulky geometry at the metal center sterically hindered approach to the stacked DNA bases. Based on the results obtained from these two studies, the optimal system appeared to be Type I utilizing a quencher which (1) was relatively stable after photo-excitation processes and (2) exhibited stronger DNA binding properties.

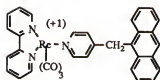
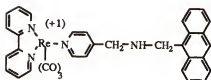
This chapter describes the photophysical and DNA binding characteristics of the Type I Re-An series of CQ complexes. In these systems the chromophore *fac*-(2,2'-bipyridyl)Re^I(CO)₃ is covalently linked to an anthracene (AN) quencher by way of a flexible tether which varies in lengths of 3, 6, 8 and 10 atoms. The structures for these complexes, their model compounds and the acronyms used to name them are shown in Figure 3.1.

The choice of anthracene (AN) was based on previous studies which indicated AN quenches the $d\pi(\text{Re}) \rightarrow \pi^*(\text{bpy})$ metal-to-ligand charge transfer (MLCT) excited state by electron-exchange triplet-triplet (TT) energy transfer¹³⁸ (E_nT), and is a strong DNA intercalator.²⁷

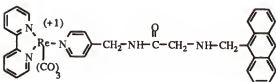
A variety of anthracene derivatives are known to display considerable biological activity^{139,140,141,142} and much evidence attributes their antineoplastic toxicity to activity at the DNA level. Several groups have studied the DNA binding properties of simple derivatives of anthracene substituted at different positions with different types of side chains.^{27,143} Their results support the intercalative mode of binding based on the following observations. The UV/visible absorption spectra display extensive hypochromism, red shifts and broadening upon binding with various sequences of synthetic and natural DNA. Fluorescence from the bound compound to DNA is substantially quenched by the DNA bases,²⁷ the vibronic bands show significant broadening and red shifts,²⁷ and bi-exponential decay behavior is exhibited in the time-resolved fluorescence spectra^{27,145}. Increases in DNA melting temperature and viscosity are observed upon binding of the anthracene derivatives.^{27,145} All of the above evidence is in agreement with an intercalative interaction for AN with DNA.

Studies by MacQueen and Schanze¹³⁸ on the CQ complex Re^IPyAn, shown in Figure 3.1, demonstrated the occurrence of triplet-triplet exchange E_nT in this complex with the following experimental evidence. First, the MLCT emission of the AN-substituted complex is almost completely quenched compared with model Re complexes which do not

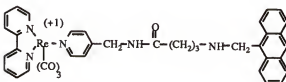
Chromophore-Quencher Complexes

RepyAn^a

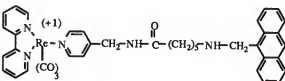
Re3An



Re6An

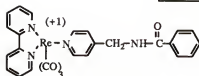
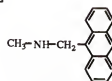


Re8An



Re10An

Model Compounds

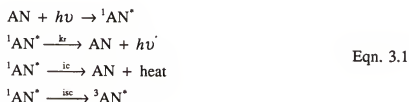
ReCH₂B

ANMOD

Figure 3.1. Structures and names of the Re-An chromophore-quencher complexes and their model compounds. ^a RepyAn was used in previous studies^{1*} where the occurrence of exchange energy transfer within this complex was established.

contain the AN chromophore. Second, nanosecond laser excitation of the RePyAN complex at a wavelength where > 90% of the light is absorbed by the Re moiety leads to swift ($k > 10^8 \text{s}^{-1}$) formation of the triplet excited state of AN [$^3\text{AN}^*$]. Third, based on thermodynamic considerations, quenching by a competitive electron transfer pathway from AN to photoexcited Re in this complex is considered to be unimportant ($\Delta G_{\text{ET}} = -0.07 \text{ eV}$).¹³⁸

Excited state diagrams illustrating the relative energy levels and photophysical pathways available in the Re-An CQ complexes and the model compounds ReCH_2B and ANMOD are shown in Figure 3.2. Focusing first on ANMOD, (3.2a), photoexcitation produces the first excited singlet state ($^1\text{AN}^*$) which can decay radiatively by fluorescence or nonradiatively through internal conversion (ic) to the ground state (S_0) or intersystem crossing (isc) to the lowest triplet state ($^3\text{AN}^*$). These processes are illustrated in the following equations,



The triplet state of anthracene is non-emissive at room temperature. This is due to the fact that phosphorescence is a spin-forbidden process and is very slow relative to non-radiative decay, therefore non-radiative decay by isc predominates. As mentioned in previous chapters photoexcitation of ReCH_2B (Figure 3.2b) rapidly produces the $^3\text{MLCT}^*$ state, and since it contains a non-quenching ligand the complex will relax to its ground state via normal radiative and nonradiative modes.

In the excited state scheme for the Re-An CQ complexes (Figure 3.2c) additional decay pathways are available to both the $^1\text{AN}^*$ state and the $^3\text{MLCT}^*$ state. The pathway from $^3\text{MLCT}^*$ to $^3\text{AN}^*$, labeled $\text{E}_{\text{N}}\text{Tee}$, represents the electron exchange energy transfer mechanism which strongly reduces the amount of light emitted from $^3\text{MLCT}^*$, effectively

Excited State Energy Schemes for Models and CQ Complexes

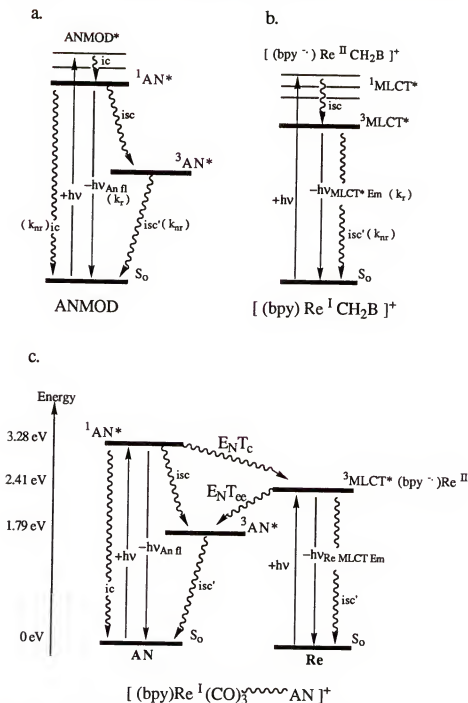
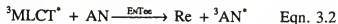


Figure 3.2. Excited state energy levels and photophysical processes which can occur upon photoexcitation of the models (a) ANMOD, (b) $ReCH_2B$ and (c) the Re-An CQ complexes. Energies given in (c) correspond to the $E_{0,0}$ levels for the excited states of the component chromophores where $1AN^* = 3.28$ eV, $3MLCT^* = 2.41$ eV and $3AN^* = 1.79$ eV.

quenching the MLCT emission in the complexes.



The anthracene moiety also has a new decay pathway available to its S_1 level; its energy can be transferred to the MLCT^* manifold by way of coulombic energy transfer, labeled $\text{E}_\text{N}^{\text{Tc}}$.



This energy transfer process results in a reduction of excited-state energy in ${}^1\text{AN}^*$ which would normally decay by fluorescence or non-radiative routes.

The sensitivity of luminescence energy transfer to its microenvironment makes it an inherently useful tool for the study of interactions of small molecules with DNA. This is particularly relevant regarding electron-exchange energy transfer ($\text{E}_\text{N}^{\text{Tee}}$) since the distinguishing feature of this mechanism is the requirement that the energy donor (M^*) and acceptor (Q) molecules be within "encounter" distance in order for efficient transfer to occur (ca. 6 - 20 Å). It involves a double electron transfer mechanism where the excited electron on M^* (${}^3\text{MLCT}^*$) transfers into the LUMO of Q (${}^3\text{AN}^*$) with a simultaneous transfer of an electron from the HOMO of Q (AN) into the corresponding orbital on M (Re). Therefore energy initially supplied to M ends up on Q in the form of Q^* , concomitant with a reduction in the amount of M^* and thus a reduction in total emission from M^* . The mechanism is illustrated in Figure 3.3. The short distance dependence is a result of the necessity for overlap of the electron orbitals involved in the electron "hopping" process.¹⁴⁴

Figure 3.4 illustrates the effect DNA intercalation should have on the intramolecular quenching by the exchange energy transfer process in the Re-An complexes. Free in buffer solution the complexes can fold back upon themselves forming encounter complexes between the Re ("C") and AN ("A") moieties. Upon excitation in this conformation the ${}^3\text{MLCT}^*$ state will be efficiently quenched by energy transfer to nearby AN (see eqn. 3.2). However, if DNA is added to the solution, AN can intercalate into the DNA double helix leaving the Re chromophore either extended out in solution or lying in the DNA groove.

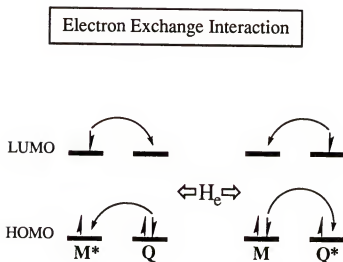


Figure 3.3. Electron exchange energy transfer mechanism ($E_N T_{ee}$). Illustrates how the energy of an electronically excited compound is quenched by the exchange of the excited electron in the LUMO of the donor (M^* on the left and Q^* on the right) with an electron in the HOMO of the acceptor. H_e is the electronic matrix coupling element that determines the favorability of the $E_N T_{ee}$ process and is defined in Chapter I.

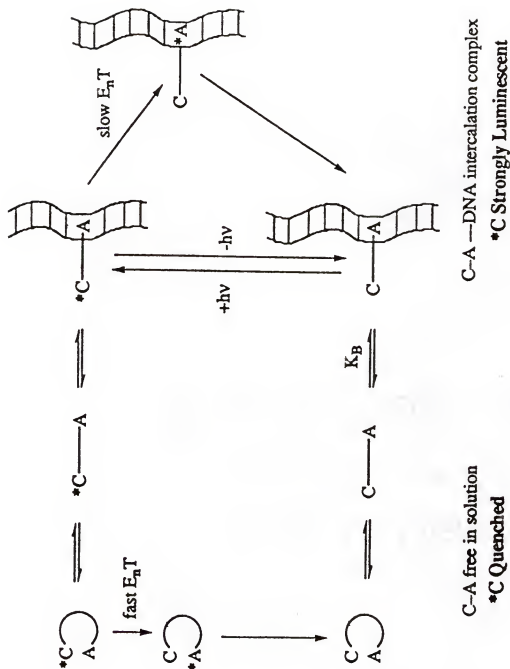


Figure 3.4. Effect of DNA intercalation on intramolecular quenching by exchange energy transfer (E_{nT}). In the C-A complex, C is the chromophore and A is the energy acceptor which also serves as a DNA binder.

Upon excitation, if the complex remains bound to DNA, the efficiency of energy transfer will be reduced such that the Re chromophore will have time to emit its excited state energy as a photon of light. Therefore the overall luminescence of the solution will be dramatically increased in the presence of DNA much like a molecular signaling device.

With this in mind, the interactions of the different Re-An CQ complexes with DNA have been examined in order to determine (1) how the length of the tether between Re and AN affects the efficiency of energy transfer and the changes observed upon DNA binding and (2) the effect the length of tether has on the strength of DNA binding of the complexes.

Studies of the UV-visible absorbance characteristics of the complexes in the absence and presence of DNA will be examined in the results section. Following will be presented the findings of steady-state emission studies in the absence and presence of DNA with calculations of the binding characteristics according to Scatchard analyses. Emission decay data will also be examined followed by results from transient absorption studies.

Experimental

Materials

All materials and purification procedures for reagents are listed in Chapter 4.

Methods

Buffers employed were 25 mM Tris (Tris = Tris(hydroxymethyl)aminomethane hydrochloride) pH 7.2, 20 mM Tris/10 mM NaCl pH 7.2 and 20 mM Tris/0.1 M NaCl. pH 7.2. To increase solubility of the complexes and decrease precipitation of the DNA at high Re/DNA ratios 20% MeOH / Buffer solutions were employed for all the studies. Compared to data obtained in buffer solution without MeOH, the results are not affected by the presence of the organic solvent except to improve reproducibility and reduce random noise in the spectra. These low levels of MeOH should not appreciably affect the DNA structure.¹⁴⁵

Calf thymus DNA Type I was purchased from Sigma Chemical Co. Stock solutions were typically prepared 12 hrs in advance by dissolving ca. 75 mg of DNA into 1.5 ml of buffer, storing at 4° C overnight, mixing thoroughly and passing approximately thirty times through a 22 gauge syringe needle to reduce the strand lengths. Concentrations of the stock DNA solutions were approximately 0.01 M in nucleotides (or 0.005 M in base pairs) and were determined according to Beer's Law using $\epsilon_{260} = 6600 \text{ M}^{-1}\text{cm}^{-1}$ per nucleotide.¹⁴⁶

Metal complex concentrations employed ranged from $2.0 \times 10^{-5} \text{ M}$ to $5.0 \times 10^{-5} \text{ M}$. With minimum exposure to light, the metal-DNA solutions were prepared by maintaining constant metal complex concentration and varying the DNA concentrations. Best results were obtained by adding a fresh 3 ml aliquot of the metal complex solution via pipet to a quartz cuvette, adding the appropriate amount of DNA via syringe and capping with a rubber septum. Once prepared the solutions were mixed by inverting ~ 30 times, bubbled with argon gas for 15 min. and the spectra recorded. Fresh aliquots of metal solution were necessary for each measurement since repeat exposure of the same solution to the spectroscopic measurements (both absorbance and emission) resulted in increases in the absorbance at 320 nm and in the emission in the 380 - 500 nm region. These changes were not observed when separate solutions were used for each measurement.

Instrumentation

Instrumentation and procedures used to conduct the experiments are described in detail in the corresponding sections in Chapter 4.

Syntheses

Complete experimental procedures for the syntheses of the Re-An compounds are given in Chapter 4. General outlines for these syntheses are displayed in Figures 3.5 and 3.6. The syntheses of the complexes Re6An, Re8An and Re10An (Figure 3.5) all followed the same general route starting with their corresponding CBZ-protected amino acid

Synthesis of Re10An, Re8An & Re6An

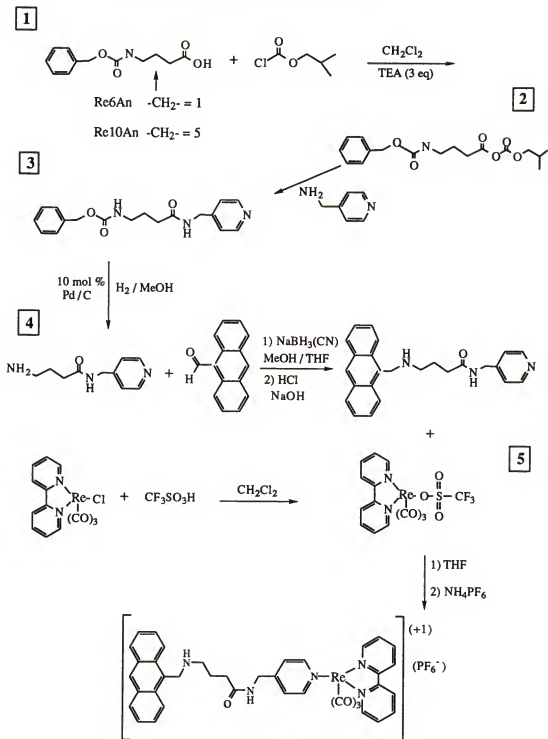


Figure 3.5

Synthesis of Re3An

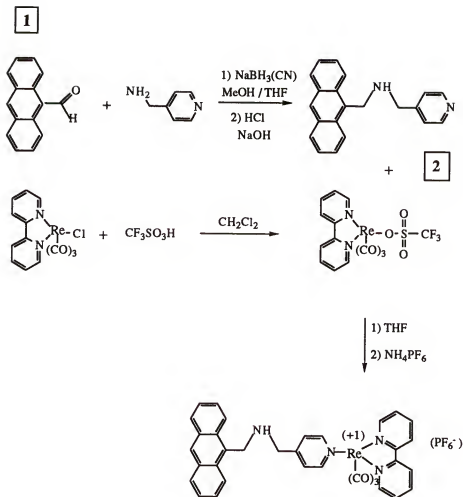


Figure 3.6.

derivatives. The protected amino acids were coupled with 4-(aminomethyl)pyridine by way of their isobutyl chloroformate esters in the presence of triethylamine (steps 1 & 2). Cleaner products and higher yields were obtained using isobutyl rather than ethyl chloroformate. The CBZ protecting group was then cleaved by hydrogenolysis using palladium on carbon catalyst (step 2). This procedure eliminated the problem of excess salts encountered when removing acid labile protecting groups, and was performed under less rigorous conditions. The final ligands were obtained by subsequent reductive amination of 9-anthraldehyde with the free amine using $\text{NaBH}_3(\text{CN})$ in methanol/tetrahydrofuran solution (step 4). Overall yields generally ranged from 16% for pyr6An, 36% for pyr8An and 30% for pyr10An. The ligand pyr3An was synthesized through a more straightforward route (Figure 3.6, step 1) by simple reductive amination of 9-anthrylaldehyde with 9-(aminomethyl)pyridine again using the milder reducing agent $\text{NaBH}_3(\text{CN})$ in methanol/THF solution to give a yield of 85%.

Formation of the metal complexes (Figure 3.5, step 5; Figure 3.6, step 2) involved coupling the corresponding ligand with the triflate $(\text{bpy})\text{Re}(\text{CO})_3$ complex in THF (or THF/ethanol) solution in the presence of excess NH_4PF_6 salt using minimal heat ($\sim 50^\circ\text{C}$), nitrogen atmosphere and minimal exposure to light. The yields were generally fair to low for these kinds of metal complex reactions (35% Re3An; 50% Re6An; 18% Re8An; 30% Re10An).

Results

Structures of the Re-An Complexes: ^1H NMR

The ^1H NMR spectra of each of the Re-An compounds with the corresponding anthracene-pyridine ligand spectra are shown in Chapter 4 Figures 4.1 - 4.4. The most notable features in the ^1H resonances for the anthracene-pyridine ligand upon complexation to the metal center are (1) the down field shifts of the proton resonances for the two

methylenes in the linker chain connected on either side to the amine functionality, and (2) the down field shifts for the proton in the #10 position on AN. The spectra for Re3An and Re6An (Figures 4.1 & 4.2) do not show any major chemical shift changes in comparison to their ligand spectra, whereas Re8An and Re10An (Figures 4.3 & 4.4) both show significantly large down field chemical shifts for the above mentioned protons. These changes indicate a decrease in electron density surrounding the protons and could be a result of the degree of protonation of the amino functionality as well as the type of counter ion balancing the positively charged aminium ion.

The linker chains have been designed to incorporate an amine functionality which is protonated in the pH 7.2 buffer solutions.^{142,96,147} These positively charged amino groups improve the water solubility of the large CQ complexes while also imparting greater affinity towards the negatively charged phosphate backbone of the DNA strands. Studies on anthracene-based intercalators have shown a strong correlation between the DNA binding strengths and the position and number of amino groups in the 9-position chain.¹⁴³

UV-Visible Absorption Spectra of the Complexes

The absorption spectra for all of the Re-An complexes closely approximate the sum of the spectra of the component chromophores. This is illustrated in Figure 3.7 which shows an overlay of the UV-visible absorbance spectrum of Re6An with the model complexes ReCH₂B and ANMOD. At 340 nm the absorbance of the Re MLCT band is nearly equal to or slightly larger than that of AN, thus the distribution of excitation energy at this wavelength would be approximately 50 % for each chromophore. In Table 3.1 are listed the assignments for the peaks of the Re-An complexes (20% MeOH/Buffer) in the 308 to 388 nm region and their experimentally determined molar absorptivities (ϵ_A). Molar absorptivity values for the model compounds are listed as well as calculated ϵ_A values determined from additive values of the model compounds. Determination of the molar absorptivities of the Re-An compounds was complicated due to the presence of excess salts

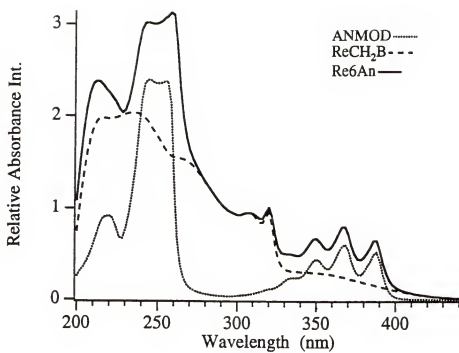


Figure 3.7. Overlay of UV-visible absorption spectra of ANMOD, ReCH₂B and Re6An in 20% MeOH/Buffer solutions. Concentrations are approximately 8.0×10^{-5} M for all samples shown.

Table 3.1. Absorbance Transitions and Molar Absorptivities of Re-An Compounds^a

Abs. λ (nm)	Transition	Re3An $\epsilon(\text{M}^{-1}\text{cm}^{-1})$	Re6An $\epsilon(\text{M}^{-1}\text{cm}^{-1})$	Re8An $\epsilon(\text{M}^{-1}\text{cm}^{-1})$	Re10An $\epsilon(\text{M}^{-1}\text{cm}^{-1})$	ReCH ₂ B $\epsilon(\text{M}^{-1}\text{cm}^{-1})$	ANMOD $\epsilon(\text{M}^{-1}\text{cm}^{-1})$	ReCH ₂ B + ANMOD ϵ
308	$\pi-\pi^*(\text{bpy})$	12300 $\pm 9\%$	11200 $\pm 9\%$	9700 $\pm 3\%$	11200 $\pm 6\%$	11600 $\pm 0.3\%$	640 $\pm 5\%$	12200
320	$\pi-\pi^*(\text{bpy})$	13000 $\pm 8\%$	12000 $\pm 9\%$	10400 $\pm 3\%$	12200 $\pm 9\%$	11800 $\pm 0.4\%$	1310 $\pm 3\%$	13100
334	MLCT & $\pi-\pi^*$ AN	5800 $\pm 12\%$	6100 $\pm 9\%$	5110 $\pm 3\%$	5900 $\pm 10\%$	3570 $\pm 1\%$	2900 $\pm 2\%$	6470
340	MLCT & $\pi-\pi^*$ AN	5660 $\pm 12\%$	5700 $\pm 9\%$	5100 $\pm 3\%$	5880 $\pm 11\%$	3500 $\pm 1\%$	2900 $\pm 2\%$	6400
350	$\pi-\pi^*$ AN & MLCT	7200 $\pm 9\%$	7900 $\pm 9\%$	6800 $\pm 3\%$	7500 $\pm 10\%$	3400 $\pm 1\%$	5450 $\pm 1\%$	8850
355	$\pi-\pi^*$ AN & MLCT	---	6710 $\pm 9\%$	---	7210 $\pm 10\%$	3350 $\pm 1\%$	---	---
368	$\pi-\pi^*$ AN	8200 $\pm 8\%$	9400 $\pm 8\%$	7840 $\pm 2\%$	9300 $\pm 9\%$	2800 $\pm 1\%$	7540 $\pm 1\%$	10340
388	$\pi-\pi^*$ AN	6360 $\pm 9\%$	7600 $\pm 8\%$	6200 $\pm 2\%$	7400 $\pm 10\%$	1740 $\pm 2\%$	6450 $\pm 1\%$	8190
320/388		2.03	1.57	1.68	1.65			1.60
320/308		1.93	1.47	1.56	1.51			1.49

^a. All measurements in 20% MeOH/Buffer solutions.

in the purified samples. This is reflected in the overall suppression of their ϵ_A values from the additive values of the models, particularly for Re8An. A relative measure of purity for each complex was determined through evaluation of the $\epsilon_{308}/\epsilon_{388}$ ratios or the $\epsilon_{320}/\epsilon_{388}$ ratios, which correspond to an estimate of the Re content versus AN content, respectively. Examination of these ratios implicates Re6An ($\epsilon_{308}/\epsilon_{388} = 1.47$) and Re10An ($\epsilon_{308}/\epsilon_{388} = 1.51$) as the closest to the ratio from the calculated model values ($\epsilon_{308}/\epsilon_{388} = 1.49$). These two complexes were the easiest to purify by column chromatography since the unreacted starting materials (pyridine-anthracene ligand and metal complex) were more readily separable from the final Re-An complexes. Re3An formed impurities soon after purification, as indicated by strong $^3\text{MLCT}^*$ emission. Evidence for this impurity included unusually high steady state MLCT emission from solutions of the impure samples and identification by TLC of an emitting species which migrated with an R_f similar to uncomplexed Re. Samples of Re8An appeared to contain excess salts (possibly PF_6^-) since the optical densities of solutions of this complex were considerably lower in value than what was expected based on the weight of the samples. Additional evidence of excess salts was the persistent presence of a white solid (in contrast to the yellow color of the complex) that remained when dissolving Re8An samples in less polar organic solvent, but which was soluble in certain solvents of higher polarity.

DNA absorbance titrations

In order to examine the binding interaction of the different Re-An complexes with double-stranded DNA, the changes in their electronic absorption bands in the 350 to 400 nm region were monitored in the presence of increasing amounts of calf thymus DNA. In these and other spectra the DNA concentrations are expressed as $[\text{DNA}]_{\text{bp}}/[\text{Re}]$ ratios (or DNA/Re ratios) where $[\text{DNA}]_{\text{bp}}$ is the concentration of nucleic acids in molar base pairs and $[\text{Re}]$ is the molar concentration of the Re-An complex. Using this notation the concentration of nucleic acids will often be referred to as the amount of DNA *times* (or "x") the Re concentration. For example, 2x DNA is two times the amount of DNA base pair

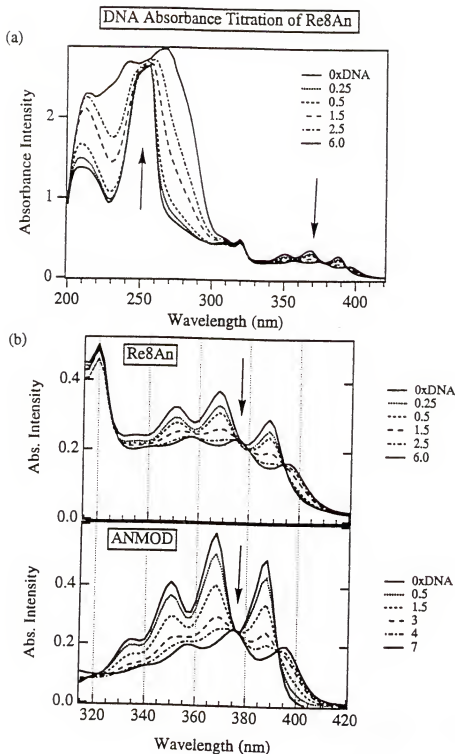


Figure 3.8. (a) UV/visible absorption titration of Re8An [4.8×10^{-5} M] with CT DNA in 20% MeOH/20 mM Tris:10mM NaCl pH 7.2. The concentrations of DNA in the legend are expressed as ratios of $[DNA]_{bp}/[Re]$. (b) Enlargement of the long wave-length absorption bands from the DNA titration of Re8An shown in (a) and the corresponding transitions for the DNA titration of the model ANMOD [7.8×10^{-5} M] in 20% MeOH/20 mM Tris:10 mM NaCl pH 7.2. The $[DNA]_{bp}/[AN]$ concentrations are listed to the right of the figure.

concentration to Re concentration. A typical spectroscopic titration of Re8An with up to 6 times [DNA]_{bp} to [Re] ratios is shown in Figure 3.8a. The large peak growing in at ~ 270 nm is due to the increasing nucleic acid concentration. Distortions in the spectra appear once the absorbance rises above 2.0 AU due to instrument response. In the lower portion of Figure 3.8 is shown the enlargement of the long wavelength bands for the DNA absorbance titration of Re8An in comparison to spectra for the titration of the model ANMOD. The addition of increasing amounts of DNA to solutions of the Re-An complexes causes hypochromism and red shifts in the anthracene chromophore absorption bands in the 350 to 400 nm region similar to the behavior of the ANMOD model. In Figure 3.9 the spectral titrations for all the complexes in the long wavelength region are displayed. Saturation of binding to the nucleic acids occurs by 6 times [DNA]_{bp} to [Re] ratios for the complexes as shown in Figure 3.10 by the reciprocal plots of their normalized absorption at 388 nm vs. DNA/Re ratios, where A^0/A is the ratio of the 388 nm absorbance intensity at zero [DNA]_{bp} divided by the 388 nm absorbance intensity at the respective DNA concentration. Two different titrations are plotted for Re6An and Re3An in order to illustrate the repeatability of the results. Comparison of the graphs indicates that the largest degrees of hypochromism are seen in Re10An and Re8An. Quantitatively this can be visualized in Table 3.2 which lists the percent decreases in the spectra at 388 nm in going from 0 to 6x DNA, along with their corresponding red shifts. The decreases were determined by¹⁴⁸

$$\frac{A_{0_{\text{DNA}}} - A_{6_{\text{DNA}}}}{A_{0_{\text{DNA}}}} \times 100 = \% \text{ Decrease in Intensity at 388 nm} \quad \text{Eqn. 3.4}$$

where $A_{0_{\text{DNA}}}$ is the absorbance of the corresponding peak for the free complex and $A_{6_{\text{DNA}}}$ is the 388 nm absorbance at 6 times DNA to Re ratio. For all the complexes the largest decreases occur at 388 nm since at this wavelength the Re MLCT band contributes minimally to the absorbance. At shorter wavelengths the underlying MLCT band interferes

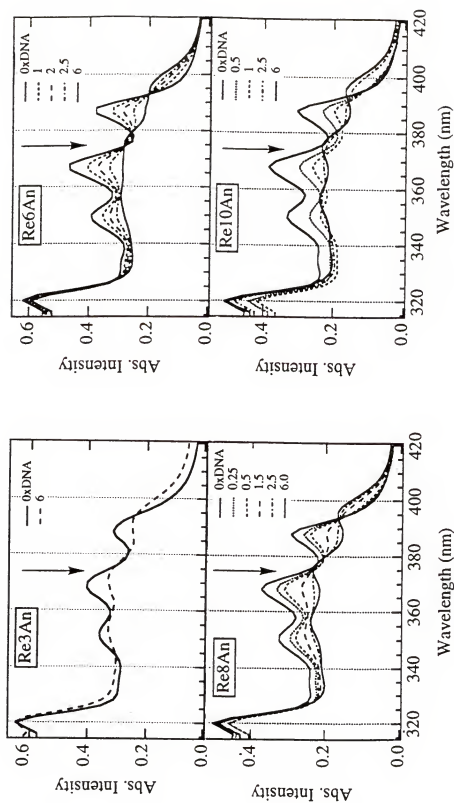


Figure 3.9. UV/visible absorption DNA titrations of Re-An complexes with CT DNA showing changes in the long- λ regions of their spectra. DNA concentrations are expressed as $[DNA]_{bp}/[Re]$ ratios (i.e. $0xDNA = 0$ "times" $[DNA]_{bp}$ to $[Re]$ concentration). Arrows indicate the intensities decrease with increasing additions of DNA. All measurements were in 20% MeOH/buffer solutions pH 7.2 where $Re3An = [4.6E-5 M]$, $Re6An = [4.9E-5 M]$, $Re8An = [4.7E-5 M]$ and $Re10An = [4.5E-5 M]$.

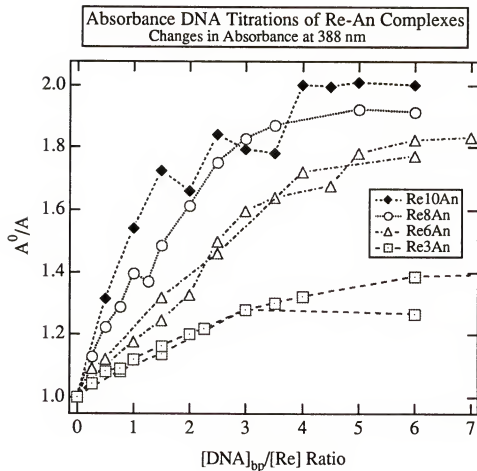


Figure 3.10. Reciprocal plots of the changes in the UV/visible absorbance intensities at 388 nm for the Re-An complexes with increasing amounts of $[DNA]_{bp}$. The term A^0/A refers to the absorbance at 388 nm in the absence of DNA divided by the absorbance at 388 nm with added DNA. Experimental data from two separate titrations are shown for Re3An and Re6An. All experiments were performed in 20% MeOH/Tris buffer solutions.

Table 3.2. Absorbance Changes of Re-An Compounds with DNA.^a

Complex	Abs Shift @ 350 nm	(%) ^b Decr. Intensity 350 nm	Abs Shift @ 368 nm	(%) Decr. Intensity 368 nm	Abs Shift @ 388 nm	(%) Decr. Intensity 388 nm
Re3An	4 nm	8 % ($\pm 16\%$)	2 nm	18 % ($\pm 8\%$)	2 nm	20 % ($\pm 10\%$)
Re6An	6	28 % ($\pm 20\%$)	6	38 % ($\pm 20\%$)	6	43 % ($\pm 12\%$)
Re8An	6	33 % ($\pm 15\%$)	8	42 % ($\pm 16\%$)	8	48 % ($\pm 15\%$)
Re10An	6	35 % ($\pm 20\%$)	6	44 % ($\pm 16\%$)	6	50 % ($\pm 16\%$)
ANMOD	8	51 % ($\pm 8\%$)	6	56 % ($\pm 9\%$)	6	60 % ($\pm 9\%$)
ReCH₂B	0	0 % ($\pm 2\%$)	0	0 % ($\pm 2\%$)	0	0 % ($\pm 2\%$)

^a In 20% MeOH/Buffer solutions. The changes are for solutions where the ratio of [DNA]_{bp} concentration to [ReAn] concentration was equal to 6 ([DNA]_{bp}/[Re] = 6). The numbers in parentheses given as \pm % indicate the percent error in the data.

^b Refers to the decrease in the absorbance intensity at the corresponding wavelength given as a percentage of the intensity in the absence of DNA according to eqn. 3.4.

with the hypochromic effects. Among the Re-An complexes the hypochromism increases in the order $\text{Re3An} \ll \text{Re6An} < \text{Re8An} < \text{Re10An}$. The model ANMOD displays the largest percent decrease overall (60 % at 388 nm), in approximate agreement with values obtained for similar anthracene intercalators.^{27,143} ReCH_2B , which does not contain a DNA interactive ligand, shows no changes in its spectrum. The hypochromism observed at 388 nm for Re10An , in comparison to ANMOD, is approximately 83 % of that observed in the model, while Re8An shows nearly the same amount at 80 %.

The changes in absorbance at 388 nm with increasing additions of DNA were used to determine intrinsic binding constants (K_b) for the complexes and ANMOD to calf thymus DNA according to an analysis described as Method I in Appendix A. The binding equation utilized in Method I (eqn. A.5) is based on a neighbor-exclusion binding model of the Scatchard equation and has been applied to the absorption titration data of several other DNA intercalating compounds.^{27,33,149} Intrinsic binding constants, which were extracted from plots of the absorption data constructed according to Eqn. A.5 (shown in Figures A.1 and A.2, Appendix A), are listed in Table 3.3. Data in the range of 60-100 % binding was chosen except for Re10An which gave a straight line at lower values. Large experimental error was observed at very low DNA/Re ratios, and can be attributed to nonspecific binding modes since there are so many drug molecules per base pair involved. These binding modes, which could include stacking of the drug molecules on top of each other, have been observed in previous studies of anthracene intercalators.¹⁴²

Emission Spectra of the Complexes

In Figure 3.11a is shown an overlay of the steady state emission spectra of the models ANMOD and ReCH_2B normalized to that of Re10An . The bands in the 380 nm to 500 nm region correspond to $^1\text{AN}^*$ fluorescence, and the broad envelope in the 500 nm to 800 nm region corresponds to $^3\text{MLCT}^*$ luminescence. It is clear that the energies for the peaks in the CQ complex match the energies of the peaks in the individual model

Table 3.3 Absorbance Titration Binding Parameters
According to Method I.^a

Compound ^b	$ \Delta\epsilon _{388\text{nm}}^{\text{d}}$	$K_{\text{b}} (\text{M}^{-1})$	Std Dev. ^e
Re3An	2050	1.6×10^4	0.94
Re6An	3626	3.5×10^4	0.97
Re8An	3160	4.9×10^4	0.98
Re10An	3950	5.1×10^4	0.99
ANMOD ^c	4355	4.7×10^4	0.99

^a See appendix A for description of Method I.

^b Measured in 30% MeOH/Buffer solutions unless otherwise noted.

^c Measured in 25 mM Tris buffer.

^d $|\Delta\epsilon|$ is the absolute value of the difference between the molar absorptivities of the complex in the absence of DNA and in the presence of 6x DNA determined from the slopes of the graphs.

^e Standard deviation of the data determined from least squares linear regression analysis of the binding plots constructed according to eqn. A.5 in appendix A.

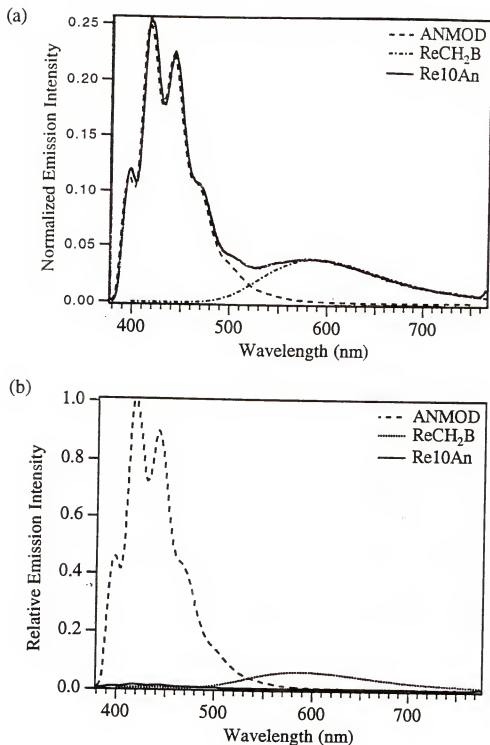


Figure 3.11. (a) Overlay of the steady-state emission spectrum of Re10An normalized to the $^3\text{MLCT}^*$ emission band of ReCH₂B (500-800 nm) and the fluorescence bands of ANMOD (380-500 nm). The model spectra were obtained in degassed 25 mM Tris buffer, and Re10An in degassed 20% MeOH/20 mM Tris:10 mM NaCl. (b) Overlay of emission spectrum of Re10An relative to the model emission spectra using a scale based on their QY values. This illustrates the efficiency of the E_NT quenching mechanisms in Re10An.

chromophores and hence complexation does not disturb the electronic levels in the Re and An moieties. Figure 3.11b displays the steady state emission spectra for the models *relative* to that of Re10An. This overlay clearly illustrates the efficient quenching of the $^3\text{MLCT}^*$ state in the CQ complex relative to the model. Additionally it is evident that the AN fluorescence in the CQ complex is dramatically reduced relative to its model ANMOD. Steady state emission spectra for all of the Re-An complexes in 20% MeOH/buffer pH 7.2 solution are shown in Figure 3.12. Focusing on the individual emission spectra for the complexes several features are worth noting. In all of the spectra the Re MLCT emission is nearly completely quenched. Table 3.4 lists quantum yield values pertaining to $^3\text{MLCT}^*$ emission (ϕ_{EmRe}) and $^1\text{AN}^*$ fluorescence (ϕ_{EmAN}) in the Re-An complexes and the models. Comparing the ϕ_{EmRe} values of the CQ complexes to the unquenched ReCH_2B model it is very clear the complexes display highly efficient energy transfer quenching, with their yields ranging from 2 % to 8 % of that of the Re model. The short-chained Re3An possesses the greatest degree of quenching (lowest ϕ_{EmRe}) and the quenching becomes slightly less efficient as the length of the linker chain in the complexes increases (ϕ_{EmRe} increases: $\text{Re3An} < \text{Re6An} < \text{Re8An} < \text{Re10An}$).

The second feature worth noting is the difference in the quantum yields of emission for AN (ϕ_{EmAN}) in the complexes. It is evident that an overall quenching mechanism is occurring to reduce the AN fluorescence in the complexes to a level significantly lower than that of the ANMOD model (ϕ_{EmAN} values for the complexes range from 0.03 % to 1.0 % of ANMOD). Additionally, the quenching efficiency parallels the length of the linker chains in the order of ϕ_{EmAN} $\text{Re3An} < \text{Re6An} < \text{Re8An} < \text{Re10An}$. This quenching phenomenon, mentioned earlier in Figure 3.2, is attributed to coulombic energy transfer from $^1\text{AN}^*$ to the MLCT manifold. It occurs through a dipole-dipole interaction between the two chromophores, as described in Chapter 1, and can take place over large distances (20 to 100 Å). This will be further addressed in the section on AN photophysics.

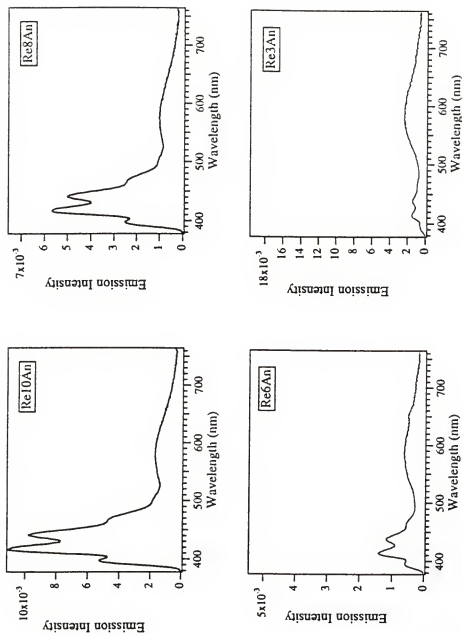


Figure 3.12. Steady-state emission spectra of the CQ complexes in degassed 20 % MeOH/Tris buffer solutions pH 7.2 where the metal complex concentrations are $\text{Re3An} = [4.7\text{E-}5 \text{ M}]$, $\text{Re6An} = [4.9\text{E-}5 \text{ M}]$, $\text{Re8An} = [4.7\text{E-}5 \text{ M}]$ and $\text{Re10An} = [4.5\text{E-}5 \text{ M}]$. The spectra are normalized to their $^3\text{MLCT}^*$ QY's in order to visually show the relative intensities of their emission spectra. All samples were excited at 340 nm.

Table 3.4. Steady-State Emission Characteristics of Re-An Compounds in Solution.^a

Compound	$\lambda_{\text{Em}}^{\text{peak}}$ $^3\text{MLCT}^*$ (nm)	$\phi_{\text{EmRe}}^{\text{d}}$	$\frac{\phi_{\text{EmRe}}^{\text{Re-An}}}{\phi_{\text{EmRe}}^{\text{Re-CHB}}}$	$\lambda_{\text{Em}}^{\text{peaks}}$ $^1\text{AN}^*$ (nm)	$\phi_{\text{EmAN}}^{\text{e}}$	$\frac{\phi_{\text{EmAN}}^{\text{Re-An}}}{\frac{\phi_{\text{EmAN}}^{\text{ANMOD}}}{\phi_{\text{EmAN}}^{\text{Re-An}}}}$
Re3An^b	590	0.00046 ($\pm 10\%$)	0.020	395, 415 442, 470	0.0001 ($\pm 10\%$)	0.00025
Re6An	590	0.00055 ($\pm 15\%$)	0.024	395, 415 442, 470	0.0004 ($\pm 10\%$)	0.0010
Re8an	590	0.0012 ($\pm 3\%$)	0.052	395, 415 442, 470	0.002 ($\pm 10\%$)	0.0051
Re10An	590	0.0018 ($\pm 7\%$)	0.078	395, 415 442, 470	0.004 ($\pm 10\%$)	0.010
ReCH₂B^c	590	0.023 ($\pm 1\%$)	1	---	---	---
ANMOD^c	---	---	---	398, 422 445, 470	0.39 ($\pm 7\%$)	1

^a In degassed 20% MeOH/20 mM Tris; 10 mM NaCl buffer pH 7.2 unless otherwise noted.

^b In degassed 20% MeOH/25 mM Tris buffer pH 7.2.

^c In degassed 25 mM Tris buffer pH 7.0.

^d Emission QY's for $^3\text{MLCT}^*$ calculated from the integrated area of emission in 490-762 nm region relative to $[\text{Ru}(\text{bpy})_3]^{2+}$ in air saturated H_2O where $\phi_{\text{EmRu}} = 0.0379$. QY's determined according to eqn. 4.1 in Chapter 4.

^e Fluorescence QY's for $^1\text{AN}^*$ calculated from the integrated area of emission in 380-490 nm region relative to fluorescein in air saturated 0.1 M NaOH where $\phi_{\text{EmFl}} = 0.87$. QY's determined according to eqn. 4.1 in Chapter 4.

Steady-state emission DNA titrations for Re

Addition of increasing amounts of DNA to solutions of the Re-An complexes (20% MeOH/Buffer) causes dramatic increases in the luminescence from the $^3\text{MLCT}^*$ state (500-800 nm region). This can be visualized from the spectra of the emission DNA titrations for each of the Re-An complexes displayed in Figures 3.13 - 3.16. The emission intensities of the $^3\text{MLCT}^*$ in the complexes show step-wise increases with each addition of DNA and reach saturation when the $[\text{DNA}]_{\text{bp}}/[\text{Re}]$ ratios are ≈ 6 . The model ReCH_2B , which does not possess a DNA binding ligand, shows no changes in its MLCT emission in the presence of DNA. Quantum yields for the MLCT emission (ϕ_{EmRe}) at $[\text{DNA}]_{\text{bp}}/[\text{Re}] = 6$, were determined according to equation 4.1 in Chapter 4 and are listed in Table 3.5. Re10An displays the highest ϕ_{EmRe} in the presence of excess nucleic acids ($\phi_{\text{EmRe}} = 0.0126$) while the QY's of the other complexes follow in the order $\text{Re10An} > \text{Re6An} > \text{Re8An} \gg \text{Re3An}$. It is interesting that Re6An shows higher QY's than Re8An at high DNA/Re ratios, however the QY's for all three of the longer-chained complexes are within close proximity to each other. When comparing the QY *increases* of each complex, Re6An clearly has the largest change (20x increase) from its QY in the absence of DNA. The small changes in the ϕ_{EmRe} for Re3An with DNA is expected since its short chain likely allows energy transfer to occur even when it is bound to DNA. To better visualize the relative modulations in ϕ_{EmRe} for the CQ complexes, their QY changes with increasing additions of DNA are plotted in Figure 3.17. Close inspection reveals that there are slight differences in the binding behavior between the longer-chained complexes even if they do display similarly large increases in their QY's.

Analysis of emission titration data for DNA binding parameters

The enhancements in the MLCT emission of the Re-An complexes with increasing additions of CT DNA provide valuable information towards determination of the extent of binding of the CQ complexes to the ds nucleic acids. The MLCT QY data was analyzed for binding affinities according to two different methods, termed Method II and Method III,

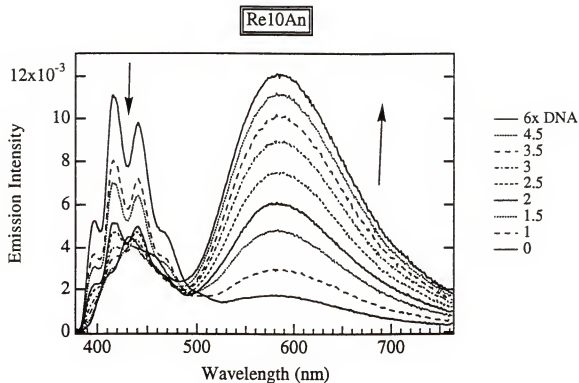


Figure 3.13. Steady-state emission DNA titration of Re10An [4.5×10^{-5} M] with CT DNA in degassed 20% MeOH/20 mM Tris:10 mM NaCl pH 7.2. Excitation was at 340 nm and slit widths were 2.50 and 1.25, respectively, on the excitation monochromator and 1.25×2 on the emission monochromator. Fresh solutions were used for each measurement where the metal complex concentration was held constant and the $[\text{DNA}]_{\text{bp}}$ concentration was varied. DNA concentrations are expressed as $[\text{DNA}]_{\text{bp}}/[\text{Re}]$ ratios and are listed to the right of the figure.

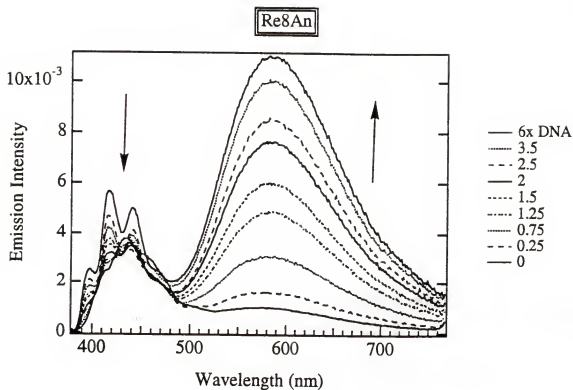


Figure 3.14. Steady-state emission DNA titration of Re8An [4.7×10^{-5} M] with CT DNA in degassed 20% MeOH/20 mM Tris:10 mM NaCl pH 7.2. Conditions were exactly as described in the caption for Figure 3.13. The DNA concentrations are described as $[\text{DNA}]_{\text{bp}}/[\text{Re}]$ ratios and are listed to the right of the figure. Arrows indicate the step-wise increases in the $^3\text{MLCT}^*$ band and the decreases in the $^1\text{AN}^*$ fluorescence bands with increasing concentrations of $[\text{DNA}]_{\text{bp}}$.

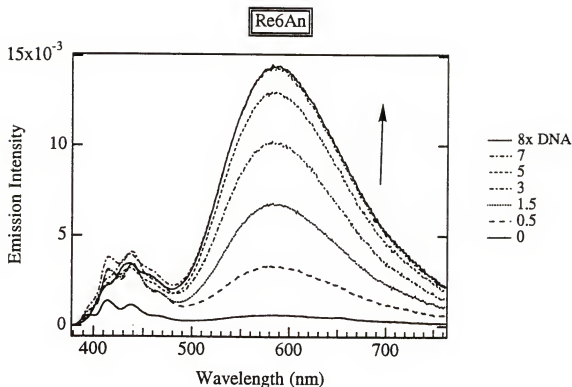


Figure 3.15. Steady-state emission DNA titration of Re6An [4.9×10^{-5} M] with CT DNA in degassed 20% MeOH/ 20 mM Tris: 10 mM NaCl pH 7.2. The same instrumental conditions and experimental procedures as listed in the caption of Figure 3.13 apply to this titration. The DNA concentrations are listed as $[\text{DNA}]_{\text{bp}}/[\text{Re}]$ ratios to the right of the figure. For this complex step-wise increases in the $^3\text{MLCT}^*$ band were evident with increasing $[\text{DNA}]_{\text{bp}}$ concentrations while the AN fluorescence bands generally showed variable small increases.

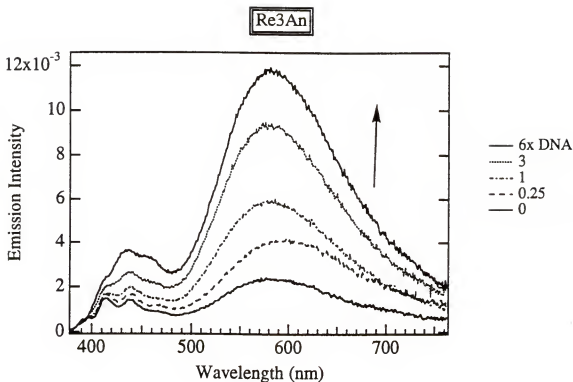


Figure 3.16. Steady-state emission titration of Re3An [$4.7 \times 10^{-5} \text{ M}$] with CT DNA in degassed 20% MeOH/25 mM Tris pH 7.2. Excitation was at 340 nm and the slit widths were 2.5×2 on the excitation monochromator and 1.25×2 on the emission monochromator. Due to the difference in instrumental conditions the intensity scale of this experiment can not be directly compared to the other spectra. However the QY's are determined relative to the actinometer $\text{Ru}(\text{bpy})_3^{2+}$ which then cancels out differences in experimental conditions. DNA concentrations are expressed as $[\text{DNA}]_{\text{bp}}/[\text{Re}]$ ratios to the right of the figure.

Table 3.5. Steady-State Emission Characteristics of $^3\text{MLCT}^*$ state in Re-An Compounds with DNA.^a

Compound	$\lambda_{\text{Em peak}}^{\text{3MLCT}^*}$ (nm)	$\phi_{\text{EmRe}}^{\text{d}}$ 0 DNA	$\phi_{\text{EmRe}}^{\text{e}}$ 6x DNA ^c	Increase ^f in ϕ_{EmRe}
Re3An^b	590	0.00046 $\pm 10\%$	0.0025 $\pm 15\%$	5
Re6An	590	0.00055 $\pm 15\%$	0.0115 $\pm 5\%$	20
Re8an	590	0.0012 $\pm 3\%$	0.0105 $\pm 3\%$	8.75
Re10An	590	0.0018 $\pm 7\%$	0.0126 $\pm 4\%$	7
ReCH₂B^c	590	0.023 $\pm 1\%$	0.022 $\pm 2\%$	0

^a Measured in argon degassed 20% MeOH/20 mM Tris:10 mM NaCl buffer pH 7.2 unless otherwise noted. Samples excited at 340 nm.

^b Measured in degassed 20% MeOH/25 mM Tris buffer pH 7.2.

^c In degassed 25 mM Tris buffer pH 7.0.

^d Emission quantum yields calculated from the integrated area of emission in the 490 - 762 nm region, relative to $[\text{Ru}(\text{bpy})_3]^{2+}$ in air saturated H_2O where $\phi_{\text{EmRu}} = 0.0379$.

^e Indicates the concentration of $[\text{DNA}]_{\text{bp}}$ was "six times" (6x) the concentration of Re-An complex in solution. That is, the ratio of DNA concentration to Re-An concentration was equal to $[\text{DNA}]_{\text{bp}}/[\text{Re}] = 6$

^f Determined by dividing the ϕ_{EmRe} at 6x DNA by the ϕ_{EmRe} at 0 DNA.

^g The numbers given as $\pm\%$ indicate the percent error in the QY values.

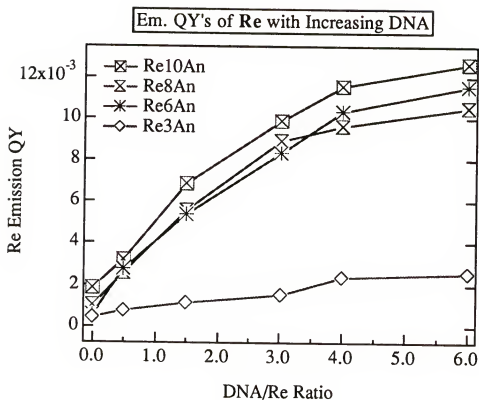


Figure 3.17. Changes in the steady-state $^3\text{MLCT}^*$ emission QY's of the Re-An complexes with increasing $[\text{DNA}]_{\text{bp}}$. The DNA concentrations are expressed as $[\text{DNA}]_{\text{bp}}/[\text{Re}]$ ratios. Experimental conditions are listed under Table 3.5.

which are described in detail in Appendix A. Both analyses provide DNA equilibrium binding constants, K_b , and binding site sizes, n , where n is the number of base pairs on the ds helix covered by the bound molecule. An additional parameter, ω , the co-operativity constant, is provided by method II only and is the unitless equilibrium constant for the process of moving a bound ligand from an isolated binding site to a binding site next to another ligand. In Method II the experimental QY data was used to construct plots according to an equation derived by McGhee and von Hippel^{72,142} which is a modification of the Scatchard¹⁵⁰ equation that takes into account both neighbor exclusion (n) and ligand-ligand co-operativity (ω). Theoretical curves based on this equation were then fit to the experimental data by varying the values of K_b , n and ω until adequate fits were obtained, thus providing the binding parameters. Method III followed a procedure where a mathematically generated curve that is based on the Scatchard equation was directly fit to plots of the experimental QY data vs. $[\text{DNA}]_{bp}$. From this curve-fitting procedure the binding parameters K_b and n were extracted. The values for the binding parameters K_b and n from both methods, and ω from method II, are listed in Table 3.6.

Data in the range from approximately 60 - 100 % binding was used for the analyses since accurate fitting of the entire range of data for most of the complexes could not be achieved with satisfactory results. At very low $[\text{DNA}]_{bp}/[\text{Re}]$ ratios the experimental error is significant on account of there being a large number of Re-An molecules per DNA base pair which can bind in nonspecific modes other than intercalation. This was particularly noticeable with Re3An where at low DNA/Re ratios the strands of polymer visibly precipitated out of solution. Many intercalators will precipitate nucleic acids at $[\text{DNA phosphate}]/[\text{ligand}]$ ratios lower than 2,¹⁰ due to the fact that at low DNA/ligand ratios the cationic charges of the ligand neutralize the negatively charged phosphates on the DNA backbone. This removes the repulsive charges within the polymer such that it condenses in solution. In addition to the binding complications for the Re-An complexes, the signal-to-noise is poor at small DNA/Re ratios since the QY's are very low in this range.

Table 3.6. DNA Binding Parameters for Re-AN Complexes and ANMOD from Emission QY Data^a

Compound	K_b (M^{-1})		Site Size (n)		Cooperativity Const. ^c (ω)
	DNA Binding Method II ^c	DNA Binding Method III ^d	Base Pairs II ^c	III	
Re3An	3.0×10^5	1.5×10^5	2.5	3.6	0.05
Re6An	4.8×10^5	2.5×10^5	2.8	3.7	0.09
Re8An	8.0×10^5	5.7×10^5	2.8	3.1	0.10
Re10An	6.8×10^5	2.9×10^5	2.6	3.4	0.05
ANMOD ^b	6.5×10^5	6.5×10^5	2.1	2.3	0.001

^a Measured in degassed 20% MeOH/20 mM Tris:10 mM NaCl pH 7.2 unless otherwise noted. Calf thymus DNA was used for all studies. Quantum yields (QY) were determined from the steady-state emission DNA titrations.

^b Measurements done in degassed 25 mM Tris pH 7.2.

^c Determined according to Method II in Appendix A.

^d Determined according to Method III in Appendix A.

Focusing first on the equilibrium binding constants for the complexes determined by method II, it can be seen that Re8An displays the largest K_b at $8.0 \times 10^5 \text{ M}^{-1}$, while Re10An and Re6An show slightly lower values at $6.8 \times 10^5 \text{ M}^{-1}$ and $4.8 \times 10^5 \text{ M}^{-1}$, respectively. This might appear surprising since Re10An and Re6An both reach higher QY values at saturation of binding than Re8An, however the binding constant reflects the step-wise changes in QY with increasing DNA, and not necessarily the absolute increase in QY over the entire data range. Re8An consistently reaches saturation of binding at lower DNA/Re ratios than the latter complexes, thus indicating a stronger binding interaction. Re3An possesses the lowest binding constant at $3.0 \times 10^5 \text{ M}^{-1}$, as expected from its small QY changes. Notice similar general trends are observed within the binding constants determined by method III. Again Re8An possesses the largest K_b at $5.7 \times 10^5 \text{ M}^{-1}$ and the K_b 's for the other CQ complexes follow in the order Re8An (5.7×10^5) > Re10An (2.9×10^5) > Re6An (2.5×10^5) > Re3An (1.5×10^5). All the complexes have similar binding site sizes, approximately 3 base pairs according to method II and between 3 and 4 base pairs as determined by method III. These site sizes are close to the neighbor exclusion model of $n = 2$ base pairs, and are within good agreement to site sizes found for other DNA intercalators, as will be addressed further in the discussion section. The cooperativity constants, ω , are less than one for all the data, which is indicative of anti-co-operative behavior.⁷² Anti-co-operativity has been attributed to charge repulsions upon binding of cationic complexes. Condensation theory predicts that 0.2 - 0.3 sodium counter-ions should be released from the negatively-charged phosphate groups with the binding of a compound to DNA, regardless of the compound's positive charge. If a compound possesses a higher cationic charge, it will counter-balance a larger number of negative phosphate charges, therefore reducing the affinity of nearby compounds towards binding to the helix. The Re-An complexes should be dications on account of the protonated amine in the linker chain and the +1 charge of the Re chromophore. Closer inspection of the experimental fits to the emission QY plots (Figures A.3 & A.4, Appendix A) reveals that

the data for some of the complexes (Re8An and Re6an, in particular) show a slight sigmoidal shape to their curves which also is evidence of an anti-co-operative process.¹⁰ However, interpretation of the individual values of both ω and n can be complicated since they are highly correlated for compounds which have negative cooperativity and site exclusion.¹⁵¹ Adequate fits to the data can be achieved with slight variations in ω and n while K_b is much less flexible. It should be noted that the ω values are generally low for all the complexes which indicates the degree of co-operativity is not very large.

Comparison between the binding parameters obtained by methods II and III (Table 3.6) indicates that the K_b values are consistently larger for method II, except for the model ANMOD, and the site sizes (n) are consistently smaller by this method. Method III does not take into account co-operativity effects (ω), in which case the ω values are absorbed by the site size parameter resulting in larger values for n by this method. The equilibrium constants determined by method III, as well, give relative binding affinities in the absence of co-operative effects from other molecules, while K_b 's calculated from method II take into account these effects and give binding constants from a range of concentrations of bound and unbound complexes. It is of interest to note that K_b for the model ANMOD is the same by either binding analysis, suggesting lower sensitivity of this monocationic compound to co-operative effects.

Emission Decays

Emission lifetimes for the ³MLCT* state in the absence and presence of increasing amounts of calf thymus DNA were obtained for all complexes. Multi exponential decays are exhibited by all the CQ complexes free in solution, while the model ReCH₂B shows only a single exponential decay. The emission decays were fitted to a 3-component exponential decay function (eqn. 3.5),

$$I_{em}(\tau) = \sum_{i=1}^3 \alpha_i \tau_i \quad \text{Eqn. 3.5}$$

where τ_i and α_i are, respectively, the lifetime and amplitude of the i^{th} components. The amplitudes are normalized according to

$$\sum_i \alpha_i = 1.0 \quad \text{Eqn. 3.6}$$

A median lifetime $\langle \tau \rangle$ was calculated for each decay using the normalized amplitudes (α'_i) in the following equation,

$$\langle \tau \rangle = \sum_{i=1}^3 \alpha'_i \tau_i \quad \text{Eqn. 3.7}$$

The parameter $\langle \tau \rangle$ is proportional to the total emission yield for the complex. The product $\alpha_i \times \tau_i$ is proportional to the emission quantum yield of the i^{th} component according to equation 3.6,

$$\text{emission yield for } i^{\text{th}} \text{ component} = \phi_{\text{total}}^{\text{em}} \times \frac{\alpha_i \tau_i}{\langle \tau \rangle} \quad \text{Eqn. 3.8}$$

The decay data for the complexes free in solution and in the presence of CT DNA is listed in Table 3.7. Inspection of the decay data for the complexes free in solution reveals several trends. Each complex displays a short-lived component (τ_1), an intermediate-lived component (τ_2) and a long-lived one (τ_3). The longest-lived component, since it has a lifetime comparable to the ReCH_2B model, can be assigned to emission from unquenched $^3\text{MLCT}^*$ which originates from those molecules which are in fully extended conformations. In extended conformations, the separation distance between the Re chromophore and AN is large enough that the efficiency of E_{NT} quenching should be reduced such that there is sufficient time for emission of a photon from the $^3\text{MLCT}^*$ state to occur before quenching can take place. Notice that the amplitude (α_3) of this component for all the complexes is very small, which suggests few of the molecules exist in this conformation in solution. The large value of α_3 for Re3An is due to small amounts of impurity which formed soon after purification. The shortest-lived component τ_1 represents the lifetime of molecules in which the $^3\text{MLCT}^*$ state is efficiently quenched. This component emanates from molecules which are folded over such that Re and AN are in

Table 3.7. Emission Lifetimes of ³MLCT* state in Re-An Compounds and ReCH₂B.^a

Compound	No DNA			6x DNA ^d			χ^2
	τ_1 (α_1 (%))	τ_2 (α_2 (%))	τ_3 (α_3 (%))	τ_1 (α_1 (%))	τ_2 (α_2 (%))	τ_3 (α_3 (%))	
Re10An	1.7 (14) ±5%	6.8 (86) ±4%	147 (0.4) ±15%	6.7 ±15%	0.90	2.6 (15) ±10%	66 ±10%
Re8An	1.4 (39) ±15%	3.6 (61) ±15%	111 (0.58) ±15%	3.3 ±15%	0.97	2.8 (23) ±15%	55 ±15%
Re6An	1.9 (97) ±15%	8.9 (2.0) ±15%	130 (0.94) ±15%	3.2 ±15%	0.29	2.6 (23) ±15%	65 ±15%
Re3An	1.1 (94) ±3%	6.5 (4.1) ±14%	140 (2.33) ±6%	4.5 ±14%	1.03	5.1 (40) ±15%	16 ±15%
ReCH₂B	107 (100) ±5%			107 ±5%	1.20	107 (100) ±5%	107 ±5%

^a All lifetimes are in nanoseconds. Measurements obtained in degassed 20% MeOH/Buffer solutions. Samples were excited at 355 nm and emission collected at 600 nm.

^b Median lifetimes $\langle \tau \rangle$ calculated according to eqn. 3.7.

^c Chi squared χ^2 indicates the goodness of the triple-exponential fits to the experimental data obtained from the Decan fitting program. The numbers given as \pm % under each individual component lifetime indicate the percent variance of the listed data from data obtained in separate measurements.

^d Indicates the ratio of the [DNA]₀ concentration to [Re] concentration is equal to 6 for all measurements. The concentration of Re-An complex was typically $\sim 2 \times 10^{-5}$ M.

close proximity to each other, enabling quenching to occur rapidly after excitation. Clearly Re3An and Re6An display the largest percentages of this short-lived quenched species as indicated by the large amplitudes (α_1) of this component for these complexes. This would be in agreement with their structures which contain shorter linker chains placing Re and AN in closer proximity and allowing more efficient energy transfer. Re8An and Re10An contain much lower percentages of τ_1 , indicating the lower probability of Re and AN to achieve the proper conformation for E_NT to occur efficiently.

The middle component τ_2 represents lifetimes of those complexes where the orientation of the AN ligand is intermediate between fully extended away from Re and completely folded over in close proximity to the Re center. In this conformation E_NT is not as efficient as when Re and AN are very close together, therefore the $^3MLCT^*$ state is slightly longer-lived. For the longer-chained Re10An and Re8An this component (τ_2) has the largest contribution to their lifetimes in solution, as evidenced by the large amplitudes (α_2) of this component displayed by these complexes. The linker chains of Re8An and Re10An contain more rotational freedom due to the increased number of methylene linkages, which results in a greater number of conformations for these complexes.

The median lifetimes $\langle \tau \rangle$ for all the CQ complexes in solution are considerably reduced in comparison to the model, in agreement with the reductions in emission quantum yields for these complexes compared to the unquenched model. The median lifetimes follow the same trend as the emission quantum yields (Table 3.4) within the CQ complexes where $\langle \tau \rangle$ is greatest for Re10An at 6.7 ns and slightly lower for Re8An (3.3 ns) and Re6An (3.2 ns). The median lifetime for Re3An cannot be accurately determined due to the presence of impurities.

Emission Decays with DNA

The $^3MLCT^*$ emission decays of the CQ complexes show complex changes, but overall are characterized by decreases in decay rates upon addition of calf thymus DNA. Triple-exponential decay functions were used to fit the emission decays of the Re-An

complexes while the model compound was fit to a monoexponential decay function. Table 3.7 lists the median lifetimes, $\langle \tau \rangle$, and the three component lifetimes which comprise each decay for all the complexes in the presence of $[\text{DNA}]_{\text{bp}}/[\text{Re}]$ ratios equal to 6. The changes in tau median, $\langle \tau \rangle$, for each complex with increasing additions of DNA are plotted in Figure 3.18 (individual τ and α values for data corresponding to DNA/Re ratios below 6 are listed in Appendix B). From this graph it is clear that the three longer-chained complexes all show significant increases in their median lifetimes with saturation occurring at $[\text{DNA}]_{\text{bp}}/[\text{Re}] = 6$, while Re3An shows only a slight increase. Quantitatively (Table 3.7) Re10An and Re6An possess the longest median lifetimes ($\langle \tau \rangle$) in the presence of high $[\text{DNA}]_{\text{bp}}$ with $\langle \tau \rangle = 66$ ns and 65 ns, respectively, and Re8An is just 10 ns lower at 55 ns. The changes parallel those seen in the emission QY's and indicate that the same effects are being monitored in both experiments.

Interesting trends can be seen in the individual component lifetimes (τ_1 , τ_2 , τ_3) of each complex at $6 \times [\text{DNA}]_{\text{bp}}$ in comparison to their values at zero $[\text{DNA}]$. All the complexes retain a short-lived species, an intermediate-lived species and a long-lived species in the presence of DNA, but their lifetimes and contributions of the components to the total emission decay change. For Re10An, Re8An and Re6An there is a significant increase in the contribution of τ_3 in the presence of DNA. In fact this component shows the largest overall change of the three lifetime components (τ_1 , τ_2 , τ_3) for the three longer-chained complexes (see also Appendix B). The change can be visualized from Figure 3.19(a-c) which shows the individual τ components multiplied by their normalized amplitudes $\{(\tau_1 \times \alpha_1), (\tau_2 \times \alpha_2), (\tau_3 \times \alpha_3)\}$ versus DNA/Re ratios for each complex. These products ($\alpha_i \times \tau_i$) are proportional to the emission quantum yields of the individual components (1, 2 & 3) according to eqn. 3.8 and therefore are a valuable measure of which components contribute the most to the overall lifetime. Although the lifetime of τ_3 for Re10An and Re8An in the presence of DNA is shorter than the lifetime of the unquenched model complex, this component is still considered to represent those molecules whose

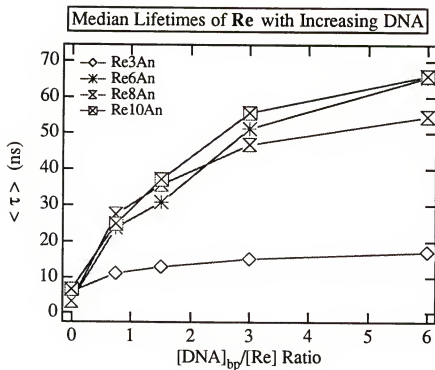


Figure 3.18. Changes in the median $^3\text{MLCT}^*$ emission lifetimes of the Re-An complexes with increasing concentrations of $[\text{DNA}]_{\text{bp}}$. DNA concentrations are expressed as $[\text{DNA}]_{\text{bp}}/[\text{Re}]$ ratios. Median lifetimes $\langle \tau \rangle$ were calculated according to eqn. 3.7. Experimental conditions are listed under Table 3.7.

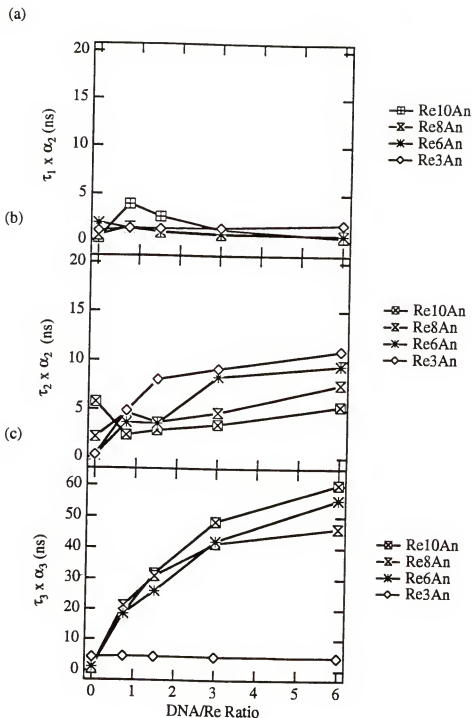


Figure 3.19. (a) Changes in (a) $(\tau_1 \times \alpha_1)$, (b) $(\tau_2 \times \alpha_2)$ and (c) $(\tau_3 \times \alpha_3)$ with increasing $[\text{DNA}]_{\text{bp}}/[\text{Re}]$ ratios for the Re-An complexes. The $(\tau_i \times \alpha_i)$ values are proportional to the emission QY of the i^{th} component according to eqn. 3.8, therefore indicating the component's contribution to the overall lifetime ($\langle \tau \rangle$). Plots (a) and (b) have the same y-axis scale while the y-axis scale of (c) is three times larger. Experimental conditions are listed under Table 3.7.

$^3\text{MLCT}^*$ emission is quenched weakly or not at all by the $\text{E}_\text{N}\text{T}$ mechanism. The amplitude for τ_3 among the complexes increases in the order $\text{Re3An} \ll \text{Re6An} < \text{Re8An} < \text{Re10An}$, and as seen from Figure 3.19c, indicates the longer-chained complexes possess significantly large amounts of this long-lived species in the presence of high DNA concentrations. Significant changes are also seen in the contribution of τ_1 for Re3An and Re6An . There is a 57% reduction in the contribution of τ_1 for Re3An , a 76% reduction for Re6An and a 41% reduction in its contribution for Re8An . Notice that Re10An essentially shows no change in its τ_1 component. Finally, the intermediate-lived component τ_2 appears to increase in its length for all the complexes ($\sim 20 - 30$ ns) while its fractional contribution shows prominent *decreases* for Re10An and Re8An , a moderate *increase* for Re6An and a dramatic *increase* in contribution for Re3An .

The relative changes for the $\tau_i \times \alpha_i$ values with increasing $[\text{DNA}]_\text{bp}$ within the four Re-An complexes are plotted in Figure 3.20. Again it can be seen that $\tau_3 \alpha_3$ exhibits the largest overall increases for Re10An , Re8An and Re6An and is the major contributor to the overall lifetime changes in these complexes. Re3An exhibits the largest changes in $\tau_2 \alpha_2$ among all the complexes, and it is this component that contributes the most to the overall lifetime increases seen in Re3An . Since τ_1 is so short, its changes can not be visualized as readily. Clearly these changes in decay behavior of the CQ complexes in the presence of DNA can be attributed to a decrease in the energy transfer quenching of the $^3\text{MLCT}^*$ state due to binding of the complexes to the double helix.

Photophysics of AN moiety

Steady-state emission studies of AN

Recall from the first section in which the emission characteristics of the Re-An complexes was presented that the fluorescence from the AN moiety within the complexes was observed to be quenched, presumably by energy transfer to the Re MLCT state. The efficiency of quenching was shown to parallel the length of the linker chains in the order of

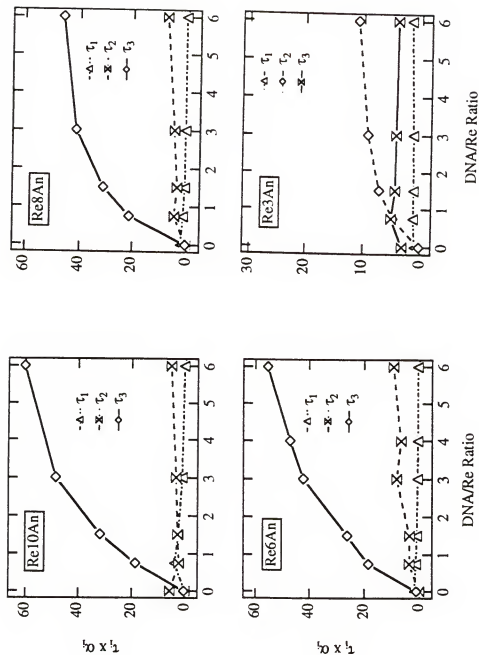


Figure 3.20. Relative changes in $\tau_i \times \alpha_i$ with increasing $[\text{DNA}]_{\text{bp}}/[\text{Re}]$ ratios within each CQ complex. The $\tau_i \times \alpha_i$ values are in ns, and the y-axis scale for Re3An is one half the size of the scales for the other complexes in order to expand the plot for easier visualization of the lifetime changes in this complex. All experimental conditions are listed under Table 3.7.

$\Phi_{\text{EmAN}} \text{Re3An} < \text{Re6An} < \text{Re8An} < \text{Re10An}$. This quenching phenomenon, mentioned earlier in Figure 3.2, is attributed to coulombic energy transfer ($E_{\text{N}}T_{\text{C}}$) from $^1\text{AN}^*$ to the Re^* MLCT manifold (see eqn. 3.3). It occurs through a dipole-dipole interaction between the two chromophores and can take place over larger distances (20 to 100 Å).

In light of these photophysical phenomena, it is expected that the fluorescence quantum yields for the AN moiety in the complexes would exhibit complicated changes in the presence of calf thymus DNA. These changes as a function of DNA/Re ratios are plotted in Figure 3.21. Values of the AN QY's for the complexes and the model at 0 and 6x DNA/Re are listed in Table 3.8. Focusing on the graph, Re10An and Re8An both show decreases in their AN QY's which level out by $[\text{DNA}]_{\text{bp}}/[\text{Re}] = 5$. The AN QY's for Re6An increase up to the same plateau as Re8An, while Re3An displays a very slight increase in QY remaining approximately one order of magnitude below the other complexes. The model ANMOD behaves in a similar fashion to the longer-chained complexes, although its QY decreases more dramatically, down to 20% of its original value (see Table 3.8).

Previous studies on anthracene derivatives have shown that DNA strongly quenches the fluorescence of the bound complex.²⁷ The luminescence of other polycyclic aromatic chromophores such as pyrene¹⁵² and the anthracycline compounds³² is also quenched when bound to DNA. The mechanism for this quenching, although not fully understood as of yet, has been suggested to be due to electron transfer quenching between the bound molecules and the DNA bases.^{27,80,88,153} It is known that only some of the DNA bases participate in the quenching, therefore the AN fluorescence does not disappear completely. An estimate of the ability of the nucleosides to participate in ET with $^1\text{AN}^*$ can be calculated from the redox potentials of the ground state compounds and the energy of the excited state of ^1AN according to equations 1.4 and 1.5 in Chapter I. Guanosine monophosphate (GMP), considered the easiest DNA base to oxidize, has been estimated to have a reduction potential for its cation (GMP^+/GMP vs. SCE) of $\geq 0.92 \text{ V}$.^{81,154}

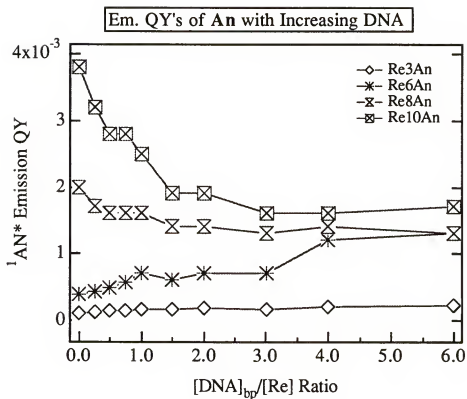


Figure 3.21. Changes in the steady-state emission QY's for $^1\text{AN}^*$ in the Re-An complexes with increasing concentrations of CT DNA. The DNA concentrations are expressed as $[\text{DNA}]_{\text{bp}}/[\text{ReAn}]$ ratios. Measurements were performed in degassed 20% MeOH/Tris buffer solutions with excitation at 340 nm.

Table 3.8. Steady-State Emission Characteristics of ¹AN* in Re-An Compounds with and without DNA.^a

Compound	λEm peaks An (nm)	Φ _{EmAn} ^d 0 DNA	Φ _{EmAn} 6x DNA ^c	$\frac{\Phi_{EmAn}^{6xDNA}}{\Phi_{EmAn}^{0DNA}}$ ^f	λEm peaks ^g w/ 6x DNA
Re3An^b	395, 415 442, 470	0.0001 ± 15%	0.0002 ± 15%	2 (Incr.)	410, 434 458
Re6An	395, 415 442, 470	0.0004 ± 10%	0.0013 ± 15%	3.25 (Incr.)	410, 434 458
Re8an	395, 415 442, 470	0.002 ± 9%	0.0013 ± 12%	0.65 (Decr.)	410, 433 458
Re10An	395, 415 442, 470	0.004 ± 14%	0.0017 ± 8%	0.42 (Decr.)	410, 432 455
ANMOD^c	398, 422 445, 470	0.44 ± 7%	0.087 ± 1%	0.20 (Decr.)	

^a Measured in argon degassed 20% MeOH/20 mM Tris:10 mM NaCl buffer pH 7.2 unless otherwise noted. Samples excited at 340 nm.

^b Measured in degassed 20% MeOH/25 mM Tris buffer pH 7.2.

^c Measured in degassed 25 mM Tris buffer pH 7.0.

^d Quantum yields determined from the integrated area of emission in the 380-490 nm region for the Re-An complexes relative to fluorescein in air saturated 0.1 M NaOH (Φ_{emf} = 0.87) and calculated according to eqn. 4.1 in Chapter 4.

^e Indicates the [DNA]_{bp} concentration was "six times" (6x) the concentration of Re-An complex in solution (i.e. [DNA]_{bp}/[Re] = 6).

^f This is the ratio of the Φ_{EmAn} in the presence of 6x DNA divided by the Φ_{EmAn} in the absence of DNA. Incr. means "increase" and Decr. means "decrease".

^g The error in these values is approximately ± 3 nm. The central peak (~434 nm region) shows the greatest intensity.

The base thymidine is easily reduced with a reduction potential for unprotonated thymidine monophosphate (TMP/TMP $^{\cdot-}$ vs. SCE) of -1.35 V.^{154,81} The reduced form of cytosine is known to be quickly protonated by its base-paired partner guanosine, and therefore because of this reaction, protonated reduced cytosine is estimated to be 0.2 V easier to form than the reduced thymidine radical in ds DNA.^{154,81} The redox potential of the nucleoside adenosine is not considered favorable for ET reactivity. Using the above redox potentials for the nucleosides, a reduction potential for AN (AN/AN $^{\cdot-}$ vs. SCE) of -1.93 V,¹⁵⁵ an oxidation potential for AN (AN $^+$ /AN vs. SCE) equal to 1.16 V¹⁵⁶ and an excited state energy ($E_{0,0}$) for $^1\text{AN}^*$ of 3.28 V^{157,158} the free energies for excited state ET with the DNA bases have been calculated using equations 1.4 and 1.5 and are given by the following values: $\Delta G^0(\text{GMP}^+/\text{AN}^{\cdot-}) = -0.43$ eV; $\Delta G^0(\text{TMP}^{\cdot-}/\text{AN}^+ \cdot) = -0.77$ eV; and $\Delta G^0(\text{CMP}^{\cdot-}/\text{AN}^+ \cdot) = -0.97$ eV. The large negative free energy values determined from these estimates, although only approximate, never-the-less suggest that ET between the DNA bases and $^1\text{AN}^*$ is highly favorable, with the greatest reactivity expected to be reductive ET from the pyrimidine bases (thymidine and cytosine) to $^1\text{AN}^*$. The changes exhibited by the AN moiety in the Re-An complexes reflect this interaction with DNA. Since Re10An and Re8AN retain some degree of unquenched AN in solution, due to slightly less efficient energy transfer to Re, upon intercalation into DNA their excited state energy will be quenched by certain of the bases. The AN fluorescence of Re6An in solution is quenched intramolecularly more efficiently than when it is bound to DNA, therefore the ϕ_{EmAN} for this complex increases in the presence of DNA. Notice that both Re8An and Re6An level out to the same value for ϕ_{EmAN} at high DNA. This could indicate that they are bound to the same degree and prefer similar kinds of base pair sites.

The position of the AN fluorescence bands in the steady-state spectra for all the Re-An compounds display broadening and red shifts in addition to their QY changes (Figure 3.22). The broadening is due to overlap of the spectra of bound and free forms of the complexes. The red shifts are characteristic changes exhibited by intercalating ligands and

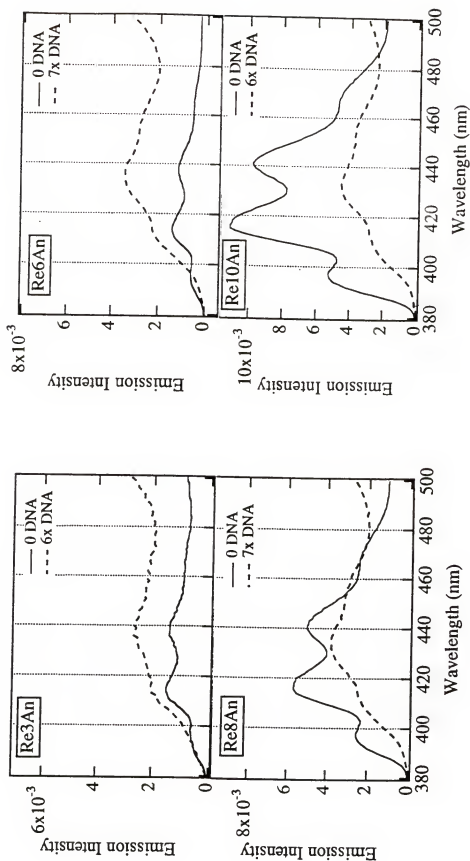


Figure 3.22. Steady-state emission spectra of $^1\text{AN}^*$ fluorescence bands in the 380 - 500 nm region for the CQ complexes in the absence and presence of CT DNA. Measurements were performed in degassed 20% MeOH/Tris buffer solutions pH 7.2 where the metal complex concentrations are Re3An = $[4.7\text{E}-5 \text{ M}]$, Re6An = $[4.9\text{E}-5 \text{ M}]$, Re8An = $[4.7\text{E}-5 \text{ M}]$ and Re10An = $[4.5\text{E}-5 \text{ M}]$. The spectra are normalized roughly to their AN QY's. See Table 3.8 for more details.

are attributed to the hydrophobic environment of the DNA bases which lowers the energy of the AN emission bands.²⁷

Emission decays for AN moiety

Emission decay lifetimes of the AN moiety in the Re-An complexes were measured in degassed 20% MeOH/Buffer solution in the absence and presence of $[DNA]_{bp}/[Re]$ ratios equal to 6. The decays were fit to double exponential (in some cases) and triple exponential kinetic traces (most cases), and the results are listed in Table 3.9. The lifetime for the model ANMOD is also listed for comparison. Free in solution the Re-AN complexes possess very short median lifetimes ($\langle \tau \rangle$), generally ≤ 1 ns. Their individual component lifetimes (τ_1 , τ_2 , τ_3) are composed of a short-lived species of less than one nanosecond (τ_1), and one or more species (τ_2 , τ_3) with a lifetime close to that of the model. The short-lived component (τ_1) overwhelmingly contributes 90 - 99% of the total emission decay of the complexes in solution, and represents those molecules which are quenched by the energy transfer mechanism to the Re MLCT state. Re6An and Re3An both contain a third component (τ_3) with a lifetime longer than that of the model. This component is due to an impurity which could not be completely removed before data collection.

In the presence of high concentrations of CT DNA ($[DNA]_{bp}/[Re] = 6$), all the decays of the Re-An complexes, as well as the model ANMOD, were fit to triple-exponential kinetics. The decays consist of a short-lived component ($\tau_1 < 1$ ns), a slightly longer-lived component (τ_2), and a third component with the longest lifetime (τ_3) ranging from 8.5 - 28 ns. The longest-lived species is assigned to intercalated AN whose excited-state is not quenched by the DNA bases.²⁷ The model ANMOD shows an amplitude (α_3) for τ_3 at 11%, while the Re-An complexes show only small percentages of this component contributing to their overall lifetimes. For Re3An and Re6An α_3 has the same value as when they were free in solution. This would lead one to suspect that this species is merely an impurity and not representative of intercalated complex. τ_3 for Re10An is nearly the same in length and fractional contribution as τ_2 in its solution phase. It appears that for the

Table 3.9. Emission Lifetimes of $^1\text{An}^*$ state in Re-An Compounds.^a

Compound	No DNA			6x DNA ^d			χ^2
	τ_1 ($\alpha_1(\%)$)	τ_2 ($\alpha_2(\%)$)	τ_3 ($\alpha_3(\%)$)	τ_1 ($\alpha_1(\%)$)	τ_2 ($\alpha_2(\%)$)	τ_3 ($\alpha_3(\%)$)	
Re10An	0.63 (99.8) ($\pm 16\%$)	8.46 (0.15) ($\pm 15\%$)		0.65 (73) ($\pm 15\%$)	2.75 (27) ($\pm 13\%$)	8.5 (0.52) ($\pm 20\%$)	0.86
Re8An	0.47 (97) ($\pm 10\%$)	10.6 (3.2) ($\pm 5\%$)		0.75 (84) ($\pm 15\%$)	3.3 (15) ($\pm 15\%$)	20 (0.96) ($\pm 5\%$)	1.20
Re6An^e	0.22 (98.9)	8.2 (0.89)	17.6 (0.23)	0.48 (87)	1.64 (12)	15 (0.24)	1.20
Re3An^f	0.70 (86) ($\pm 3\%$)	6.2 (12) ($\pm 15\%$)	15.8 (2.2) ($\pm 20\%$)	0.75 (89)	6.0 (9)	25 (2.0)	1.20
ANMOD^f	10.8 (100) ($\pm 1\%$)			1.36 (25)	10.5 (64)	28 (11)	0.94

^a All lifetimes (τ) are in nanoseconds. Measurements obtained in argon degassed 20% MeOH/Buffer solutions pH 7.2. Samples were excited at 355 nm and emission collected at 450 nm.

^b Median lifetimes $\langle \tau \rangle$ calculated according to eqn. 3.7.

^c Chi squared χ^2 indicates the goodness of the computer generated fits to the experimental data according to the Decan fitting program. The numbers given as $\pm \%$ under each individual component lifetime indicate the percent variance of the listed data from data obtained in separate measurements.

^d Indicates that the ratio of the $[\text{DNA}]_{\text{bp}}$ concentration to $[\text{Re}]$ concentration is equal to 6 for all measurements. The concentration of Re-An complex was typically $\sim 2 \times 10^{-5}$ M.

^e Only one set of data obtained for this complex.

^f Only one data set obtained with DNA for this complex.

lifetimes of the complexes in the presence of DNA it is the intermediate-lived component τ_2 that represents those AN moieties which are intercalated but quenched by the DNA bases. The length of this lifetime is close to the shortest-lived lifetime in the model. This species was not present in the complexes or the model when free in solution. The shortest-lived τ_1 in the complexes is most likely due to intramolecularly quenched AN, but it cannot be assumed to be solely from those molecules which are not bound to DNA. It is possible that energy transfer from $^1\text{AN}^*$ to Re can occur even in the bound forms of the complexes, particularly since this type of transfer is less distance dependent than the electron-exchange mechanism which occurs from the $^3\text{MLCT}^*$ to $^3\text{AN}^*$.

Transient absorbance studies

Transient absorption spectroscopy was carried out on ANMOD, Re10An and Re6An in degassed 20% MeOH/buffer solutions in the absence and presence of $[\text{DNA}]_{\text{bp}}/[\text{Re}]$ ratios equal to 7.5. The studies were conducted in order to compare the decays and relative intensities of the AN triplet observed in the complexes and the model in solution and to determine how intercalation into DNA affects these intensities and lifetimes. The samples were excited by using the third harmonic output of a Q-switched Nd:YAG laser (355 nm, 10 ns fwhm, 5 mJ/pulse). Decays for all the samples in solution in the absence of DNA were obtained using a 50 μs /division time scale, and decays for the samples in the presence of $[\text{DNA}]_{\text{bp}}/[\text{Re}] = 7.5$ were collected on a 200 μs /division time scale. An example of the transient absorption spectra for ANMOD in degassed solution taken at delay times ranging from 0 to 0.80 μs following laser excitation is illustrated in Figure 3.23a. The spectra show a characteristic intense peak centered at 426 nm with a less intense broad shoulder in the 390 - 415 nm region. These spectra are in agreement with those reported for anthracene and 9-methylantracene.^{138,159} Decays of the transient spectra for ANMOD were determined using a 50 μs /division time scale and fit to double-exponential kinetics with $\tau_1 = 18 \mu\text{s}$ ($\alpha_1 = 63\%$) and $\tau_2 = 67 \mu\text{s}$ ($\alpha_2 = 37\%$) as listed in Table 3.10. Figures 3.24a and 3.25a illustrate the transient absorption spectra for Re6An

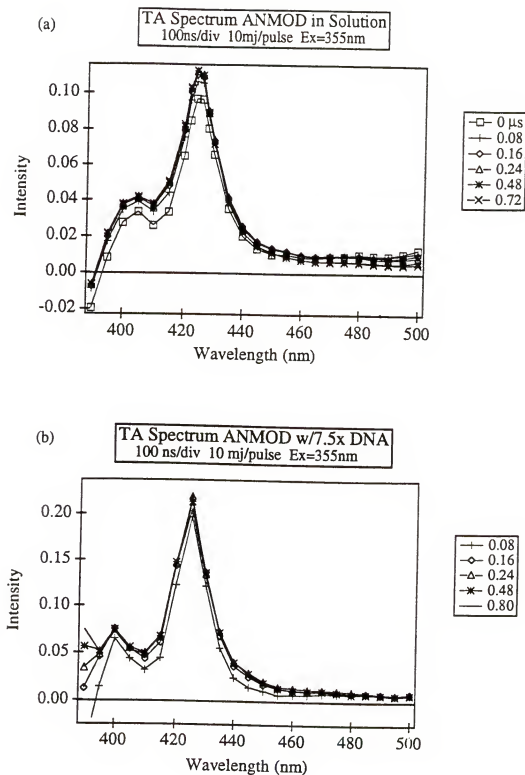


Figure 3.23. Transient absorption spectra of ANMOD in argon degassed 20% MeOH/20 mM Tris:10mM NaCl pH 7.2 solutions (a) in the absence of DNA where $[AN] = 7.2 \times 10^{-5} \text{ M}$ ($OD_{355nm} = 0.389$) and (b) in the presence of $[DNA]_{bp}/[AN] = 7.5$ where $[AN] = 7.6 \times 10^{-5} \text{ M}$ (optical density not obtained).

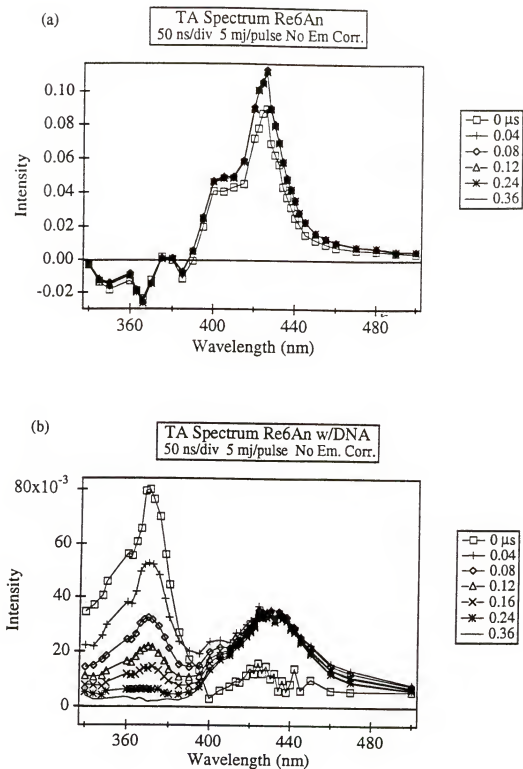


Figure 3.24. Transient absorption spectra of Re6An in argon degassed 20% MeOH/20 mM Tris:10 mM NaCl pH 7.2 solutions in (a) the absence of DNA where $[Re] = 7.2 \times 10^{-5}$ M ($OD_{355nm} = 0.449$) and (b) the presence of $[DNA]_{bp}/[Re] = 7.5$ where $[Re] = 9.5 \times 10^{-5}$ M ($OD_{355nm} = 0.496$).

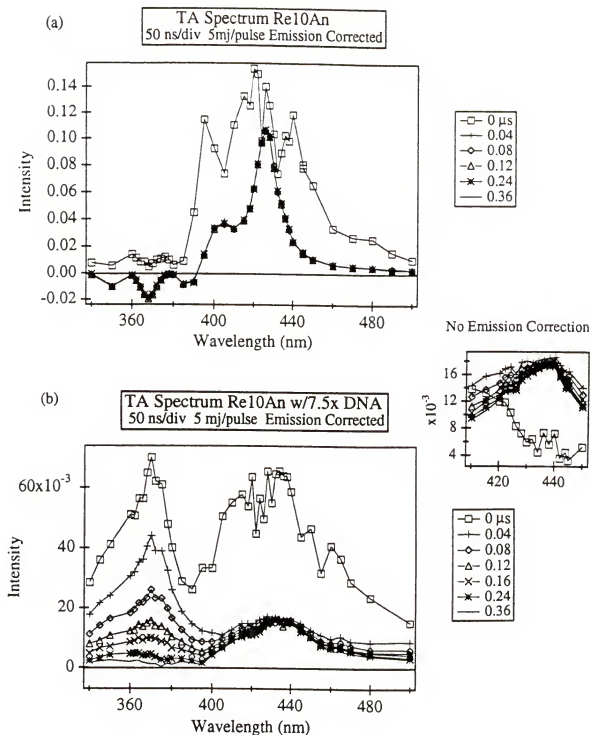


Figure 3.25. Transient absorption spectra of Re10An in argon degassed 20% MeOH/20 mM Tris:10 mM NaCl pH 7.2 solutions in (a) the absence of DNA where $[Re] = 6.2 \times 10^{-5}$ M ($OD_{355nm} = 0.0447$) and (b) the presence of $[DNA]_{bp}/[Re] = 7.5$ where $[Re] = 8.7 \times 10^{-5}$ M ($OD_{355nm} = 0.476$). An emission correction factor implemented in these spectra caused over-corrected peaks at 0 time. The spectra at 0 μ s appear normal when the correction is turned off as seen from the inset for (b).

Table 3.10. Transient Absorbance Lifetimes and Decay Rates of $^3\text{AN}^*$ and $^3\text{MLCT}^*$.^a

Compound	No DNA				6x DNA ^b			6x DNA		
	$\tau_{^3\text{AN}^*}^c$ (μs)	$\tau_{^3\text{AN}^*}^c$ (%)	$k_{^3\text{AN}^*}^c$ (s^{-1})	$\langle\tau\rangle_{^3\text{AN}^*}^e$ (μs)	$\tau_{^3\text{AN}^*}^d$ (μs)	$\tau_{^3\text{AN}^*}^d$ (%)	$k_{^3\text{AN}^*}^d$ (s^{-1})	$\langle\tau\rangle_{^3\text{AN}^*}^e$ (μs)	$\tau_{^3\text{MLCT}^*}$ (ns)	$k_{^3\text{MLCT}^*}$ (s^{-1})
ANMOD	17.7 (63%) 67.0 (37%)		5.66×10^4 1.49×10^4	35.9	8.5 (55%) 82 (23%) 392 (22%)		1.2×10^5 1.2×10^4 2.6×10^3	109.8		
Re10An	28.1 (46%) 99.8 (54%)		3.6×10^4 1.0×10^4	66.8	60 (28%) 331 (34%) 1038 (38%)		1.7×10^4 3.0×10^3 9.6×10^2	527	75.8	1.3×10^7
Re6An	17.2 (57%) 84.3 (43%)		5.82×10^4 1.19×10^4	46.1	27 (24%) 174 (37%) 571 (39%)		3.7×10^4 5.7×10^3 1.8×10^3	293	81.3	1.2×10^7

^a All measurements were obtained in argon degassed 20% MeOH/20 mM Tris:10 mM NaCl buffer pH 7.2. Degassing the samples involved bubbling with argon gas via a needle inserted through a vented septum cap for 20 minutes and sealing prior to measurements. This method however does not insure that all oxygen has been removed from the sample.

^b Indicates the $[\text{DNA}]_{\text{bp}}$ concentration is 6 "times" (x) the concentration of the compound (i.e. $[\text{DNA}]_{\text{bp}}/[\text{ANM}] = 6$).

^c TA lifetimes of all compounds in solution are composed of 2 components.

^d In the presence of DNA the lifetimes consist of 3 components.

^e Median lifetimes were calculated according to eqn. 3.7.

and Re10An, respectively, in degassed solution taken at delay times ranging from 0 - 0.36 μ s after laser excitation. An instrumental emission correction factor was implemented in the spectra for Re10An and caused an over-correction to occur at zero time after the laser pulse. This can be observed by the multiple intense peaks displayed at 0 time that resemble AN emission bands in Figures 3.25a and b, and should not be considered as triplet species. Similar to ANMOD, the transient spectra for the CQ complexes in solution exhibit sharp intense peaks at 426 nm and broad shoulders in the 400 to 415 nm region which are characteristic of the AN $T_2 \leftarrow T_1$ transition. The region from 340 to 390 nm would normally show a broad absorption assigned to the $d\pi(\text{Re}) \rightarrow \pi^*(\text{bpy})$ MLCT state of the Re-An complexes. Its absence is in accordance with the quenching of this state in solution by intramolecular energy transfer to AN. Decays for the 426 nm transients in the Re-An complexes obey double-exponential kinetics with values of $\tau_1 = 17 \mu$ s (57%) and $\tau_2 = 84 \mu$ s (43%) for Re6An, and $\tau_1 = 28 \mu$ s (46%) and $\tau_2 = 100 \mu$ s (54%) for Re10An (see Table 3.10). Median lifetimes, $\langle \tau \rangle$, were calculated from the individual component lifetimes according to eqn. 3.7, and are listed in Table 3.10. The median lifetimes indicate Re10An has the longest-lived overall transient species at 67 μ s, Re6An has the second longest at 46 μ s, and ANMOD possesses the shortest overall lifetime of 36 μ s.

Intensities of the 426 nm transient absorption for ANMOD, Re10An and Re6An were measured relative to the actinometer ReBz, and were calculated using the formula:

$$\text{TA Intensity} = \left\{ \left(\text{TA Int. Sample} / \text{fr. } h\nu_{\text{sample}} \right) / \left(\text{TA Int. ReBz} / \text{fr. } h\nu_{\text{ReBz}} \right) \right\} \quad \text{Eqn. 3.9}$$

where TA Int.Sample is the experimentally measured maximum intensity of the sample at 426 nm after laser excitation, TA Int. ReBz is the experimentally measured maximum intensity of ReBz at 370 nm after laser excitation. fr. $h\nu_{\text{sample}}$ and fr. $h\nu_{\text{ReBz}}$ are the fractional absorbances of the sample and ReBz, respectively, determined from their optical densities at 355 nm with the following equation:

$$\text{fr. } h\nu = \left(1 - 10^{(-\text{Absorbance}@355\text{ nm})} \right) \quad \text{Eqn. 3.10}$$

Table 3.11. Relative Transient Absorbance Intensities at 426 nm.^a

Compound →	No DNA			6x DNA		
	ANMOD	Re10An	Re6An	ANMOD	Re10An	Re6An
TA Intensity ^b @ 426 nm	0.410 ± 0.064	1.133 ± 0.10	0.743 ± 0.076	0.0494 ± 0.002	0.160 ± 0.021	0.211 ± 0.025

^a Measurements performed in argon degassed 20% MeOH/Buffer solutions with laser excitation at 355 nm (10 ns fwhm, 5 mJ/pulse). Optical densities for all samples were matched as closely as possible prior to measurement and were generally in the range of 0.3 - 0.5.

^b Relative intensities were determined according to eqn. 3.9 which is repeated below and the individual terms are defined in the text: TA Intensity = $\left\{ \left(\text{TA Int. Sample} / \text{fr. } h\nu_{\text{sample}} \right) / \left(\text{TA Int. ReBz} / \text{fr. } h\nu_{\text{ReBz}} \right) \right\}$ where

$\text{fr. } h\nu = \left(1 - 10^{(-\text{Absorbance} @ 355\text{nm})} \right)$. ReBz is an actinometer with a known extinction coefficient for its transient absorption peak at 370 nm. The numbers with ± preceding them indicate the amount of variance in the data.

Table 3.11 lists values obtained for the relative intensities of the 426 nm transients observed for ANMOD, Re10An and Re6An in degassed 20% MeOH/buffer solution and in the presence of 7.5x DNA. For the solution samples it is clear that Re10An displays the highest triplet intensity of 1.13 which is 2.75 times larger in value than the triplet intensity of ANMOD (0.41). Re6An exhibits an intensity of 0.743 for the 426 nm transient which is 1.8 times larger than the value for ANMOD and only 0.66 as large as the value for Re10An.

Transient absorption spectra for ANMOD in the presence of 7.5x DNA at delay times ranging from 0 to 0.80 μ s after laser excitation are displayed in Figure 3.23b. The spectra are nearly identical to the spectra of ANMOD alone in solution with a sharp peak at 426 nm and a lower intensity broad shoulder centered at 400 nm. The intensity of the 426 nm transient for ANMOD in the presence of 7.5x DNA, listed as 0.05 in Table 3.11, is considerably lower in yield than that observed for ANMOD in solution. Similar behavior has been observed for the complex 9-(aminomethyl)anthracene (9-AMAC)²⁷ when intercalated into calf thymus DNA. Kumar suggested that quenching of the triplet when AN was intercalated into DNA indicated either that the singlet excited state was quenched directly to form the ground state without intervention of the triplet or that the triplet was quenched faster than it was produced.²⁷ The 426 nm transient for ANMOD in the presence of 7.5x DNA decays by triple-exponential kinetics with $\tau_1 = 8.5 \mu$ s (55%), $\tau_2 = 82 \mu$ s (23%), and $\tau_3 = 392 \mu$ s (22%) (Table 3.10).

Figures 3.24b and 3.25b illustrate transient absorption spectra for Re6An and Re10An, respectively, in the presence of $[\text{DNA}]_{\text{bp}}/[\text{Re}] = 7.5$ at delay times ranging from 0 to 0.36 μ s after laser excitation. Unlike the spectra for the complexes alone in solution, a considerable amount of MLCT absorption is observed in the 340 to 390 nm region for the complexes in the presence of 7.5x DNA. Decays of the ³MLCT* transients at 370 nm were fit to single-exponential kinetics giving lifetimes of 81 ns for Re6An and 76 ns for Re10An (see Table 3.10). These lifetimes are similar to those obtained from the time-correlated

single photon counting method listed in Table 3.7. The appearance of the MLCT transient for the Re-An complexes in the presence of DNA is attributed to a reduction in the $^3\text{MLCT}^*$ excited state energy transfer to $^3\text{AN}^*$ by way of the electron-exchange mechanism (E_{NTee}). Coinciding with the appearance of the $^3\text{MLCT}^*$ transient species is a definite reduction in the yield of the $^3\text{AN}^*$ transient in the 426 nm region. The triplet peaks are considerably broadened and less well-defined than the solution spectra. Comparing the relative triplet intensities from Table 3.11 for ANMOD, Re10An and Re6An in the presence of $7.5\times [\text{DNA}]_{\text{bp}}$ indicates that the CQ complexes show considerably larger triplet intensities than ANMOD. Re6An exhibits the largest value at 0.21, which is 4.3 times higher than ANMOD, while Re10An displays a slightly lower yield at 0.16, which is 3.2 times larger than ANMOD. This would indicate that there is still some energy transfer occurring from the $^3\text{MLCT}^*$ to $^3\text{AN}^*$ even when the CQ complexes are bound to DNA. If the triplet intensities in the presence of DNA are compared to the intensities in solution it is clear that both the complexes and ANMOD experience reductions in their triplet yields when in the presence of DNA. The intensities for ANMOD, Re10An and Re6An in the presence of $7.5\times [\text{DNA}]_{\text{bp}}$ are 12 %, 14 % and 28 %, respectively, of their values in solution. These correspond to reductions of 88 %, 86 % and 72 % for ANMOD, Re10An and Re6An, respectively, upon going from solution to $[\text{DNA}]_{\text{bp}}/[\text{Re}] = 7.5$.

The decays for the 426 nm transient of the CQ complexes in the presence of DNA were fit to triple-exponential kinetics and are listed in Table 3.10. Similar to the model they exhibit a relatively short-lived species, an intermediate-lived species and a long-lived species, but overall the lifetimes are longer than those of the model. The complexes show more of the longest lived species (~ 39 %), than the model (22 %), and about half as much of the short-lived species (~ 26 %) as ANMOD (55 %). In general, all the lifetimes are considerably lengthened as compared to when in the absence of DNA.

Discussion

Photophysics of Re-An Complexes

General UV-visible and emission characteristics

The UV-visible absorption spectra of the Re-An CQ complexes are an exact superposition of the combined absorption spectra of the model compounds ReCH₂B and ANMOD, as represented in the overlay of Figure 3.7. The three structured peaks in the 350 to 388 nm region are characteristic of the AN $S_0 \rightarrow S_1 \pi - \pi^*$ transitions and are elevated by the underlying weak $d\pi(\text{Re}) \rightarrow \pi^*(\text{bpy})$ MLCT transitions. The peak at 320 nm is almost exclusively attributed to $\pi - \pi^*$ (bpy) while the higher energy transitions are summations of AN, diimine and intraligand transitions. The fact that the transitions for the component chromophores in the Re-An complexes retain their shapes and positions indicates that there is at best only weak electronic interaction between the Re and AN moieties within the complexes. Therefore the energy levels of the ground and excited states of the complexes can be considered to be equal to the energies of the individual model compounds, as illustrated in Figure 3.2.

The bands in the steady-state emission spectra of the CQ complexes also retain their positions relative to the spectra for the Re and AN models (Figure 3.11a). The resolved vibronic bands in the 380 to 500 nm region of the complexes are a superposition of the $S_1 \rightarrow S_0$ fluorescence transitions for ANMOD, while the broad unstructured emission envelope centered at 590 nm matches the model ReCH₂B $^3\text{MLCT}^*$ transition. This strongly suggests that the emission spectra of the CQ complexes emanate from the same excited states as the model compounds.

In contrast to the steady-state emission spectra of the models, the spectra for the CQ complexes are drastically reduced in intensity as evidenced in Figure 3.11b and Table 3.4. Additionally the emission lifetimes for the Re-An complexes are sharply reduced in length and exhibit multi-dimensional decay behavior in contrast to the single-exponential decays of

the respective models (see Table 3.7 for Re and Table 3.9 for AN). The extremely low quantum yields of emission and short lifetimes displayed by the CQ complexes clearly demonstrate the occurrence of quenching phenomena for both Re and AN.

TT E_NT quenching of MLCT state

As mentioned in the introduction to this chapter, it has been established from previous studies that AN quenches the Re ³MLCT* state by triplet-triplet (TT) exchange energy transfer^{1*}, labeled E_NT_{ee} in Figure 3.2. The reaction, shown below, involves a double electron-transfer between the excited ³MLCT* state to ground state AN, producing the ³AN* and simultaneously reducing emission from the ³MLCT* (see Figure 3.3 for the electron-exchange mechanism).



The (bpy)Re(CO)₃ chromophore is known to react from its lowest-lying ³MLCT* state,^{160,110} which lies ~20 kcal/mol¹²⁹ below the ¹AN* state¹⁵⁷ and ~14.3 kcal/mol above the ³AN* state.^{161,162,163} Energy transfer from the ³MLCT level of Re to the ¹AN* level would be highly endothermic ($\Delta E_{\text{E}_{\text{NT}}} = + 0.87 \text{ eV}$) while transfer to the ³AN* level is exothermic ($\Delta E_{\text{E}_{\text{NT}}} = - 0.62 \text{ eV}$) ($\Delta E_{\text{E}_{\text{NT}}}$ values were determined from the differences, in eV, of the corresponding energy levels for the respective chromophores). Energy transfer from the Re ¹MLCT* state to ³MLCT*, while also exothermic, is too slow to compete with the rate of isc for this state (~10¹² s⁻¹)¹⁶⁴.

The rate for exchange energy transfer (E_NT_{ee}), as determined by Dexter,¹⁰³ is dependent on (1) the exponential of the distance (r) between the donor (M*) and acceptor (Q) and (2) the spectral overlap integral (J), which is the overlap of the emission spectrum of M* and the absorption spectrum of Q according to eqn. 3.10.

$$k_{\text{E}_{\text{NT}}} = \frac{2\pi}{h} \exp(-2r/l) J \quad \text{Eqn. 3.10}$$

where r is the distance between donor and acceptor molecules and l is the van der Waals radius of the donor-acceptor pair. Figure 3.26a illustrates the near complete overlap between the Re $^3\text{MLCT}^*$ emission band and the AN $T_0 \leftarrow S_0$ absorption bands.¹⁶⁵

The transient absorption studies clearly show a higher production of the $^3\text{AN}^*$ state within the Re-An complexes relative to the model (Table 3.11). Anthracene and its derivatives are known to exhibit large intersystem crossing efficiencies, with quantum yields (ϕ_{isc}) in the range of 0.70 for anthracene and 0.65 for 9-methylantracene.^{157,159,166,167} The elevated production of $^3\text{AN}^*$ in the Re-An complexes, above that produced in AN alone, coupled with the dramatic reduction of $^3\text{MLCT}^*$ emission, would support an energy transfer mechanism from a triplet donor to AN.

Due to an exponential distance dependence the efficiency of exchange energy transfer rapidly diminishes as the donor-acceptor separate beyond the sum of their van der Waals radii. Although the $^3\text{MLCT}^*$ state of all the Re-An complexes is highly quenched in solution (very low QY's), the efficiency of quenching of the emission from this state appears to follow the order $\text{Re3An} > \text{Re6An} > \text{Re8An} > \text{Re10An}$ (Table 3.4). This decrease in quenching parallels the increase in length of the linker chain between the acceptor Re and the donor AN in the complexes.

The median lifetimes of the complexes in solution follow similar trends to the quantum yields. MLCT quenching rates ($k_{q\text{Re}}$) in the Re-An complexes were calculated using equation 3.11:

$$k_{q\text{Re}} = (1/\langle \tau \rangle_{\text{ReAn}}) - (1/\langle \tau \rangle_{\text{ReCHB}}) \quad \text{Eqn. 3.11}$$

where $\langle \tau \rangle$ values are the $^3\text{MLCT}^*$ median lifetimes of the Re-An and ReCH_2B complexes, respectively. The values for $k_{q\text{Re}}$ are listed in Table 3.12 (also listed are the rates for quenching of the $^1\text{AN}^*$ state ($k_{q\text{AN}}$) which will be discussed in the following section). Focusing on $k_{q\text{Re}}$, the overall quenching rates follow the order $k_{q\text{Re}} \text{Re6An} > \text{Re8An} > \text{Re3An} > \text{Re10An}$. Re3An shows a slower rate due to the presence of a long-lived

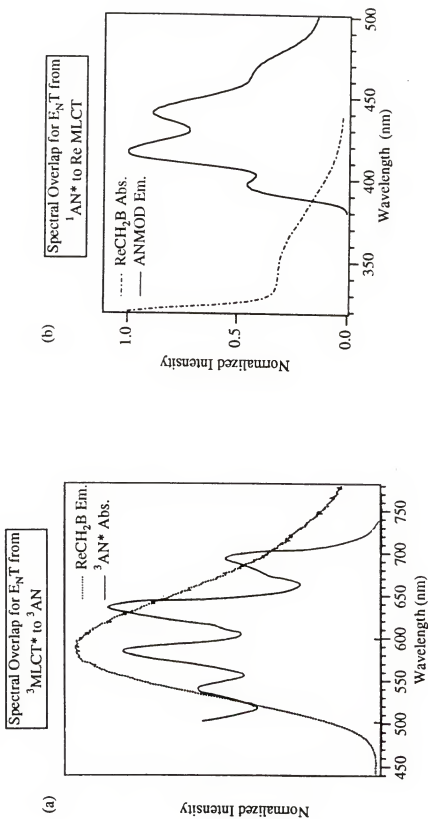


Figure 3.26. (a) Overlay of the 3AN absorption transitions normalized to the Re $^3MLCT^*$ emission band of $ReCH_2B$ showing the large overlap between the two spectra. The 3AN absorbance spectrum is from D. F. Evans, *J. Chem. Soc., 1957*, 1351, on 9-methylanthracene in chloroform at 76 atm. (b) Normalized overlay of the Re $MLCT$ absorption spectrum (320 - 440 nm) of $ReCH_2B$ with the spectrum of the $^1AN^*$ fluorescence transitions (380 - 500 nm) of ANMOD.

Table 3.12. Rate Constants for $E_N T$ in Re-An Complexes.

Complex	No DNA		6x DNA	
	k_{qRe}^a (s ⁻¹)	k_{qAN}^b (s ⁻¹)	k_{qRe}^c (s ⁻¹)	k_{qAN}^d (s ⁻¹)
Re10An	1.4×10^8	1.5×10^9	5.8×10^6	7.0×10^8
Re8An	2.9×10^8	1.2×10^9	8.8×10^6	6.6×10^8
Re6An	3.03×10^8	2.9×10^9	6.0×10^6	1.42×10^9
Re3An	2.1×10^8	6.2×10^8	5.3×10^7	4.9×10^8

a Calculated from $k_{qRe} = (1/\langle\tau\rangle_{EmReAn}) - (1/\langle\tau\rangle_{EmReHB})$ using the ${}^3MLCT^*$ median lifetimes listed in Table 3.7. This is the rate for quenching of emission from the Re ${}^3MLCT^*$ state depicted in eqn. 3.2.

b Calculated from $k_{qAN} = (1/\langle\tau\rangle_{EmReAn}) - (1/\langle\tau\rangle_{EmANMOD})$ using the ${}^1AN^*$ median lifetimes listed in Table 3.9. This is the rate for quenching of fluorescence from the ${}^1AN^*$ state depicted in eqn. 3.3.

c Rate constant was calculated from the k_{qRe} eqn. in note (a) using the respective $\langle\tau\rangle$ values in the presence of $[DNA]_{bp}/[Re] = 6$.

d Rate constant was calculated from the k_{qAN} eqn. in note (b) using the respective $\langle\tau\rangle$ values in the presence of $[DNA]_{bp}/[Re] = 6$.

impurity which could not be completely removed prior to measurement. If the rates are calculated in the same manner except with the exclusion of τ_3 from Table 3.7 (which contributes minimally to the median lifetimes in solution), the quenching rates become $k_{qRe} Re3An (7.6 \times 10^8 \text{ s}^{-1}) > Re6An (4.85 \times 10^8 \text{ s}^{-1}) > Re8An (3.55 \times 10^8 \text{ s}^{-1}) > Re10An (1.55 \times 10^8 \text{ s}^{-1})$. These corrected rates clearly show a strong correlation between the rate of quenching of the $^3MLCT^*$ state and the length of the flexible tether between Re and AN in the CQ complexes. Overall the quenching rates reflect the behavior observed in the quantum yield studies and provide direct evidence of the distance dependence of the E_{NT} mechanism.

Importantly, the individual component lifetimes (τ_1 , τ_2 , τ_3) of the $^3MLCT^*$ state in the complexes (Table 3.7) give a more detailed picture of the differences in energy transfer kinetics between the complexes. The lifetimes of Re6An and Re3An are almost completely dominated (97% and 94%, respectively) by a very short-lived component (τ_1) that has a lifetime of less than 2 ns and a decay rate that is on the order of $5 - 9 \times 10^8 \text{ s}^{-1}$. This short-lived component has been assigned to $^3MLCT^*$ states which are rapidly quenched after excitation, and occurs within complexes where the Re and AN chromophores are folded over in close proximity to each other. In contrast, the lifetimes of Re10An and Re8An, although they do exhibit small percentages of this short-lived component (τ_1), are dominated by a slightly longer-lived species (τ_2) (contributing 86% and 61%, respectively) that has a lifetime of 7 ns for Re10An and 4 ns for Re8An with decay rates of $1.5 \times 10^8 \text{ s}^{-1}$ and $2.8 \times 10^8 \text{ s}^{-1}$, respectively. This component (τ_2) is considered to emanate from CQ complexes that are in conformations intermediate between tightly folded over and fully extended. Thus the results indicate that in solution both Re3An and Re6An are able to attain the closely folded conformation necessary for efficient E_{NT} more easily than Re8An and Re10An. The difference in folding capabilities lies in the length of the linker chains separating the Re and AN chromophores. As more methylene linkages are added to the chain, more degrees of rotational freedom are available therefore increasing the number of

orientations of the AN ligand. Only a small percentage of Re10An molecules and slightly more of Re8An complexes appear to achieve a tightly folded conformation, and instead seem to remain in an intermediate conformation where Re and AN are not as close together resulting in slightly slower E_NT quenching rates. It is important to note that all of the complexes show a fractional percentage of a species (τ_3) that has a lifetime on the order of unquenched Re emission. The presence of this component would indicate that the lifetimes are originating from the same MLCT state as the model.

Energy transfer quenching of AN : Coulombic mechanism

A second type of quenching phenomenon appears to take place in the Re-An complexes evoking a sharp reduction of the $^1AN^*$ fluorescence as evidenced from the steady-state emission spectra (Figure 3.12). Since at 340 nm AN absorbs approximately 50% of the excitation light, and its fluorescence spectrum partially overlaps the Re MLCT emission, it is possible for energy from $^1AN^*$ to transfer to lower-lying MLCT excited states. The most probable mechanism would involve E_NT from $^1AN^*$ to produce the $^1MLCT^*$ state, which lies ~ 0.68 eV below the $^1AN^*$ level, followed by rapid relaxation of the $^1MLCT^*$ to $^3MLCT^*$. This would be considered singlet-singlet energy transfer in which spin is conserved and consequently is an allowed transition by either coulombic or electron-exchange energy transfer. An overlay of the absorption spectrum for ReCH₂B (acceptor) with the fluorescence spectrum of ANMOD (Figure 3.26b) illustrates their region of spectral overlap (J), which is a requirement of either mechanism.

Direct evidence for the occurrence of energy transfer from AN^* to Re is provided from excitation emission spectra of the Re-An complexes. Emission derived solely from the $^3MLCT^*$ state was monitored (590 nm) while excitation of an optically dilute solution of the Re-An complex was scanned from 320 to 450 nm. This was compared to an excitation spectrum, obtained under the same conditions, of the model ReCH₂B which does not contain an energy donor. The excitation emission spectra normalized to the respective absorption spectra for ReCH₂B, Re10An and Re6An in degassed 30% MeOH/Tris buffer

Excitation Emission Spectra Normalized to Absorption Spectra

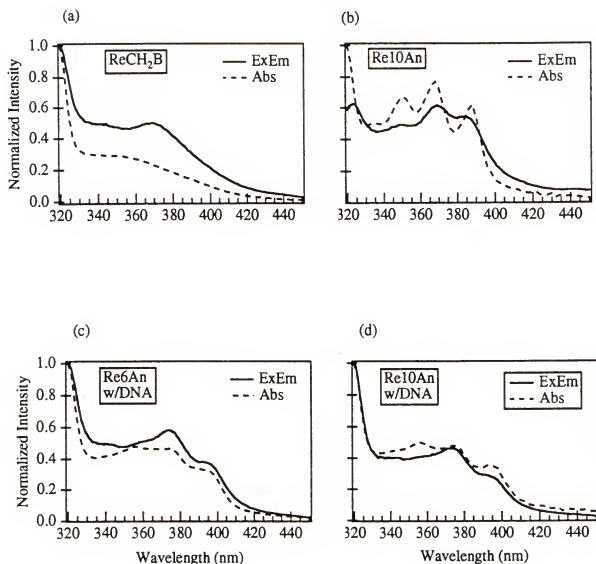


Figure 3.27. Excitation emission spectra for (a)ReCH₂B, (b) Re10An, (c) Re10An with 6x [DNA]_{bp} and (d) Re6An w/ 6x [DNA]_{bp} normalized to their absorption spectra. In the excitation emission experiments samples were excited from 320 to 500 nm and emission monitored at 600 nm where light is emitted exclusively by the Re chromophore. All measurements were done in degassed 20% MeOH/buffer solutions pH 7.2.

are displayed in Figure 3.27(a-d). In the absence of the AN energy donor, the excitation spectrum of the Re chromophore resembles its MLCT absorption spectrum, as seen for ReCH₂B (Figure 3.27a). For the Re-An complexes, if energy initially supplied to AN is transferred to the Re MLCT, then it will be signaled by peaks in the spectrum which resemble the AN absorption transitions. Again, since the emission is monitored in a region where only ³MLCT* emits, then it indicates the observed spectral peaks are due to energy transfer from ¹AN* to Re. The emission excitation spectra for Re10An in solution (b) and Re10An and Re6An in the presence of 6x [DNA]_{bp} (d & c, respectively) normalized to their absorption spectra are shown in Figure 3.27. It is clearly evident that the excitation spectra for the CQ complexes contain peaks that closely resemble the AN absorption transitions, and which are not present in the excitation spectrum for the model (3.27a). This is unequivocal evidence for the occurrence of energy transfer from ¹AN* to the Re MLCT. Notice the excitation spectra for the CQ complexes in the presence of DNA are red-shifted similar to their absorption spectra. In the absence of DNA the ³MLCT emission of the CQ complexes is very weak due to E_{NT} to ³AN*, thus the excitation emission signal to noise ratios are poor and the spectra show slight distortions as evidenced in 3.27b.

Table 3.12 lists the quenching rates of the ¹AN* state (k_{qAN}) in the Re-An complexes, which were calculated using the equation,

$$k_{qAN} = (1/\langle \tau \rangle_{ReAN}) - (1/\langle \tau \rangle_{ANMOD}) \quad \text{Eqn. 3.12}$$

where $\langle \tau \rangle$ values are the median ¹AN* fluorescence lifetimes of the Re-An complexes and ANMOD, respectively. Re3An, as mentioned above, possesses a unusually slow rate which is likely due to the presence of impurities in the sample. The fastest quenching rate is displayed by Re6An ($k_{qAN} = 2.9 \times 10^9 \text{ s}^{-1}$) while Re8An and Re10An have nearly equivalent rates ($1.2 \times 10^9 \text{ s}^{-1}$ and $1.5 \times 10^9 \text{ s}^{-1}$, respectively) which are approximately one-half the value for Re6An. The data show trends similar to the ³MLCT* quenching rate constants in that the shorter-chained Re6An possesses the most efficient energy transfer quenching. The results are more ambiguous for the other complexes and this could be

caused by interference from slight amounts of impurity. More importantly, comparing the k_{qAN} values to the k_{qRe} values in solution it is clear the $^1AN^*$ E_NT quenching occurs on a time scale which is nearly an order of magnitude faster than the $^3MLCT^*$ quenching rates. The energy gap for the E_NT processes, ΔE_{E_NT} , calculated from the equation $\Delta E_{E_NT} = E_A - E_D$ where E_A is the energy of the excited state of the acceptor and E_D is the excited state energy of the donor, was calculated for the quenching of the $^3MLCT^*$ by $^3AN^*$ (-0.62 eV) and quenching of $^1AN^*$ by the $^1MLCT^*$ (-0.68 eV). The ΔE_{E_NT} values are very close for the two processes, although ΔE_{E_NT} for the latter mechanism is slightly more exothermic. However, the difference is not large enough to explain the faster quenching rates of $^1AN^*$. The most probable cause for the higher E_NT rates of k_{qAN} versus k_{qRe} , likely lies in the mechanism through which the process occurs. Recall that the rate of exchange energy transfer (E_NT_{ee}), as shown in eqn. 3.10, depends on the exponent of the distance (r) between donor and acceptor, in which case the efficiency of E_NT_{ee} falls off substantially beyond a separation distance of 10 Å between donor and acceptor molecules. The rate of Coulombic energy transfer (E_NT_c) has an inverse sixth dependence ($1/r^6$) upon the distance (r) between the donor and acceptor molecules (eqn. 1.29, Chapter I). This is due to the fact that the mechanism occurs through a long-range dipole-dipole interaction. Thus energy transfer by the Coulombic mechanism can occur over much larger distances (up to 100 Å) than by exchange transfer. Taking this into consideration when comparing k_{qAN} and k_{qRe} , it is evident that within the same complexes $^1AN^*$ fluorescence is quenched at a rate that is nearly an order of magnitude faster than the rate of quenching of $^3MLCT^*$ emission. This would strongly suggest that energy transfer occurs from $^1AN^*$ to the Re MLCT by way of the Coulombic mechanism.

DNA binding studies

Having established the basic photophysical properties of the CQ complexes in solution, the changes in their properties with the addition of increasing amounts of CT DNA were monitored and used in determination of binding coefficients. A wide variety of

methods are available for the study of the interactions of small molecules with DNA, however the purpose of this study was to take advantage of the readily accessible light absorbing and emitting properties of these CQ complexes and, in particular, their energy transfer properties. The sensitivity of energy transfer to a local environment serves as a powerful tool for probing interactions of small molecules with nucleic acids. The optical methods utilized in characterization of the DNA interactions of the Re-An complexes included UV-visible absorption, steady-state and time-resolved emission and transient absorption spectroscopies. Of these different physical methods all except the first mentioned can directly measure the changes in the energy transfer properties of the complexes with DNA. Two types of energy transfer were available for study in the Re-An complexes due to unavoidable direct excitation of both chromophores. While Coulombic energy transfer from $^1\text{AN}^*$ to Re complicated the present study, excitation of the AN chromophore provided additional useful information regarding the binding of these complexes.

Absorption titrations

The manifestation of hypochromism and red-shifts in the long-wavelength UV-visible absorption bands of AN upon addition of DNA to solutions of the Re-An complexes provides direct evidence of strong interaction with the nucleic acids. As discussed in Chapter I, the extent of hypochromism depends on the inverse cube of the distance between interacting chromophores since it involves coupling of the transition dipole moment of the absorbing chromophore with the induced dipoles of neighboring chromophores.⁷⁶ Only molecules that are within close proximity to each other and stacked in a parallel array will exhibit this effect, therefore it is useful in determining the degree of order between the CQ complexes and the DNA helix. The binding constants determined from the absorption titrations according to method I (Appendix A) are listed for comparison in Table 4.13 along with binding parameters from the steady-state emission titrations. The K_b 's from method I for the Re-An complexes are within range of values of K_b determined through the same

Table 3.13. DNA Binding Parameters for Re-An Complexes and Model^a

Compound	K _b (M ⁻¹)		Site Size (n)		Cooperativity Const. (ω) II
	Method I (Absorptn. Titratn.)	Method II (Emission Titratn.)	Method III (Emission Titratn.)	Base Pairs II III	
Re3An	1.6 x 10 ⁴	3.0 x 10 ⁵	1.5 x 10 ⁵	2.5 3.6	0.05
Re6An	3.5 x 10 ⁴	4.8 x 10 ⁵	2.5 x 10 ⁵	2.8 3.7	0.09
Re8An	4.9 x 10 ⁴	8.0 x 10 ⁵	5.7 x 10 ⁵	2.8 3.1	0.10
Re10An	5.1 x 10 ⁴	6.8 x 10 ⁵	2.9 x 10 ⁵	2.6 3.4	0.05
ANMOD	4.7 x 10 ⁴	6.5 x 10 ⁵	6.5 x 10 ⁵	2.1 2.3	0.001

^a Specific information concerning experimental conditions and description of methods are listed with the corresponding tables from which the data was extracted: method I data see Table 3.3, for data from methods II & III see Table 3.6.

method by Kumar for 9-AMAC ($1.5 \pm 0.5 \times 10^4 \text{ M}^{-1}$)²⁷ and by Barton et al. for a series of mixed-ligand Ru^{II} complexes.³³ Within the series of Re-An complexes the trends in binding strength by method I appear to follow the order $K_b \text{ Re10An} \geq \text{Re8An} > \text{Re6An} > \text{Re3An}$, which parallels the length of linker chains from longest to shortest. This could indicate that the longer-chained complexes have less steric bulk when intercalating in-between base pairs of the DNA helix since the Re chromophore can extend farther away from the AN chromophore. The flat aromatic AN chromophore would have increased freedom to imbed more deeply into the hydrophobic environment of the helix therefore enabling greater overlap of its polycyclic rings with the DNA base pairs. Notice the K_b 's for Re8An and Re10An are approximately equivalent to K_b for ANMOD which does not contain sterically hindering appendages. Although the binding constants from method I are about an order of magnitude lower than the values found from the emission titrations, they do reflect similar trends in relative behavior among the complexes. That is Re10An, Re8An and Re6An consistently show stronger interactions (greater changes in light absorbing and emitting properties) with calf thymus DNA than does Re3An. This observation is important when considering the nature of the changes observed in the emission studies and will be elaborated upon in the discussion of the latter data. The depressed K_b values of method I are likely due to the nature of the binding analysis since the equation used for method I does not take into consideration effects caused by interactions between neighboring chromophores. It is most accurate at very high concentrations of DNA where restrictions on the number of potential binding sites can be neglected. It should be emphasized that the values obtained from the absorption titrations contain an inherent degree of error since they are based on a limited number of measurements. Additionally, interference from the underlying MLCT band at 388 nm, although considered to be minimal at this wavelength, might give falsely elevated absorption values. For comparison to other methods as well as a test of accuracy of the present analysis, it would be useful to apply the other binding methods to the absorbance data.

Emission DNA titrations

Results of the emission DNA titrations showed dramatic increases in $^3\text{MLCT}^*$ luminescence, substantial lengthening of the $^3\text{MLCT}^*$ emission lifetimes and broadening and red-shifts in the $^1\text{AN}^*$ fluorescence bands for the CQ complexes in the presence of DNA. Taken as a whole the data provide unequivocal evidence that the complexes bind strongly to the double helix. Individually the studies reveal a microscopic view of the macro-interactions between the different complexes and the biopolymer.

Re10An, Re8An and Re6An all showed profound increases in their ϕ_{EmRe} with addition of DNA while for Re3An only small increases of ϕ_{EmRe} were detected (Table 3.5). At saturation ($[\text{DNA}]_{\text{bp}}/[\text{Re}] = 6$) the order of emission yields from greatest to lowest was $\text{Re10An} \geq \text{Re6An} > \text{Re8An} \gg \text{Re3An}$. This was also the order of the lengths of median lifetimes of the complexes in the presence of 6x DNA (Table 3.7). However, if the overall *enhancements* in going from free to bound forms are considered then a different picture emerges. The largest enhancement in ϕ_{EmRe} is seen for Re6An at 20 times, followed by Re8An at 8.8 times, Re10An at 7 times and Re3An at 5 times increase. These values are comparable to the enhancements observed in the median lifetimes for Re in the complexes which are $\text{Re6An} (20\text{x}) > \text{Re8An} (17\text{x}) > \text{Re10An} (10\text{x}) > \text{Re3An} (3.6\text{x})$. This reflects the differences in efficiency of intramolecular quenching of the $^3\text{MLCT}^*$ between the bound and free forms of the complexes. Re6An and Re3An both display the most efficient exchange energy transfer (E_{NTee}) quenching in solution (lowest quantum yields). In the presence of DNA this energy transfer mechanism is effectively reduced for Re6An resulting in a large increase in emission from the $^3\text{MLCT}^*$ state to a level that is approximately equal to that of Re10An. Whereas Re3An does not experience any appreciable decrease in this energy transfer sink which could indicate either that (1) the complex can intercalate into DNA but binding does not attenuate the E_{NTee} mechanism because of the short linker chain between Re and AN or (2) the complex does not intercalate into the DNA helix but rather binds along the surface of the polymer in a mode

that does not drastically disturb the quenching route. If the above evidence is combined with the DNA absorbance titration results it would appear that Re3An has a significantly weaker interaction with the DNA bases than the other complexes due to the steric bulk of the nearby Re chromophore. Based on the small amount of hypochromism of the AN absorbance bands and the shift of the emission lifetimes from a very short-lived species (1.1 ns, 94 %) assigned to quenched Re to an intermediate-lived species (20 ns, 55 %) that is still substantially shorter in lifetime than the unquenched model, the most probable binding mode for Re3An would be a partially intercalated surface-bound complex with DNA. The linker chain in this complex does not contain the additional amide linkage that the other CQ complexes possess, which can provide H-bonding contacts with the DNA groove, and the large bulky Re chromophore may create steric contacts with the ds polymer. Even in the fully extended form of the Re3An complex, that would result from intercalation of the AN chromophore, the separation between Re and AN is at most 7 Å which is within the distance requirement for efficient E_NT to occur.

DNA binding constants from emission titrations

Parameters for binding of the CQ complexes to DNA determined from the steady-state emission titration data by the two different analyses described in Appendix A as method II and method III are listed in Table 3.13. Similar to the binding constants determined by method I (absorption titrations), although not following exactly the same order, the K_b 's from methods II and III decrease in the order $K_b \text{ Re8An} > \text{Re10An} > \text{Re6An} > \text{Re3An}$. The binding strength of Re8An according to these analyses is consistently larger than the binding strengths of the other complexes, however the K_b 's for Re10An and Re6An are only slightly lower in value. The binding site sizes (n) are consistent among the complexes where n ranges between 2.5 - 4 base pairs depending on the method of analysis. The co-operativity parameter, ω , which takes into account any kind of positive or negative interaction between the bound ligands, is less than one for all the complexes which indicates anti-co-operativity. However, as the value of ω becomes

increasing less than one (i.e., as ω approaches zero) its contribution to the binding equation is reduced.¹⁶⁸ Therefore since the ω values for the Re-An complexes are considerably lower than one, their anti-co-operative behavior is considered to be small. The extracted binding parameters obtained from the fits of the Re-An complexes are within the ranges found for other anthracene-based intercalating compounds^{27,142,143,151,169,170} and classically known intercalators such as ethidium bromide,^{21,48} propidium^{48,71} and the anthracycline antibiotics.³⁰ Examples of experimentally determined binding parameters for the above mentioned DNA intercalating compounds are listed in Table 3.14 with structures for the numbered complexes shown in Figure 3.29. The differences in binding parameters among structurally similar compounds (listed in Table 3.14), in some cases, are a result of the use of different binding analyses, fitting of different regions of the binding curves and/or differences in ionic strength of the solutions. A dependence of K_b on $[Na^+]$ has been studied for several of the listed compounds in Table 3.14 and, in general, the binding affinities decrease as the salt concentrations are raised.^{48,71} At low salt concentrations, as well, the association of the ligands with DNA have been found to depend primarily on the charge of the intercalator.^{48,71,151} In comparing the value of K_b determined for the model compound ANMOD in Table 3.13, which is approximately 8 times larger than K_b obtained for the structurally similar 9-AMAC, it might appear that salt effects play a role in differences in binding strengths for these compounds. (It is unlikely that the additional methyl substituent would have a significant influence on the binding constant.) However, the largest contributor to the difference between the binding results obtained from this study on ANMOD and those obtained by Kumar on 9-AMAC is most likely due to the differences in analyses used and error involved in the fitting of the data.

Considering the similarity in binding parameters for the Re-An complexes to binding parameters of other anthracene derivatives listed in Table 3.14, it would be reasonable to extrapolate some of the binding characteristics of the latter DNA intercalators to the binding of the Re-An complexes. The experimental evidence strongly suggests that

Table 3.14. Literature Binding Parameters for DNA Intercalators with Calf Thymus DNA.

Compound	K_b^a	n	ω	$[Na^+]/mM$	Charge pH ~7	Binding ^b Eqn.	Ref.
1	$2.2 \pm 1 \times 10^7$	6.2		5	+3	see Ref.	169
2	5.72×10^4	2.8		Pipes Buffer	+1	2	170
3	1.95×10^6	2.0	NA	19	+2	4 or 5	143
4	1.0×10^5	1.5	0.14	100	+2	3	141
9-AMAC	$1.5 \pm 0.5 \times 10^4$			50	+1	1	27
9-AMAC	7.8×10^4	4.8 ± 1		50	+1	2	27
Bisantrene	9.0×10^6	0.9	0.11	100	+2	3	141
Ethidium	2.5×10^6	5.0		15	+1	6	21
Ethidium	9.5×10^5	2.0		216	+1	1	71
Ethidium	9.1×10^4	5.0		500	+1	6	21
Ethidium	2.9×10^4	2.0		500	+1	4	48
Propidium	1.9×10^6	2.0		216	+2	1	71
Propidium	3.0×10^5	2.0	0.2	200	+2	5	48
Propidium	2.0×10^4	2.0	0.2	500	+2	5	48
Proflavin	2.3×10^6			200	+1	1	181
Duanomycin	7.0×10^5	3.25		200	+1	2	30

^a Equilibrium or intrinsic binding constants with calf thymus or salmon testes DNA, except for compound #1 which is for binding with poly [(dG-dC)•(dG-dC)], n is the binding site size (# of base pairs) and ω is defined in the text and in Appendix A. All parameters in the following equations are also defined in Appendix A.

^b Indicates the binding analysis used for determination of parameters where 1 = Equation similar to method I; 2 = $r/C_f = K_b(1-nr)[1-(n-1)r]^{n-1}$ which is for ligands which display neighbor exclusion but non-co-operative behavior; 3 = same equation as used in method II that includes neighbor exclusion & co-operativity effects; 4 = same as

$$2 \text{ (2 lines above) except } n = 2; 5 = \frac{r}{C_f} = K_b(1-nr) \left[\frac{(2\omega-1)(1-nr) + r-R}{2(\omega-1)(1-nr)} \right]^{n-1} \left[\frac{1-(n+1)r+R}{2(1-nr)} \right]^2 \text{ and}$$

Table 3.14--continued

$R = \left\{ \left[1 - (n+1)r \right]^2 + 4nr(1-nr) \right\}$. In their analysis they set $n = 2$; $\mathbf{6} = \text{Scatchard eqn. } r/C_f = K_s(1-nr)$.

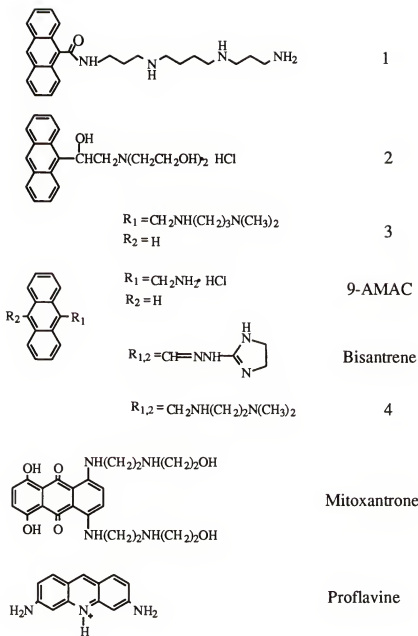


Figure 3.28. Structures of compounds listed in Table 3.14 except for Ethidium, Propidium and Duanomycin which are shown in Figures 1.2 and 1.3 in Chapter I. Mitoxantrone is not listed in Table 3.14, however it is displayed in a computer-generated intercalation complex with duplex DNA in Figure 3.30.

Re10An, Re8An and Re6An intercalate between the base pairs of the DNA double helix. However, it is unclear what the exact binding geometry of the complexes might be and whether the Re chromophore extends into or out of the major or minor grooves. Molecular modeling studies of mitoxantrone intercalated in a tetradeoxyribonucleotide duplex¹⁷¹ suggested that intercalation into the minor groove was favored by 2-8 kcal mol⁻¹, and a geometry where the anthraquinone skeleton was nearly perpendicular to the line joining the base pairs appeared to be a more favorable arrangement (see Figure 3.30). A major contribution to stabilization of the complex was found from H-bonds between the phosphate groups and the two terminal amino and hydroxy groups of the side chain. Although the skeletal structure of mitoxantrone is the same as AN, the number and attachment of substituent groups differs widely and therefore makes it difficult to relate the binding of this complex to the binding of the Re-An complexes. A closer example might be the crystal structures of complexes between proflavin dCpG (Figure 3.31a) and proflavin CpG (Figure 3.31b)¹⁷² which are typical of many small molecule-dinucleotide phosphate complexes. In this case the long axis of the acridine ring lies perpendicular to the long axis of the base pairs therefore allowing substantial overlap with the heteroaromatic ring systems of the nucleotides. It is likely that the geometry of the AN chromophore in the Re-An complexes might also prefer to be situated between the base pairs in this manner, therefore optimizing stacking interactions between the hydrophobic aromatic ring system with the base pairs. Studies of compound 1 in Table 3.14, where a spermine side chain was attached at the 9-position of AN, suggest that the AN chromophore intercalates in between base pairs with the side chain preferring to lie down the major groove where the positively charged amines of the spermine can make H-bonds to guanines in the groove.¹⁷⁰ It should be noted that the side chains often dictate the major or minor groove preference of compounds. For complex 1 previous studies on spermine have suggested that the most stable binding mode for this polyamine is one with the spermine lying down the major groove of DNA,^{170,173} therefore imparting major groove preference for the side chain of

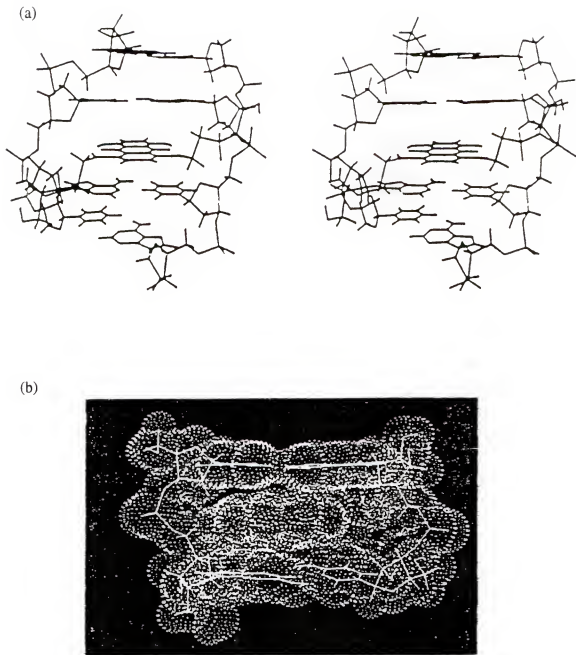


Figure 3.29. (a) Computer modeled structure of mitoxantrone intercalated in a tetradexynucleotide duplex shown in a side view parallel to the axis of the helix. (b) Energy-minimized intercalation complex of mitoxantrone and a 2-deoxycytidyl-3',5'-guanosine duplex [MAXIMIN 2 molecular mechanics calculations with the SYBYL program]. Atomic coordinates of the base-paired dinucleotide were extracted from an X-ray analysis. (From Pindur, U., Haber, M., Sattler, K. J. *J. Chem. Educ.*, 1993, 70, 263.)

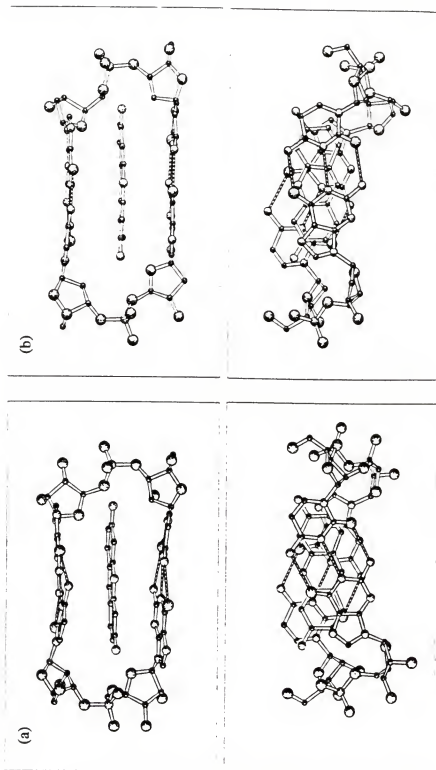


Figure 3.30. Crystal structure based complexes of proflavin intercalated in (a) dCpG and (b) CpG shown in side and top views. (From Saenger, W. *Principles of Nucleic Acid Structure*; Springer, New York, 1983, p. 355.)

the complex and stronger binding to GC base pairs over AT base pairs. The positively charged amine in the linker chain of the Re-An complexes is too close to the AN chromophore to be able to make H-bonding contacts with the bases in the groove, however it can make strong H-bond/ionic interactions with nearby phosphate oxygens of one of the sugar phosphate backbones. This contact could be more easily achieved with the phosphates on the major groove side of the helix since the geometry of this groove is more shallow (wider) than the minor groove. Contact of this sort might rotate the AN chromophore in the plane of the bases such that it does not overlap as completely with their long axis. However, as discussed in Chapter I, most groove binding compounds contain a number of peptide linkages, such as the one in the Re-An linker chains for Re10An, Re8An and Re6An, that generally prefer to make H-bond contacts with thymine O-2 and adenine N-3 in AT-rich regions of the minor groove.¹⁷⁴ The closer fit of the narrow minor groove appears to play a part in the preference of groove binding molecules for this side of the helix. Comparing the structures of the Re-An complexes, the longer chains of Re10An and Re8An would allow easier access of the peptide linkage towards establishing H-bonding contacts in the groove. The additional methylene linkages in the chains would also increase the hydrophobicity of the complexes resulting in greater affinities of the complexes for the DNA polymer and increasing the number of van der Waals contacts for the linker chains in the groove. This could explain the larger binding constants of Re10An and Re8An over the K_b 's for the shorter-chained complexes. The positively charged Re^{I} center could possibly interact favorably with the helix through electrostatic association, however the geometry of the Re chromophore might create repulsive interactions with the phosphates and bases in the minor groove. The diameter of the $(\text{bpy})\text{Re}^{\text{I}}(\text{CO})_3$ chromophore has been estimated to be $\sim 8 \text{ \AA}$ wide.¹²⁹ This is substantially smaller than the diameter of $\text{Ru}(\text{phen})_3^{2+}$ (16 \AA diameter)¹³⁰ which is considered to intercalate into the major groove of B-form DNA. The widths of the major and minor grooves of B DNA are 11.7 \AA and 5.7 \AA , respectively, while the major and minor groove depths are 8.5 \AA and 7.5 \AA , respectively. Essentially the

groove depths are very similar in B DNA, B-form considered to be the common form of native DNA, however the minor groove is significantly more narrow thus conveying greater shape selectivity for small molecules. Based on the size of the Re chromophore, it may prefer the smaller geometry of the minor groove where the bpy ligand would lie on the floor of the groove making weak van der Waals contacts, at best, with the bases. The CO groups protruding out from the Re center, however, might possibly create unfavorable steric and electronic contacts which could counteract any affinity of the chromophore towards the helix. This has been suggested from molecular modeling studies of the complex (phen)Re^I(CO)₃CH₂Q, which contains the stronger-binding phen ligand, studied in Chapter II. Considering the ReCH₂B model in this study does not appear to display significant binding affinity towards DNA, and the Ru(bpy)₃²⁺ transition metal complex from Barton's studies³³ also does not interact with DNA, it is safe to assume that any interaction of the Re chromophore in the Re-An complexes with DNA would be due solely to anchoring by intercalation of AN and groove binding contacts of the linker chains. Again, the longer length of the linker chains in Re8An and Re10An would suggest that in these complexes greater groove binding contacts can be achieved by the chains which would lead to more likelihood of the Re chromophore lying in or close to the groove. In light of this explanation, re-examination of the ³MLCT* lifetimes in the presence of DNA (Table 3.7), and in particular τ_3 , the length of the lifetime of this component follows the order Re8An (83 ns) < Re10An (87 ns) < Re6An (109 ns) among these three complexes. The reduction in lifetime of τ_3 , which is considered to be the equivalent of unquenched ³MLCT* emission, in comparison to the lifetime of the model (107 ns) in the presence of DNA, would suggest an interaction with the nucleic acids effects the lifetime of the ³MLCT* state. It may very well be that the negative charge on the bpy ligand when promoted to the excited state [(bpy⁻)Re^{II}(CO)₃L]¹⁺ encounters negative charge repulsions from the DNA phosphates or negative potential in the groove which would cause destabilization of the MLCT state.

The above proposed picture of the binding geometry of the Re-An complexes with DNA is helpful in discerning the difference in binding constants and quenching mechanisms of the bound form of the complexes. As discussed in the results section, the larger binding constant for Re8An is a result of the fact that the experimental QY curves (Figures 3.22 and 3.23) and emission lifetime plots (Figure 3.27) for this complex reach saturation at lower DNA/Re ratios than the other complexes. Yet the emission QY for Re8An at saturation of binding is not as large as the emission QY's for Re10An and Re6An. It appears, based on the $^3\text{MLCT}^*$ lifetime data, that the lower QY and lifetimes of the DNA-bound form of this complex emanate from the shorter length of the longest-lived emissive lifetime component (τ_3), compared to Re10An and Re6An, combined with a slightly lower percentage (α_3) of this component in comparison to Re10An.

The lower percentage of τ_3 for Re8An has already been established as due to the shorter linker chain and thus lower number of conformational degrees of freedom for this complex compared to Re10An. Even when the complexes are bound to DNA the Re chromophore, in limited cases, would be able to fold over close to the intercalated AN chromophore and participate in $\text{E}_\text{N}\text{T}$ quenching.

The shorter length of τ_3 , as mentioned above, could be caused by tighter binding of Re8An. A second consideration is that some $\text{E}_\text{N}\text{T}$ quenching of the $^3\text{MLCT}^*$ state in the bound form of Re8An can occur through interaction of the Re chromophore in one complex with an AN chromophore which is intercalated at the next adjacent site. However, if this was the case, the QY of the complex would continue to increase to a level equal to the other complexes as the binding density decreased with additional $[\text{DNA}]_\text{bp}$. A third possibility might be that the energy transfer kinetics are more favorable in this complex due to a particularly favorable length of its linker chain. Since the Re8An complex does not appear to display faster quenching behavior than Re6An in solution, it is doubtful that this could explain its lower QY (than the QY of Re6An) when bound to DNA.

The tighter binding kinetics of Re8An, over the other complexes, might be due to a more favorable structure of its linker chain and possibly a larger degree of protonation of the amine in the chain. The number of methylene spacers between functional groups in the side chain of a variety of biologically active compounds have been shown to strongly influence their toxicities and activity.^{127,143} Re8An contains three methylene spacers between the amine and the amide linkage in its chain while Re10An possesses five methylene spacers in the same position of its chain. Considering that the vertical DNA base pair spacing is approximately 3.4 Å in the double helix, the three methylene spacers position the functional groups in the Re8An chain in more favorable proximity for interaction with the bases. Looking back at Table 3.13, Re8An displays a slightly larger anti-co-operativity parameter ω . The higher the cationic charge of the compound the larger the value of ω should be (when considering ω values less than one). Generally compounds with charges of +1 or less, such as ethidium, show significantly small values of ω and instead fit best to the nearest-neighbor-exclusion binding isotherm that does not take into account co-operativity. Notice that ANMOD, which is a monocationic species in solution, has a rather low value for ω . Considering that Re8An displays the highest ω among the Re-An complexes might indicate that it has a slightly higher degree of protonation in the pH 7.2 buffer solutions used in the studies. Studies by Wilson et al.⁴⁸ have correlated larger DNA binding constants with increased cationic charge. Their studies associated slower dissociation kinetics with greater charge of the ligand.

Conclusions

The above studies on the Re-An series of CQ complexes have demonstrated several interesting and highly useful dimensions to these molecules. Within the same complex, two types of energy transfer mechanisms, triplet-triplet exchange E_NT and coulombic E_NT , have been established to be concurrently operating. For both of these mechanisms the distance dependence of their mechanisms was demonstrated by differences in quenching

rates within the series of Re-An complexes, where their rates increased in the order $\text{Re10An} < \text{Re8An} < \text{Re6An} < \text{Re3An}$ correlating with the decreasing lengths of their spacer chains between the Re and AN chromophores. Rates of coulombic (E_{NTc}) energy transfer (E_{NTc}) were approximately an order of magnitude faster than rates for the electron exchange mechanism (E_{NTEE}) in agreement with the differences in their distance requirements.

DNA binding studies clearly demonstrate the light-switch properties of the CQ complexes when added to the nucleic acid solutions. The complexes display dramatic increases in emission quantum yields and emission lifetimes when bound to DNA. Re10An , Re8An and Re6An all exhibit the most significant increases and show the strongest binding interaction with the ds DNA, in a mode where the AN chromophore is considered to be intercalated in between the DNA bases and the Re chromophore is extended either in the groove or out into solution. Small differences in binding strengths among the complexes are attributed to the differences in their linker chains, where Re8An has the highest equilibrium binding constant and the other complexes follow in the order $\text{Re10An} > \text{Re6An} > \text{Re3An}$. The binding site sizes of the complexes with DNA are all within 3 to 4 base pairs, similar to other known DNA intercalators. The fact that the complexes occupy the same site size on the double helix, even though they have progressively longer spacer chains between the Re and AN chromophores, suggests the Re chromophore does not interact strongly with neighboring complexes bound on the helix. Small anti-co-operative effects are seen in their binding behavior attributed to the 2+ charge of the complexes in pH 7 solutions.

Improvements in the design of the Re-An complexes which might increase their binding affinities to DNA and the changes seen in their E_{NT} quenching rates upon binding, would be to include additional positively charged amines in the linker chains and additional amide linkages for interaction with the grooves of the helix. The inclusion of more of these groups would also lengthen the linker chains, thus imparting different E_{NT} properties to

the complexes. Exchanging the bpy ligand on the Re chromophore with a diimine ligand would help in anchoring Re so that it could not reach the intercalated AN moiety as easily and therefore result in increased emission QY's of the bound complexes.

Molecular modeling studies on the solution conformations of the Re-An complexes and their DNA-bound forms would add insight towards interpreting the results obtained from the experimental studies. Additionally the modeling studies would aid in the design of new complexes. This has grown into an invaluable technique for the design of potentially useful drugs for various medical applications.

CHAPTER 4 EXPERIMENTAL

Materials and Syntheses

All materials used in the syntheses were of reagent grade and used as received unless otherwise noted. Purification and drying of particular solvents was accomplished as follows: DMF (dimethylformamide, Fisher) was dried over molecular sieves and vacuum distilled (10 mm Hg, 45°), THF (tetrahydrofuran, Fisher) was distilled twice, the second time over Na/K benzophenone, TEA (triethylamine, Fisher) was dried over KOH, distilled with acetic anhydride and redistilled over KOH, CH₂Cl₂ and CH₃CN were distilled over CaH₂.

Silica gel (Merck Kieselgel 60, 230-400 mesh) and Alumina (Fisher, Brockman activity III) were used for column chromatography.

Proton and carbon-13 NMR spectra were obtained on a GE QE-300 MHz spectrometer at 300 MHz and 75 MHz, respectively. Mass spectra were obtained on a Finnigan MAT 95 high-resolution mass spectrometer.

The metal complexes Re(CO)₅Cl, (bpy)Re(CO)₃Cl and (bpy)Re(CO)₃CH₂B were prepared according to previously reported procedures^{175,129} and (phen)Re(CO)₃Cl was prepared using an adaptation of the same procedures. The ligands N-(4-pyridyl)methylbenzamide (CH₂B) and N-(4-pyridyl)methyl-N-(4-dimethyl)benzamide (CH₂Q) were previously prepared in this laboratory.¹²⁹ All metal complexes were isolated as their PF₆ salts, and conversion to their chloride salts, when desired, was accomplished by ion-exchange chromatography on Dowex 1x2-100 ion-exchange resin.

(1) Synthesis of BpyRePTZ Complex

β -(10-phenothiazyl)propionitrile (PTZpnCN) (1)

The propionitrile was prepared according to a procedure reported by Smith.¹⁷⁶ A mixture of phenothiazine (200 g, 1.0 mol) (Aldrich) and acrylonitrile (300 ml, 242 g, 4.56 mol) (Kodak) was stirred and cooled to 0° C over an ice bath before 3.0 ml (1.65 mmol) of Triton B (benzyltrimethylammonium hydroxide in 40% methanol) (Aldrich) was slowly added. Heat was evolved during the addition and a greyish-green precipitate formed in the brown solution. The solution was heated with stirring over a steam bath for 1.5 hrs, and the resultant brown sludge was cooled, dried under vacuum and the crude product recrystallized from ethanol/acetone to yield 175 g of fine pale-yellow needle crystals (69%). Spectral Data: ¹H NMR (CDCl₃) δ 2.8 (t, 2H, -CH₂-CH₂-CN), 4.2 (t, 2H, -CH₂-CH₂-CN), 6.8 (d, 2H, PTZ), 6.96 (t, 2H, PTZ), 7.17 (d, 4H, PTZ); ¹³C NMR (CDCl₃) δ 16.5 (adjacent to -CN), 43.5 (benzylic), 115.4 (PTZ), 117.5 (CN), 123.5, 126.3, 127.5, 127.9, 143.9 (all PTZ). HRMS (EI) calc'd for C₁₅H₁₂N₂S 252.072, found: 252.071.

3-(10H-phenothiazine-10)propionic acid (PTZpnCOOH) (2)

The carboxylic acid was prepared according to the procedure of Godefroi and Wittle.¹⁷⁷ A solution of methanol/water (195 ml 50:45 v:v) containing 15.0 g (59 mmol) of PTZpnCN (1) and 15.0 g (375 mmol) of NaOH was refluxed for 16 hrs at which point TLC analysis (silica benzene) indicated starting material no longer remained. The solution was cooled and poured into ice-water, acidified with dilute HCL to a pH of 4, then filtered to obtain a blue solid which was dried under vacuum. Recrystallization from absolute ethanol gave 8.11 g of fine blue-gray needle crystals (30%) mp 160 - 162° C. Spectral Data: ¹H NMR (CDCl₃) δ 2.90 (t, 2H, -CH₂-CH₂-COOH), 4.23 (t, 2H, -CH₂-CH₂-COOH), 6.9 (m, 4H, PTZ), 7.20 (m, 4H, PTZ); ¹³C NMR (CDCl₃) δ 32.7 (adjacent to carbonyl), 43.4 (benzylic), 116.4, 123.5, 125.6, 128.0, 128.4, 145.8 (all PTZ), 172.7 (carbonyl). HRMS (EI) calc'd for C₁₅H₁₃O₂NS 271.067, found 271.066.

1-[3-(10H-phenothiazine-10)propanoyloxy]-2,5-pyrrolidinedione (PTZpnOSU) (3)

The following synthesis followed a procedure from the T. J. Meyer group.¹⁷⁸ In a previously dried 25 ml round bottom flask was dissolved 270 mg (1.0 mmol) of PTZpnCOOH (2) in 7 ml of dry DMF. To this stirring solution was added 115 mg (1.0 mmol) of N-hydroxysuccinimide (Aldrich) followed by 191 mg (1.0 mmol) of EDC (1-(3-dimethylaminopropyl)-3-ethylcarbodiimide hydrochloride) (Aldrich). A drierite drying tube was fitted onto the flask to exclude moisture and the solution was stirred for 25 hrs at room temperature. The solvent was subsequently removed by rotary evaporation and a light-maroon colored oil was recovered and dried further under vacuum. Purification was achieved by refluxing the oily residue in CCl₄ (10 ml), decanting the oil away from the hot CCl₄ (making sure to save the oil), and filtering the CCl₄ solution while hot through a glass frit. The CCl₄ solution was temporarily set aside while the same oil was run through the procedure a second time in order to extract out more product. The CCl₄ filtrates were then combined, cooled to room temperature and stored overnight at 5° C. A white solid had crystallized out of the CCl₄ solution by the next day and was collected via filtration to yield 190 mg (52%) of product. Spectral Data: ¹H NMR (CDCl₃) δ 2.84 (s, 4H, CH₂'s on succinimide), 3.15 (t, 2H, -CH₂-CH₂-COOR), 4.30 (t, 2H, -CH₂-CH₂-COOR), 6.90 (m, 4H, PTZ), 7.20 (m, 4H, PTZ); ¹³C NMR (CDCl₃) δ 25.4, 25.6 (CH₂'s on succinimide), 29.7 (-CH₂-CH₂-COOR), 42.4 (benzylic), 115.2, 115.3, 123.1, 125.6, 127.5, 127.8, 144.3(all PTZ), 166.9 (succinimide carbonyls), 168.9 (amide carbonyl).

N-4-(3-(10H-phenothiazine-10)propanoyl)aminomethylpyridine (PTZpnpyr) (4)

In an oven-dried 100 ml round bottom flask equipped with a drierite drying tube was suspended 0.51 ml (0.542 g, 5.0 mmol) of 4-(aminomethyl)pyridine (Aldrich) in 58 ml of dry DMF. To this stirring solution was added 1.50 g (4.08 mmol) of PTZpnOSU (2). The solution was heated to 40° C over a water bath and stirred for 1.5 hrs. At this point TLC analysis indicated formation of mostly lower-lying products (silica, CH₂Cl₂/Ethyl Acetate 3:1) therefore the solution was cooled and the solvent removed by

rotary evaporation to yield a yellow residue. Purification via silica column (50 mm wide) eluting with 4% MeOH:CHCl₃ yielded 1.15 g of product (78%). Spectral Data: ¹H NMR (CDCl₃) δ 2.70 (d, 2H, adjacent to carbonyl), 4.22 (t, 2H, benzylic), 4.3 (d, 2H, -NH-CH₂-pyridyl), 6.94 (m, 4H, PTZ), 6.98 (d, 2H, pyridyl), 7.18 (m, 4H, PTZ), 8.33 (d, 2H, pyridyl); ¹³C NMR (CDCl₃) δ 34.8 (adjacent to carbonyl), 42.5 (benzylic), 43.5 (-NH-CH₂-pyridyl), 116 (PTZ), 122.5 (pyridyl), 124, 126.5, 128 (2C), 144 (all PTZ), 147 (pyridyl), 150 (pyridyl), 172 (carbonyl). HRMS (CI) calc'd for C₂₁H₂₀N₃OS d(M + H) 362.133, found 362.133.

fac-(bpy)Re^I(CO)₃-PTZ (**5**)

Due to the photoreactivity of this compound it was necessary to exclude light during this general procedure. An oven-dried 25 ml round bottom flask equipped with a condenser and thermometer was purged with N₂ gas for 20 min before 0.211 g (0.585 mmol) of PTZpnpyr (**4**), 0.135 g (0.292 mmol) of bpyRe(CO)₃Cl and 74 mg (0.292 mmol) of AgPF₆ salt were placed in it and dissolved into 10 ml of dry DMF. The gold-yellow solution was stirred under N₂ and heated to 70^o C. After 1 hr of stirring TLC analysis (silica, CH₃CN/MeOH/CH₂Cl₂ 30:3:66 v:v:v) showed formation of a small amount of product, therefore an additional 46 mg (0.182 mmol) of AgPF₆ was added and the solution heated and stirred for 3 more hours. After a total of 4 hrs there appeared to be no further formation of product so the solution was cooled and the solvent removed by rotary evaporation. The resultant viscous gold oil was dissolved into CH₂Cl₂ and the cloudy solution filtered through a glass frit to remove the insoluble AgCl salt. The filtrate was collected and the solvent was removed by rotary evaporation to yield a gold residue which was purified via column chromatography using gradient elution (silica, CH₃CN/CH₂Cl₂, 1:9 --> 4:6 v:v). The recovered pure oil was dissolved into a minimal amount of dry CH₂Cl₂ and precipitated out of dry diethyl ether to yield 105 mg of a powdery yellow solid (39%). Spectral Data: ¹H NMR (CD₃CN) δ 2.60 (t, 2H, adjacent to carbonyl), 4.17, (m, 4H, adjacent to pyridyl and benzylic), 6.87 (t, 1H, NH), 7.17 (m, 4H, PTZ), 7.45 (d, 2H,

pyridyl), 7.97 (m, 4H, PTZ), 7.82 (t, 2H, bpy), 8.01 (d, 2H, pyridyl), 8.28 (t, 2H, bpy), 8.39 (d, 2H, bpy), 9.21 (d, 2H, bpy); ^{13}C NMR (CD_3CN) δ 33.2 (adjacent to carbonyl), 40.9 (benzylic), 42.5 (adjacent to pyridyl), 115.6, 122.6 (PTZ), 124.3, 124.5 (bpy), 127.0, 127.4, 127.5 (PTZ), 128.6, 140.9 (bpy), 144.6 (PTZ), 151.0, 153.1 (pyridyl), 153.5, 155.5 (bpy), 170.8 (carbonyl). HRMS (positive ion FAB) calc'd for $\text{C}_{34}\text{H}_{27}\text{N}_5\text{O}_4\text{ReS}$ 788.134, found 788.104.

Synthesis of (phen)ReCH₂X Complexes

(phen)Re(CO)₃CH₂B

An oven-dried 25 ml round bottom flask was purged with N_2 gas for 20 min before 0.095 g (0.196 mmol) of (phen)Re(CO)₃Cl, 7 ml of dry DMF and 0.127 g (0.491 mmol) of AgPF_6 were added. To this stirring solution was added 0.125 g (0.587 mmol) of CH_2B ligand and the solution was heated to 70° C and stirred under N_2 for 1.5 hrs. At this point an additional 49 mg (0.194 mmol) of AgPF_6 was added and the solution heated and stirred another 3.5 hrs. The solvent was then removed by rotary evaporation, the yellow residue dissolved into CH_2Cl_2 and filtered through a glass frit, and the solvent evaporated resulting in a brownish-gold oil. The crude product was initially purified via silica column using $\text{CH}_3\text{CN}/\text{CH}_2\text{Cl}_2$ (20:80 v:v) as the eluant. A second column using alumina and eluting with $\text{CH}_3\text{CN}/\text{CH}_2\text{Cl}_2$ (10:90 v:v) was necessary in order to obtain the pure product which was a gold oil. The oil was dissolved into a minimal amount of CH_2Cl_2 and precipitated from 50 ml of dry diethyl ether to yield 60 mg of a bright yellow powdery solid (37%). Spectral Data: ^1H NMR (CD_3CN) δ 4.39 (d, 2H, adjacent to pyridyl), 7.13 (d, 2H, pyridyl), 7.48 (m, 4H, benzene), 7.72 (d, 2H, benzene), 8.10 (q, 2H, phen), 8.19 (d & s, 4H, phen & pyridyl), 8.83 (d, 2H, phen), 9.60 (d, 2H, phen); ^{13}C NMR (CD_3CN) δ 41.9 (adjacent to pyridyl), 124.3, 126.5, 126.7, 127.8, 128.2, 130.4, 131.0, 140.0, 150.9, 151.3, 154.2 (all aromatic), 167.6 (carbonyl).

(phen)Re(CO)₃CH₂Q

Techniques were used to exclude as much light as possible during this procedure. To a dry 25 ml round bottom flask which had been flushed for 15 min with N₂ gas was added 0.100 g (0.206 mmol) of phenRe(CO)₃Cl and 7 ml of dry DMF. The solution was further purged with N₂ before 0.144 g (0.568 mmol) of AgPF₆ and 0.157 g (0.620 mmol) of N-(4-pyridyl)methyl-N-(4-dimethyl)benzamide (CH₂Q ligand) were added. The solution was stirred under N₂ and heated at 70° C for 1.5 hrs, at which point another 0.090 g (0.356 mmol) of AgPF₆ was added. Heating and stirring under N₂ were continued for 3.5 more hrs, by which time there did not appear to be any further increase in product (TLC: silica, CH₃CN/toluene 35:65 v:v). The solvent was evaporated and the residue dissolved into CH₂Cl₂, filtered through a fritted filter, and the solvent evaporated to yield an oily residue, which was stored under vacuum overnight. Two different columns were used to purify the crude product; an alumina column with CH₂Cl₂/CH₃CN (100:0 --> 88:12 v:v) as eluant was used to remove unreacted metal complex, followed by a silica column using CH₃CN/MeOH/CH₂Cl₂ (25:3:72 v:v:v) as eluant which separated the product from unreacted ligand. The pure gold oil was dissolved into a minimal amount of CH₂Cl₂ and precipitated out of 50 ml of n-pentane to give 62 mg of a yellow solid (35%). Spectral Data: ¹H NMR (CD₃CN) δ 2.95 (s, 6H, -(CH₃)₂), 4.31 (d, 2H, adjacent to pyridyl), 6.64 (d, 2H, benzene), 7.12 (d, 2H, pyridyl), 7.27 (broad t, 1H, -NH-), 7.54 (d, 2H, benzene), 8.07 (q, 2H, phen), 8.13 (s, 2H, phen), 8.16 (d, 2H, pyridyl), 8.81 (d, 2H, phen), 9.58 (d, 2H, phen); ¹³C NMR (CD₃CN) δ 40.9 (-N(CH₃)₂), 41.3 (adjacent to pyridyl), 113.4, 124.4, 127.8, 128.4, 131.0, 140.1, 146.3, 153.6, 154.2 (all aromatic), 166.4 (carbonyl).

Synthesis of Re-An Complexes

Synthesis of Anthryl Ligands

Pyr3An

N-(4-pyridyl)methyl-(N-(9-anthryl)methyl)amine (pyr3An)

To a stirring solution of 9-anthraldehyde (0.808 g, 3.92 mmol) (Aldrich) in dry THF (15 ml) was added 1.2 ml (1.28 g, 11.8 mmol) of 4-(aminomethyl)pyridine in 15 ml of methanol (dried over sieves). The pH of the solution was adjusted to 6.5 with glacial acetic acid and allowed to stir for 5 min before NaBH_3CN (0.248 g, 3.95 mmol) was added followed by 5 ml of methanol. The solution was stirred under N_2 gas at 25°C for 1 hr at which point TLC analysis (silica $\text{CH}_3\text{CN}/\text{MeOH}/\text{CH}_2\text{Cl}_2$ 15:2:83 v:v:v) indicated no presence of the starting aldehyde. The clear solution was brought to pH 2.0 with 4 ml of aqueous HCl (5M), during which process the solution turned from orange-gold to cherry red in color and became cloudy. The solvent was evaporated, the red solid dissolved into 200 ml of H_2O and the pH raised to 10.0 by addition of NaOH pellets. The resulting cloudy white solution was extracted with ethyl acetate (5 x 5 ml), the combined organics washed with saturated NaCl solution (2 x 25 ml), dried over MgSO_4 and the solvent evaporated to give a tan oil which was stored under vacuum for several hours. A 40 mm wide silica column eluted with $\text{CH}_3\text{CN}/\text{MeOH}/\text{CH}_2\text{Cl}_2$ (20:1:79 v:v:v) was used to purify the crude product resulting in 0.99 g (85%) of a tan oil. Spectral Data: ^1H NMR (CD_3CN) δ 2.2 (br, 1H, NH), 3.70 (s, 2H, adjacent to pyridine), 4.40 (s, 2H, adjacent to AN), 7.12 (d, 2H, pyridyl), 7.43 (quintet, 4H, AN), 7.86 (d, 2H, AN), 8.19 (s & d, 3H, AN), 8.46 (d, 2H, pyridyl); ^{13}C NMR (CDCl_3) δ 45.0 (adjacent to pyridine), 52.7 (adjacent to AN), 123.1 (pyridyl), 124.0, 125.0, 126.1, 127.4, 129.2, 130.3, 131.0, 131.5 (all AN), 149.5, 149.7 (pyridyl).

Pyr6An(a) N'-(4-Pyridyl)methyl N-CBZ-β-aminoethylamide (pyrGlyCBZ)

A stirring THF/CH₂Cl₂ solution (23 ml 15:8 v:v) of CBZ-Glycine (8.01 g, 38.3 mmol) (Sigma) and triethylamine (16 ml, 115 mmol) was cooled to 0° C with an ice/salt bath and isobutyl chloroformate (7.45 ml, 57.4 mmol) in CH₂Cl₂/THF (10 ml 1:1 ratio) was added dropwise via an addition funnel. A white precipitate, indicating the TEA/HCl salt, formed during the addition, and after 0.5 hrs of stirring 4-(aminomethyl)pyridine (7.78 ml, 76.5 mmol) in CH₂Cl₂/THF was added dropwise. The resultant thick cloudy yellow solution was stirred for 24 hrs with slow warming of the ice bath to room temperature. After evaporation the solid was suspended in CHCl₃ (300 ml) and washed with aqueous Na₂CO₃ (10%) repeatedly (4 x 50 ml). To ensure complete recovery of the product the aqueous layers were re-extracted with ethyl acetate (4 x 100 ml) and CHCl₃ (5 x 100 ml), and a precipitate which had formed in the extraction funnel was collected by filtration, stirred in CHCl₃, and the solvent collected by filtration. All of the organic fractions were combined, dried (MgSO₄) and the solvent was evaporated. The crude product was purified via column chromatography (silica, MeOH/CH₂Cl₂ 10:90 --> 13:87 v:v) to yield 4.96 g (43%) of a powdery white solid. Spectral Data: ¹H NMR (DMSO) δ 3.68 (d, 2H, -NH-CO-CH₂-NH-CBZ), 4.29 (d, 2H, adjacent to pyridine), 5.03 (s, 2H, benzyl), 7.23 (d, 2H, pyridyl), 7.29 (m, 5H, benzene), 7.54 (broad t, 1H, -NH-CBZ), 8.46 (d, 2H, pyridyl), 8.51 (broad t, 1H, -NH b to pyridine); ¹³C NMR (DMSO) δ 41.6 (-CH₂- α to amide carbonyl), 44.2 (-CH₂- adjacent to pyridine), 66.0, (-CH₂- adjacent to benzene), 122.46 (pyridyl), 128.12, 128.16, 128, 137.44 (all benzene), 148.8, 149.83 (pyridine), 156.97 (ester carbonyl), 169.96 (amide carbonyl).

(b) N-(4-Pyridyl)methyl β-aminoethylamide (pyrGlyNH)

A stirring solution of pyrGlyCBZ (3.53 g, 11.8 mmol) in methanol/ethyl acetate (250 ml, 20:5 ratio) was purged with N₂ gas for 15 min before 1.25 g (1.18 mmol) of 10% palladium on activated carbon (Aldrich) was added. The solution was bubbled for 5 min

with N₂ gas, then switched to H₂ gas and the solution stirred and bubbled for 5 hrs. Complete conversion to the product was evidenced by TLC analysis (silica, CH₃CN/MeOH/CH₂Cl₂ 30:3:67 v:v:v). The solution was filtered through a medium porosity fritted filter and the solvent evaporated to yield 1.97 g of a clear tan oil (100%). Spectral Data: ¹H NMR (DMSO) δ 3.18 (s, 2H, adjacent to carbonyl), 4.34 (d, 2H, adjacent to pyridine), 7.26 (d, 2H, pyridyl), 8.48 (d, 2H, pyridyl); ¹³C NMR (DMSO) δ 41.4 (adjacent to carbonyl), 45.3 (adjacent to pyridine), 150.0, 122.5 (pyridyl), 173.9 (carbonyl).

(c) N-(4-Pyridyl)methyl β-[N'-(9-anthryl)methyl]aminoethylamide (pyr6An)

To a stirring solution of 9-anthraldehyde (0.821 g, 3.98 mmol) in MeOH/THF (30 ml 1:2 ratio) was added dropwise a solution of pyrGlyNH (1.97 g, 11.9 mmol) in MeOH (33 ml). The pH was adjusted to 6.5 with glacial acetic acid and the solution stirred for 1/2 hr before NaBH₃(CN) (0.25 g, 4.0 mmol) was added and the resultant gold tinted solution stirred under N₂ gas for 24 hrs. The solution was acidified to pH 1.0 with 5M HCl (5 ml), the solvent evaporated and the oily residue suspended in 40 ml of H₂O and made basic (pH 10) with NaOH pellets. A thick white precipitate formed at pH 6.0, then partially dissolved back into solution and the solvent turned pink at higher pH (10). The solution was extracted with ethyl acetate (4 x 25 ml) and CHCl₃ (2 x 25 ml), the organics combined, dried (MgSO₄) and the solvent evaporated to give a dark yellow residue. Purification by repeated flash chromatography (silica MeOH/THF/ethyl acetate 3:20:77 v:v:v) resulted in 0.53 g of yellow solid (37%). Spectral Data: ¹H NMR (CDCl₃) δ 2.1 (br, 1H, NH), 3.53 (s, 2H, adjacent to carbonyl), 4.30 (d, 2H, adjacent to pyridine), 4.72 (s, 2H, adjacent to AN), 6.99 (d, 2H, pyridyl), 7.37 (m, 4H, AN), 7.65 (broad t, 1H, amide -NH), 7.93 (m, 2H, AN), 8.16 (m, 2H, AN), 8.35 (s, 1H, AN), 8.43 (d, 2H, pyridyl); ¹³C NMR (CDCl₃) δ 41.79 (-CH₂- α to carbonyl), 45.73 (-CH₂- adjacent to AN), 52.44 (-CH₂- adjacent to pyridine), 122.25 (pyridine), 123.44, 125.01, 126.42, 127.81, 129.38, 129.96, 130.21, 131.52 (all AN), 147.22, 150.02 (pyridyl), 171.75 (carbonyl).

Pyr8An(a) N'-(4-Pyridyl)methyl N-CBZ- γ -aminobutyramide (pyrGabCBZ)

A THF/CH₂Cl₂ solution (7 ml, 3:7 ratio) of N-CBZ- γ -aminobutyric acid (4.9 g 20 mmol) (Sigma) and TEA (8.5 ml, 61 mmol) was cooled to 0° C with an ice bath and isobutyl chloroformate (4.0 ml, 31 mmol) dissolved in THF/CH₂Cl₂ (5 ml) was added dropwise. After 0.5 hr of stirring 4-(aminomethyl)pyridine in CH₂Cl₂ (3 ml) was slowly added and the resulting thick gold colored solution stirred overnight while allowing the ice bath to warm to 25° C. After evaporation of the reaction solvent, the product residue was dissolved into CHCl₃ (150 ml), extracted with H₂O (100 ml), 2% NaHCO₃ (4 x 50 ml), dried (MgSO₄), and evaporated to yield a tan oil that was purified by flash chromatography (silica) eluting with MeOH/CH₃CN/CH₂Cl₂ (1:3:6 ratio). The product was isolated as a white solid, yield 3.03 g (45%). Spectral Data: ¹H NMR (CDCl₃) δ 1.71 (quintet, 2H, -CO-CH₂-CH₂-CH₂-NH-CBZ), 2.18 (t, 2H, -CO-CH₂-(CH₂)₂-NH-CBZ), 3.10 (quartet, 2H, -CO-(CH₂)₂-CH₂-NH-CBZ), 4.26 (d, 2H, adjacent to pyridine), 4.97 (s, 2H, benzyl), 5.57 (broad t, 1H, -NH-CBZ), 7.07 (d, 2H, pyridine), 7.13 (broad t, 1H, -NH- β to pyridine), 7.23 (m, 5H, benzene), 8.37 (d, 2H, pyridyl).

(b) N-(4-Pyridyl)methyl γ -aminobutyramide (pyrGabNH)

Utilizing the same procedure used for pyrGlyNH, to a stirred solution of pyrGabCBZ (3.0 g, 9.1 mmol) in methanol (45 ml) previously bubbled with N₂ gas, was added 10% palladium on activated carbon (0.97 g, 0.91 mmol). The resulting solution was then bubbled with H₂ gas and stirred for 3 hrs, filtered twice and evaporated to yield 1.6 g of a viscous oil (90%). Spectral Data: ¹H NMR (DMSO) δ 1.60 (m, 2H, β to carbonyl), 2.20 (t, 2H, adjacent to carbonyl), 2.52 (t, 2H, γ to carbonyl), 4.26 (d, 2H, adjacent to pyridine), 7.20 (d, 2H, pyridyl), 8.51 (d, 2H, pyridyl), 8.58 (broad t, 1H, amide -NH); ¹³C NMR (DMSO) δ 29.2 (β to carbonyl), 33.3 (adjacent to carbonyl), 41.5 (γ to carbonyl), 49.0 (adjacent to pyridine), 122.5, 149.2, 149.8 (pyridyl), 173 (carbonyl).

(c) N-(4-Pyridyl)methyl γ -[N'-9-anthryl)methyl]aminobutyramide (pyr8An)

A solution of pyrGabNH (1.6 g, 8.24 mmol) in methanol (15 ml) was added dropwise to a stirring solution of 9-anthraldehyde (0.57 g, 2.75 mmol) in dry THF (10 ml), and the pH was adjusted to approximately 6.5. After stirring for 15 min, $\text{NaBH}_3(\text{CN})$ (0.17 g, 2.8 mmol) was added and the solution stirred at 25° C under N_2 for 42 hrs. The solution was consequently acidified to pH 2.0 with 5M HCl and the solvent evaporated. The resultant residue was dissolved into H_2O (250 ml), and the solution was brought up to pH 10 by addition of NaOH pellets. The aqueous solution was extracted with ethyl acetate (5 x 50 ml), the organic layers were combined, dried (MgSO_4) and evaporated to yield the crude product as a gummy solid. Purification was achieved by flash chromatography (silica) with gradient elution using the following solvents in order of application:

CHCl_3 /hexane (1:1 ratio), CHCl_3 , ethyl acetate and MeOH/ethyl acetate/THF (0.5:5.5:4 ratio). The product was obtained as a viscous oil, yield 0.94 g (89%). Spectral Data: ^1H NMR (CDCl_3) δ 1.6 (br, 1H, NH), 1.71 (quintet, 2H, β to carbonyl), 2.14 (t, 2H, α to carbonyl), 2.72 (t, 2H, γ to carbonyl), 3.91 (d, 2H, adjacent to pyridine), 4.50 (s, 2H, adjacent to AN), 6.75 (d, 2H, pyridyl), 7.35 (m, 4H, AN), 7.60 (broad t, 1H, amide -NH), 7.82 (d, 2H, AN), 8.16 (s & d, 3H, AN), 8.24, (d, 2H, pyridyl); ^{13}C NMR (DMSO) δ 25.6 (β to carbonyl), 39.6 (adjacent to carbonyl), 41.9 (γ to carbonyl), 45.5 (adjacent to AN), 49.4 (adjacent to pyridine), 122.0 (AN), 123.8 (pyridyl), 125.0, 126.2, 127.4, 129.2, 130.2, 130.9, 131.4 (AN), 147.7 (pyridyl), 149.6 (AN), 173.4 (carbonyl).

Pyr10An

(a) N'-(4-Pyridyl)methyl N-CBZ- ϵ -aminohexanamide (pyrCapCBZ)

A stirring solution of N-CBZ-caproic acid (5.41 g, 20.4 mmol) (Aldrich) and TEA (8.5 ml, 61.2 mmol) in dry distilled CH_2Cl_2 (30 ml) was cooled to 0° C with an ice/salt bath, and isobutyl chloroformate (3.97 ml, 30.6 mmol) in CH_2Cl_2 (10 ml) was added dropwise via an addition funnel. After 0.5 hr of stirring 4-(aminomethyl)pyridine (4.15 ml, 30.6 mmol) in CH_2Cl_2 (10 ml) was slowly added and the resultant thick light gold colored

solution was stirred under N₂ for 20 hrs with slow warming to room temperature. The solvent was evaporated and the yellow solid dissolved into CHCl₃ (200 ml), washed with H₂O (2 x 50 ml), 5% Na₂CO₃ (3 x 50 ml) and H₂O (50 ml), dried over NaSO₄ and the CHCl₃ solvent evaporated to yield a gold colored solid which was stored under vacuum. Purification by flash chromatography (silica) with gradient elution using the following sequence of solvents: CH₃CN/CH₂Cl₂ (3:7 ratio) and CH₃CN/MeOH/CH₂Cl₂ (35:2:63 ratio), yielded 3.88 g (53%) of a fine white crystalline solid. Spectral Data: ¹H NMR (CDCl₃) δ 1.26 (quintet, 2H, -CO-(CH₂)₂-CH₂-(CH₂)₂-NH-CBZ), 1.41 (quintet, 2H, -CO-(CH₂)₃-CH₂-CH₂-NH-CBZ), 1.60 (quintet, 2H, -CO-CH₂-CH₂-(CH₂)₃-NH-CBZ), 2.18 (t, 2H, -CO-CH₂-(CH₂)₄-NH-CBZ), 3.10 (quartet, 2H, -CO-(CH₂)₄-CH₂-NH-CBZ), 4.33 (d, 2H, adjacent to pyridine), 5.01 (s, 2H, benzyl), 7.10 (d, 3H, pyridyl & -NH β to pyridyl), 7.28 (m, 5H, benzene), 8.42 (d, 2H, pyridyl).

(b) N-(4-Pyridyl)methyl ε-aminohexanamide (pyrCapNH)

Utilizing the same procedure as for pyrGlyNH, substituting pyrCapCBZ (3.88 g, 10.9 mmol), in methanol (80 ml) and using 1.17 g (10.9 mmol) of palladium on activated carbon, the solution was stirred and bubbled under H₂ gas for 3.5 hrs, filtered twice by gravity filtration and the solvent evaporated to yield 2.6 g (100%) of a clear viscous oil. Spectral Data: ¹H NMR (DMSO) δ 1.32 (m, 4H, δ & γ to carbonyl), 1.53 (m, 2H, β to carbonyl), 2.17 (t, 2H, adjacent to carbonyl), 2.52 (t, 2H, adjacent to amine), 4.28 (d, 2H, adjacent to pyridyl), 7.23 (d, 2H, pyridyl), 8.49 (d & t, 3H, pyridyl & amide -NH).

(c) N-(4-Pyridyl)methyl-ε-[N'-(9-anthryl)methyl]aminohexanamide (pyr10An)

A methanol solution (50 ml) of pyrCapNH (2.4 g, 10 mmol) was slowly added to a THF solution (25 ml) of 9-anthraldehyde (0.75 g, 3.64 mmol) and the pH was adjusted to 7.0 with glacial acetic acid. After 15 min of stirring NaBH₃(CN) (0.23 g, 3.66 mmol) was added and the solution stirred under N₂ for 28 hrs protected from light, at which time TLC analysis (silica CH₃CN/MeOH/CH₂Cl₂ 30:5:65 v:v:v) indicated little presence of the starting aldehyde. The pH of the solution was reduced to 2.0 with 5M HCl, the solvent

evaporated and the oily yellow residue dissolved into H₂O (300 ml) and its pH raised to 9.0 with NaOH pellets. The now cloudy white solution was extracted with CHCl₃ (5 x 50 ml), the combined organics washed with saturated NaCl solution (50 ml), dried (MgSO₄) and evaporated to give a yellow oil which was dried under vacuum. The crude product was purified by flash chromatography (silica) eluting with CH₃CN/MeOH/THF/ethyl acetate (4:1:5:10 ratio) to yield 0.82 g (55%) of a viscous oil. Spectral Data: ¹H NMR (CDCl₃) δ 1.35 (m, 2H, γ to carbonyl), 1.58 (m, 4H, β & δ to carbonyl), 2.15 (t, 2H, adjacent to carbonyl), 2.5 (br, 1H, NH), 2.85 (t, 2H, ε to carbonyl), 4.24 (d, 2H, adjacent to pyridine), 4.68 (s, 2H, adjacent to AN), 6.54 (t, 1H, amide -NH), 7.02 (d, 2H, pyridyl), 7.65 (m, 4H, AN), 7.88 (d, 2H, AN), 8.25 (d, 2H, AN), 8.28 (s, 1H, AN), 8.40 (d, 2H, pyridyl); ¹³C NMR (CDCl₃) δ 25.46 (-CH₂- γ to carbonyl), 26.85 (-CH₂- β to carbonyl), 29.56 (-CH₂- δ to carbonyl), 35.94 (-CH₂- α to carbonyl), 41.79 (-CH₂- ε to carbonyl), 45.56 (-CH₂- adjacent to AN), 50.15 (-CH₂- adjacent to pyridine), 122.07, (pyridyl), 124.0, 124.9, 126.06, 127.15, 129.09, 130.11, 131.38 (all AN), 148.20, 149.39 (pyridyl), 173.49 (carbonyl).

Metal Complexes

Due to slight variations in the syntheses of the different Re-An metal complexes, a general recipe could not be applied. Common practices for all syntheses included use of techniques which excluded any exposure of light to the reactants or products, and nitrogen atmosphere during syntheses and column purifications. The (bpy)Re(CO)₃TFMS¹⁷⁹ complex (TFMS = trifluoromethane sulfonate) was generally prepared the day previous to synthesis. The ¹H NMR spectra for the Re-An complexes pictured with their corresponding ligand spectra are shown in Figures 4.1 - 4.4 following the four syntheses described in this section.

Re3An

A solution of (bpy)Re(CO)₃TFMS (0.50 g, 0.91 mmol), pyr3An (0.46 g, 1.54 mmol) and NH₄PF₆ (1.5 g, 9.09 mmol) in dry distilled THF (16 ml) was purged with N₂ gas and then stirred under N₂ for 24 hrs at 25° C. By this time TLC analysis (silica, CH₃CN/MeOH/CH₂Cl₂ 4:1:15 v:v:v) showed mostly formation of the desired product (a dark orange spot which gradually turned bright yellow upon exposure to light, R_f = 0.68) and near disappearance of the Re-TFMS complex (R_f = 0.5). After evaporation of the solvent the crude yellow solid was purified by repeated flash chromatography (silica) with gradient elution using CH₃CN/CH₂Cl₂ (13:87 --> 15:85 ratios). The resultant pure oil was dissolved into CH₂Cl₂ and precipitated from dry diethyl ether (50 ml) to yield 0.28 g (35%) of a yellow powdery solid. Spectral Data: ¹H NMR (CD₃CN) δ 3.89 (s, 2H, adjacent to pyridine), 4.61 (s, 2H, adjacent to AN), 7.08 (d, 2H, pyridyl), 7.46 (m, 4H, AN), 7.78 (t, 2H, bpy), 8.27 (m, 4H, bpy & AN), 8.37 (d & s, 3H, pyridyl & AN), 9.18 (d, 2H, bpy); ¹³C NMR (CD₃CN) δ 44.4 (adjacent to pyridine), 51.3 (adjacent to AN), 124.1 (AN), 124.4, 124.8 (pyridyl & bpy), 125.0, 125.6, 126.8, 128.5 (AN), 128.6 (bpy), 130.0, 131.2, 131.1 (AN), 140.8, 150.7 (bpy), 153.5 (pyridyl), 155.4 (bpy). HRMS (Positive ion FAB) calc'd for C₃₄H₂₆N₄O₃Re 725.156, found 725.150.

Re6An

A solution of pyr6An (0.17 g, 0.47 mmol) and (bpy)Re(CO)₃TFMS (0.18 g, 0.31 mmol) in THF/ethanol (23 ml, 18:5 v:v) was purged with N₂ and stirred under N₂ at 35° C for 20 hrs, before NH₄PF₆ (0.52 g, 3.2 mmol) was added and the solution stirred at 25° C for 24 hrs. At this point TLC analysis (silica, CH₃CN/MeOH/CH₂Cl₂ 15:1:34 v:v:v) showed complete conversion of the product to its PF₆ salt (dark orange spot which turned to bright gold color over time, R_f = 0.7). After evaporation the yellow residue was dissolved into CH₂Cl₂ (100 ml), filtered, the solvent evaporated and the crude solid purified by repeated flash chromatography on silica using CH₃CN/MeOH/CH₂Cl₂ (20:1:79 v:v:v). The resultant gold oil was dissolved into CH₂Cl₂ and precipitated out of dry diethyl

ether to yield 0.146 g (50%) of a fine yellow powdery solid. Spectral data: ^1H NMR (CD_3CN) δ 3.42 (s, 2H, adjacent to carbonyl), 4.22 (d, 2H, adjacent to pyridine), 4.70 (s, 2H, adjacent to AN), 7.01 (d, 2H, pyridyl), 7.47 (m, 4H, AN), 7.76 (t, 2H, bpy), 8.05 (m, 4H, pyridyl & AN), 8.20 (t, 2H, bpy), 8.33 (m, 4H, bpy & AN), 8.50 (s, 1H, AN), 9.20 (d, 2H, bpy); ^{13}C NMR (CD_3CN) δ 40.76 ($-\text{CH}_2-$ α to carbonyl), 44.76 ($-\text{CH}_2-$ adjacent to pyridine), 51.03 ($-\text{CH}_2-$ adjacent to AN), 124.0 (AN), 124.5, 124.5 (bpy & pyridyl), 125.0, 126.2, 127.7, 128.6 (AN), 128.9 (bpy), 129.2, 130.3, 131.3 (AN), 140.9 (bpy), 151.4, 153.0 (pyridyl), 153.6, 155.5 (bpy), 170.9 (carbonyl). HRMS (Positive ion FAB) calc'd for $\text{C}_{36}\text{H}_{30}\text{O}_4\text{N}_5\text{PF}_6\text{Re}$ ($\text{M}+\text{H}+\text{PF}_6$) 928.150, found 928.149. Peak observed at 782 corresponds to $\text{C}_{36}\text{H}_{29}\text{O}_4\text{N}_5\text{Re}$ ($\text{M}+$).

Re8An

A stirring solution of $\text{bpyRe}(\text{CO})_3\text{TFMS}$ (0.45 g, 0.78 mmol) and pyr8An (0.51 g, 1.33 mmol) in THF/ethanol (30 ml, 1:1 ratio) was purged with N_2 gas, heated to 35°C and stirred under N_2 for 15 hrs, before NH_4PF_6 (1.28 g, 7.85 mmol) was added and the solution stirred at 30°C for 24 hrs. TLC analysis (silica, $\text{CH}_3\text{CN}/\text{MeOH}/\text{CH}_2\text{Cl}_2$ 20:2:33 v:v:v) indicated complete conversion to the PF_6^- salt of the metal complex ($R_f = 0.45$, a dark brown spot which slowly turned bright gold upon exposure to light). After evaporation of the solvent the crude residue was partially dissolved into $\text{CH}_3\text{CN}/\text{CH}_2\text{Cl}_2$ (1:4 ratio) and filtered, the solvent evaporated and the yellow solid purified by repeated flash chromatography on silica with gradient elution using the following sequence of solvents: $\text{CH}_3\text{CN}/\text{CH}_2\text{Cl}_2$ (5:17, 1:4) and $\text{CH}_3\text{CN}/\text{MeOH}/\text{CH}_2\text{Cl}_2$ (25:1:74). The gold oil was dissolved into CH_2Cl_2 and precipitated out of dry ether to yield 55 mg of a finely powdered, yellow solid (18%). Spectral data: ^1H NMR (CD_3CN) δ 1.90 (m, 2H, β to carbonyl), 2.54 (t, 2H, α to carbonyl), 3.36 (t, 2H, γ to carbonyl), 5.11 (s, 2H, adjacent to AN), 4.17 (d, 2H, adjacent to pyridine), 7.13 (d, 2H, pyridyl), 7.48 (m, 4H, AN), 7.76 (t, 2H, bpy), 8.17 (m, 8H, bpy, AN & pyridyl), 8.27 (d, 2H, bpy), 8.72 (s, 1H, AN), 9.20 (d, 2H, bpy); ^{13}C NMR (CD_3CN) δ 28.5 ($-\text{CH}_2-$ β to carbonyl), 33.66

(-CH₂- α to carbonyl), 41.36 (-CH₂- γ to carbonyl), 43.32 (-CH₂- adjacent to AN), 48.77 (-CH₂- adjacent to pyridine), 123.0 (AN), 124.36 (bpy), 124.41 (pyridine), 125.35 (AN), 127.18 (AN), 128.58 (bpy), 129.19, 130.03, 130.5, 131.1 (all AN), 140.87 (bpy), 151.46, 152.28 (pyridyl), 153.56, 155.46 (bpy), 175.03 (carbonyl). HRMS (Positive ion FAB) calc'd for C₃₈H₃₄N₅O₄Re (M⁺) 810.208, found 810.206; calc'd for C₃₈H₃₄N₅O₄PF₆Re (M+H+PF₆) 956.181, found 956.177.

Re10An

A stirring THF solution (40 ml) of (bpy)Re(CO)₃TFMS (0.24 g, 0.42 mmol) and pyr10An (0.30 g, 0.73 mmol) was purged with N₂ gas, heated to 35° C and stirred under N₂ for 20 hrs, before NH₄PF₆ (0.69 g, 4.2 mmol) was added, the heat removed and the solution stirred at 25° C for 5 hrs. Near complete conversion of the product to its PF₆⁻ salt was indicated by TLC (silica, CH₃CN/MeOH/CH₂Cl₂ 25:1:24 v:v:v) therefore the solvent was evaporated and the yellow solid partially dissolved into CH₃CN/CH₂Cl₂ (3:17 ratio), filtered and the solvent evaporated. The resulting crude residue was purified by 2 separate silica columns, the first eluted with CH₃CN/MeOH/CH₂Cl₂ (25:1:74 v:v:v) and the second with gradient elution using the following solvent sequences: CH₃CN/CH₂Cl₂ (1:4) and CH₃CN/MeOH/CH₂Cl₂ (25:1:74). The final gold oil was precipitated from CH₂Cl₂ to yield a yellow solid (30% yield). Spectral data: ¹H NMR (CD₃CN) δ 1.53 (quintet, 2H, δ to carbonyl), 1.36 (quintet, 2H, γ to carbonyl), 1.74 (quintet, 2H, β to carbonyl), 2.16 (t, 2H, α to carbonyl), 3.29 (t, 2H, ε to carbonyl), 4.13 (d, 2H, adjacent to pyridine), 5.21 (s, 2H, adjacent to AN), 6.86 (t, 1H, amide -NH-), 7.10 (d, 2H, pyridyl), 7.59 (m, 4H, AN), 7.78 (t, 2H, bpy), 8.10 (m, 4H, pyridyl & bpy), 8.29 (m, 6H, AN & bpy), 8.72 (s, 1H, AN), 9.20 (d, 2H, bpy); ¹³C NMR (CD₃CN) δ 23.5 (γ to carbonyl), 24.7 (β to carbonyl), 25.0 (δ to carbonyl), 34.4 (α to carbonyl), 41.0 (ε to carbonyl), 43.9 (adjacent to pyridine), 48.5 (adjacent to AN), 123.0 (AN), 124.4, 124.5 (bpy & pyridyl), 125.4, 127.4 (AN), 128.6 (bpy), 129.3, 130.6, 130.7, 131.1 (AN), 140.9 (bpy), 151.3, 153.3

(pyridyl), 153.6, 155.5 (bpy), 173.2 (carbonyl). HRMS (Positive ion FAB) calc'd for $C_{40}H_{37}N_5O_4Re$ (M^+) 838.232, found 838.233. (See next page for 1H NMR spectra).

Methods

RePTZ and (phen)ReCH₂Q solutions: Chapter 2

For the studies in Chapter 2 the following buffers were employed: 5 mM Tris/50 mM NaCl pH 7.15, 25 mM Tris pH 7.15, 0.1 M Sodium Acetate/50 mM NaCl pH 4.73 and pH 6.15. The latter two buffers were used solely in the RePTZ experiments. Due to the low solubility of the complexes in aqueous solutions 30% MeOH/Buffer solutions were employed for the latter half of the RePTZ experiments and throughout the PhenReCH₂Q studies. These levels of organic solvent should not affect the structure of the DNA helix.^{148,180}

Re-An solutions: Chapter 3

Buffers employed for the Re-An studies (Chapter 3) were 25 mM Tris (tris(hydroxymethyl)aminomethane hydrochloride) pH 7.2, 20 mM Tris/10 mM NaCl pH 7.2 and 20 mM Tris/0.1 M NaCl, pH 7.2. To increase solubility of the complexes and decrease precipitation of the DNA at high Re/DNA ratios 20% MeOH / Buffer solutions were employed for all the studies. Compared to data obtained in buffer solution without MeOH, the results are not affected by the presence of the organic solvent except to improve reproducibility and reduce random noise in the spectra. These low levels of MeOH should not appreciably affect the DNA structure.^{148,183}

DNA preparation

Calf thymus DNA Type I was purchased from Sigma. Stock solutions were prepared 12 hrs in advance by dissolving ca. 75 mg of DNA into 1.5 ml of buffer, storing at 4° C overnight, mixing thoroughly and passing approximately thirty times via syringe with a 22-gauge needle. Concentrations of the stock DNA solutions were ≈ 0.01 M in nucleotides and were determined according to Beer's Law using $\epsilon_{260} = 6600 \text{ M}^{-1}\text{cm}^{-1}$.¹⁴⁹

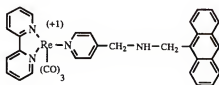
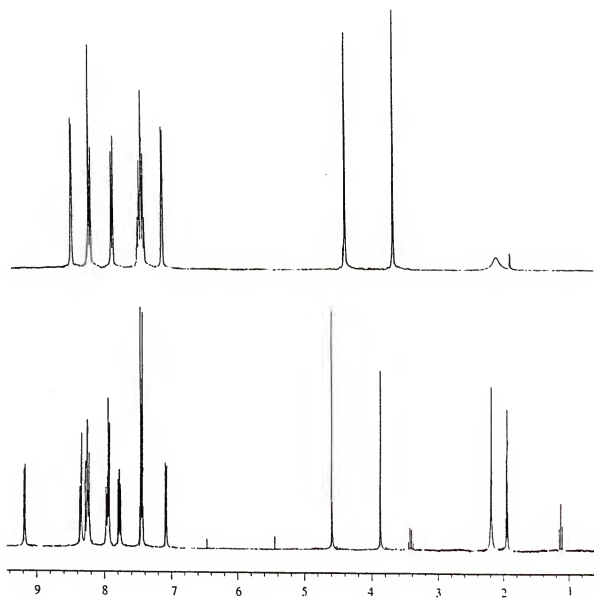


Figure 4.1. ^1H NMR spectra of Re3An (CD_3CN , bottom) and pyr3An ligand (CD_3CN , top).

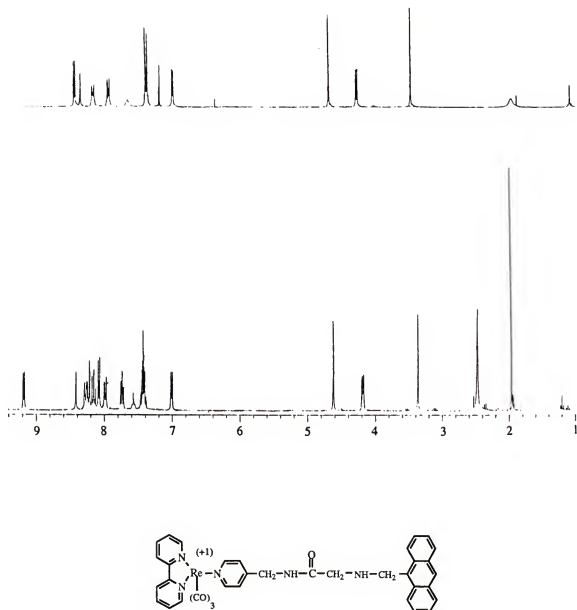


Figure 4.2. ^1H NMR spectra of Re6An (CD_3CN , bottom) and pyr6An ligand (CDCl_3 , top).

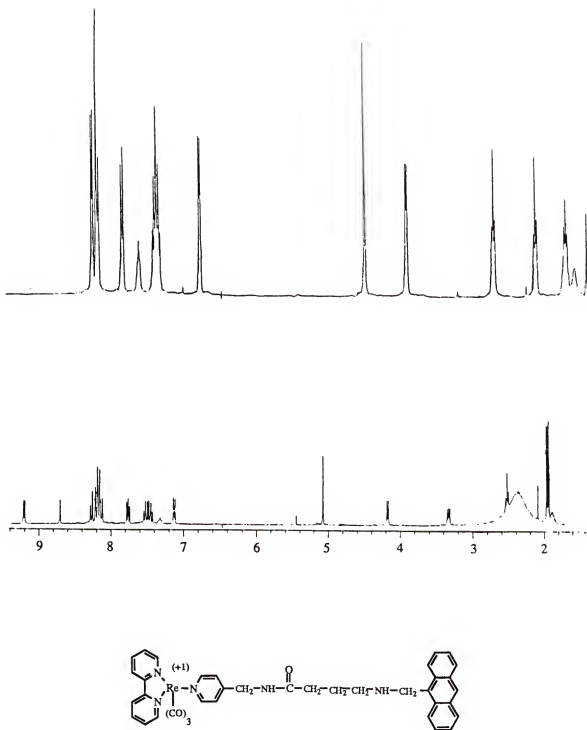


Figure 4.3. ^1H NMR spectra of Re8An (CD_3CN , bottom) and pyr8An ligand (CDCl_3 , top).

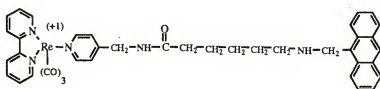
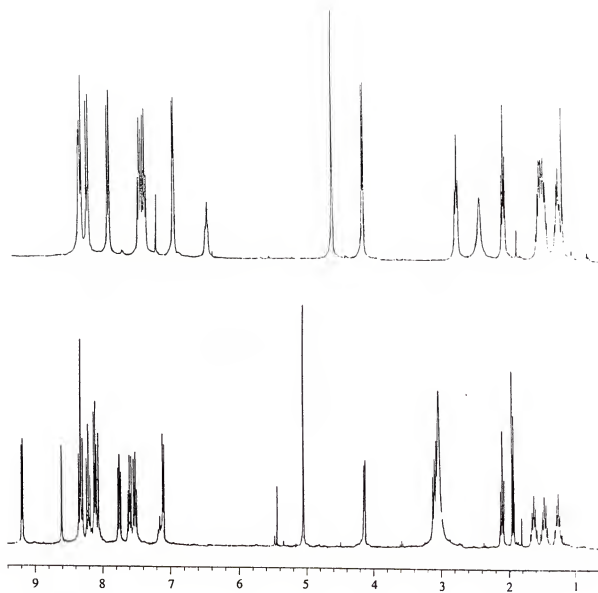


Figure 4.4. ^1H NMR spectra of Re10An (CD_3CN , bottom) and pyr10An ligand (CDCl_3 , top).

General conditions for experimental studies

Metal complex concentrations employed ranged from 2.0×10^{-5} M to 5.0×10^{-5} M. With minimum exposure to light, the metal-DNA solutions were prepared by maintaining constant metal complex concentration and varying the DNA concentrations. Best results were obtained by adding a fresh 3 ml aliquot of the metal complex solution via pipet to a quartz cuvette, adding the appropriate amount of DNA via syringe and capping with a rubber septum. Once prepared the solutions were mixed by inverting ~ 30 times, bubbled with argon gas for 15 min. and the spectra recorded.

RePTZ and (phen)ReCH₂Q DNA titrations

For the RePTZ and PhenReCH₂Q DNA titrations, increasing amounts of DNA were added to the same metal complex solution. The DNA stock was sufficiently high in concentration that only small amounts needed to be added for each incremental increase. Therefore the metal complex concentrations remained essentially constant throughout the titrations while the ratio of DNA to metal was increased.

Re-An DNA titrations

The DNA titrations of the Re-An complexes required fresh solutions for each measurement since repeat exposure of the same solution to the spectroscopic measurements (both absorbance and emission) resulted in increases in the absorbance at 320 nm and in the emission in the 380 - 500 nm region. These changes were not observed when separate solutions were used for each measurement.

Instrumentation

UV-visible absorbance and steady-state emission

UV-visible absorption spectra were recorded on an HP 8452A Diode Array spectrophotometer.

Steady state emission Spectra were measured on a Spex F-212A spectrophotometer. Measurements were made at room temperature. For the studies in

Chapter 2 the complexes (RePTZ, PhenReCH₂Q and models) were excited at 350 nm, and in some cases for the phenanthroline complexes, at 360 nm corresponding to the Re MCLT band. Emission was collected from 400 to 800 nm, with various slit widths dependent on the solution concentrations. A long-wavelength pass filter (Schott, LG 400) was placed at the entrance to the emission monochromator to attenuate the second-order transmitted excitation light which appears at 800 nm.

The Re-An complexes and models in Chapter 3 were excited at 340 nm, which also corresponds to the Re MLCT band. At this wavelength the molar absorptivity of the Re chromophore is approximately equal to that of the AN chromophore. Excitation at longer wavelengths increased the fraction of light absorbed by the AN long-wavelength band, while at shorter wavelengths light is absorbed by the DNA bases. Emission was collected from 380 to 800 nm, with slit widths of 2.50 and 1.25 mm for the input and output slits, respectively, on the excitation monochromator and 1.25 mm for both slits in the emission monochromator. A long-wavelength pass filter (Schott, LG 400) was placed at the entrance to the emission monochromator to attenuate the second-order transmitted excitation light at 800 nm.

Emission quantum yields for ³MLCT* (ϕ_{Re}) were measured relative to [Ru(bpy)₃²⁺][Cl⁻]₂ for which $\phi_{\text{em}} = 0.0379$ in air saturated aq. soln. at 295K, while emission quantum yields for An (ϕ_{AN}) were measured relative to fluorescein¹⁵⁸ for which $\phi_{\text{em}} = 0.87$ in air saturated 0.1 M NaOH at 295K. The quantum yields were calculated according to eqn. 4.1:

$$\phi_{\text{em}} = \phi_{\text{r}} (F_{\text{r}} / F_{\text{s}})(I_{\text{s}} / I_{\text{r}})(n_{\text{s}} / n_{\text{r}})^2 \quad \text{Eqn. 4.1}$$

where F is the fraction of light absorbed at the excitation wavelength ($F = (1 - 10^{-A})$, where A = absorption), I is the integrated area of the emission band, and n is the refractive index for the sample (s) and the reference (r) solutions. The values for n_{s} and n_{r} were taken to be equal to those of the pure solvents since the solutions were optically dilute.

Emission decays

Luminescence lifetime measurements were carried out by using time-correlated single photon counting on a commercially available instrument manufactured by Photochemical Research Associates (PRA). All samples were degassed prior to measurement by bubbling argon gas through the solution for 20 min. Samples were excited with a model 510B Nanosecond H₂-filled spark gap light source filtered through a Schott UG-11 band pass filter with maximum transmittance at 350 nm. Emission light for Re measurements was filtered through a 70 nm wide band pass interference filter centered at 600 nm (Corion P70-600-S-H708), while for AN emission measurements a 10 nm wide band pass interference filter centered at 450 nm (Corion P10-450-S-H089) was used. Decay data were collected with a TN7200 multichannel analyzer. The number of counts acquired in the maximum channel was 10,000. The data were transferred to an IBM XT computer and analyzed using the DECAN (v. 1.0, 1993) single-wavelength fluorescence lifetime analysis software.

Transient absorption

Transient absorption experiments were carried out using an instrument that has been previously described.¹⁰⁷ The samples were excited with the third harmonic output of a Q-switched Nd:YAG laser (355 nm, 10 ns fwhm) with a dose of 5 mJ/pulse. All samples were degassed prior to measurements by bubbling argon gas for 20 min. through a needle inserted into the solution by way of a septum cap.

For the experiments measuring the relative triplet yields of the 426 nm transient, the optical densities at 355 nm of all samples were matched as closely as possible (~0.4 to 0.5 AU, checked by UV absorption), and three sets of data were obtained for each sample using fresh solutions each collection. The samples were stirred during measurements and the absolute intensity of the 426 nm peak was used to determine the relative AN triplet yields. All triplet intensities were measured relative to the intensity of the 370 nm ³MLCT* of the actinometer ReBz which at this wavelength has an extinction coefficient of 11900 M⁻¹

$l\text{cm}^{-1}$. Optimal results were obtained when samples were all run on the same day, however to compare relative yields from separate days the intensities were multiplied by the intensity of the actinometer. The intensities were calculated using the formula:

$$\text{TA Intensity} = \left\{ (\text{TA Int. Sample} / \text{fr. } h\nu_{\text{sample}}) / (\text{TA Int. ReBz} / \text{fr. } h\nu_{\text{ReBz}}) \right\} \quad \text{Eqn. 4.2}$$

where TA Int.Sample is the experimentally measured maximum intensity of the sample at 426 nm after laser excitation, TA Int. ReBz is the experimentally measured maximum intensity of ReBz at 370 nm after laser excitation. fr. $h\nu_{\text{sample}}$ and fr. $h\nu_{\text{ReBz}}$ are the fractional absorbances of the sample and ReBz, respectively, determined from their optical densities at 355 nm with the following equation:

$$\text{fr. } h\nu = \left(1 - 10^{(-\text{Absorbance}@355\text{nm})} \right) \quad \text{Eqn. 4.3}$$

APPENDIX A

DNA Binding Analyses

Three different methods were employed to determine the binding affinity of the Re-An complexes with calf thymus DNA. The first one is based on a neighbor-exclusion binding model developed by Crothers and Schmechel¹⁸¹ for absorption spectroscopic titrations. The second and third methods analyze the steady-state emission DNA titration data using an equation derived by McGhee and von Hippel,⁷² and a fitting process which was developed from the conventional Scatchard equation.¹⁵⁰ All three methods will be described in the following sections.

Binding Equilibria from Spectroscopic Methods

The first step in analyzing the binding of a ligand (compound/drug) to nucleic acids is to determine the amount of bound ligand as a function of free ligand concentration, and to then graph this data in the form of a Scatchard equivalent binding plot. The binding equilibria can be monitored spectroscopically if the properties of the free ligand change upon binding. In the simplest case the observed compound's property is an average of the properties of the free and bound species, provided there is only one spectroscopically distinguishable type of binding site. These quantities are all measured at the same wavelength. For instance, the total quantum yield of emission from the solution of a ligand or dye molecule with DNA would be equal to:¹⁸²

$$QY_T = \left(\frac{C_f}{C_T} \right) QY_f + r \left(\frac{[DNA]_{bp}}{C_T} \right) QY_B \quad A.1$$

where QY_T is the experimentally observed quantum yield of the solution, QY_f is the quantum yield of emission of the free dye, C_f is the concentration of the free dye species in the solution, C_T is the total concentration of the dye species, QY_B is the quantum yield of the bound species, r is the binding density equal to the moles of bound dye per moles of total nucleic acid base pairs, and $[DNA]_{bp}$ is the total concentration of DNA base pairs in the solution. The amount of bound ligand (C_b) per addition of DNA to solution can be determined according to equation A.1:

$$C_b = C_T \times [(QY_T - QY_f)/(QY_B - QY_f)] \quad A.2$$

where C_T is the total concentration of the dye in solution, QY_T (as defined above) is the observed emission QY of the dye for each addition of DNA, QY_f is the emission QY of the free dye in the absence of DNA, and QY_B is the QY of the fully bound dye. QY_B can be found from extrapolation to conditions of complete binding, or at the point the optical property remains constant upon further addition of DNA. The amount of free dye (C_f) at any concentration can then be calculated from

$$C_f = (C_T - C_b). \quad A.3$$

Once having obtained this information a plot of r/C_f versus r where $r = C_b/[DNA]_{bp}$ can be plotted according to the Scatchard equation:

$$r/C_f = K_b (1 - nr) \quad A.4$$

where the slope is equal to $-K_b n$, the product of the binding constant (K_b) and the binding site size, n (number of base pairs covered by the bound dye), and the intercept is equal to K_b . The Scatchard equation assumes that the ligands do not interact with each other upon

binding (do not affect the binding of neighboring ligands) and occupy a site size of one DNA base pair. Therefore the above plot of r/C_f vs. r should give a straight line. Any deviation from linearity is interpreted to mean that there is more than one class of binding site and/or ligand-ligand interactions (co-operativity) are occurring. This is valid only if the ligand occupies a site size of one DNA base pair. However, if a bound ligand covers more than one base pair site, the problem of overlapping sites arises. In this case at any degree of binding saturation the number of open ligand binding sites depends not only on the number of ligands already bound, but also on the distribution of these bound ligands on the DNA helix. This situation will result in a curved Scatchard plot, but in this case the curvature arises solely as a consequence of the overlap of potential binding sites and is not due to binding site heterogeneity or ligand binding co-operativity.⁷² Attempting to determine the binding constant and site size by extrapolation from linear regions of the curve can result in substantial error of their actual values. In addition to this problem, if any type of co-operative interaction or binding heterogeneity is occurring these must be further taken into account. Several groups have addressed these problems through derivation of revised binding equations which include terms for neighbor-exclusion and co-operative interactions. Schmechel and Crothers¹⁸¹ formulated a neighbor-exclusion model in order to more accurately describe the intercalative binding mechanism which supposes that the space between any two base pairs can serve as an intercalation site, but that intercalation at one site prevents binding at the adjacent potential sites. One of the most comprehensive treatments of complicated binding equilibria was done by McGhee and von Hippel.⁷² They derived modifications of the conventional Scatchard equation which could be applied to neighbor-exclusion models of ligands which are non-interacting, positively co-operative or negatively co-operative. An additional parameter, ω , in their equations accounts for ligand co-operativity where if $\omega > 1$, the ligands attract each other and the binding is positively co-operative, if $\omega < 1$, the ligands repel each other and the binding is anti or negatively co-operative, and if $\omega = 1$, the binding is non-co-operative.

With the choice of binding equations available, it can be difficult determining which best describes the binding of a ligand with DNA. The easiest approach is to plot the data as r/C_f versus r and examine the degree of curvature as well as roughly determine K_b and n from the plots according to the conventional Scatchard equation. A straight line indicates $n = 1$ and non-co-operativity, whereas if the plot falls slightly below a straight line and n is greater than one but not large, then the interaction is likely non-co-operative with neighbor-exclusion. Plots pertaining to co-operative binding tend to have a larger degree of curvature, where convex upward (or humped) indicates positive interaction and convex downward represent negative interaction. A large value for n is also indicative of anti-co-operativity.

Method I

Intrinsic binding constants were determined for the Re-An complexes and ANMOD to calf thymus DNA from their absorption titrations according to the half-reciprocal form¹⁸³ of the neighbor-exclusion model by Schmechel and Crothers¹⁸¹:

$$[\text{DNA}]_{bp}/\Delta\epsilon_{sp} = [\text{DNA}]_{bp}/\Delta\epsilon + 1/\Delta\epsilon K \quad \text{A.5}$$

Where

$$\Delta\epsilon_{sp} = |\epsilon_a - \epsilon_f|$$

$$\Delta\epsilon = |\epsilon_b - \epsilon_f|$$

ϵ_f = extinction coefficient of the free ligand at 388 nm

ϵ_b = extinction coefficient of the fully bound ligand at 388 nm

ϵ_a = apparent extinction coefficient of the solution after each addition of DNA calculated from $\epsilon_a = A_{\text{obsd}@388\text{nm}}/[\text{ReAn}]$ where

$A_{\text{obsd}@388\text{nm}}/[\text{ReAn}]$ is the absorption of the complex at 388 nm divided by the total concentration of the CQ complex.

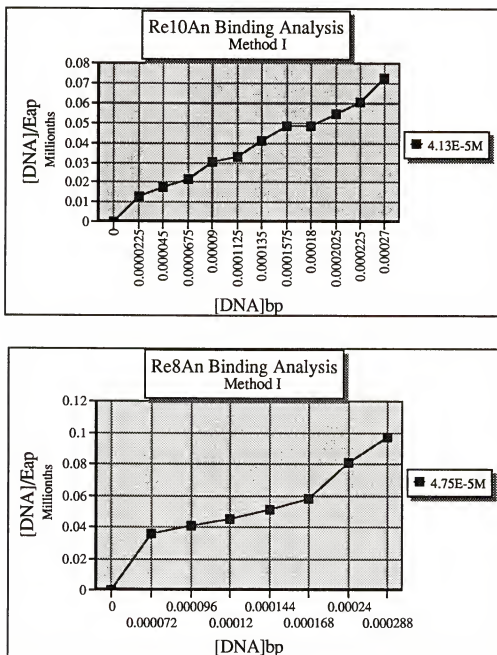


Figure A.1. Binding plots for Re10An and Re8An from DNA absorption titrations (single experiments) using changes in absorbance at 388 nm to construct the plots according to eqn. A.5 (Method I). The legend indicates the concentration of Re-An complex.

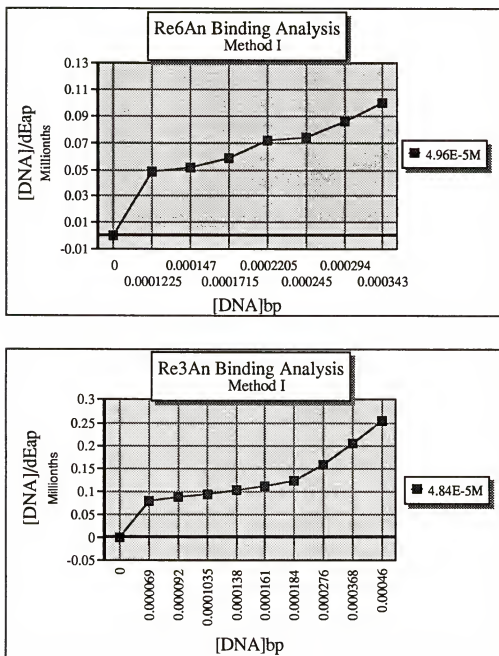


Figure A.2. Binding plots for Re6An and Re3An from DNA absorption titrations (single experiments) using changes in absorbance at 388 nm to construct the plots according to eqn. A.5 (Method I). The legend indicates the concentration of Re-An complex.

A plot of $[\text{DNA}]_{bp}/\Delta\epsilon_{ap}$ vs. $[\text{DNA}]_{bp}$ gives a slope of $1/\Delta\epsilon$ and a y-intercept of $1/\Delta\epsilon K$ from which the binding parameter, K , can be obtained. The intrinsic binding constant from this equation takes into account only the binding properties of the individual ligands apart from neighbor effects. Examples of the half-reciprocal plots constructed from the absorbance changes of the Re-An complexes at 388 nm are shown in Figures A.1 and A.2.

Steady-State Emission DNA Titrations

Determination of the DNA binding of the Re-An complexes from the experimental QY data obtained from DNA emission titrations was done using two separate procedures which are described as Method II and Method III. These two procedures rely on different binding equations which will be discussed below.

Method II

In method II the emission QY data from several experiments on each complex was first analyzed using a non-linear least squares curve fitting program (IGOR for Macintosh) to extract best fit curves which could be used for the binding analysis (Figures A.3 and A.4). The data from these fits was then used to construct plots of r/C_f vs. r (where $r = C_b/[\text{DNA}]_{bp}$ and C_f = the concentration of free Re-An complex) according to the procedure described above in the introductory section on binding equilibria. That is, first the amount of bound complex (C_b) was determined according to equation A.2. Then the amount of free complex (C_f) at each DNA concentration was calculated from equation A.3. From this data plots of r/C_f vs. r were then constructed according to the conventional Scatchard equation (eqn. A.4). The Scatchard plots constructed from the QY data are curved convex upward and show no linear regions from which to obtain binding parameters. It is visibly apparent that neighbor-exclusion is occurring and possibly anti-co-operative behavior based on the large degree of curvature for some of the graphs.

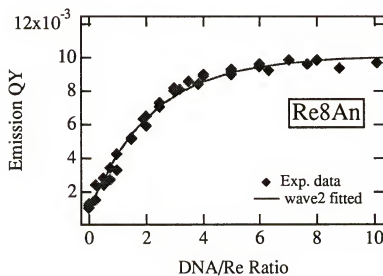
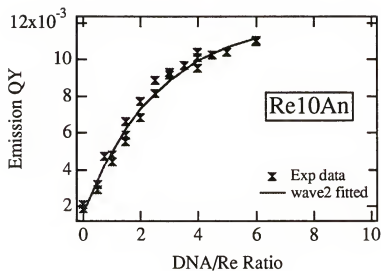


Figure A.3. Igor curve fits to the experimental QY data from steady-state emission DNA titrations. The points are experimental data and the solid line is the generated fit (based on a single-exponential curve fit). The data from the best fit curves is then used the method II analysis.

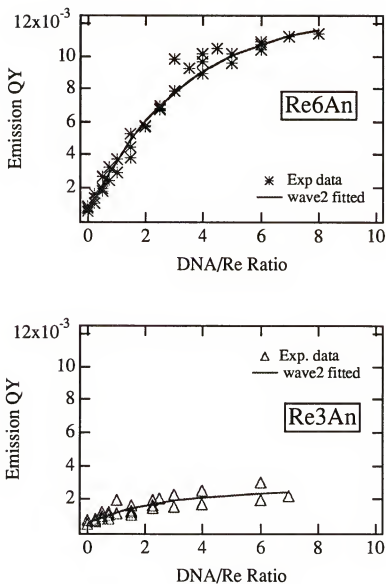


Figure A.4. Igor curve fits to the experimental QY data from steady-state emission DNA titrations. The points are experimental data and the solid line is the generated fit (based on a single-exponential curve fit). The data from the best fit curves is then used for the method II analysis.

In order to test the hypothesis, an empirical curve of r/C_f vs. r was constructed by the following method. The same values of r calculated from the experimental data were used, but r/C_f was determined from the McGhee-von Hippel equation for co-operative ligands^{72,141} (eqn. A.6) by setting K_b , n and ω to initial values and varying these values using a spreadsheet program (Lotus for Macintosh) until the empirical plot matched the experimental data as closely as possible (plots are shown in Figures A.5 and A.6).

$$\frac{r}{C_f} = K_b(1 - nr) \left[\frac{(2\omega - 1)(1 - nr) + (r - R)}{2(\omega - 1)(1 - nr)} \right]^{n-1} \left[\frac{1 - (n-1)r + R}{2(1 - n)} \right]^2 \quad \text{A.6}$$

where $R = \left\{ [1 - (n-1)r]^2 + 4\omega r(1 - nr) \right\}^{1/2}$ and ω is a co-operativity factor. The value of K_b from a plot of eqn. A.6 is equal to the y-intercept and the x-intercept is equal to $1/n$. The co-operativity parameter ω is the unitless equilibrium constant for the process of moving a bound ligand from an isolated site on the DNA helix to a singly contiguous site, or from a singly contiguous site to a doubly contiguous site. In the case of $\omega > 1$, the ligands attract each other and the binding is positively co-operative. For $\omega < 1$, the ligands repel each other and the binding is anti or negatively co-operative, and for $\omega = 1$, the binding is non-co-operative.

Method III

This method of obtaining binding parameters from the experimental QY data involved the following procedure. The Scatchard equation was set to the form of a quadratic equation in order to obtain the concentration of bound ligand (C_b). The steps leading to the quadratic formula are listed in order below.

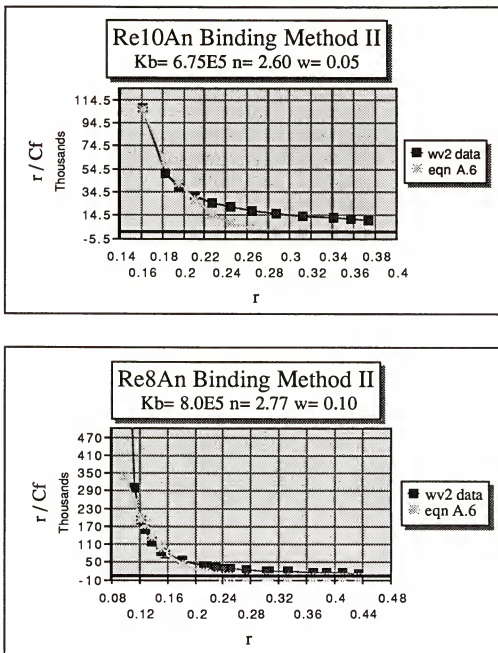


Figure A.5. Binding analysis of steady-state emission DNA titration data according to method A.5. The experimental curve (squares) is fit by an empirical curve (stars) generated from eqn. A.6. The values of K_b , n and w are varied until the best fit of the empirical curve (eqn. A.6) to the experimental data is obtained. The experimental data points for Re10An and Re8An are from the Igor curve fits in Figure A.3.

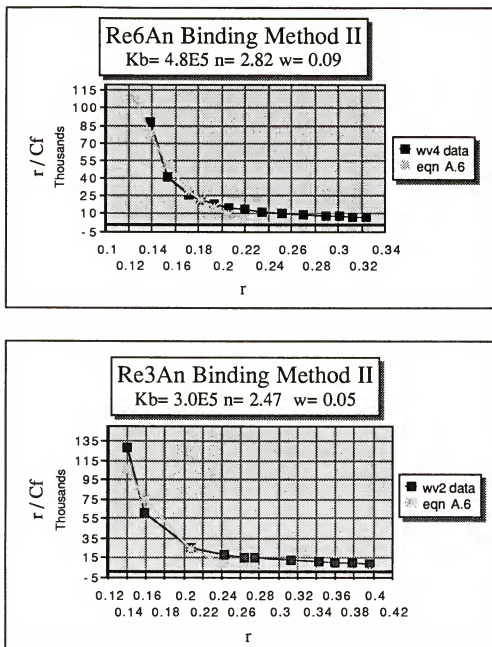


Figure A.6. Binding analysis of steady-state emission DNA titration data according to method II. The experimental curve (squares) is fit by an empirical curve (stars) generated from eqn. A.6. The values of K_b , n and w are varied until the best fit of the empirical curve (eqn. A.6) to the experimental data is obtained. The experimental data points for Re6An and Re3An are from the Igor curve fits in Figure A.4.

$$r/C_f = K_b (B_0 - r) \quad \text{where } B_0 = 1/n \quad \text{A.7}$$

$$\frac{C_b}{[\text{DNA}]} \times \frac{1}{C_f} = K_b B_0 - K_b \frac{C_b}{[\text{DNA}]} \quad \text{A.8}$$

$$\frac{C_b}{[\text{DNA}]} \times \frac{1}{C_f} = \gamma - K_b \frac{C_b}{[\text{DNA}]} \quad \text{where } \gamma = K_b B_0 \quad \text{A.9}$$

$$\frac{C_b}{[\text{DNA}]} \times \frac{1}{C_T - C_b} = \gamma - K_b \frac{C_b}{[\text{DNA}]} \quad \text{A.10}$$

$$\frac{C_b}{[\text{DNA}]} = \gamma (C_T - C_b) - K_b \frac{C_b (C_T - C_b)}{[\text{DNA}]} \quad \text{A.11}$$

$$C_b = \gamma [\text{DNA}] (C_T - C_b) - K_b C_b (C_T - C_b) \quad \text{A.12}$$

$$C_b = \gamma [\text{DNA}] C_T - \gamma [\text{DNA}] C_b - K_b C_b C_T + K_b C_b^2 \quad \text{A.13}$$

$$C_b = \gamma [\text{DNA}] C_T - (\gamma [\text{DNA}] + K_b C_T) C_b + K_b C_b^2 \quad \text{A.14}$$

$$0 = \gamma [\text{DNA}] C_T - (\gamma [\text{DNA}] + K_b C_T + 1) C_b + K_b C_b^2 \quad \text{A.15}$$

Equation A.15 is now in the form of the quadratic equation $0 = ax^2 + bx + c$ where

$$a = K_b$$

$$b = -(\gamma [\text{DNA}] + K_b C_T + 1) \quad \text{A.16}$$

$$c = \gamma [\text{DNA}] C_b$$

The quadratic is then solved by

$$C_b = \frac{-b \pm \sqrt{b^2 - 4ac}}{2a} \quad \text{A.17}$$

Using a lotus spread sheet the amount of Re-An complex bound at any DNA concentration is determined by

$$[Re_{bound}] = (C_b) \quad \text{A.18}$$

$$\text{where } (C_b) = \frac{-b - \sqrt{b^2 - 4ac}}{2a} \quad \text{A.19}$$

$$\text{and } [Re_{free}] = Re_{Total} - Re_{bound} \quad \text{A.20}$$

Using the above values for bound and free Re-An at different DNA concentrations a theoretical curve for the emission QY's can be constructed according to the following equation

$$QY_{em} \text{ Theor.} = \left(\frac{Re_{free}}{[Re_{Total}]} \right) \times QY_0 + \left(\frac{Re_{bound}}{[Re_{Total}]} \right) \times QY_B \quad \text{A.21}$$

where QY_0 is the QY of the free complex and QY_B is the QY of the fully bound species. These QY values are determined from the experimental data and are set to defined values in the spread sheet. The values of B_0 and K_b are also set to initial values which upon plotting of $QY_{em} \text{ Theor.}$ vs. [DNA] along with $QY_{em} \text{ Experimental}$ vs. [DNA], can be varied to obtain the best fit of the theoretical curve to that of the experimental curve. Plots from the curve fits from this method are illustrated in Figures A. 7 and A.8.

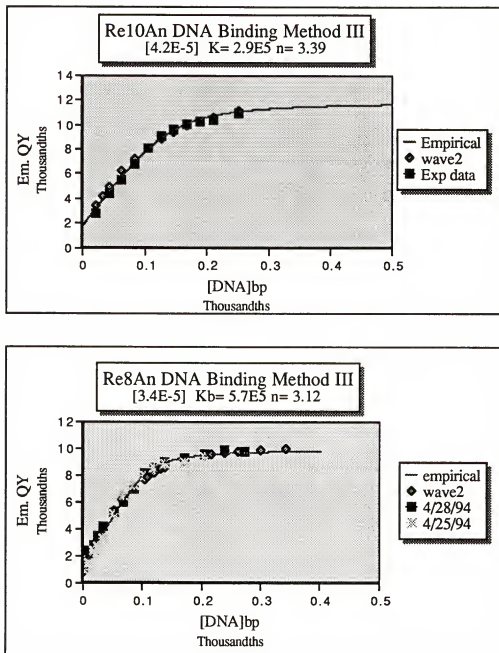


Figure A.7. Binding analyses of steady-state emission DNA titration QY data according to method III. The points (squares and stars) represent different experimental data sets, the diamonds represent the data obtained from Igor curve fits in Figure A.3, and the solid line is the empirical curve generated from method III from which K_b and n are obtained.

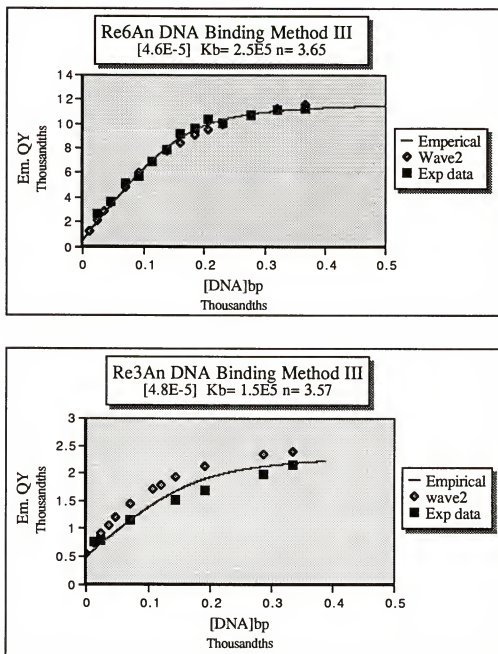


Figure A.8. Binding analyses of steady-state emission DNA titration QY data according to method III. The points (squares) represent experimental data, the diamonds represent the data obtained from Igor curve fits in Figure A.4, and the solid line is the empirical curve generated from method III from which K_b and n are obtained.

APPENDIX B

Emission QY and Lifetime Data for $^3\text{MLCT}^*$ State of Re-An Complexes from DNA Titrations

Table B.1. Steady-state Emission QY's for Re-An complexes from DNA Titrations.^a

$\frac{[\text{DNA}]_{\text{bp}}}{[\text{Re}]}$	Re3An ^b	Re6An	Re8An	Re10An
0	0.00046	0.00055	0.0010	0.0018
0.5	0.0010	0.0027	0.0025	0.0032
1.5	0.0012	0.0054	0.0056	0.0068
3	0.0020	0.0083	0.0089	0.0098
4	0.0024	0.0103	0.0096	0.0115
6	0.0025	0.0115	0.0105	0.0126

^a In degassed 20% MeOH/20 mM Tris:10 mM NaCl buffer pH 7.2 unless otherwise noted. Emission QY's for $^3\text{MLCT}^*$ calculated from the integrated area of emission in 490-762 nm region relative to $[\text{Ru}(\text{bpy})_3]^{2+}$ in air saturated H_2O where $\phi_{\text{EmRu}} = 0.0379$. QY's determined according to eqn. 4.1 in Chapter 4.

^b In degassed 20% MeOH/25 mM Tris buffer pH 7.2.

Table B.2. Emission lifetimes of $^3\text{MLCT}^*$ state for Re-An complexes from DNA Titrations.^a

Compound	[DNA] _{bp} / [Re] ratio	τ_1 (α_1 (%)) (ns)	τ_2 (α_2 (%)) (ns)	τ_3 (α_3 (%)) (ns)	$\langle\tau\rangle$ (ns)	χ^2
Re10An	0	1.7 (14)	6.8 (86)	147 (0.4)	6.7	0.90
	0.75	5.9 (66)	25 (2.3)	77 (24)	25	
	1.5	5.6 (46)	24 (12)	76 (42)	37	1.13
	3	3.2 (27)	29 (12)	80 (61)	53	
	6	2.6 (15)	33 (16)	87 (69)	66	
Re8An	0	1.4 (39)	3.6 (61)	111 (0.6)	3.3	0.97
	0.75	2.6 (57)	30 (16)	77 (27)	27	
	1.5	2.0 (43)	23 (16)	75 (42)	36	1.03
	3	2.2 (30)	28 (17)	78 (53)	47	
	6	2.8 (23)	36 (21)	83 (56)	55	
Re6An	0	1.9 (97)	8.9 (2.0)	130 (0.9)	3.2	0.29
	0.75	1.9 (69)	30 (12)	100 (19)	23	
	1.5	1.6 (59)	26 (14)	96 (27)	31	1.02
	3	2.2 (34)	33 (25)	104 (41)	51	
	6	2.6 (23)	36 (26)	109 (51)	65	
Re3An	0	1.1 (94)	6.5 (4.1)	140 (2.3)	4.5	1.03
	0.75	1.9 (67)	17 (29)	106 (4.3)	11	
	1.5	2.7 (49)	18 (46)	79 (4.9)	13	1.12
	3	3.2 (43)	18 (51)	77 (5.7)	15	
	6	5.1 (40)	20 (55)	71 (4.6)	16	

^a All lifetimes are in nanoseconds. Measurements were obtained in argon degassed 20% MeOH/Tris buffer solutions with excitation at 355 nm and emission collected at 600 nm. The data are from single experimental measurements where the lifetimes for a given compound were obtained all on the same day and therefore under the same experimental conditions.

^b Indicates the concentration of [DNA]_{bp} to [Re] concentration expressed as a ratio. The concentration of Re-An complex was typically $\sim 2 \times 10^{-5}$ M.

^c Median lifetimes $\langle\tau\rangle$ calculated according to eqn. 3.7.

^d Chi squared χ^2 indicates the goodness of the triple-exponential fits to the experimental data obtained from the Decan fitting program.

LIST OF REFERENCES

- ¹ Zurer, P. *Chem. & Engineering News*, **1994**, 72, 41, 8.
- ² Elmer-Dewitt, P. *Time*, **1994**, 143. 46.
- ³ Lakowicz, J.R. *Principles of Fluorescence Spectroscopy*; Plenum Press; New York, **1983**.
- ⁴ Turro, N. J. *Modern Molecular Photochemistry*; Benjamin/Cummings Press; Menlo Park, CA; **1978**, 6 - 7.
- ⁵ Eftink, M. R. *Biophys. J.*, **1994**, 66, 482.
- ⁶ Rye, H., Drees, B., Nelson, H. C., Glazer, A. N. *J. Biol. Chem.*, **1993**, 268, 25229.
- ⁷ Glazer, A. N., Rye, H. S. *Nature*, **1992**, 359, 859.
- ⁸ Huang, X., Quesada, M., Mathies, R. A. *Anal. Chem.*, **1992**, 64, 2149.
- ⁹ Clark, S. M., Mathies, R. A. *Anal. Chem.*, **1993**, 215, 163.
- ¹⁰ Kapuscinski, J., Darzynkiewicz, Z. *Struct. Methods, Proc. Conversation Discip. Biomol. Stereodyn.*, 6th, **1989** (Pub. 1990), 3, 267 - 281.
- ¹¹ Yoshikawa, K., Matsuzawa, Y., Minagawa, Y., Minagawa, K., Doi, M., Matsumoto, M. *Biochem. Biophys. Reas. Comm.*, **1992**, 188, 1274.
- ¹² Chi, H.-I., Ishibashi, Y., Shima, A., Mihara, I., Otsuka, F. *J. Investigative Derm.*, **1990**, 95, 154.
- ¹³ Haugland, R., Minta, A. *Noninvasive Techniques in Cell Biology, Modern Cell Biology Vol 9*; Foscitt, J. K., Grinstein, S. (eds); Wiley-Liss; New York; **1990**, 1- 20.
- ¹⁴ Tsien, R. Y. *Chem. Eng. News*, **1994**, 72, 29, 34 - 44.
- ¹⁵ Jain, R. K., *Scientific American*, July, **1994**, 58 - 65.
- ¹⁶ Klimtchuk, E. S., Ajtai, K., Burghardt, T. P. *The Origin of Induced DC in Muscle Protein Bound Dyes Deduced by Chiral Template Model System*; Sixth Winter Conference Inter-American Photochemical Society; Clearwater, FL. **1994**.
- ¹⁷ Carver, T. E., Millar, D. P. *Proc. SPIE-Int. Soc. Opt. Eng., Time-Resolved Laser Spectroscopy in Biochemistry IV*, **1994**, 2137, 469.

- 18 Omelyanenko, V., Jiskoot, W., Herron, J. *Biochemistry*, **1993**, 32, 10423.
- 19 Rapaport, D., Shai, Y. *J. Biol. Chem.*, **1991**, 266, 23769.
- 20 Root, D. D., Wang, K. *Biochemistry*, **1994**, 33, 12581.
- 21 LePecq, J., Paoletti, C. *J. Mol. Biol.*, **1967**, 27, 87.
- 22 Markovits, J., Roques, B., Lepecq, J. *Anal. Biochem.*, **1979**, 94, 259.
- 23 Glazer, A. N., Peck, K., Mathies, R. A. *Proc Natn. Acad. Sci. U.S.A.*, **1990**, 87, 3851.
- 24 Reese, H. R. *Biopolymers*, **1994**, 34, 1349.
- 25 Kapuscinski, J., Darzynkiewicz, Z., *Nucleic Acids Research*, **1983**, 11, 7555.
- 26 Rye, H. S., Dabora, J., Quesada, M., Mathies, R. A., Glazer, A. N. *Anal. Biochem.*, **1993**, 208, 144.
- 27 Kumar, C. V., Ascuncion, E. H. *J. Am. Chem. Soc.*, **1993**, 115, 8547.
- 28 Brun, A., Harriman, A. *J. Am. Chem. Soc.*, **1991**, 113, 8153.
- 29 Geacintov, N., Zhao, R., Kuzmin, V., Kim, S., Pecora, L. *Photochem. and Photobiol.*, **1993**, 58, 185.
- 30 Chaires, J., Dattagupta, N., Crothers, D. *Biochemistry*, **1982**, 21, 3933.
- 31 Feinstein, E., Canaani, E., Weiner, L. *Biochemistry*, **1993**, 32, 13156.
- 32 Eriksson, M., Norden, B., Eriksson, S. *Biochemistry*, **1988**, 27, 8144.
- 33 Pyle, A., Rehmann, J., Meshoyrer, R., Kumar, C., Turro, N., Barton, J. K. *J. Am. Chem. Soc.*, **1989**, 111, 3051.
- 34 Chow, C., Barton, J. K. *J. Am. Chem. Soc.*, **1990**, 112, 2839.
- 35 Pyle, A. M., Morrii, T., Barton, J. K. *J. Am. Chem. Soc.*, **1990**, 112, 9432.
- 36 Campsisi, D., Morii, T., Barton, J. K. *J. Am. Chem. Soc.*, **1994**, 33, 4130.
- 37 Kirsch-De Mesmaeker, A., Orellana, G., Barton, J. K., Turro, N. *Photochem. Photobiol.*, **1990**, 52, 461.
- 38 Lerman, L. S. *J. Mol. Biol.*, **1961**, 3, 18.
- 39 Blackburn, G. M., Gait, M. J. *Nucleic Acids in Chemistry and Biochemistry*; IRL Press; New York, **1990**, 298.

- ⁴⁰ Hartl, D. L., Freifelder, D., Snyder, L. A. *Basic Genetics*, Jones and Bartlett, Boston, **1987**, 100- 103.
- ⁴¹ Watson, J. D., Crick, F. H. *Nature*, **1953**, 171, 737.
- ⁴² Saenger, W. *Principles of Nucleic Acid Structure*, Springer-Verlag, New York, **1984**, 221-226.
- ⁴³ Saenger, W. *Principles of Nucleic Acid Structure*, Springer-Verlag, New York, **1984**, 137 - 138.
- ⁴⁴ Patrick, M. H. *Photochemistry and Photobiology of Nucleic Acids*, Wang, S. Y. (eds), Academic Press, New York, **1976**, 5.
- ⁴⁵ Saenger, W. *Principles of Nucleic Acid Structure*, Springer-Verlag, New York, **1984**, 135.
- ⁴⁶ Manning, G. S. *Rev. Biophys.*, **1978**, 11, 179.
- ⁴⁷ Cantor, C. R., Schimmel, P. R. *Biophysical Chemistry Part III, The Behavior of Biological Macromolecules*; Freeman; New York; **1980**, 1154 - 1160.
- ⁴⁸ Wilson, W. D., Krishnamoorthy, C., Wang, Y.-H., Smith, J. C. *Biopolymer*, **1985**, 24, 1941.
- ⁴⁹ Patrick, M. H. *Photochemistry and Photobiology of Nucleic Acids*; Wang, S. Y. (eds); Academic Press; New York, **1976**, 16.
- ⁵⁰ Singleton, S. F., Dervan, P. B. *Biochemistry*, **1993**, 32, 13171.
- ⁵¹ Wilson, W. D., Tanious, F., Mizan, S., Yao, S., Kiselyov, A., Zon, G., Stekowski, L. *Biochemistry*, **1993**, 32, 10614.
- ⁵² Blackburn, G. M., Gait, M. J. *Nucleic Acids in Chemistry and Biochemistry*, IRL Press, New York, **1990**, 299 - 302.
- ⁵³ Coll, M., Frederick, C. A., Wang, A., Rich, A. *Proc. Natl. Acad. Sci. U.S.A.*, **1987**, 84, 8385.
- ⁵⁴ Dervan, P. B. *Science*, **1986**, 232, 464.
- ⁵⁵ Pelton, J. G., Wemmer, D. E. *J. Am. Chem. Soc.*, **1990**, 112, 1393.
- ⁵⁶ Zimmer, C., Wahnert, U. *Prog. Biophys. Mol. Biol.*, **1986**, 47, 31.
- ⁵⁷ Edwards, K. J., Jenkins, T. C., Neidle, S. *Biochemistry*, **1992**, 31, 7104.
- ⁵⁸ Barcellona, M. L., Favilla, R., von Berger, J., Avatibile, M., Ragusa, N., Masotti, L. *Arch. Biochem. Biophys.*, **1986**, 250, 48.

- 59 Kubota, Y. *Bull. Chem. Soc. Jpn.*, **1990**, 63, 758.
- 60 Jenkins, T. C., Lane, A. N., Neidle, S., Brown, D. G. *Eur. J. Biochem.*, **1993**, 213, 1175.
- 61 Norden, B., Eriksson, S., Kim, S. K., Kuvista, M., Lyng, P., Akerman, B. *Proceeding of the twenty-third Jerusalem symposium on quantum chemistry and biochemistry*; Pullman, B., & Jortner, J., (Eds.); Kluwer Academic Publishers; Dordrecht; The Netherlands, **1990**, 32-41.
- 62 Golden, J. A., Chernoff, D., Hollander, H., Feigal, D., Conte, J. E. *Lancet i*, **1989**, 654.
- 63 Jansen, K., Lincoln, P., Norden, B. *Biochemistry*, **1993**, 32, 6605.
- 64 Bailly, C., Michaux, C., Colson, P., Houssier, C., Sun, J.-S., Garestier, T., Helene, C., Henichart, J.-P., Rivalle, C., Bisagni, E., Waring, M. J. *Biochemistry*, **1994**, 33, 15348.
- 65 Wade, W. S., Mrksich, M., Dervan, P. B. *Biochemistry*, **1993**, 32, 11385.
- 66 Nunn, C. M., Jenkins, T. C., Neidle, S. *Biochemistry*, **1993**, 32, 13838.
- 67 Gao, Y.-G., Sriram, M., Denny, W. A., Wang, A. H.-J. *Biochemistry*, **1993**, 32, 9639.
- 68 Tsai, C., Jain, S. C., Sobell, H. M. *J. Mol. Biol.*, **1977**, 114, 301.
- 69 Saenger, W. *Principles of Nucleic Acid Structure*; Springer-Verlag; New York; **1984**, 360.
- 70 Hopkins, Jr., H. P., Fumero, J., Wilson, W. D. *Biopolymers*, **1990**, 29, 449.
- 71 Chou, W. Y., Marky, L. A., Zaunczkowski, D., Breslauer, K. J. *J. Biomol. Struct. Dyn.*, **1987**, 5, 345.
- 72 McGhee, J. D., von Hippel, P. H. *J. Mol. Biol.*, **1974**, 86, 469.
- 73 Saenger, W. *Principles of Nucleic Acid Structure*; Springer-Verlag; New York; **1984**, 352.
- 74 Long, E. C., Barton, J. K. *Acc. Chem. Res.*, **1990**, 23, 273.
- 75 Patrick, M. H. *Photochemistry and Photobiology of Nucleic Acids*; Wang, S. Y. (eds); Academic Press; New York; **1976**, 24 - 26.
- 76 Cantor, C. R., Schimmel, P. R. *Biophysical Chemistry, Part II, Techniques for the Study of Biological Structure and Function*; Freeman; New York; **1980**, 399 - 404.

- 77 Baguley, B. C., Le Bret, M. *Biochemistry*, **1984**, 23, 937.
- 78 Friedman, A. E., Chambron, J.-C., Sauvage, J.-P., Turro, N. J., Barton, J. K. *J. Am. Chem. Soc.*, **1990**, 112, 4960.
- 79 Stoeffler, H. D., Thornton, N. B., Schanze, K. S. *Unusual Photophysics of a Re(I) Dipyridophenazine Complex in Solution and Bound to DNA*, **1995**, In press.
- 80 Shafirovich, V., Levin, P. P., Kuzmin, V., Thorgeirsson, T., Kliger, D., Geacintov, N. *J. Am. Chem. Soc.*, **1994**, 116, 63.
- 81 Netzel, T. L., Nafisis, K., Zhao, M., Manoharan, M., Tivel, K. *Base-Sequence Dependence of Emission Lifetimes for DNA Oligomers and Duplexes Covalently Labeled with Pyrene: Relative Electron-Transfer Quenching Efficiencies of dA, dG, dC, and dT Nucleosides Toward Pyrene*. **1995**, In press.
- 82 Wu, C. W., Stryer, L. *Proc Natl. Acad. Sci.*, **1972**, 69, 1104.
- 83 Ben-Efraim, I., Bach, D., Shai, Y. *Biochemistry*, **1993**, 32, 2371.
- 84 Franks-Skiba, K., Hwang, T., Cooke, R. *Biochemistry*, **1994**, 33, 12720.
- 85 Leonard, D., Evans, T., Hart, M., Cerione, R. A., Manor, D. *Biochemistry*, **1994**, 33, 12323.
- 86 Brun, A. M., Harriman, A. *J. Am. Chem. Soc.*, **1992**, 114, 3656.
- 87 Fromgerz, P., Rieger, B. *J. Am. Chem. Soc.*, **1986**, 108, 5361.
- 88 Telser, J., Cruickshank, K., Morrison, L., Netzel, T. L., Chan, C.-K. *J. Am. Chem. Soc.*, **1989**, 111, 7226.
- 89 Smith, G., McGimpsey, W. G., Lynch, M. C., Kochevar, I. E., Redmond, R. W. *Photochem. Photobiol.*, **1994**, 59, 135.
- 90 Le Bret, M., Le Pecq, J.-B., Barbet, J., Roques, B. P. *Nucl. Acids Res.*, **1977**, 4, 1361.
- 91 Gaugain, B., Barbet, J., Capelle, N., Roques, B., Le Pecq, J.-B. *Biochemistry*, **1978** 17, 5078.
- 92 Mergny, J.-L., Slama-Schwok, A., Montenay-Garestier, T., Rougee, M., Helene, C. *Photochem. Photobiol.*, **1991**, 53, 555.
- 93 Murchie, A., Clegg, R., von Kitzing, E., Duckett, D., Diekmann, S., Lilley, D. M. *Nature*, **1989**, 341, 763.
- 94 Clegg, R., Murchie, A., Zechel, A., Carlberg, C., Diekmann, S., Lilley, D. M. *Biochemistry*, **1992**, 31, 4846.

- 95 Mergny, J.-L., Bouterine, A., Garestier, T., Belloc, F., Rougee, M., Bulychev, N., Koshkin, A., Bourson, J., Levedev, A., Valeur, B., Thuong, N., Helene, C. *Nucl. Acids Res.*, **1994**, 22, 920.
- 96 Benson, S. C., Singh, P., Glazer, A. N. *Nucl. Acids Res.*, **1993**, 21, 5727.
- 97 Sutin, N., Creutz, C. *J. Chem. Educ.*, **1983**, 60, 809.
- 98 Marcus, R. A., Sutin, N. *Biochim. Biophys. Acta.*, **1985**, 811, 265.
- 99 Baggott, J., Gilbert, A. *Essentials of Molecular Photochemistry*; Blackwell Scientific; New York, **1991**.
- 100 Turro, N. J. *Modern Molecular Photochemistry*; Benjamin/Cummings Press; Menlo Park, CA; **1978**.
- 101 Förster, T., *Discuss. Faraday Soc.*, **1959**, 27, 7.
- 102 Förster, T., *Fluoreszenz Organische Verbindungen*, **1951**, Gottingen: Vandenhoech and Ruprech.
- 103 Dexter, D. L. *J. Chem. Phys.*, **1953**, 21, 836.
- 104 Baggott, J., Gilbert, A., *Essentials of Molecular Photochemistry*, **1991**, Blackwell Scientific, 176.
- 105 Wang, Y., Schanze, K. S. *Inorg. Chem.*, **1994**, 33, 1354.
- 106 Wang, Y., Hauser, B. T., Rooney, M., Burton, R. D., Schanze, K. S. *J. Am. Chem. Soc.*, **1993**, 115, 5675.
- 107 Wang, Y., Schanze, K. S. *Chemical Phys.*, **1993**, 176, 305.
- 108 Lucia, L. A., Burton, R. D., Schanze, K. S. *Inorganica Chimica Acta*, **1993**, 208, 103.
- 109 Worl, L. A., Duesing, R., Pingyun, C., Ciana, L. D., Meyer, T. J. *J. Chem. Soc. Dalton Trans.*, **1991**, 849 - 858.
- 110 Luong, J. C., Faltynsek, R., Wrigton, M. S. *J. Am. Chem. Soc.*, **1980**, 102, 7892.
- 111 Whighton, M., Morse, D. L. *J. Am. Chem. Soc.*, **1974**, 96, 998.
- 112 Stufkens, D. J. *Comments Inorg. Chem.*, **1992**, 13, 359.
- 113 Schanze, K. S., MacQueen, D. B., Perkins, T. A., Cabana, L. A. *Coord. Chem. Rev.*, **1993**, 122, 63.
- 114 Schanze, K. S., Cabana, L. A. *J. Phys. Chem.*, **1990**, 94, 2740.

- 115 Chen, P., Westmoreland, T. D., Danielson, E., Schanze, K. S., Anthon, D., Neveux, P. E., Jr., Meyer, T. J. *Inorg. Chem.*, **1987**, 26, 1116.
- 116 Chen, P., Duesing, R., Graff, D. K., Meyer, T. J. *J. Phys. Chem.*, **1991**, 95, 5850.
- 117 Ackenheil, M., Muller-Spahn, F. *Bioactive Molecules Vol. 4, Phenothiazines and 1,4-Benzothiazines*; Gupta, R. R. (eds.); Elsevier; New York; **1988**, 649.
- 118 Ben-Hur, E., Prager, A., Green, M., Rosenthal, I. *Chem. Biol. Interact.*, **1980**, 29, 223.
- 119 Le Griebrok, J. *Proc. Natl. Acad. Sci. USA*, **1979**, 76, 469.
- 120 Motohashi, N. *Bioactive Molecules Vol. 4, Phenothiazines and 1,4-Benzothiazines*; Gupta, R. R. (eds.); Elsevier; New York; **1988**, 707-710.
- 121 Lyng, R., Hard, T., Norden, B. *Biopolymers*, **1987**, 26, 1327.
- 122 Wildenauer, D. B., Zeeb-Walde, B. C. *Biochem. Biophys. Res. Commun.*, **1983**, 116, 469.
- 123 Dahl, S. G., Hall, H. *Psychopharmacol.*, **1981**, 74, 101.
- 124 Fujita, H., Hayashi, H., Suzuki, K. *Photochem. Photobiol.*, **1981**, 34, 101.
- 125 van Den Broeke, L. T., Ouijja, E. H., Bojarski, J., Beyersbergen van Henegouwen, G. *Photochem. Photobiol.*, **1994**, 59, 140.
- 126 Stufkens, D. J. *Comments Inorg. Chem.*, **1992**, 13, 359.
- 127 Gupta, R. R., Kumar, M. *Bioactive Molecules Vol. 4, Phenothiazines and 1,4-Benzothiazines*; Gupta, R. (eds); Elsevier; New York; **1988**, 299.
- 128 Gupta, R. R., Kumar, M. *Bioactive Molecules Vol. 4, Phenothiazines and 1,4-Benzothiazines*; Gupta, R. R. (eds.); Elsevier; New York; **1988**, 271-355.
- 129 MacQueen, D. B., Schanze, K. S. *J. Am. Chem. Soc.*, **1991**, 113, 7470.
- 130 Barton, J. K., Goldberg, J. M., Kumar, C. V., Turro, N. J. *J. Am. Chem. Soc.*, **1986**, 108, 2081.
- 131 Gabbay, E. J., Scofield, R. E., Baxter, C. S. *J. Am. Chem. Soc.*, **1973**, 95, 7850.
- 132 Clark, M., Cramer, R. D., III, Van Openbosch, N. *J. Comput. Chem.*, **1989**, 10, 982.
- 133 Marcus, R. A. *J. Chem. Phys.*, **1965**, 43, 679.
- 134 Ballardini, R., Varani, G., Indelli, M., Sandola, F. *J. Phys. Chem.*, **1984**, 88, 2547.

- 135 Forster, M., Hester, R. E. *J. Chem. Soc., Faraday Trans. 2*, **1981**, 77, 1521.
- 136 Murphy, C. J., Arkin, M. R., Jenkins, Y., Ghatlia, N. D., Bossmann, S. H., Turro, N. J., Barton, J. K. *Science*, **1993**, 97, 1599.
- 137 Wakelin, L. P., Romanos, M., Chen, T. K., Glaubiger, D., Canellakis, E. S., Waring, M. J. *J. Am. Chem. Soc.*, **1978**, 17, 5057.
- 138 MacQueen, D. B., Eyler, J. R., Schanze, K. S., *J. Am. Chem. Soc.*, **1992**, 114, 1897.
- 139 Zwelling, L., Mayes, J., Altschuler, E., Satitpunwaycha, P., Trittin, T., Hacker, M., *Biochemical Pharmacology*, **1993**, 46, 2, 265.
- 140 Wilson, W. D., Ratmeyer, L., Zhao, M., Strekowski, L., Boykin, D., *Biochemistry*, **1993**, 32, 4098.
- 141 Wunz, T., Craven, M., Karol, M., Hill, G. C., Remers, W., *J. Med. Chem.*, **1990**, 33, 1549.
- 142 Summers, J., Kim, K., Mazdiyasni, H., Holms, J., Ratajczyk, J., Stewart, A., Dyer, R., Carter, G., *J. Med. Chem.*, **1990**, 33, 992.
- 143 Yoa, S., Bair, K., Cory, M., Wilson, W. D. Unpublished Results.
- 144 Turro, N. J. *Modern Molecular Photochemistry*; Benjamin/Cummings; Menlo Park, CA; **1978**, 305 - 309.
- 145 Patrick, M. H. *Photochemistry and Photobiology of Nucleic Acids Vol. II, Biology*; Wang, S. Y. (eds); Academic Press; New York; **1976**, 6.
- 146 Reichman, M. E., Rice, S. A., Thomas, C. A., Doty, P. *J. Am. Chem. Soc.*, **1954**, 76, 3047.
- 147 Peek, M. E., Lipscomb, L. A., Bertrand, J., Goa, Q., Roques, B., Gargay-Jaureguiberry, C., Williams, D., *Biochemistry*, **1994**, 33, 3794.
- 148 Marzilli, L. G., Petho, G., Lin, M., Kim, M. S., Dixon, D. W. *J. Am. Chem. Soc.*, **1992**, 114, 7575.
- 149 Wolfe, A., Shimer, G. H., Jr., Meehan, T. *Biochemistry*, **1987**, 26, 6392.
- 150 Scatchard, G., *Ann. N.Y. Acad. Sci.*, **1949**, 51, 660.
- 151 Fairley, T., Molock, F., Boykin, D. W., Wilson, W. D. *Biopolymers*, **1988**, 27, 1433.
- 152 Meehan, T., Gamper, H., Becker, J. F. *J. Biol. Chem.*, **1982**, 17, 10479.
- 153 Jernstrom, B., Graslund, A. *Biophys. Chem.*, **1994**, 49, 185.

- 154 Steenken, S., Telo, J. P., Novais, H. M., Candeis, L. P. *J. Am. Chem. Soc.*, **1992**, 114, 4701.
- 155 Kavarnos, G. J., Turro, N. J. *Chem. Rev.*, **1986**, 86, 401.
- 156 Mattes, S. L., Farid, S. *Organic Photochemistry*; Padwa, A., (eds.); Marcel Dekker; New York, **1983**, Vol. 6.
- 157 Birks, J. B. *Photophysics of Aromatic Molecules*; Wiley; New York; **1970**.
- 158 Dawson, W. R., Windsor, M. W. *J. Phys. Chem.*, **1968**, 72, 3251.
- 159 Kliger, D. S., Albrecht, A. C. *J. Chem. Phys.*, **1970**, 53, 4059.
- 160 Giordano, P. J., Wrighton, M. S., *J. Am. Chem. Soc.*, **1979**, 101, 2888.
- 161 Padhye, M., McGlynn, S., Kasha, M., *J. Chemical Physics*, **1956**, 24, 588.
- 162 Evans, D. F., *J. Chem. Soc.*, **1957**, 1351.
- 163 Wang, Z., Weininger, S., McGimpsey, W. G., *J. Phys. Chem.*, **1993**, 97, 374.
- 164 Demas, J. N. *J. Chem. Education*, **1983**, 60, 803.
- 165 Triplet absorption spectrum from Evans, D. F., *J. Chem. Soc.*, **1957**, 1351 (ref 164).
- 166 Kikuchi, K., Kokubun, H., Koizumi, M., *Bull. Chem. Soc. Japan*, **1971**, 44, 1527.
- 167 Medinger, T., Wilkinson, F. *Trans. Faraday Soc.*, **1965**, 61, 620.
- 168 Agbandje, M., McKenna, R. in *Nucleic Acid Targeted Drug Design*; Propst, C. L., Perun, T. J., (eds); Dekker; **1992**, 525 - 556.
- 169 Rodger, A., Blagbrough, I. S., Adlam, G., Carpenter, M. *Biopolymers*, **1994**, 34, 1583.
- 170 Wilson, W. D., Wang, Y.-H., Kusuma, S., Chandrasekaran, S., Yang, N. C., Boykin, D. W. *J. Am. Chem. Soc.*, **1985**, 107, 4989.
- 171 Pindur, U., Haber, M., Sattler, K. *J. Chem. Educ.*, **1993**, 70, 263.
- 172 Saenger, W. *Principles of Nucleic Acid Structure*; Springer; New York; **1983**, 355.
- 173 Basu, H. S., Shafer, R. H., Marton, L. J. *Nucleic Acids Res.*, **1987**, 5873.
- 174 Dabrowski, J. C., Stankus, A. A., Goodisman, J. in *Nucleic Acid Targeted Drug Design*; Propst, C. and Perun, T., eds.; Dekker; New York, **1992**, 93.
- 175 Wrighton, M., Bresdesen, J. J. *Organometal. Chem.*, **1973**, 50, C35.

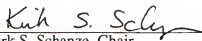
- ¹⁷⁶ Smith, N.L. (1950) JOC, 15, 1125.
- ¹⁷⁷ Godfroi, E., Wittle, E. (1956) JOC, 21, 1163.
- ¹⁷⁸ Meyer, Peek (1990) Dissertation, University of North Carolina, Chapel Hill.
- ¹⁷⁹ Sullivan, B. P., Meyer, T. J. *J. Chem. Soc.Chem. Commun.*, **1984**, 93, 3885.
- ¹⁸⁰ Saenger, W. *Principles of Nucleic Acid Structure*; Springer-Verlag; New York; **1984**, 221-228.
- ¹⁸¹ Schmechel, D. E., Crothers, D. M. *Biopolymers*, **1971**, 10, 465.
- ¹⁸² Cantor, C. R., Schimmel, P. R. *Biophysical Chemistry Part III: The Behavior of Biological Macromolecules*; Freeman; New York, **1980**, 1242 - 1245.
- ¹⁸³ Wolfe, A., Shimer, G. H., Meehan, T. *Biochemistry*, **1987**, 26, 6392.

BIOGRAPHICAL SKETCH

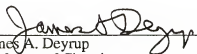
Nancy Eloise Byrnes was born on October 3, 1961, in South Bend, Indiana, the fourth of six children for Edward E. Byrnes and Mary E. Leinfelder Byrnes. Her family moved to North Central New Jersey in 1963 where her father, a mechanical engineer, worked as vice president of operations at several different companies throughout the next twenty years, and her mother, a registered dietitian, artist and musician, dedicated her time to raising the family. Nancy led an active childhood as a good student interested in reading, drawing, music, animals, and athletic activities such as swimming, diving, horseback riding, basketball and wrestling with her brothers. She played the clarinet in concert band for eight years and swam and dove for the local swim team during her high school years. She attended the University of New Hampshire for a semester after high school, but due to undeveloped goals, decided to postpone college and instead work at various jobs while establishing residency in New Hampshire. During this time she was married for several years and eventually found an interesting position working as a phlebotomist and part-time technician in a hospital laboratory. She discovered an interest in chemistry, particularly the medical aspects of the science, and proceeded to pursue a Bachelor of Arts degree in chemistry at Plymouth State College where she graduated magna cum laude four years later. During the summer after her junior year at PSC she participated in the NSF Undergraduate Research program at Dartmouth College under the supervision of Dr. Gordon Gribble and realized that graduate school held many opportunities for further study in specialized areas of chemistry. Therefore she decided to pursue a Ph.D. in organic chemistry at University of Florida where she has been studying and participating in research under the supervision of Dr. Kirk S. Schanze since the summer of 1990. After

receiving her Ph.D. Nancy will participate in postdoctoral research at Georgia State University in the laboratories of Dr. Dabney Dixon and Dr. Thomas Netzel studying electron transfer in various DNA binding molecules.

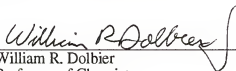
I certify that I have read this study and that in my opinion it conforms to acceptable standards of scholarly presentation and is fully adequate, in scope and quality, as a dissertation for the degree of Doctor of Philosophy.


Kirk S. Schanze, Chair
Associate Professor of Chemistry

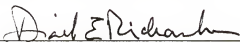
I certify that I have read this study and that in my opinion it conforms to acceptable standards of scholarly presentation and is fully adequate, in scope and quality, as a dissertation for the degree of Doctor of Philosophy.


James A. Deyrup
Professor of Chemistry


I certify that I have read this study and that in my opinion it conforms to acceptable standards of scholarly presentation and is fully adequate, in scope and quality, as a dissertation for the degree of Doctor of Philosophy.


William R. Dolbier
Professor of Chemistry

I certify that I have read this study and that in my opinion it conforms to acceptable standards of scholarly presentation and is fully adequate, in scope and quality, as a dissertation for the degree of Doctor of Philosophy.


David E. Richardson
Professor of Chemistry

I certify that I have read this study and that in my opinion it conforms to acceptable standards of scholarly presentation and is fully adequate, in scope and quality, as a dissertation for the degree of Doctor of Philosophy.


Laszlo Prokai
Assistant Professor of Pharmaceutics

This dissertation was submitted to the Graduate Faculty of the Department of Chemistry in the College of Liberal Arts and Sciences and to the Graduate School and was accepted as partial fulfillment of the requirements for the degree of Doctor of Philosophy.

May, 1995

Dean, Graduate School